Title

Carbonate clumped isotope systematics for lacustrine carbonates and applications to late Pleistocene hydroclimate in Western North America

Author

Arnold, Alexandrea Jay

Publication Date

2024

Peer reviewed|Thesis/dissertation

UNIVERSITY OF CALIFORNIA

Los Angeles

Carbonate clumped isotope systematics for lacustrine carbonates and applications to late Pleistocene hydroclimate in Western North America

A dissertation submitted in partial satisfaction

of the requirements for the degree

Doctor of Philosophy in Atmospheric and Oceanic Sciences

by

Alexandrea Jay Arnold

2024

ABSTRACT OF THE DISSERTATION

Carbonate clumped isotope systematics for lacustrine carbonates and applications to late Pleistocene hydroclimate in Western North America

by

Alexandrea Jay Arnold
Doctor of Philosophy in Atmospheric and Oceanic Sciences
University of California, Los Angeles, 2024
Professor Aradhna K. Tripati, Chair

Lakes are responsive to climate, and in turn, sediment formed within lakes function as recorders of environmental change. This dissertation explores how the clumped and bulk stable isotope geochemistry of lacustrine sediments can be used to understand the terrestrial hydrologic cycle, both in the modern and past. To better understand the modern systematics of clumped isotopes in freshwater carbonates to extend to paleo-applications, Chapter 1 discusses the first extensive calibration study of different types of field-collected carbonates. We examine the uncertainties associated with the use of a single calibration in different types of carbonates, and evaluate relationships for material-specificity, allowing for more robust reconstructions of past temperature and water $\delta^{18}O$ reconstructions. In the following three chapters, these calibrations

are applied to late-Pleistocene lacustrine sediments from eleven lake basins in Western North America to evaluate multiple hydroclimate parameters, including temperature, water $\delta^{18}O$, evaporation, and precipitation, including for the Last Glacial Maximum (LGM; 23-19 ka) and deglaciation. In Chapter 2, we examine Lake Bonneville, which reached the size of a modern-day Great Lake at its maximum extent, and report the importance of evaporation suppression in setting and sustaining the lake, while also quantifying precipitation, with maxima during the early LGM and Heinrich Stadial 1 (HS1). In Chapter 3, we examine four basins in the Northern Great Basin to quantify the magnitude of evaporation and precipitation variation in the mid-latitudes, and test for a hypothesized precipitation dipole. At the two northernmost sites, we report evidence in support of enhanced evaporation depression and westerly-derived precipitation during the LGM and deglacial, leading to the presence of lakes in the region. We find at the southernmost site evidence for reduced evaporation and evidence for moisture advection into the continental interior from the south (e.g. higher atmospheric river and North American monsoonal precipitation) during the deglacial. In Chapter 4, we evaluate hydroclimatic changes using six basins in Arizona, New Mexico, and Northern Mexico, and find reduced temperatures and evaporation rates with increases in precipitation during the LGM and deglacial. The drivers of LGM and deglacial precipitation vary, with winter-derived precipitation the primary source of high levels of moisture in the Southwestern US, and tropical storms the likely origin of more modest enhancements in Northern Mexico.

The dissertation of Alexandrea Jay Arnold is approved.

Gang Chen

Yongkang Xue

Robert Alfred Eagle

Aradhna K. Tripati, Committee Chair

University of California, Los Angeles

2024

DEDICATION

To Ryan, Mary, and Dick.

TABLE OF CONTENTS

LIST OF FIGURES

LIST OF TABLES

ACKNOWLEDGEMENTS

The origin of my interest in climate started when my father and I used to take our cameras to go 'lightning chasing' in the summers in Tucson, Arizona, in hopes of getting a perfect shot. A reporter from the *Arizona Daily Star* wrote an article about our unconventional hobby: "Alexandrea Arnold was 9 years old when she took this photo from the parking lot at Pima Canyon. The sixth grader says she wants to be a meteorologist when she grows up."

Today, as a grown-up, I would consider myself as a paleoclimatologist rather than a meteorologist (but close enough). My dreams could not have been reached without the steadfast support from my family and partner. Ryan, Mary, and Dick – you three were my source of inspiration – thank you for always believing in me and making me believe in myself. Dave – thank you for your love, patience, and motivation to accomplish my goals within and beyond graduate school.

I feel very lucky to be under the guidance of my advisor, Aradhna Tripati, throughout the last eight years. Words feel shallow in expressing my gratitude for her mentorship and guidance throughout my undergraduate and graduate career. She has supported my interests and growth inside and outside of academia and because of her, I am a better scientist and person.

This work would not have been possible without my colleagues in the Tripati-Eagle lab, my AOS cohort, my collaborators, and my mentors – to those that sent samples from their collections for our studies, to those helped me acquire samples in the field, to those assisted in mass spectrometry and analysis, and to those helped develop ideas through discussion – I am thankful for their contributions and that this journey is one that we had the opportunity to share together.

In writing this dissertation, I am so grateful to have had the opportunity to have driven many miles through beautiful swaths of land in North America for sample collection in six states. I wish to acknowledge the Indigenous peoples that are the past, present, and future caretakers and stewards of the lands in which my research areas encompass.

Chapter 1 is in review at *The Depositional Record* and work was supported by NSF CAREER award EAR-1352212 and NSF ICER-1936715 and Heising-Simons Foundation 2021-3137, with mass spectrometry supported by the Department of Energy through BES grant DE-FG02-13ER16402. Chapter 2 is being prepared for submission to *PNAS* and work was supported by NSF CAREER award EAR-1352212 and NSF ICER-1936715 and Heising-Simons Foundation 2021-3137. Chapter 3 is being prepared for submission to *Nature Communications* and work was supported by NSF CAREER award EAR-1352212 and NSF ICER-1936715 and Heising-Simons Foundation 2021-3137. Chapter 4 is being prepared for submission to *Nature Geoscience* and work was supported by UCMexus Grant to Aradhna Tripati and Priyadarsi Roy, NSF CAREER award EAR-1352212 and NSF ICER-1936715 and Heising-Simons Foundation 2021-3137. Funding support for my graduate education was provided by the Cota-Robles Fellowship, the Center for Diverse Leadership in Science Fellowship, a NSF Cultural Transformations in the Geosciences Community Fellowship, and the University of California Office of the President's Dissertation Year Fellowship.

VITA

2023 University of California, Los Angeles

Ph.D. Candidate in Atmospheric and Oceanic Sciences

2019 University of California, Los Angeles

M.S. in Atmospheric and Oceanic Sciences,

2017 University of California, Los Angeles

B.S. in Atmospheric, Oceanic, and Environmental Sciences

B.A. in Earth and Environmental Sciences,

2013 Santa Barbara City College

A.A, Liberal Arts and Science: Science and Math Emphasis, Honors

A.A, Liberal Arts and Science: Social and Behavioral Science Emphasis, Honors

PUBLICATIONS

*Indicates joint first-author

Arnold, A.J., Kowler, A., Roy, P., Terrazas A., Smith, V., Santi, L., Tripati, A., Late-Pleistocene hydroclimates in Southwestern North America from clumped isotopes, *in preparation for Nature Geoscience*

Arnold, A.J.*, Santi L.M.*, Ibarra, D.E., Lombarda, R., Lora, J., Tripati, A.K., Clumped Isotope Hydroclimates of Late Pleistocene Pluvial Lakes in the Great Basin, *in preparation for Nature Communications*

Arnold, A.J.*, Mering, J.A.*, Santi L.M., Lee, H., Lerback, J., Petryshyn, V.A., D.E. Ibarra, Oviatt, C.G. Lora, J.M., Tripati, A.E., Rainfall or Evaporation? Controls on Great Lake Bonneville, *in preparation for PNAS.*

Arnold, A.J., Mering, J.A., Santi L.M., Román-Palacios, C., Petryshyn, V., Li, H., Mitsunaga, B., Elliott, B., Wilson, J., Lucarelli, J.K., Boch, R., Ibarra, D.E., Li, L., Fan, M., Kaufmann, D., Cohen, A.S., Dunbar, R.B., Russell, J.M., Lalonde, S., Roy, P., Dietzel, M., Liu, X., Chang, F.,

Eagle, R.A., Tripati, A.K. Comparative clumped isotope temperature relationships in freshwater carbonates, *in revision for The Depositional Record*

Lopez-Maldonado, Bateman, J., Ellis, A., Bader, N., Ramirez, P., **Arnold, A.J.**, Ajoku, O., Jesmok, G., Upadhyay, D., Mitsunaga, B., Elliott, B., Lora, J., Tabor, C., Tripati, A., (2023), Temperature and hydrological cycle changes in the Pacific Northwest Over the Past 36,000 years from clumped isotope and model analysis. *Paleoceanography and Paleoclimatology.*

Cheng, F., Garzione, C., Li, X., Salzmann, U., Schwarz, F., Haywood, A., Tindall, J., Nie, J., Li, L., Wang, L., Elliot, B., Liu, W., Upadhyay, D., **Arnold, A.J.**, Tripati, A., (2022), Paleoclimate shows alpine permafrost accounts for a third of carbon release. *Nature Communications.*

Linol, B., Montañez, I., Lombardo, A., Kuta, D., Upadhyay, D., **Arnold, A.J.**, Tripati, A., Bauer, A., Musa, S., (2021), Towards disentangling co-evolving sea-level and tectonic changes in Upper Cretaceous-Cenozoic marine sequences flanking southernmost Africa using strontium isotope stratigraphy and clumped isotope thermometry, *South African Journal of Geology.*

Upadhyay, D., Lucarelli, J., Jesmok, G., **Arnold, A.J.**, Bricker, H., Bateman, J., Ulrich, R., Deflise, W., Eagle, R., Elliott, B., Tripati, A., (2021) , Intercomparability and reproducibility of standard values for carbonate clumped isotope analysis (Δ47 and Δ48) via gas source isotope ratio mass spectrometry using different approaches for standardization on four instrumental configurations, *Rapid Communications in Mass Spectrometry.*

Li, H., Liu, X., **Arnold, A.J.**, Elliott, B., Flores, R., and Kelley, A.M., Tripati, A., 2021. Mass 47 clumped isotope signatures in modern lacustrine authigenic carbonates in Western China and other regions and implications for paleotemperature and paleoelevation reconstructions. *Earth and Planetary Science Letters*, 10.1016/j.epsl.2021.116840

Li, H., Liu, X., Tripati, A., Feng, S., Elliott, B., Whicker, C., **Arnold, A.J.**, and Kelley, A.M., 2020. Factors controlling the oxygen isotopic composition of lacustrine authigenic carbonates in Western China: implications for paleoclimate reconstructions. *Scientific Reports*, 10.1038/s41598-020-73422-4

Santi, L., **Arnold, A. J.**, Ibarra, D., Whicker, C., Mering, J., Lombarda, R., Lora, J., Tripati, A., 2020, Clumped Isotope Constraints on Changes in Latest Pleistocene Hydroclimate in the Northwest Great Basin: Lake Surprise, California. *GSA Bulletin*, 10.1130/B35484.1

Santi, L., **Arnold, A.J.**, Ibarra, D., Whicker, C., Mering, J., Oviatt, C., Tripati, A., 2019. Lake level fluctuations in the Northern Great Basin for the last 25,000 years. *Desert Symposium Conference Proceedings*, 10.31223/osf.io/6as7t

INTRODUCTION

A majority of climate model projections in Western North America disagree on both the sign and magnitude of future precipitation change (IPCC, 2023; Maloney et al., 2014). As climate warms and evaporation rates rise, the projected impacts on the water cycle also remain uncertain in an already water-stressed region. The study of the past can improve our ability to study how different earth system processes respond to changing climate forcing, but there is still a high degree of variability in predictions of climate models of past precipitation changes (Oster et al., 2015). To better understand how the moisture budget in Western North America may evolve in the future, paleoenvironmental proxy evidence from the sedimentary record can be critical to extend our understanding of atmospheric processes and their behavior in different climatic regimes.

In comparison to marine proxies, quantitative terrestrial proxies with a strong physical grounding are relatively scarce. While different types of physical (e.g. tree rings; Esper et al., 2018), biological (e.g. pollen; Bartlein et al., 2011) or chemical (e.g. isotopes; Santi et al., 2020) terrestrial materials can serve as recorders of past conditions and provide insight into past climate variability with varying degrees of uncertainty, many proxies are limited in not being thermodynamically-based. Carbonate clumped isotopes (denoted by Δ_{47}) stands out because of originating from zero-point energy differences between isotopologues of carbonate minerals, and thus for samples forming at equilibrium, the proxy provides a relatively assumption-free constraint on temperature (Eiler & Schauble, 2004; Ghosh et al., 2006; Schauble et al., 2006). At the same time, Δ_{47}-temperatures can be used to calculate evaporation rates (Mering, 2015; Santi et al., 2020). Further, the resultant isotopic data from clumped isotope measurements can be applied within a hydrologic modeling framework to lacustrine sediments from endorheic, or

internally-draining, lakes to estimate precipitation, since their area and extent represents the delicate balance between precipitation and evaporation (Mering, 2015; Santi et al., 2019).

Given the potential of lacustrine carbonate minerals to disentangle terrestrial climatic history, the first chapter of this thesis calibrates Δ_{47} in a wide variety of modern freshwater carbonates. We incorporate new measurements of modern freshwater carbonates in concert with previously published data to construct the largest freshwater calibration dataset for clumped isotopes to date. Using our compiled dataset, we constrain the relationship between Δ_{47} and temperature for biologic, abiotic, and biologically-mediated carbonate groups and evaluate material specificity in the clumped isotope-temperature dependence.

The second section of this thesis (Chapters 2-4) utilizes the new calibrations derived in the first section and explores applications of clumped isotope thermometry for paleohydrological reconstructions in Western North America (24-42°N, 100-120°W) using lacustrine sediments from the Last Glacial Maximum (LGM), roughly 23,000-19,000 years ago (ka) (Clark et al., 2009), and the subsequent deglaciation. During the LGM and deglacial, cool and wet conditions prevailed due to reductions in greenhouse gas concentrations and the presence of large ice sheets in North America, associated with the dramatic reorganization of hydroclimates. These conditions allowed for the existence of hundreds of pluvial lakes in Western North America, many of which have subsequently disappeared (Reheis, 1999; Ibarra et al., 2018). However, the hydrologic mechanisms and relative influence of each component of the moisture budget that supported the existence and extent of lakes over time has been the subject of debate (Lyle et al., 2012; Munroe and Laabs, 2013; Oster et al., 2015; Lora et al., 2017; Santi et al., 2020). Thus, the LGM and deglacial present unique opportunities to understand the drivers of hydroclimate in climate states that are fundamentally different than at present (Braconnot et al., 2012).

We use our clumped isotope derived estimates of lake temperature and water isotopes within a novel hydrologic and isotopic mass balance model that accounts for basin hypsometry to quantify past precipitation and evaporation rates at each site. We test hypotheses on the evolution of moisture sources, moisture transport, and the magnitude of precipitation changes. Chapter 2 examines Lake Bonneville, to explore the drivers of the growth and decay of the largest and most studied late Pleistocene lake in Western North America. Chapter 3 explores the spatially and temporally asynchronous nature of pluvial maxima and subsequent retreat at a suite of 4 lakes in the Northern Great Basin and quantifies an asymmetry in moisture delivery to different watersheds and probes the origins. Chapter 4 analyzes a suite of six lakes in Southwestern United States and Northern Mexico to evaluate large-scale dynamical changes and the drivers of regional hydroclimatic change.

References

Bartlein, P.J., Harrison, S.P., Brewer, S., Connor, S., Davis, B.A.S., Gajewski, K., Guiot, J., Harrison-Prentice, T.I., Henderson, A., Peyron, O., Prentice, I.C., Scholze, M., Seppä, H., Shuman, B., Sugita, S., Thompson, R.S., Viau, A.E., Williams, J. & Wu, H. (2011) Pollen-based continental climate reconstructions at 6 and 21 ka: a global synthesis. *Climate Dynamics*, *37*(3), 775–802. https://doi.org/10.1007/s00382-010-0904-1.

Eiler, J.M. & Schauble, E. (2004) 18O13C16O in Earth's atmosphere. *Geochimica et Cosmochimica Acta*, *68*(23), 4767–4777. https://doi.org/10.1016/j.gca.2004.05.035.

Esper, J., St. George, S., Anchukaitis, K., D'Arrigo, R., Ljungqvist, F.C., Luterbacher, J., Schneider, L., Stoffel, M., Wilson, R. & Büntgen, U. (2018) Large-scale, millennial-length temperature reconstructions from tree-rings. *Dendrochronologia*, *50*, 81–90. https://doi.org/10.1016/j.dendro.2018.06.001.

Ghosh, P., Adkins, J., Affek, H., Balta, B., Guo, W., Schauble, E.A., Schrag, D. & Eiler, J.M. (2006) 13C–18O bonds in carbonate minerals: a new kind of paleothermometer. *Geochimica et Cosmochimica Acta*, *70*(6), 1439–1456. https://doi.org/10.1016/j.gca.2005.11.014.

Ibarra, D.E., Egger, A.E., Weaver, K.L., Harris, C.R. & Maher, K. (2014) Rise and fall of late Pleistocene pluvial lakes in response to reduced evaporation and precipitation: Evidence from Lake Surprise, California. *GSA Bulletin*, *126*(11–12), 1387–1415. https://doi.org/10.1130/B31014.1.

Ibarra, D.E., Oster, J.L., Winnick, M.J., Caves Rugenstein, J.K., Byrne, M.P. & Chamberlain, C.P. (2018) Warm and cold wet states in the western United States during the Pliocene–Pleistocene. *Geology*, *46*(4), 355–358.

Intergovernmental Panel on Climate Change (IPCC) (Ed.) (2023) North America. In: *Climate Change 2022 – Impacts, Adaptation and Vulnerability: Working Group II Contribution to the Sixth Assessment Report of the Intergovernmental Panel on Climate Change*. Cambridge, Cambridge University Press, pp. 1929–2042. https://doi.org/10.1017/9781009325844.016.

Lora, J.M., Mitchell, J.L., Risi, C. & Tripati, A.E. (2017) North Pacific atmospheric rivers and their influence on western North America at the Last Glacial Maximum. *Geophysical Research Letters*, *44*(2), 1051–1059. https://doi.org/10.1002/2016GL071541.

Lyle, M., Heusser, L., Ravelo, C., Yamamoto, M., Barron, J., Diffenbaugh, N.S., Herbert, T. & Andreasen, D. (2012) Out of the Tropics: The Pacific, Great Basin Lakes, and Late Pleistocene Water Cycle in the Western United States. *Science*, *337*(6102), 1629–1633. https://doi.org/10.1126/science.1218390.

Maloney, E.D., Camargo, S.J., Chang, E., Colle, B., Fu, R., Geil, K.L., Hu, Q., Jiang, X., Johnson, N., Karnauskas, K.B., Kinter, J., Kirtman, B., Kumar, S., Langenbrunner, B., Lombardo, K., Long, L.N., Mariotti, A., Meyerson, J.E., Mo, K.C., Neelin, J.D., Pan, Z., Seager, R., Serra, Y., Seth, A., Sheffield, J., Stroeve, J., Thibeault, J., Xie, S.-P., Wang, C., Wyman, B. & Zhao, M. (2014) North American Climate in CMIP5 Experiments: Part III: Assessment of Twenty-First-Century Projections. *Journal of Climate*, *27*(6), 2230–2270. https://doi.org/10.1175/JCLI-D-13-00273.1.

Mering, J.A. (2015) *New constraints on water temperature at Lake Bonneville from carbonate clumped isotopes*. University of California, Los Angeles.

Munroe, J.S. & Laabs, B.J. (2013) Temporal correspondence between pluvial lake highstands in the southwestern US and Heinrich Event 1. *Journal of Quaternary Science*, *28*(1), 49–58.

Munroe, J.S. & Laabs, B.J.C. (2013) Latest Pleistocene history of pluvial Lake Franklin, northeastern Nevada, USA. *GSA Bulletin*, *125*(3–4), 322–342. https://doi.org/10.1130/B30696.1.

Oster, J.L., Ibarra, D.E., Winnick, M.J. & Maher, K. (2015) Steering of westerly storms over western North America at the Last Glacial Maximum. *Nature Geoscience*, *8*(3), 201–205.

Reheis, M.C. (1999) *Extent of Pleistocene lakes in the western Great Basin*.

Santi, L., Arnold, A., Mering, J., Arnold, D., Tripati, A., Whicker, C. & Oviatt, C.G. (2019) Lake level fluctuations in the Northern Great Basin for the last 25,000 years. *Exploring Ends of Eras in the Eastern Mojave Desert: 2019 Desert Symposium Field Guide and Proceedings*, 176–186. https://doi.org/10.31223/osf.io/6as7t.

Santi, L., Arnold, A.J., Ibarra, D.E., Whicker, C.A., Mering, J.A., Lomarda, R.B., Lora, J.M. & Tripati, A. (2020) Clumped isotope constraints on changes in latest Pleistocene hydroclimate in the northwestern Great Basin: Lake Surprise, California. *GSA Bulletin*, *132*(11–12), 2669–2683. https://doi.org/10.1130/B35484.1.

Schauble, E.A., Ghosh, P. & Eiler, J.M. (2006) Preferential formation of 13C–18O bonds in carbonate minerals, estimated using first-principles lattice dynamics. *Geochimica et Cosmochimica Acta*, *70*(10), 2510–2529. https://doi.org/10.1016/j.gca.2006.02.011.

CHAPTER 1

Comparative clumped isotope temperature relationships in freshwater carbonates

Alexandrea Arnold, John Mering, Lauren Santi, Cristian Román-Palacios, Huashu Li, Victoria Petryshyn, Bryce Mitsunaga, Ben Elliott, John Wilson, Jamie Lucarelli, Ronny Boch, Daniel Ibarra, Lin Li, Majie Fan, Darrell Kaufman, Andrew Cohen, Rob Dunbar, James Russell, Stefan Lalonde, Priyadarsi D. Roy, Martin Dietzel, Xingqi Liu, Fengming Chang, Robert A. Eagle, Aradhna Tripati

Abstract

Lacustrine, riverine, and spring carbonates represent archives of terrestrial climates and their geochemistry has been used to study paleoenvironments. Clumped isotope thermometry is an emerging tool that has been applied to freshwater carbonates. Limited work has been done to evaluate comparative relationships between clumped isotopes and temperature in different types of modern freshwater carbonates. This study assembles an extensive calibration dataset with 135 samples of modern freshwater carbonates from 96 sites and constrain the relationship between independent observations of water temperature and the clumped isotopic composition of carbonates (denoted by Δ_{47}), including new measurements and published data that have been recalculated in accordance with current community-defined standard values. A composite freshwater calibration is derived and the Δ_{47}-temperature dependence for different types of materials is examined for biogenic carbonates (freshwater gastropods and bivalves), fine-grained carbonate (e.g. micrites), biologically mediated carbonates (microbialites and tufas), and travertines. Material-specific calibration trends show a convergence of slopes that are in agreement with recently published syntheses, but statistically significant differences in intercepts occur between some materials (e.g., some biogenics, fine-grained carbonates). These differences

may arise due to unresolved seasonal biases, kinetic isotope effects, and/or varying degrees of biological influence. Both types of calibrations are applied to new data for glacial and deglacial age travertines from Austria and published datasets. While material-specific calibrations may yield more accurate results for biogenic and fine-grained carbonate samples, the use of material-specific and the composite freshwater calibrations generally produces values within 1.0-1.5^{o}C of each other, and typically fall within calibration uncertainty given limitations of precision.

1. Introduction

Paleoenvironmental reconstructions from freshwater sediments can be used to enhance our understanding of aquatic systems and their proximal terrestrial environments (Aravena et al., 1992; Schelske and Hodell, 1995; Brenner et al., 1999; Xu et al., 2006; Das et al., 2013; Li et al., 2016; Santi et al., 2020). Of particular interest are carbonate-bearing sediments deposited in freshwater systems, as they are widespread and are sensitive to changes in the local environment, tectonic setting, and hydrological conditions, and thus provide a promising archive of continental paleoclimatic information (Arenas-Abad *et al.*, 2010; Gierlowski-Kordesch, 2010; Hren and Sheldon, 2012). However, quantitative temperature proxies that can be applied to terrestrial carbonate sediments are relatively scarce. Multiple proxies have been used to estimate terrestrial temperatures with varying degrees of uncertainty, including soil carbonates, speleothems, fracture veins, ostracods, trace element ratios in lacustrine sediments, tree rings, leaf margin analysis, pollen, biomarkers, and noble gasses in groundwater (Wilf, 1997; Stute and Schlosser, 2000; Powers *et al.*, 2010; Gallagher and Sheldon, 2013; Esper *et al.*, 2018; Boch *et al.*, 2019; Kaufman *et al.*, 2020; Meckler *et al.*, 2021; Wrozyna *et al.*, 2022), of which only the first five types of proxies are carbonate-associated.

Previous work has shown that multiply-substituted carbonate "clumped" isotope thermometry presents a promising proxy for reconstructing temperature. This tool is based on the thermodynamic exchange of isotopes among isotopologues of carbonate-containing groups (Ghosh *et al.*, 2006; Schauble *et al.*, 2006; Hill *et al.*, 2014; Tripati *et al.*, 2015) with widespread applicability in paleoclimatic, paleohydrological, and paleoelevation contexts (Csank *et al.*, 2011; Eagle *et al.*, 2013; Hren *et al.*, 2013; Huntington *et al.*, 2010, 2015; Huntington and Lechler, 2015; Santi *et al.*, 2020; Tripati *et al.*, 2010, 2014). Theoretical calculations indicate that measurements of clumped isotopes can be used for paleothermometry because at equilibrium, the abundance of the multiply-substituted isotopologue $^{13}C^{18}O^{16}O_2$ in carbonates is related solely to the formation temperature of the mineral (Ghosh *et al.*, 2006; Schauble *et al.*, 2006; Hill *et al.*, 2014; Tripati *et al.*, 2015), with cooler temperatures favoring enhanced "clumping" of heavy isotopes within the mineral lattice (i.e., the forward reaction in Equation 1).

$$Ca^{12}C^{18}O^{16}O_2 + Ca^{13}C^{16}O_3 \rightleftharpoons Ca^{13}C^{18}O^{16}O_2 + Ca^{12}C^{16}O_3 \quad (1)$$

This technique is based on measuring the abundance of mass-47 isotopologues of CO_2 gas (containing one or both heavy isotopes (^{13}C and/or ^{18}O)) liberated from carbonate minerals digested in phosphoric acid. The excess of mass-47 CO_2 liberated from a sample is compared to a randomized (stochastic) distribution of clumping in a sample. This excess is reported using the Δ_{47} notation in Equation 2, where R^i = (mass i/mass 44).

$$\Delta_{47}\,(‰) = [(R^{47}/(R^{47}_{stochastic}) - 1) - (R^{46}/(R^{46}_{stochastic}) - 1) - (R^{45}/(R^{45}_{stochastic}) - 1)] \times 1000 \quad (2)$$

An advantage of carbonate clumped isotope-derived temperature estimates is that they are independent of the $^{18}O/^{16}O$ ratio ($\delta^{18}O$) of the precipitating fluid, as the relevant isotope exchange reaction (Equation 1) takes place within a single phase. Carbonate $\delta^{18}O$ ratios are

simultaneously measured during clumped isotope analysis and can be combined with temperature estimates obtained from Δ_{47} analysis to calculate $\delta^{18}O$ values of water at the time of carbonate formation (Urey, 1947; Epstein *et al.*, 1953; Vasconcelos *et al.*, 2005).

Clumped isotopes have been previously used to constrain past lake and river water temperature (Huntington *et al.*, 2010, 2015; Kele *et al.*, 2015; Petryshyn *et al.*, 2015; Horton *et al.*, 2016; Hudson *et al.*, 2017; Santi *et al.*, 2020; Li *et al.*, 2021; Wang *et al.*, 2021; Cheng *et al.*, 2022). The additional temperature constraint provided from Δ_{47} measurements allows for a calculation of the $\delta^{18}O$ of lake and river waters, which can provide constraints on past hydrology and elevation. The Δ_{47}-temperature and Δ_{47}-derived water $\delta^{18}O$ in freshwater carbonates and other types of terrestrial archives have in turn been used to evaluate the representation of various processes in climate models (Eagle *et al.*, 2013; Tripati *et al.*, 2014; Santi *et al.*, 2020; Cheng *et al.*, 2022), constrain hydrologic parameters (Santi *et al.*, 2020), and for paleoaltimetry (Ghosh *et al.,* 2006; Huntington *et al.*, 2010, 2015; Ingalls *et al.*, 2017; Li *et al.*, 2019).

However, the accuracy of these reconstructions is fundamentally underpinned by the calibration(s) used for calculations. Thus, this study presents new clumped isotope calibrations derived for freshwater carbonates by synthesizing clumped isotope data from 135 samples collected from 96 sites in modern lakes, rivers, and springs. New clumped isotope measurements (159 analyses) are presented for 25 new samples collected from 25 different sites. Measurements from published datasets are incorporated, including samples from 59 sites that have been recalculated on the new reference frame proposed by Bernasconi et al. (2021) that defines carbonate standard values to reduce interlaboratory differences and uses newer data handling procedures (Daëron, 2021). Measurements from 12 sites that were recalculated on the new reference frame elsewhere are also included (Anderson *et al.*, 2021).

Recently published syntheses have limited freshwater carbonate data; the synthesis from Petersen et al. (2019) had no freshwater carbonates, and Anderson et al. (2021) had 16 carbonates (tufas and travertines) of which seven samples were from T < 10 ºC, and six samples were from T > 30 ºC. Most clumped isotope studies of freshwater carbonates have analyzed a small number of samples (Huntington *et al.*, 2010, 2015; Kele *et al.*, 2015; Petryshyn *et al.*, 2015; Grauel *et al.*, 2016; Horton *et al.*, 2016; Zaarur *et al.*, 2016; Hudson *et al.*, 2017; Kato *et al.*, 2019; Santi *et al.*, 2020; Anderson *et al.*, 2021; Li *et al.*, 2021; Wang *et al.*, 2021); some do not report calibrations, are not updated to the new reference frame, and published studies utilize different methods for constraining modern water temperatures. Of these 12 studies reporting data for modern freshwater carbonates, five report new data for <5 samples, while nine have data for <11 samples. Only four studies have larger numbers of samples (n=25-33). The smaller size of most published datasets means that there are few calibration constraints on certain types of lacustrine carbonates, such as freshwater gastropods, and that the similarities or differences between different types of lacustrine carbonates is poorly known. In marine carbonates, which have been more extensively studied, there is a body of literature supporting material-specificity or kinetic effects in some archives (e.g., coral, echinoderms; cf. Ghosh *et al.*, 2006; Saenger *et al.*, 2012; Kimball *et al.*, 2016; Spooner *et al.*, 2016; Davies and John, 2019). Additionally, possible influences of seasonal and temperature biases in carbonate formation, are likely to be important for lacustrine carbonates (Hren and Sheldon, 2012; Horton *et al.*, 2016), as might kinetic effects given the range of freshwater ionic compositions (Hill *et al.*, 2014; Hill *et al.*, 2020; Tripati *et al.*, 2015).

The freshwater carbonate dataset synthesized for this study contains new data, recalculated data, and recently published data, and is used to examine clumped isotope signatures

in travertines, fine-grained carbonates, biogenic (freshwater mollusks), and biologically mediated (tufas and microbialites) to provide a foundation for intercomparison and calibration of carbonate clumped isotope results from terrestrial aquatic systems. Sample localities within this study are geographically diverse, and include equatorial, mid-latitude, and polar sites at a variety of elevations and climates (Fig. 1.1). A composite freshwater calibration and material-specific calibrations are presented here for different carbonate types for community use. The impact of the calibrations derived in this study on reconstructed water temperature and source water $\delta^{18}O$ in both modern and past contexts is also assessed.

2. Materials and methods

2.1 Sample and site selection

Carbonate materials included in this dataset were selected to represent modern lacustrine surface-water conditions. For lakes, biogenic and biologically mediated samples selected for analysis are types that grow nearshore or occupy the photic zone above the thermocline. Fine-grained carbonates were selected because formation occurs in surface waters, where evaporation and photosynthesis have the strongest effect on water chemistry (Platt and Wright, 2009; Gierlowski-Kordesch, 2010; Hren and Sheldon, 2012).

For this synthesis, localities were only included where modern surface water temperatures have been measured (Table 1.A.1). Temperatures are representative of the typical season of carbonate formation for each type of carbonate. For sites where multiple years of hydrographic data are available, temperature variability of one standard deviation of the monthly average temperatures during the typical season of carbonate formation for each type of carbonate is reported (see Supplementary Text 1; Table 1.A.1). In sites where the average modern water

temperature during the interval of carbonate growth was limited to data from a short time interval (i.e., less than one year), given that there is year-to-year variability in temperatures, a temperature uncertainty of two standard deviations of the available measurements is reported. For samples and locations described in Li et al. (2021), the standard error of the regression used to constrain water temperatures and the temperature error reported in the original publication is propagated in quadrature to estimate error for lake temperature values. Sites that did not have sufficient temperature measurements to constrain the variation (e.g., where only a season average value is available or only a measured temperature value without reported uncertainty) have been assumed to have an uncertainty of ± 2°C, which is the average standard deviation observed for localities in our study where temperatures were well constrained. This approach to error estimation is conservative in some settings and not in others, as seasonal temperature variation varies based on the location and properties of each lake system. For example, low elevation lakes in the tropics are subject to less monthly temperature variation while high elevation, high latitude lakes would be impacted by larger fluctuations in temperature. Most lakes in this synthesis reside within the low-to-mid latitudes, with most site elevations under 2 km, thus, the assignment of error represents an average for our dataset (Fig. 1.A.1). Since temperature uncertainty for our samples is variable and was calculated in different ways, errors are not used within models to derive relationships in this study but plotted to visualize a bound of uncertainty in the figures below.

2.2 Sample preparation

2.2.1 Biogenic carbonates

Aquatic gastropods and bivalve shells were first separated by taxon. Organic material was removed from shells by scraping and sonicating in Milli-Q deionized water until clean. Samples were dried overnight at 50°C, and complete shells were powdered using a mortar and pestle, and reacted with 3% hydrogen peroxide for 60 minutes to remove any remaining organic material (Eagle *et al.*, 2013). Depending on carbonate content of the gastropod and bivalve shells and instrument sensitivity at the time of analysis, samples were weighed out for mass spectrometric analysis, typically in amounts varying between 5 and 10 mg for a single replicate.

2.2.2 Fine-grained carbonates

Samples of unconsolidated calcareous particles were disaggregated in Milli-Q deionized water, after which the mixture was poured through a 212 μm steel mesh filter and left to settle in a beaker for 10 minutes. The residue was poured into a second beaker after filtration to remove any remaining suspended material, and this process was repeated until virtually no observable settling occurred. The final residue was treated with 3% hydrogen peroxide for 60 minutes to remove any remaining organic material (Eagle *et al.*, 2013). Resulting fine-grained carbonate was collected on a 0.45 μm cellulose nitrate filter membrane and dried at 50°C. Depending on carbonate content and instrument sensitivity, the amount of sample used for mass spectrometry varied between 10 and 30 mg for a single replicate.

2.2.3 Biologically mediated carbonates

Tufas and microbialites were cut perpendicular to laminae, and polished slabs and thin sections were prepared to target specific zones for analysis. Samples were ground into a fine powder using a microdrill. To prevent potential solid state isotopic reordering of C-O bonds due to frictional heating, the drilling during this process was limited in duration and speed (rpm). Samples were reacted with 3% hydrogen peroxide for 60 minutes to ensure removal of any organics and dried overnight at 50°C (Eagle *et al.*, 2013). Drilled samples were weighed out in 5 to 15 mg aliquots for mass spectrometry depending on the carbonate content of the sample and instrument sensitivity at time of analysis.

2.3 Stable isotope measurements

All samples were analyzed at the University of California, Los Angeles on a Thermo 253 Gas Source isotope ratio mass spectrometer in the Eagle-Tripati Laboratory from 2012-2019, primarily between 2013 and 2015. Sample introduction and measurement procedures are described in detail in Upadhyay et al. (2021). Briefly, carbonate samples were first reacted with 105% phosphoric acid for 20 minutes on a 90°C on-line common acid bath system, whereby solid carbonate reacted to produce CO_2 gas for analysis. Acid temperature was monitored with a thermocouple throughout each analysis and checked daily for drift. Each sample gas was cryogenically purified using an automated purification system that was modeled on the previously described system at the California Institute of Technology (Passey *et al.*, 2010) in the Eiler lab. The liberated gas from each sample passed through two separate gas traps to ensure the removal of water and other compounds: the first (containing ethanol) is kept at -76°C by dry ice, and the second (containing liquid nitrogen) is kept at -196°C. Next, the sample gas is passed

through silver wool to remove sulfur compounds (e.g. halocarbons and hydrocarbons; Spencer and Kim, 2015) and remaining trace contaminants were separated by moving the resultant gas through a Thermo Trace GC Ultra gas chromatograph column, which is filled with a divinyl benzene polymer trap, Porapak Q at -20°C (Tripati *et al.*, 2015; Santi *et al.*, 2020). The purified sample gas was passed on to the mass spectrometer for analysis.

Data was collected over nine acquisitions consisting of 10 cycles each to determine $\delta^{13}C$, $\delta^{18}O$, Δ_{47}, Δ_{48}, and Δ_{49}. During each acquisition on the mass spectrometer, sample isotope values were measured relative to high purity Oztech brand CO_2 reference gas ($\delta^{18}O$ = 25.03‰ VSMOW, $\delta^{13}C$ = -3.60‰ VPDB). Each run was started with an equilibrated CO_2 gas standard of varying composition and temperature (25°C and 1000°C), which were used along with ETH-1 and ETH-2 to correct for non-linearity. Carbonate standards, including the community ETH suite from Bernasconi et al. (2021) and in-house standards described in Upadhyay et al. (2021) and Lucarelli et al. (2023), were run every 2-4 analyses and used for the empirical transfer function for projection into the I-CDES reference frame. Accepted standard values used for corrections are from Bernasconi et al. (2021) for all ETH standards and from Lucarelli et al. (2023) for all in-house carbonate standards. Averages for our standard values in this study can be found in Table 1.A.2. At least three replicate analyses of each sample were performed, unless the amount of material available limited the number of analyses.

2.4 Data handling

The replicate level values for new and reprocessed samples are archived in the EarthChem database.

2.4.1 New data

Table 1.1 reports isotopic data for samples used within this study. Detailed information about data processing can be found in Upadhyay et al. (2021). Data are reported on the I-CDES scale which projects values into a 90ºC reference frame, following recommendations from Bernasconi et al. (2021). Acid digestion fractionation factors used for calcite and aragonite $\delta^{18}O$ are from Swart et al. (1991) and Kim et al. (2007), respectively; for calculation of water $\delta^{18}O$, the equation from Kim and O'Neil (1997) was used for calcite and the equation from Kim et al. (2007), was used for aragonite, respectively. For samples measured in the Eagle-Tripati Lab, data was processed using *Easotope* (Daëron *et al.*, 2016; John and Bowen, 2016) and is included in the supplement, and archived on EarthChem. Replicated measurements were excluded if results were consistent with high organic content, as indicated by anomalous Δ_{48} or Δ_{49} for a given correction interval, with samples having values that are more than 3σ from the replicate mean being flagged for possible exclusion (Upadhyay *et al.*, 2021). Replicates were also excluded if they had with anomalous values of Δ_{47} (I-CDES), $\delta^{13}C$ (VPDB) and $\delta^{18}O$ (VPDB), of more than 3σ from the remaining replicates, which can reflect incomplete digestion or contamination (Tripati *et al.*, 2015). If less than three replicates were run for a sample, uncertainty of the reported value was determined by propagating both the internal reproducibility of the sample and the average external reproducibility of the samples in this study.

2.4.2 Data from prior studies

Detailed information about each dataset can be found in the original publication and our methodology for including these values in our study is as follows:

Anderson et al. (2021): Data is presented in the I-CDES reference frame.

Bernasconi et al. (2018): In their study, the Δ_{47} values from Kele et al. (2015) was reprocessed using the Brand parameter set. Their results were presented in CDES, but projected into I-CDES using the following equation from Bernasconi et al. (2021):

$$\Delta_{47}\,(\text{I-CDES, ‰}) = -0.035545 - 0.000180\,\delta_{47} + 0.942483\,\Delta_{47}\,(\text{CDES}_{25})$$

Huntington et al. (2010), Huntington et al. (2015), Petryshyn et al. (2015): The Δ_{47} measurements for these studies were completed in the Eiler laboratory at CalTech. Samples from these studies were either digested independently at 25°C and collected in breakseals or in a common acid bath at 90°C for analysis in the mass spectrometer. For samples at 90°C, an acid fractionation factor of 0.088‰ was used to project into the CDES reference frame at 25°C (Petersen *et al.*, 2019). Sample and standard data from Caltech for these studies were imported into *Easotope* for data processing on the CDES reference frame (John and Bowen, 2016). Data was reprocessed using the Brand parameter set. Non-linearity in the mass spectrometer was corrected using 1000°C equilibrated gases with varying bulk compositions. The empirical transfer function was constructed using both carbonates and gas standards. Mean standard values associated with these analyses are reported in Table 1.A.2. Accepted standard values used for corrections came from processing I-CDES values in Lucarelli et al. (2023) into the CDES reference frame. To project these measurements into the I-CDES reference frame, the methodology in Bernasconi et al. (2021) was applied to construct the following equation:

$$\Delta_{47}\,(\text{I-CDES, ‰}) = -0.034927 - 0.000181\,\delta_{47} + 0.942466\,\Delta_{47}\,(\text{CDES}_{25})$$

Li et al. (2021), Wang et al. (2021): Clumped isotope data from this study was generated in the Eagle-Tripati laboratory. Data was reprocessed in *Easotope* (John and Bowen, 2016) using updated values for the ETH standards from Bernasconi et al. (2021). Samples from Wang et al.

(2021) were updated to the Brand parameter set. Data was processed identically to the original studies.

2.5 Regression methodology

Recent work has shown that models derived using ordinary least squares (OLS) perform better, under synthetic datasets comparable to the one assembled in this study (<500 samples), than their error-in-variables counterparts (e.g. York regression, Deming regression). OLS has higher accuracy and precision for regression parameters, and performs similarly to Bayesian simple linear models for both calibration of clumped isotopes and for temperature reconstruction (Román Palacios *et al.*, 2021). This study evaluates the relationship between Δ_{47} and growth temperature using Ordinary Least Square regression models fit in the lm R function in the stats package (R Core Team, 2022). Due to the varying temporal resolution of our independently measured water temperatures and lack of long-term temperature records for some sites, an Ordinary Least Squares regression model was used instead of an errors-in-variables model. Calibration data in Table 1.1 was utilized to derive regressions for our entire dataset (a composite freshwater calibration), and material-specific calibrations for biogenic carbonates (bivalves and gastropods), biologically mediated carbonates (microbialites and tufas), fine-grained carbonates, and travertines.

To evaluate material specificity within our dataset and compare our derived regression parameters to other studies, an analysis of covariance (ANCOVA) was used to evaluate pairwise differences in slopes and intercepts between groups of data. Our composite calibration, which includes all data from this study, along with our material-specific calibrations are compared to two additional studies: a recently published calibration that includes natural and synthetic

samples (Anderson *et al.*, 2021) and a 'universal' calibration created from a synthesis of clumped isotope calibration studies (Petersen *et al.*, 2019). Comparisons to previously published calibration equations are also shown, with data brought into the 90°C reference frame here using acid fractionation factor values reported in Petersen et al. (2019), which yield similar values given that both reference frames are considering acid fractionation at 90°C.

3. Results

3.1 Δ_{47}-temperature relationships

Samples in this study are from modern lakes (including playas), rivers, and springs, from geographically and climatically diverse settings (Fig. 1.1; Table 1.1). Calibration data from Table 1.1 was used to derive regressions for our entire dataset (a composite freshwater calibration), and material-specific calibrations for biogenic carbonates (bivalves and gastropods), biologically mediated carbonates (microbialites and tufas), fine-grained carbonates, and travertines. Δ_{47} values for samples within this study range from 0.409 to 0.682‰ with independently measured water temperatures ranging from 5 to 95°C. Calibrations derived in this study are presented in Fig. 1.2 and Table 1.2.

3.2 Comparative regression models for different materials

Calibrations were derived for biogenic carbonates (bivalves and gastropods), biologically mediated carbonates (microbialites and tufas), fine-grained carbonates, and travertines to test the hypothesis that there is material-specificity in Δ_{47}-temperature relationships and to evaluate whether regression parameters are significantly different between these groups of materials (Table 1.2; Fig. 1.3; Table 1.3).

3.2.1 Biogenic carbonates

Our biogenic carbonate calibration was developed using 137 analyses from 23 samples with Δ_{47} values and independently constrained water temperatures ranging from 0.573-0.643‰ and 7 - 29°C, respectively. This dataset includes 16 new samples, alongside reprocessed data from Huntington et al. (2015) and Wang et al. (2021) that have been brought onto the I-CDES reference frame. This calibration shows a significant temperature dependence (Fig. 1.3A; r^2 = 0.7811, p = <0.0001).

3.2.2 Fine-grained carbonates

Two new samples of fine-grained carbonates are presented in this study, in addition to reprocessed data from 3 samples from Huntington et al. (2010) and 33 samples from Li et al. (2021) onto the I-CDES reference frame. Fine-grained carbonates in this study include water temperatures between 9.8 and 29.0°C and Δ_{47} values from 0.596 to 0.682‰. Fine-grained carbonates evaluated in this study demonstrate a significant degree of variability (Fig. 1.3B; r^2 = 0.5170).

3.2.3 Biologically mediated carbonates

The calibration for biologically mediated carbonates is constructed with 255 analyses of 24 samples, including 7 new samples, 13 reprocessed samples from Bernasconi et al. (2018), Huntington et al. (2015), Huntington et al. (2010), Petryshyn et al. (2015), and Santi et al. (2020) that were converted into I-CDES, and 4 samples from Anderson et al. (2021). Water temperatures for biologically mediated samples span 18.9°C (10.1 - 29.0°C) and Δ_{47} values range between 0.585 - 0.666‰. Significant variability is observed in our dataset (Fig. 1.3C; r^2 = 0.5669) and a significant relationship between Δ_{47} and temperature is present (p = <0.0001).

3.2.4 Travertines

A regression for travertine samples containing 543 analyses from 23 samples was created to assess material-specificity in the clumped isotope-temperature relationship of freshwater carbonates. The travertine dataset includes 15 recalculated samples from previous publications projected onto the I-CDES reference frame (Kele *et al.*, 2015; Bernasconi *et al.*, 2018) following methodology in the supplement of Bernasconi et al. (2021) and 8 new published measurements (Anderson et al., 2021). Travertine samples encompass the largest range of independently measured water temperatures (5 - 95°C) and Δ_{47} values (0.409 - 0.637‰). Similar to the other groups of carbonates considered in this study, a significant temperature dependence is observed in the data (slope; p = <0.0001) and a high degree of agreement between the fitted values and calibration data points (r^2 = 0.9487). When restricting travertines to cover the same temperature range as other carbonate groups analyzed in this study, the highest r^2 value is observed relative to other groups investigated in this study (r^2 = 0.8806). However, this analysis only contains 6 samples within the restricted temperature range and result in a shallower slope (0.0330) and higher intercept (0.2171) relative to the calibration derived from all travertines.

4. Discussion

4.1 Comparison of material-specific and composite freshwater calibrations

4.1.1. Composite freshwater calibration

The freshwater composite calibration slope derived within this study yields a statistically significant difference in slope to that of the 'universal' calibration derived in Petersen et al. (2019) (projected into a 90°C reference frame) (Fig. 1.2E; p_{slope} = 0.0036; Table 1.3). Similarly, the freshwater composite calibration derived in this study results in a steeper slope and shallower

intercept than the recently published Anderson et al. (2021) calibration. Although the 95% confidence intervals on the estimated regression models overlap visually (Fig. 1.2E), an ANCOVA shows that the slopes for the two calibrations are significantly different from each other (p_{slope} = 0.0334; Table 1.3), with the slope for the composite regression in this study being steeper relative to those derived in the prior publications (Fig. 1.2E).

The Anderson et al. (2021) calibration includes low temperature Antarctic microbialites that are offset from other data, with half of the samples from a high pH (10.3-10.7; (Mackey *et al.*, 2018) environment (Fig. 1.2D). Low temperature and high pH are environmental factors that could give rise to potential kinetic isotope effects or DIC speciation effects (Tang *et al.*, 2014; Tripati *et al.*, 2015). In fact, all of the Antarctic samples are negatively offset from the rest of the data in this study, and thus, these data are excluded from both the composite and the biologically mediated regressions reported here (Table 1.3). These patterns (the offset of the Anderson et al. (2021) data from other data) hold up when comparing results to only the recent Eagle-Tripati Lab measurements, and the broader freshwater composite calibration (Table 1.A.3).

Table 1.A.4 shows the range of temperatures derived using different calibrations for using Δ_{47} values ranging from 0.550 to 0.700‰, in 0.025‰ increments.

4.1.2. Biogenic carbonates

Biogenic carbonates record lower Δ_{47} values relative to the regression derived from all freshwater carbonates in this study (Fig. 1.2D). The depletion in Δ_{47} observed within these samples relative to fine-grained carbonates, travertines, and biologically mediated carbonates could stem from changes in growth rate as a function of season, or other unidentified factors. As the sample size requirements for clumped isotopes is relatively large, it often requires the

analyses of either a complete shell or the majority of a shell, effectively integrating seasonal signals recorded in the shell and potentially leading to a more muted temperature sensitivity of the calibration than if seasonally resolved sampling could be carried out. There may also be a mismatch of independently measured in-situ measured water temperatures, which is representative of a multi-year average, and the temperature range experienced by biologic samples, which typically have a shorter lifespan and thus, a shorter timeline for shell growth. Another possibility is that kinetic isotope fractionations may manifest in freshwater gastropod and bivalve shells, as have been constrained in marine biogenic carbonates such as coral skeletons (Ghosh *et al.*, 2006; Saenger *et al.*, 2012).

An ANCOVA analysis finds significant differences in intercepts between biogenic carbonates and fine-grained carbonates ($p_{intercept}$ = <0.0001) and biologically mediated carbonates ($p_{intercept}$ = 0.0047) (Table 1.3), but no statistical difference in slopes between our Δ_{47}-T regression of biogenic carbonates and other carbonate groups within this study (Table 1.3). This pattern is observed whether examining the dataset as a whole, or only the UCLA-measurements of biogenic carbonates relative to both UCLA-measurements of fine-grained carbonates and biologically mediated carbonates (Table 1.A.3). However, differences between slopes derived for other carbonate groups in this study and biogenic carbonates are as large as 0.0091, which has implications for temperature reconstructions (Table 1.A.4). Regression parameters for biogenic carbonates derived in this study are of intermediate slope and intercept relative to other materials (Table 1.2).

When comparing the biogenic calibration to the calibrations presented in Anderson et al. (2021) and Petersen et al. (2019), an ANCOVA indicates shows no difference in slope between these studies and our biogenic carbonate calibration, but shows differences in intercept between

this study and the calibration derived by Petersen et al. (2019) ($p_{intercept}$ = 0.0728) (Fig. 1.3A; Table 1.3). Biogenic carbonates in this study show offsets to lower Δ_{47} values relative to the published calibrations discussed here (Fig. 1.3A). Reconstructions using our biogenic regression result in consistently lower temperatures than those derived with the calibrations of Anderson et al. (2021) and Petersen et al. (2019) throughout the range of Δ_{47} in our dataset.

A relationship is not detected between measured Δ_{47} and $\delta^{18}O_{carbonate}$ values (Fig. 1.A.2). Further, no significant relationship between the Δ_{47} and $\delta^{18}O_{carbonate}$ residual values (relative to equilibrium estimates) is observed (Fig. 1.A.3). More research is needed to examine whether kinetic effects may be present in the Δ_{47} of freshwater biogenic carbonates, such as culture experiments at controlled temperatures as well as comparison with other geochemical indicators. Specifically, dual Δ_{47}-Δ_{48} measurements (Lucarelli *et al.*, 2023) could help identify if there were kinetic effects expressed in these and other types of freshwater carbonates.

4.1.3. Fine-grained carbonates

The Δ_{47}-temperature relationship for fine-grained carbonates analyzed in this study has multiple sources of uncertainty. One factor that contributes to variability in Δ_{47} in fine-grained freshwater carbonates is potentially due to uncertainty in the timing of surface carbonate precipitation events at each site. Authigenic carbonate precipitation is enhanced by biological processes such as algal blooms and temperature effects which can peak at different times throughout the year, and timing of carbonate precipitation events varies depending on characteristics of each lake system (i.e. open or closed; location; stratification/ventilation; etc.) (Hren and Sheldon, 2012).

A second factor is that fine-grained carbonate lake sediments may have a mixture of sources, including authigenic carbonate precipitation, fragments of biogenic carbonates, and detrital carbonates deposited at the sampling location. In particular, ostracod valves in some samples may be a source of scatter seen since the timing of formation for fine-grained carbonates and ostracods may be different. Since different factors control organism growth, the inclusion of potential fragments of fossilized material may bias temperature estimates derived by clumped isotope analysis. The majority of the samples in this synthesis are from Li et al. (2021), who filtered samples through a 45 μm mesh and also screened for ostracod valves. New samples measured for this study were sieved through 212 μm mesh, juvenile or fragments of mature ostracods, and it is unclear if any screening for bioclastic fragments occurred for samples reported by Huntington et al. (2010).

Another source of the variability observed in the Δ_{47}-temperature relationship for fine-grained carbonates may be attributed to detrital influence. Catchment-derived carbonate is likely to be recording different conditions than authigenic carbonate precipitated in the water column and could bias Δ_{47} results depending on the formation temperature and the relative proportion of authigenic and detrital carbonate inputs. Samples from Li et al. (2021) were taken at least 2 km from the lake shoreline or from the middle of each lake (when possible) to minimize delivery of catchment material to the sampling site. Inclusion of detrital material, in particular at lower carbonate content, would play more of a role in biasing Δ_{47} content. However, there is no significant relationship with dilution from terrigenous material as indicated by carbonate content (Fig. 1.A.4). However, data from other sources did not evaluate detrital contributions. Future work with authigenic carbonates would benefit from other methods, such as scanning electron microscopy, to evaluate detrital input.

The calibration derived from fine-grained carbonates results in the steepest slope and shallowest intercept derived in this study (Table 1.3). When comparing our derived fine-grained carbonate parameters to other carbonate groups in this study, an ANCOVA shows no significant difference in slopes is found between carbonate materials, but significant differences in intercept is observed between fine-grained carbonates and biogenic carbonates ($p_{intercept}$ = <0.0001), biologically mediated carbonates ($p_{intercept}$ = 0.0379), and travertines ($p_{intercept}$ = 0.0050). No statistical difference between regressions is found when using the entire fine-grained carbonate dataset relative to a regression constructed only using fine-grained carbonates measured at UCLA. Additionally, the results of the ANCOVA indicate differences in regression parameters between the same groups when looking at the entire fine-grained carbonate dataset and the fine-grained carbonate dataset measured at UCLA (Table 1.3; Table 1.A.3).

Visually, the fine-grained carbonates regression is positively offset relative to both the Anderson et al. (2021) and Petersen et al. (2019) calibrations (Fig. 1.3B), however, an ANCOVA shows agreement in slope between all three regressions. and finds significant differences in intercept between the calibration from Petersen et al (2019) ($p_{intercept}$ = <0.0001), and a recently published calibration on the I-CDES scale (Anderson et al., 2021; $p_{intercept}$ = <0.0001). Applying these calibrations to the range of Δ_{47} values in the fine-grained dataset produces consistently lower values relative to the fine-grained carbonate regression derived in this study.

Fine-grained carbonates in this study show an average positive offset of 0.012‰ in residual Δ_{47} values relative to estimated equilibrium values from Lucarelli et al. (2023) (Fig. 1.A.3). There is no statistically significant relationship between residual Δ_{47} and residual $\delta^{18}O_{carbonate}$ values, consistent with equilibrium, and with prior work reporting that Δ_{47} values of

authigenic carbonates precipitate near equilibrium and are not impacted by carbonate precipitation rate or water chemistry (Li *et al.*, 2020).

4.1.4. Biologically mediated carbonates

Application of the biologically mediated regression results in warmer estimated temperatures, particularly at higher temperatures, relative to other carbonate groups analyzed in this study (Table 1.2; Table 1.A.4). This could occur if biologic processes are a factor in influencing observed Δ_{47}-temperature relationships and/or are a source of scatter/noise; r^2 =0.5669. Uncertainty in the temperatures used for the regression may also affect the dataset.

Although statistically significant differences in slopes are not observed between biologically mediated carbonates and other freshwater carbonate types, an ANCOVA detects differences in intercept between biologically mediated carbonates and biogenic carbonates ($p_{intercept}$ = 0.0047) and fine-grained carbonates ($p_{intercept}$ = 0.0379). Significant differences in intercept are found between the regression for biologically mediated carbonates and the I-CDES calibration of Anderson et al. (2021) ($p_{intercept}$ = <0.0001). Within the UCLA-measured dataset, agreement of slopes is observed between different material types and prior publications, but differences in intercept between UCLA-measured biogenic carbonates ($p_{intercept}$ = <0.0001) (Table 1.A.3). The reduced slope and elevated intercept for the calibration constructed using biologically mediated carbonates results in the largest difference in estimated temperatures at lower Δ_{47} values relative to other calibrations produced in this study and the calibrations of Anderson et al. (2021) and Petersen et al. (2019).

Kato et al. (2019) found that tufa samples recorded lower Δ_{47} values relative to synthetic calcite and application of a synthetic calcite-based regression to tufa samples resulted in

temperature estimates for tufas were higher than modern environmental temperatures. Prior studies have also found lower Δ_{47} values for tufas and travertines (Kele *et al.*, 2015; Kato *et al.*, 2019), however, our study doesn't show a relationship consistent with CO_2 degassing in the residual Δ_{47} and $\delta^{18}O_{carbonate}$ values relative to projected equilibrium values (Fig. 1.A.3). The modern tufa data from Kato et al. (2019) is not included in this synthesis due to discrepancies between standard values for Carrara Marble and NBS-19 relative to what was reported by Bernasconi et al. (2021) and Upadhyay et al. (2021), although their calibration falls within the 95% confidence interval of the biologically mediated calibration in this study.

4.1.5 Travertines

Travertines display the highest r^2 values relative to biogenic carbonates, biologically mediated carbonates, and fine-grained carbonates, which may arise if they have the least complex precipitation mechanism with little biological influence relative to the other groups. The thermal control on water temperature in most of these samples may minimize uncertainty in estimated formation temperatures and relatively low seasonality in groundwater temperatures may contribute to the high r^2. However, the alkaline nature of some springs means that it is possible for travertines to form out of equilibrium, particularly at pH >10 and at lower temperatures.

ANCOVA tests indicate the linear regression derived from travertines does not have a statistically significant slope compared to other groups of freshwater carbonates in this study but does indicate a statistically different intercept to the regression using fine-grained carbonates ($p_{intercept}$ = 0.0050; Table 1.3). The newly derived regression on the updated I-CDES reference frame has significant differences in intercept from the calibration presented in Petersen et al.

(2019) ($p_{intercept}$ = 0.0354), however, no significant differences in either slope or intercept were found between travertines and the Anderson et al. (2021) calibration (Table 1.3).

The relationship between Δ_{47} and $\delta^{18}O_{carbonate}$ values in travertines is significant (Fig. 1.A.2), however, the relationship between residual Δ_{47} and $\delta^{18}O_{carbonate}$ relative to estimated equilibrium values do not show any significant correlation (Fig. 1.A.3). Travertine samples reprojected within this analysis were selected close to vents where kinetic fractionations would be minimized, and prior analysis of these samples show no influence from water chemistry, mineralogy, and precipitation rate (Kele *et al.*, 2015).

4.2 Application of material-specific and composite freshwater calibrations

4.2.1 Reconstructed temperatures

Overall, an ANCOVA suggests no statistically significant difference between the calibration slopes derived from different materials and previously published calibrations (Table 1.3) when freshwater carbonates are divided into groups to account for potential differences in their precipitation (e.g. seasonality, ecology, etc.), calibrations converge on a common temperature dependence (slope) for clumped isotope measurements. A similar convergence of slopes was found in Petersen et al. (2019) when comparing 14 different clumped isotope studies of both biogenic and abiogenic carbonates using updated parameter values for Δ_{47} calculation. Anderson et al. (2021) also found a convergence of slopes between their new data, the Petersen calibration, and recalculated calibration lines using updated carbonate standardization procedures for 4 recent calibration studies. However, our ANCOVA analyses indicate statistically different intercepts for most of our calibrations from groups of freshwater carbonates (Table 1.3).

Figure 1.4A shows a comparison of residuals for temperatures calculated using calibrations derived from material specific carbonates and composite freshwater carbonates. For temperature, a decrease in residuals occurs when utilizing material-specific regressions for biogenic and fine-grained carbonate archives. In the case of travertines and biologically mediated carbonates, the temperature residuals are reduced when using the composite freshwater calibration relative to the material-specific calibration. To evaluate goodness of fit between the two types of models presented in this study, root mean square error (RMSE) is calculated using each calibration between our directly measured and Δ_{47}-derived measurements. RMSE shows, on average, how far away the predicted values were from the measured values (both positively and negatively) and allows for intercomparison in the same units. Applying our composite freshwater calibration to biogenic samples results in a RMSE of 4.4°C, while applying the biogenic calibration results in a RMSE of 2.9°C, showing a better fit when using the material-specific calibration. Temperatures derived from a fine-grained carbonate-specific calibration results in a slightly lower RMSE than a composite calibration (3.9°C and 4.6°C, respectively).

In contrast, the composite freshwater calibration slightly outperforms the material specific calibrations for biologically mediated carbonates and travertines, resulting in a lower RMSE than their material specific counterparts (biologically mediated carbonates: 4.4°C and 5.1°C, travertine: 6.5°C and 7.1°C). For biologically mediated carbonates and travertines, the improvement in prediction quality is small when using a material specific calibration relative to the calibration derived from all freshwater carbonates. Both calibrations overestimate formation temperature for high temperature travertines. When excluding the two highest temperature travertine samples (95°C), both the composite and material specific calibrations perform similarly when applied to the travertine dataset (RMSE = 4.9°C for both calibrations).

Thus, our results suggest that material-specific calibrations will yield more accurate results for biogenic and fine-grained carbonate samples, though the differences are relatively small for some sites, they are larger for others (Fig. 1.4). A composite freshwater calibration will yield slightly more accurate results for biologically mediated carbonates and travertines.

4.2.2 Reconstructed water $\delta^{18}O$

In addition to providing thermodynamic constraints on the temperature of formation of carbonates, Δ_{47} measurements can be paired with carbonate oxygen isotope ratios to directly calculate source water $\delta^{18}O$. To evaluate if this method can accurately reconstruct the isotopic composition of the water in which the carbonate precipitated, our clumped-isotope derived estimates of source water $\delta^{18}O$ derived with our temperature predictions ($\delta^{18}O_{w\text{-}reconstructed}$) are compared to measured modern freshwater $\delta^{18}O$ ($\delta^{18}O_{w\text{-}measured}$) values. For $\delta^{18}O_{w\text{-}measured}$, any available published measurements were synthesized for the water bodies examined to compare to reconstructed values. $\delta^{18}O_{w\text{-}measured}$ data is available for 86 of the 108 sites examined in this study (Table 1.A.5). Although some sites had long-term measurements of water body oxygen isotope composition, some of the measurements were single point measurements, and thus may not fully represent temporal variability.

The equations of Kim & O'Neil (1997) for calcite and Kim et al. (2007) for aragonite were used to constrain the relationship between formation temperature, $\delta^{18}O_{carbonate}$, and $\delta^{18}O_{water}$. A positive relationship between measured and clumped-isotope derived $\delta^{18}O_{w\text{-}reconstructed}$ is observed when using the reconstructed temperatures from the composite freshwater calibration ($p = <0.0001$; $r^2 = 0.7935$) and material-specific calibrations presented in this study ($p < 0.0001$; $r^2 = 0.8267$). Figure 1.4B shows comparison of the residuals for reconstructed $\delta^{18}O_w$ using both

the material specific and composite calibrations developed within this study. RMSE was reduced using the material specific calibration relative to the composite calibration for biogenic carbonates (material specific RMSE = 1.5‰, composite RMSE = 1.8‰), fine-grained carbonates (material specific RMSE = 1.4‰, composite RMSE = 1.7‰), and travertines (material specific RMSE = 2.1‰, composite RMSE = 2.3‰). However, for biologically mediated carbonates, the composite calibration slightly outperforms the material specific calibration (material specific RMSE = 1.4‰, composite RMSE = 1.5‰), although the mean of the residuals is closer to zero.

Overall, both the composite and material-specific calibrations perform well in reconstructing $\delta^{18}O_{w\text{-}measured}$. Out of the 87 samples from sites with measured $\delta^{18}O_{water}$ values, when using temperatures derived from the material-specific and composite freshwater calibration, 33 and 27 samples respectively fall within ±1‰ of hydrographic data (Fig. 1.4B). $\delta^{18}O_{w\text{-}reconstructed}$ values for biogenic samples generally recover $\delta^{18}O_{w\text{-}measured}$ within 2‰. However, this method yields, for fine-grained carbonates, lower $\delta^{18}O_{water}$ values than observations for more enriched $\delta^{18}O_{w\text{-}measured}$ values, which could be due to either kinetic effects and/or changes in surface water chemistry during carbonate precipitation events (Fig. 1.4B). If the latter, it is unlikely to be due to evaporative enrichment of $\delta^{18}O_{water}$ which would produce the opposite trend, but it may arise from changes in carbonate chemistry. Figure 1.4B shows biologically mediated carbonates and travertines show a positive offset from the 1:1 line, overestimating $\delta^{18}O_{water}$ relative to the measured value, that may also arise from pH related effects on isotopic fractionation or kinetic isotope effects (Beck *et al.*, 2005; Tripati *et al.*, 2015).

4.3 Comparison of multiple materials at individual sites

Five locations in this study contain two different types of freshwater carbonates that were analyzed. Samples of fine-grained carbonate (Li *et al.*, 2021) and freshwater mollusks (this study) were analyzed from three sites in China (Daija Co, Cuona Lake, and Wulungu Lake). Microbialites and ooids were analyzed from two locations in the Great Salt Lake (North Arm and South Arm, which are restricted by a causeway and chemically unique) (Pace *et al.*, 2016). Comparing water temperature estimates from different carbonate types provides another method of assessing overall calibration performance, therefore, clumped isotope-derived temperature using both material-specific and our composite freshwater calibrations are compared at these sites where different materials are present and consider what is known about the seasonality of carbonate formation.

Figure 1.5 shows increased agreement between different sample types for the same location for temperature and water $\delta^{18}O$ in a majority of cases when a material-specific calibration is used. If the model derived in this study was perfect, samples should follow the 1:1 line (denoted by grey dashes on Fig. 1.5), where the reconstructed temperatures and water $\delta^{18}O$ match the observations. In the case of water temperature, applying the material-specific calibration derives a slope and intercept pair closer to the 1:1 line in comparison to the composite calibration. Additionally, increased correlation between samples is observed when using material specific calibrations for estimates of water temperature, with r^2 values of 0.8455 and 0.7977 when applying our material specific and composite calibrations, respectively. For water $\delta^{18}O$, similar positive slopes that are slightly greater than 1 are calculated between our reconstructed and measured values for both calibrations ($slope_{material\ specific} = 1.304$, $slope_{composite} = 1.249$), but increased correlation between the samples when applying the material specific calibrations.

All three lakes in China examined in this section are terminal lakes where authigenic carbonate precipitation is expected to occur in the later part of summer, when temperatures are most elevated and carbonate supersaturation occurs in the surface waters (Hren and Sheldon, 2012). Both Daija Co and Cuona Lake are high elevation lakes (>4.5 km) where the monthly average air temperature doesn't exceed 0°C until May, thus, temperature requirements for mollusk calcification and growth are met during the similar times of year and conditions to authigenic carbonate. As expected, similar estimated temperatures are obtained from both archives when using the material-specific calibrations. However, applying our composite calibration to samples in these lakes results in a disparity between calcification temperatures projected for both types of carbonates, with mollusks estimating higher water temperatures relative to the authigenic carbonate. In contrast to the setting of Daija Co and Cuona Lake, Wulungu Lake is an inland, low elevation, and high latitude (47°N) lake with a large range of intra-annual air temperatures (~36°C). The large intra-annual air temperature range would likely extend to lake water temperatures. Authigenic carbonates are more likely to have temperature-induced precipitation and evaporative enrichment here; our results using a material specific calibration suggest that fine-grained carbonate precipitated during a narrower interval, with higher temperatures and $\delta^{18}O$ values than the mollusk samples at the same sites. The water temperatures recorded by mollusks at the same lake using the material specific calibrations suggest that the shells may be reflecting dominant calcification during comparatively cooler temperatures in spring or early summer. This is consistent with prior work showing that some mollusks have species-dependent threshold of water temperatures that allow calcification and survival (Versteegh *et al.*, 2010), thus, the disparity between the two archives may show that mollusk calcification was inhibited during the thermal maxima of lake water temperatures.

Pairs of carbonate material were also collected from locations in each arm of the Great Salt Lake and analyzed in this study. The separation of the North and South arms of the Great Salt Lake by a causeway result in a more restricted Northern arm with less freshwater input from rivers, higher water temperatures and salinity, lower pH, and more evaporation (Gwynn, 2007; Ingalls *et al.*, 2020). Ooids from the Great Salt Lake have been found to form concentrically throughout the past 6,600 years (Paradis, 2019). Recent work suggests that Great Salt Lake ooids are insensitive to short-term changes in lake conditions and/or biologically induced changes within the lake, and their isotopic composition has been shown to represent time-averaged conditions, while microbialites from the Great Salt Lake have been shown to record $\delta^{18}O_{carb}$ and Δ_{47} in equilibrium with lake water $\delta^{18}O$ (Ingalls *et al.*, 2020). Despite the longer timescale of carbonate precipitation between ooids and microbialites, prior work shows consistency between clumped isotope derived reconstructions of temperatures of both carbonate types (Ingalls *et al.*, 2020). Thus, both materials can be used to reconstruct modern temperatures and evaluate calibration performance for dual material archives.

Δ_{47}-derived temperature reconstructions derived from microbialites show elevated heating in the North Arm relative to the South Arm using both the material-specific (2.1°C) and composite calibrations (1.5°C), with a similar extent as modern lake water temperature measurements from each of our sites (1.5°C). Reconstructions from ooids fail to capture the modern temperature gradient observed between arms of the lake but are within error of each other and modern summer water temperatures. This disparity between microbialiates and ooids is likely due to the differences in timescale of carbonate formation between archives. Since the causeway separating the two arms was recently formed relative to the timescale of formation of the ooids, it is unlikely that their composition reflects these short-term changes.

Temperatures derived using material-specific calibrations have increased agreement between modern water temperatures in both arms of the lake (Fig. 1.5). The use of the composite freshwater calibration generally underestimates formation temperatures relative to modern water temperature measurements. Further study is needed to fully understand the differences in calcification in between archives in the same settings, but these findings may support the use of a material-specific calibration when developing reconstructions from multiple types of carbonates for ancient freshwater systems.

4.4 Applications to paleoclimate reconstructions

4.4.1. Origin of travertine and tufa deposits in Ainet, Austria

Our material-specific and composite freshwater calibrations were applied to examine the origins of late glacial sequence of travertine and calcareous tufa from Ainet, Austria that was first described in (Boch *et al.*, 2005). This sequence of ~2.7 m thickness formed over the course of ~1,000 years, following the rapid initiation of warming during the Bølling-Allerød, and represents the only aragonitic travertine sequence known in the Eastern Alps (Fig. 1.6). Carbonate deposition within the travertine sequence alternated between aragonite and calcite layers (on mm-scale). The alternating mineralogy was hypothesized to represent differences in seasonality, with aragonite and calcite precipitation occurring during the warm and cool seasons, respectively. Following the deposition of the compact and aragonite-dominated travertine (~2.5 m), this sequence was then capped by a calcareous tufa layer (~0.2 m) consisting solely of calcite.

Temperature estimates derived using material-specific calibrations for the tufa and travertine sequence range from 9.0 to 15.1°C, with an average value of 12.7°C for the travertine

terrace (Table 1.A.6). Modern water temperatures taken in May, July, and October range from 6.6 - 12.2°C, similar to our Δ_{47}-derived estimates. Although the initial study suggested a seasonal control on aragonite and calcite formation, with aragonite being precipitated in the warmer months and calcite being precipitated in the cooler months, a clear relationship between temperature and mineralogy is not apparent within this limited dataset (Fig. 1.6).

Our Δ_{47}-temperatures and $\delta^{18}O_{water}$ values support the hypothesis that the travertine sequence did not have a hydrothermal origin (thermal water discharge), but are consistent with being derived from rapid CO_2 degassing from groundwater discharge of meteoric origin, with sufficient time for dissolved inorganic carbon (DIC) equilibration to occur. Consistency between modern $\delta^{18}O_{water}$ values measured from a series of nearby streams (-11.5 to -12.1‰ VSMOW) and $\delta^{18}O_{water}$ estimates derived from clumped isotope analysis (-11.4 to -12.2‰ VSMOW) is observed. Given this consistency in $\delta^{18}O_{water}$, our results suggest recharged meteoric groundwater (seasonal rainfall, snowmelt) and eventually some contribution from ice melting due to a rapid increase in temperatures during the Bølling-Allerød is likely to have been the surface dominated paleofluid source for carbonate precipitation here.

The analysis of this travertine sequence illustrates the importance of an appropriate calibration selection. While application of our composite freshwater carbonate calibration would yield temperature values 2.5 - 2.7°C higher than modern streamflow, use of the material-specific calibrations yields formation temperatures more similar to modern stream temperatures, which are more likely to be correct for carbonates forming in an interval of distinct relative warmth in the last glacial period. The $\delta^{18}O_{water}$ values reconstructed from the material-specific calibration are within error of modern groundwater values, measured from spring-fed streams, while

reconstructed $\delta^{18}O_{water}$ values are 0.5 to 0.6‰ higher when using the composite calibration relative to the material-specific calibration.

4.4.2 Paleoclimatology of Lake Surprise, CA

Santi et al. (2020) reconstructed hydroclimate at Lake Surprise, California by applying clumped isotope thermometry to reconstruct terrestrial paleo-hydroclimate variables using samples of tufa from the Last Glacial Maximum (LGM; 23,000-19,000 years ago) and deglacial (19,000-11,000 years ago) (Egger *et al.*, 2018; Ibarra *et al.*, 2014; Santi *et al.*, 2019, 2020). In Ibarra et al. (2014), the authors used an isotope mass balance model to derive evaporation and precipitation rates by using pollen data to constrain the temperature changes within their model. Santi et al. (2020) expanded on this work by providing further clumped isotope-derived constraints on water temperatures and $\delta^{18}O_{water}$ for the same sample set and used these updated values within a revised modeling framework to derive new estimates of evaporation and precipitation rates. Here, the dataset presented in Santi et al. (2020) is used to evaluate the consequences of calibration choice on temperature and water $\delta^{18}O$ estimates and provide a first order estimate of how changes in these values would modify clumped isotope-derived hydroclimatic variables, including water temperature, $\delta^{18}O_{water}$, mean annual air temperature (MAAT), evaporation rates, and precipitation rates. Data was reprojected into the I-CDES reference frame following current best practices and standardization procedures (Bernasconi *et al.*, 2021; Upadhyay *et al.*, 2021).

Table 1.4 shows the impact of applying different calibrations on water temperature and $\delta^{18}O_{water}$ to the Lake Surprise dataset for LGM and Deglacial samples, relative to the original publication (see Fig. 1.A.5). On first order, the composite calibration derived from all freshwater

carbonates generally produces 0.8°C warmer water temperatures and 0.2‰ higher $\delta^{18}O_{water}$ values than the original publication (Table 1.4). This results in a similar pattern in MAAT, with 0.9 - 1.1 °C increases in MAAT, and overall increases in evaporation rates of 90-122 mm/yr and precipitation rates of 36-40 mm/yr relative to the estimates calculated from the original publication values (Fig. 1.A.5). Water temperatures and $\delta^{18}O_{water}$ estimates derived using the material-specific calibration for biologically mediated carbonates are about 1°C cooler and 0.3‰ lower than the values estimated from the freshwater composite calibration, with similar evaporation rates (ranging from 11 mm/yr decreases and 60 mm/yr increases relative estimates derived from the original publication) and precipitation rates (ranging from 15 mm/yr increases and 0 mm/yr increases relative to estimates derived from the original publication) (Table 1.4), and are relatively similar to what was reported in the original publication. In contrast, applying the calibration from Anderson et al. (2021) results in 1.8°C cooler temperatures and 0.4‰ lower $\delta^{18}O_{water}$ values relative to the original results, a similar offset from material-specific estimates, and 1.4 - 1.5°C cooler temperatures than the freshwater composite calibration. The reduction in water temperatures relative to the other calibrations results in MAAT estimates for the deglacial that are 2.5 - 2.9°C cooler than the original publication, and subsequent reductions in evaporation (139 - 180 mm/yr) and precipitation rates (73 - 95 mm/yr) (see Supplementary Text 1).

4.4.3 Paleoaltimetry of the Tibetan Plateau

Constraints on water temperature and water $\delta^{18}O$ provided from clumped isotope analyses have been used to constrain the evolution of the tectonic and topographic history of a region (Ghosh, Garzione and Eiler, 2006; Quade *et al.*, 2013; Huntington and Lechler, 2015; Li *et al.*, 2019; Richter *et al.*, 2022). This proxy relies on the premise that lake water temperature is directly related to air temperature; therefore, as basins undergo surface uplift as a result of large-scale

tectonic processes (e.g. crustal shortening and thickening, convective removal of lower lithosphere, etc.), the ambient air and water temperature should decrease, as governed by the local lapse rate (Ghosh *et al.*, 2006; Quade *et al.*, 2013; Huntington and Lechler, 2015; Li *et al.*, 2019). Reconstructed $\delta^{18}O_{water}$ can provide additional constraints on paleoelevation, because the stable isotope compositions of meteoric and surface waters decreases as altitude increases (Chamberlain and Poage, 2000; Poage and Chamberlain, 2001; Rowley and Garzione, 2007).

Our composite freshwater carbonate and material-specific calibration from fine-grained carbonates is applied on a published paleoelevation reconstruction of the Nangqian Basin, located in the east-central Tibetan Plateau, from Li et al. (2019), to assess the impact of our calibrations. Water temperatures and $\delta^{18}O_{water}$ for lacustrine samples spanning the Late Cretaceous to the Late Eocene were recalculated in Table 1.4.

Mean temperatures for the Late Cretaceous through late Eocene derived using the material-specific calibration are within 0.2 and 1.9°C of the published results, while the composite freshwater calibration results in 0.2 to 1.4 °C lower temperatures (Table 1.7). Applying the calibration of Anderson et al. (2021) results in even cooler temperatures for each unit than the equations derived in this study, ranging from 3.2 to 3.6°C lower than the original publication. $\delta^{18}O_{water}$ values (Table 1.A.7) show a similar pattern.

Our clumped-isotope derived results were used to compare estimates of elevation changes during the late Eocene (38-37 Ma) following the two approaches used in Li et al. (2019). First, Late Eocene Δ_{47}-temperature values were used to reconstruct $\delta^{18}O_{water}$ values, which are then used within a model that partitions dominant regional moisture sources to estimate paleoelevation (Li *et al.*, 2019). Using a material-specific calibration results in $\delta^{18}O_{water}$ estimates that support a mean hypsometric paleoelevation of 2.8 ±1.1 km and 3.1 ±1.1 km, similar to the

original reconstruction (2.8 ±1.1 km and 3.2 ±1.1 km), and ~1.3 km lower than the modern hypsometric mean elevation (4.2 km) of the Nangqian Basin. The cooler temperatures derived using the calibration of Anderson et al. (2021) result in more depleted water $\delta^{18}O$ values and similar estimates of paleoelevation (2.9 ±1.1 km and 3.2 ±1.1 km), but still within error of the original publication and the material-specific calibration.

Second, the authors use clumped-isotope derived estimates of water temperature and a lapse rate that relates elevation to modern lake water temperatures on the Tibetan Plateau. The material-specific calibration using Late Eocene fine-grained carbonates results in a mean T-Δ_{47} value of carbonates of 30.3°C, 0.3°C higher than the published value. This mean T-Δ_{47} value is 13.3°C higher than the estimated modern warm-season lake surface water temperature (~17°C) at 3.8 km. Post-Eocene global cooling accounts for roughly 6°C of the temperature decrease (Hansen *et al.*, 2008), while the remaining temperature decrease (6.5°C) would reflect paleoelevation increases of the basin floor after the Eocene. Applying a lapse rate of –6.1 ± 1.0 °C/km for lake surface-water temperature on the Tibetan Plateau (Huntington *et al.*, 2015) results in 1.0 ± 0.3 km of post–Late Eocene elevation increase and paleoelevation estimates of 2.8 km for the basin floor when applying a material-specific calibration.

Late-Eocene lake water temperatures estimated from the freshwater composite calibration are 10.9 °C higher than modern warm-season values, resulting in elevation change estimates of 0.8 km elevation increase. The cooler temperatures estimated from composite freshwater calibration result in paleo-elevation estimates of 3.0 km above sea level for the Nangquian Basin during this time. The Anderson et al. (2021) calibration estimates lake water temperatures are 9.1°C warmer than modern warm-season values. The reduction in estimated water temperatures relative to the other calibration results in a paleo-elevation estimate for the basin floor of 3.3 km

above sea level, with 0.5 km of uplift occurring post Late-Eocene. The paleoelevation estimates derived from Anderson et al. (2021) are 0.5 km lower than those derived using a material-specific calibration.

5. Conclusions

In order to confidently use proxies to characterize and understand past environments, it is necessary to have a solid understanding of modern systems. This work presents an extensive composite dataset of 135 clumped isotope samples of terrestrial freshwater carbonates from 96 sites and derive relationships between modern water temperatures and Δ_{47}. These freshwater Δ_{47}-temperature calibrations are well constrained, encompass a variety of types of natural lacustrine, fluvial, and spring carbonates, and span a broad range of temperatures, elevations, and latitudes. As the carbonates presented in this study are taken directly from modern freshwater settings, they are more representative of real-world systems, and may, in some circumstances, be more appropriate for application to reconstruct paleotemperatures, than Δ_{47}-temperature carbonate calibrations from experimentally grown carbonates. However, since our approach utilizes *in-situ* lake water surface temperature data, there is an added uncertainty in the timing of carbonate formation temperature and calcification timeframe for each of our calibration samples. Additionally, for some freshwater carbonates, the material-specific calibrations are still relatively limited in size (minimum n = 22). Application of material-specific calibrations is recommended for samples that fall within the range the calibration was developed, and not extrapolating far outside of the range.

Our results show a convergence of slopes but differences in the intercepts of the Δ_{47}-temperature relationship between freshwater carbonate groups. Specifically, an ANCOVA

analysis shows that material specific calibrations based on grouping freshwater carbonates (biogenic, biologically mediated, fine-grained carbonate, and travertine) have statistically indistinguishable slopes between other freshwater carbonate groups and recently published calibration studies, but in some cases, where there is strong evidence for biogenic origin, detects differences in intercepts. In many cases, implementing material-specific calibrations reduces the magnitude of residuals (offsets between Δ_{47}-derived temperatures/water $\delta^{18}O$ and measured temperature/water $\delta^{18}O$) and RMSE. However, the calculated values from the composite and material-specific freshwater calibrations are often within 1.0 to 1.5 °C of each other, indicating generally good agreement. Water $\delta^{18}O$ values derived from utilizing material-specific calibrations can recover independently measured water $\delta^{18}O$ values with reasonable accuracy, with 39% and 74% of lakes being within 1‰ and 2‰ of measured water $\delta^{18}O$, respectively, reflecting a 7% and 10% improvement relative to our composite freshwater calibration. The relatively small differences between materials could be accounted for by biases in seasonal formation and/or differential expressions of kinetic effects in various types of archives that are not well constrained.

Additionally, the impacts of calibrations relationships in this study were explored by examining three terrestrial paleo-reconstructions using Δ_{47} measurements of freshwater carbonates. First, material-specific calibrations are shown to yield the most reasonable estimates for a new dataset from a travertine sequence in Austria. This study hypothesizes that this deposit was likely derived from groundwater sources due to increased percolation of meteoric water and glacial melt. Second, the biologically mediated and composite freshwater calibrations were used to explore implications for hydroclimatic changes that occur using different calibrations at Lake Surprise in the Western US, with small differences in reconstructed hydroclimate parameters.

Third, the fine-grained carbonate calibration was applied to estimate the Eocene paleoelevation of the Nangqian Basin within the Tibetan Plateau and find that our material-specific calibration derived elevations are in agreement with the original publication, and that elevations derived using the composite freshwater calibration suggest 300 m higher uplift, which is not enough to change the conclusions of the paper. Overall, this work provides a basis for more accurate reconstructions of terrestrial paleoclimate, paleohydrology, and paleoaltimetry using freshwater archives, and opens the door to more robust understandings of paleoenvironmental processes.

6. Figures

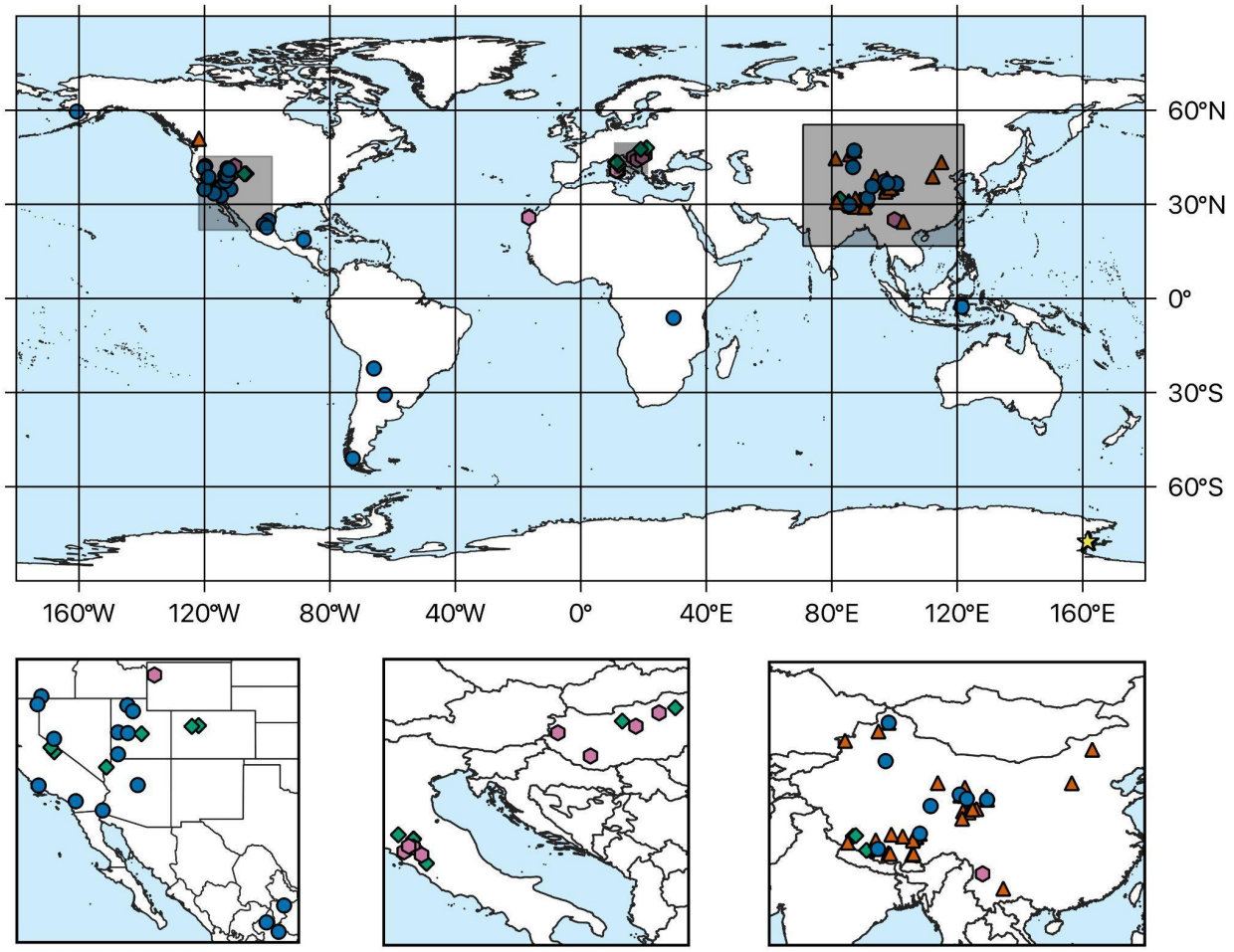

Figure 1.1: Sample locations used for this study. Clumped isotope data in this study comes from 135 samples collected from 96 sites in modern lakes, rivers, and springs. Blue circles indicate location of samples with new data from the Eagle-Tripati lab (n = 25; 159 measurements), orange triangles indicate data measured in the Eagle-Tripati lab that has been published and was recalculated onto the I-CDES reference frame for this study (n = 30), green diamonds indicate data from other labs that were recalculated onto the I-CDES reference frame as part of this study (n = 29), pink hexagons denotes sites where samples were analyzed twice, with one set of measurements being recalculated and the other taken directly from published data (n = 12), yellow stars represent data directly taken from other publications (n = 3, points overlap on main figure).

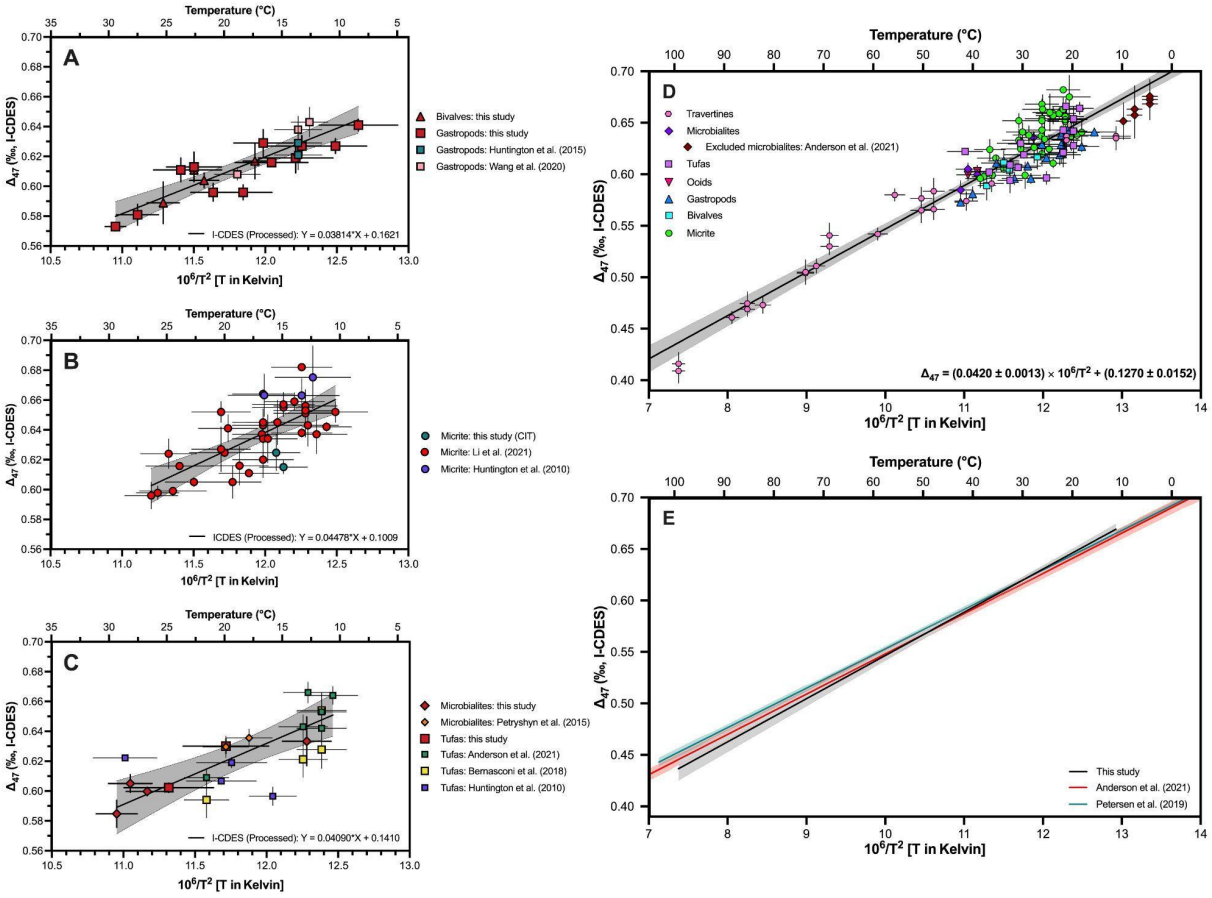

Figure 1.2: A-C) Calibration data by study for A) biologic carbonates, B) fine-grained carbonates, and C) biologically mediated carbonates. Regressions are shown for data reprocessed in the I-CDES reference frame. Symbols shaded in red colors indicate samples processed in the Eagle-Tripati laboratory. **D) Δ_{47}-temperature relationship for all 108 freshwater carbonates included in this study.** Black line represents a linear, ordinary least squares regression through the data and the gray shaded area represents the 95% confidence interval. A strong relationship is present between Δ_{47} and temperature ($p < 0.0001$; $r^2 = 0.8959$). Red diamonds represent low temperature and/or high pH lacustrine microbialites from Anderson et al. (2021) were not included in the regression. **E) Comparison of our composite freshwater regression to previously published clumped isotope calibrations.** ANCOVA results show that the slope derived for our calibration is statistically different from the acid corrected calibration of Petersen et al. (2019) and Anderson et al. (2021), with p_{slope} values of 0.0036 and 0.0334, respectively (Table 1.3).

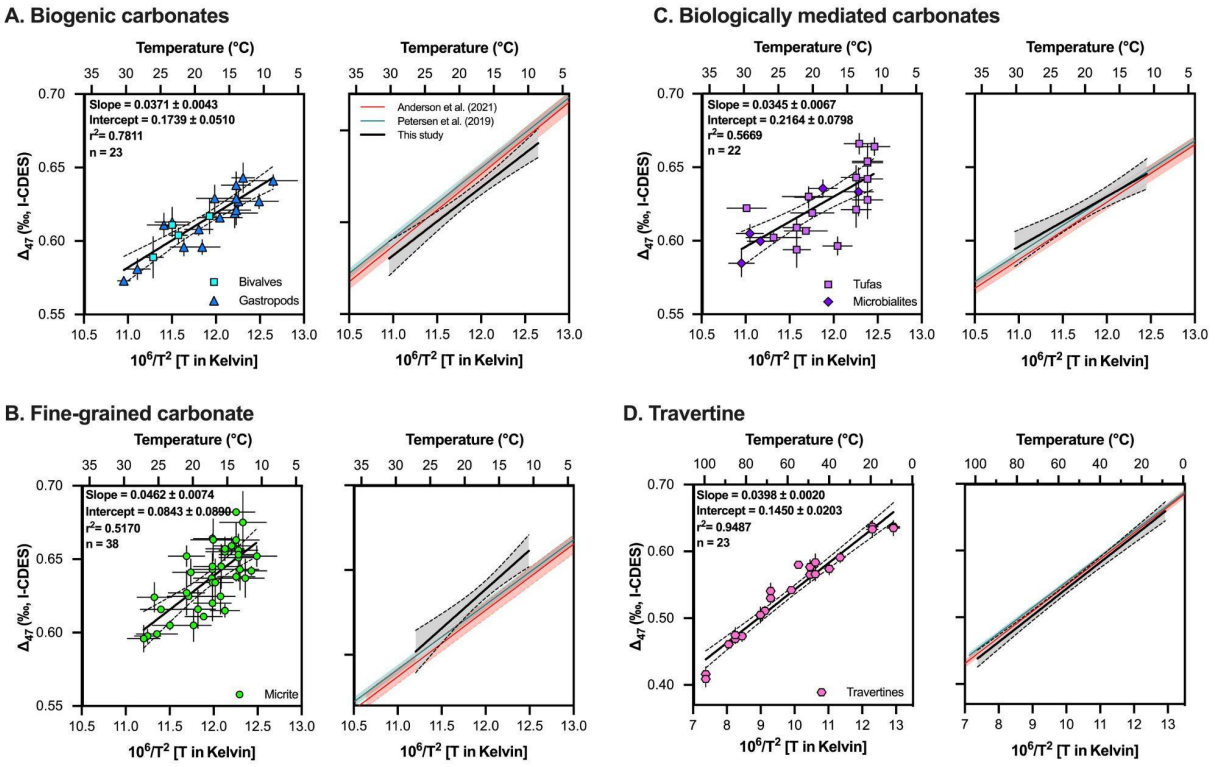

Figure 1.3: Δ_{47}-temperature relationships for different groups of freshwater carbonates. Left: Δ_{47}-temperature relationship for all carbonate types included in this study. Black line represents a linear, ordinary least squares regression through the data. A strong relationship between Δ_{47} and temperature exists for each group of data. All groups of data have statistically indistinguishable slopes, but find statistically significant differences in intercepts between a majority of datasets (Table 1.3), suggesting that material-specific calibrations may be most appropriate. Right: Derived comparison of our material-specific calibrations to previously published clumped isotope calibrations. All material-specific regressions derived in this study have statistically similar slopes to the slopes presented in Petersen et al. (2019) and Anderson et al. (2021), but significant differences in intercept (Table 1.3).

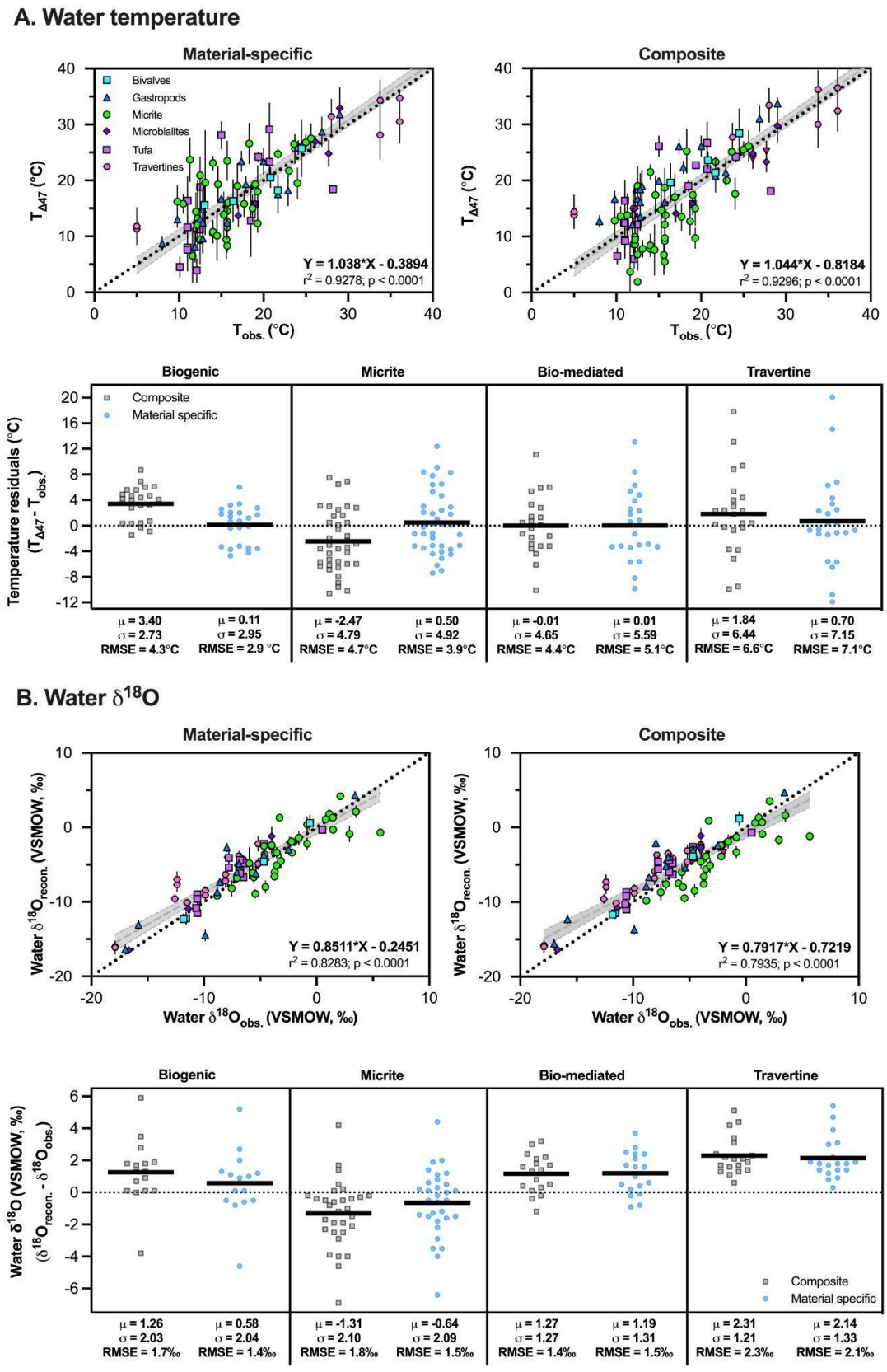
A. Water temperature
Material-specific
Composite
Bivalves
Gastropods
Micrite
Microbialites
Tufa
Travertines
T_Δ47 (°C)
T_obs. (°C)
Y = 1.038*X - 0.3894
r² = 0.9278; p < 0.0001
Y = 1.044*X - 0.8184
r² = 0.9296; p < 0.0001
Biogenic
Micrite
Bio-mediated
Travertine
Composite
Material specific
Temperature residuals (°C)
(T_Δ47 - T_obs.)
μ = 3.40
σ = 2.73
RMSE = 4.3°C
μ = 0.11
σ = 2.95
RMSE = 2.9 °C
μ = -2.47
σ = 4.79
RMSE = 4.7°C
μ = 0.50
σ = 4.92
RMSE = 3.9°C
μ = -0.01
σ = 4.65
RMSE = 4.4°C
μ = 0.01
σ = 5.59
RMSE = 5.1°C
μ = 1.84
σ = 6.44
RMSE = 6.6°C
μ = 0.70
σ = 7.15
RMSE = 7.1°C
B. Water δ18O
Material-specific
Composite
Water δ18O_recon. (VSMOW, ‰)
Water δ18O_obs. (VSMOW, ‰)
Y = 0.8511*X - 0.2451
r² = 0.8283; p < 0.0001
Y = 0.7917*X - 0.7219
r² = 0.7935; p < 0.0001
Biogenic
Micrite
Bio-mediated
Travertine
Water δ18O (VSMOW, ‰)
(δ18O_recon. - δ18O_obs.)
Composite
Material specific
μ = 1.26
σ = 2.03
RMSE = 1.7‰
μ = 0.58
σ = 2.04
RMSE = 1.4‰
μ = -1.31
σ = 2.10
RMSE = 1.8‰
μ = -0.64
σ = 2.09
RMSE = 1.5‰
μ = 1.27
σ = 1.27
RMSE = 1.4‰
μ = 1.19
σ = 1.31
RMSE = 1.5‰
μ = 2.31
σ = 1.21
RMSE = 2.3‰
μ = 2.14
σ = 1.33
RMSE = 2.1‰

Figure 1.4: Comparison of reconstructed values of temperature and $\delta^{18}O_{water}$ from material-specific and composite calibrations from this study to observations. Use of a composite Δ_{47}-temperature calibration yields less accurate and precise results. A. Comparison of measured temperature ($T_{obs.}$) to Δ_{47}-derived temperature ($T_{\Delta 47}$) values using the material-specific and composite freshwater calibration. Bottom panel shows a comparison of temperature residuals (reconstructed-observations) using the composite and material-specific calibrations. Values derived using the composite regression are represented using black squares and material-specific calibrations are represented using blue circles. Horizontal black bars represent the mean and values at the bottom of each dataset show the mean value and standard deviation for residuals along with the RMSE for each dataset using the respective calibrations. B. Comparison of measured $\delta^{18}O_{water}$ ($\delta^{18}O_{obs.}$) to Δ_{47}-derived $\delta^{18}O_{water}$ values ($\delta^{18}O_{recon.}$) using material specific and composite freshwater calibration. $\delta^{18}O_{water}$ values are calculated using temperatures derived using our composite and material-specific calibrations between Δ_{47} and temperature, and oxygen isotope mineral-water fractionation factors from Kim and O'Neil (1997) (calcite) or Kim et al. (2007) (aragonite). Bottom panel displays $\delta^{18}O_{water}$ residuals (reconstructed-observations) using the composite and material-specific calibrations. Generally, there is some improvement in RMSE for temperature and $\delta^{18}O_{water}$ reconstructions for the use of material-specific calibrations, though in the case of bio-mediated carbonates and travertines, the improvement is small to negligible.

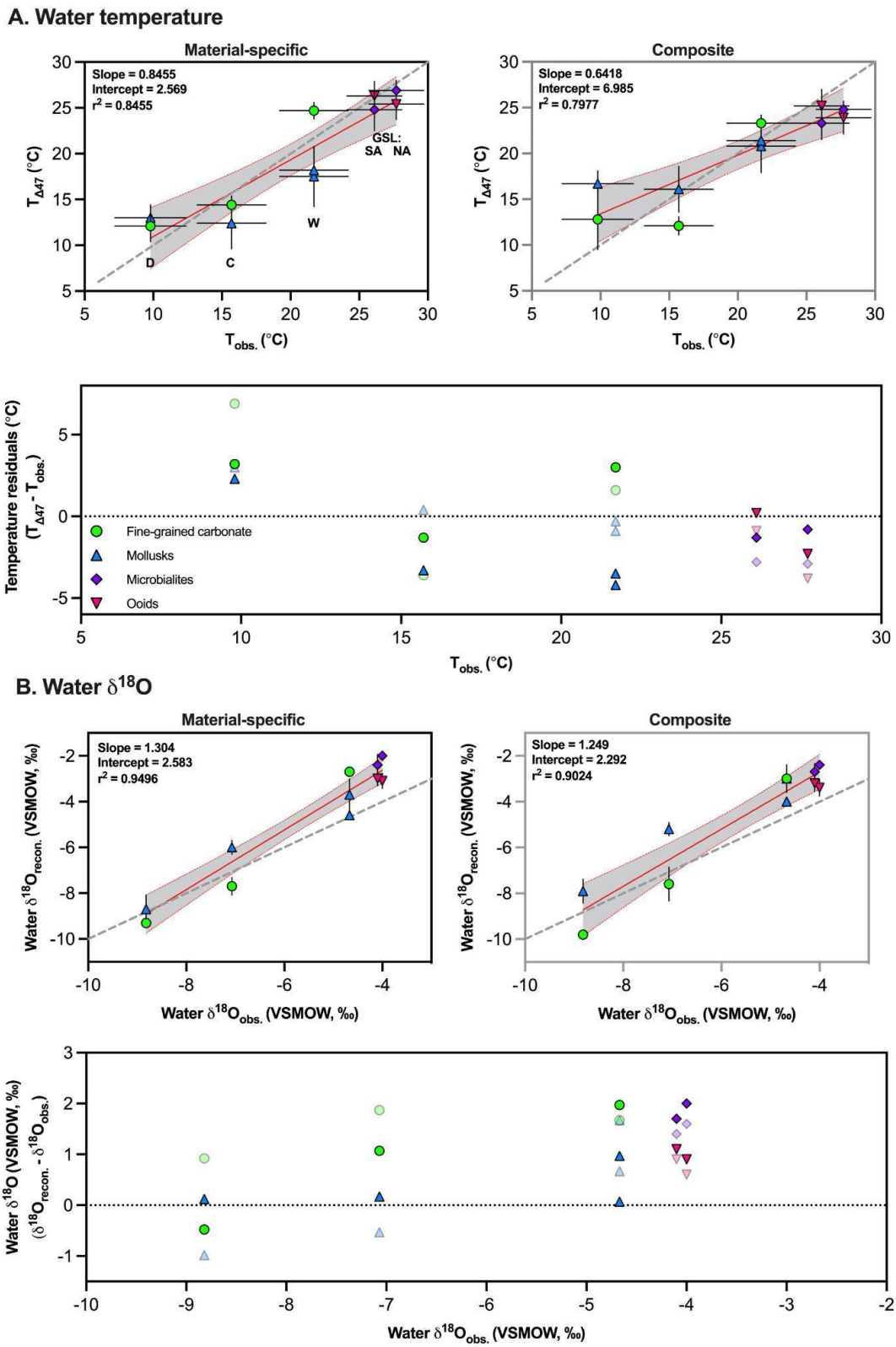
A. Water temperature
Material-specific
Slope = 0.8455
Intercept = 2.569
r² = 0.8455
GSL:
SA NA
W
D
C
T_Δ47 (°C)
T_obs. (°C)
Composite
Slope = 0.6418
Intercept = 6.985
r² = 0.7977
T_Δ47 (°C)
T_obs. (°C)
Temperature residuals (°C)
(T_Δ47 - T_obs.)
Fine-grained carbonate
Mollusks
Microbialites
Ooids
T_obs. (°C)
B. Water δ18O
Material-specific
Slope = 1.304
Intercept = 2.583
r² = 0.9496
Water δ18O_recon. (VSMOW, ‰)
Water δ18O_obs. (VSMOW, ‰)
Composite
Slope = 1.249
Intercept = 2.292
r² = 0.9024
Water δ18O_recon. (VSMOW, ‰)
Water δ18O_obs. (VSMOW, ‰)
Water δ18O (VSMOW, ‰)
(δ18O_recon. - δ18O_obs.)
Water δ18O_obs. (VSMOW, ‰)

Figure 1.5: Evaluation of clumped isotope derived temperature and $\delta^{18}O_{water}$ for locations with dual materials. A. Clumped-isotope derived temperature reconstructions using material specific calibrations (top row; black frame) and composite freshwater calibration (top row; gray frame). A linear regression and the 95% confidence interval is shown through the data using red lines and gray shading, respectively. Bottom panel shows residuals for both the material specific calibrations and composite calibrations (semi-transparent symbols), along with the average difference in temperature between the two archives (black and gray numbers and lines for material specific and composite calibration, respectively). Clumped isotope derived temperatures are denoted as $T_{\Delta 47}$, while independently observed water temperatures are denoted as T_{obs}. Sites are labeled on plot: D: Daija Co, C: Cuona Lake, W: Wulungu Lake, GSL NA: North Arm, Great Salt Lake, GSL SA: South Arm, Great Salt Lake. Using a material-specific calibration results in a reduction of temperature residuals in most cases. Material-specific calibrations also yield more realistic temperature estimates, given each lake's individual setting. B. Reconstructed water $\delta^{18}O$ values using material specific (top row, black frame) and composite (top row, gray frame) calibrations. Clumped isotope-based reconstructions of water $\delta^{18}O$ and independently measured $\delta^{18}O$ values are denoted as water $\delta^{18}O_{reconstructed}$ and water $\delta^{18}O_{observed}$, respectively. A linear regression and the 95% confidence interval is shown through the data is shown by using red lines and gray shading, respectively. The residuals from measured values are displayed on the bottom plot, and residuals between different archives are denoted by black and gray bars and values for the material specific and composite calibrations, respectively.

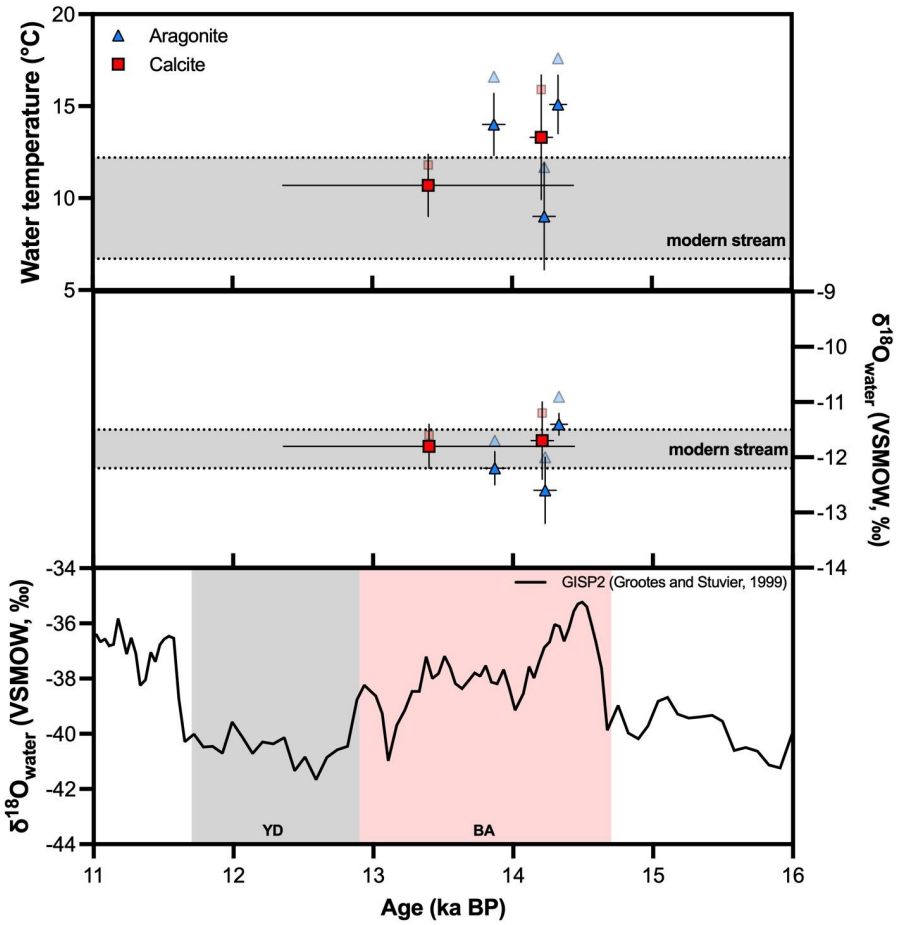

Figure 1.6: Clumped isotope derived estimates of temperature and $\delta^{18}O_{water}$ for a travertine terrace in Ainet, Austria. Solid symbols represent estimates derived from material-specific calibrations, while lighter symbols represent estimates derived from our composite freshwater calibration. Gray bands represent the range of modern stream values measured in May, July, and October (Boch *et al.*, 2005) and data for GISP2 ice core record is from (Stuiver and Grootes, 2000). Values are broadly consistent with modern temperatures and $\delta^{18}O_{water}$ of nearby streams.

7. Tables

Sample Name	Latitude	Longitude	MAAT (°C)	Water Temperature (°C)	Water Temperature Error (°C)	$\delta^{13}C$ (‰, VPDB)	$\delta^{18}O$ (‰, VPDB)	Δ_{47} (‰, I-CDES)	1 s.e.	Data Source
Bivalves										
Red Rock	34.8	-111.8	15.3	16.4	1.0	-10.0	-12.0	0.617	0.012	Eagle-Tripati lab (this study)
Colorado River	32.7	-114.7	21.9	20.8	1.3	-9.1	-13.0	0.604	0.016	Eagle-Tripati lab (this study)
Vail Lake	33.5	-117.0	12.3	24.5	1.5	-6.6	-1.1	0.589	0.014	Eagle-Tripati lab (this study)
Wulungu Lake	47.1	87.2	7.0	21.7	2.5	-3.6	-4.3	0.611	0.002	Eagle-Tripati lab (this study)
Gastropods										
Santa Clara River	37.4	-113.5	15.3	13	3.1	-7.1	-14.0	0.619	0.010	Eagle-Tripati lab (this study)
Painter Spring	39.2	-113.4	11.8	12.5	3.1	-10.2	-13.2	0.627	0.007	Eagle-Tripati lab (this study)
Lake Warner	42.2	-119.8	8.3	20	2.0	-10.6	-8.9	0.596	0.006	Eagle-Tripati lab (this study)
Clear Lake	39.1	-112.6	10.4	15	3.0	-7.0	-14.2	0.616	0.002	Eagle-Tripati lab (this study)
Lake Tanganyika	-6.2	29.6	22.3	26.9	2.0	-0.4	1.9	0.581	0.007	Eagle-Tripati lab (this study)
Lake Towuti	-2.8	121.5	23.6	29	1.0	-7.6	-7.2	0.573	0.003	Eagle-Tripati lab (this study)
Nimgun Lake	59.6	-160.8	-1.3	8	3.1	-6.1	-12.2	0.641	0.004	Eagle-Tripati lab (this study)
Fuxian Lake	24.4	102.9	17.3	17.6	3.8	-2.2	-3.5	0.608	0.004	Eagle-Tripati lab[a]
Lake Manasarovar	30.7	81.6	4.0	12.8	2.0	-3.8	-3.3	0.638	0.009	Eagle-Tripati lab[a]
Yamdrok Yumco	29.1	90.4	5.0	11.9	1.5	-6.2	-11.2	0.643	0.010	Eagle-Tripati lab[a]
Yamdrok Yumco	29.2	90.6	5.0	11.9	1.5	-0.4	-4.5	0.643	0.006	Eagle-Tripati lab[a]
Tso Nag	31.6	82.3	-1.3	12.8	2.0	-2.6	-5.7	0.621	0.010	Eiler lab[b]
Tsangpo	29.6	84.9	-2.4	12.8	2.0	-4.1	-15.9	0.621	0.010	Eiler lab[b]
Zhongba	29.7	84.2	-2.6	12.8	2.0	-5.3	-13.5	0.629	0.011	Eiler lab[b]
Bosten Lake	41.9	86.8	9.5	22.9	2.5	-3.9	-2.4	0.611	0.008	Eagle-Tripati lab (this study)
Cuona Lake	32.0	91.5	-1.1	15.7	2.5	-1.1	-7.1	0.629	0.009	Eagle-Tripati lab (this study)
Dajia Co	29.9	85.7	-2.9	9.8	2.5	0.0	-4.5	0.627	0.005	Eagle-Tripati lab (this study)
Jinzihai Lake	36.7	97.9	4.3	17.4	2.5	-10.5	-8.0	0.596	0.005	Eagle-Tripati lab (this study)
Wulungu Lake	47.1	87.2	7.0	21.7	2.5	-2.3	-3.1	0.613	0.010	Eagle-Tripati lab (this study)
Fine-grained carbonates										
Laguna Pozuelos	-22.4	-66.0	8.6	14.6	2.0	-7.4	0.4	0.625	0.012	Eiler lab (this study)
Mar Chiquita	-30.8	-62.5	18.4	29	2.0	-3.2	-1.1	0.611	0.004	Eiler lab (this study)
El Potosi	24.8	-99.7	21.8	23.6	3.1	-5.3	-7.7	0.599	0.002	Eagle-Tripati lab[c]

Kusai	35.7	92.9	-4.4	10.5	2.0	3.1	-0.4	0.642	0.003	Eagle-Tripati lab[c]
Laguna La Salada	23.4	-101.1	14.9	23	3.1	3.3	0.0	0.616	0.001	Eagle-Tripati lab[c]
Laguna Las Cruces	22.7	-100.1	20.9	19	3.1	-0.7	-4.0	0.625	0.002	Eagle-Tripati lab[c]
Zaca Lake	34.8	-120.0	13.3	25	2.0	1.5	-1.6	0.598	0.005	Eagle-Tripati lab[c]
Pipahai Lake	38.9	112.2	4.1	19.3	2.6	1.7	-2.5	0.627	0.015	Eagle-Tripati lab[c]
Chagan Lake	43.4	115.0	1.9	24	2.6	-2.4	-4.8	0.624	0.010	Eagle-Tripati lab[c]
Gahai Lake	37.0	100.6	1.3	15.8	2.5	2.2	2.0	0.637	0.004	Eagle-Tripati lab[c]
Qinghai Lake	36.6	100.7	1.9	19.3	2.6	2.9	2.3	0.652	0.007	Eagle-Tripati lab[c]
Kuhai Lake	35.3	99.2	-5.1	12.5	2.5	2.1	1.4	0.682	0.001	Eagle-Tripati lab[c]
Eling Lake	35.0	97.7	-4.3	14	2.6	-1.0	-4.3	0.655	0.006	Eagle-Tripati lab[c]
Zhaling Lake	35.0	97.4	-5.9	16.9	2.6	0.5	-2.7	0.611	0.001	Eagle-Tripati lab[c]
Xingxinghai Lake	34.9	98.1	-2.7	15.7	2.6	-0.1	-4.4	0.620	0.012	Eagle-Tripati lab[c]
Koucha Lake	34.0	97.2	-5.3	12.5	2.5	4.6	-5.1	0.638	0.003	Eagle-Tripati lab[c]
Donggi Cona Lake	35.3	98.7	-1.7	11.3	2.5	1.7	-4.7	0.637	0.013	Eagle-Tripati lab[c]
Gahai Lake2	37.1	97.6	5.4	18.3	2.5	1.6	0.0	0.605	0.011	Eagle-Tripati lab[c]
Tuosu Lake	37.2	97.0	5.0	17.7	2.5	1.5	-1.3	0.616	0.013	Eagle-Tripati lab[c]
Hala Lake	38.2	97.6	-4.1	14	2.6	3.9	1.0	0.657	0.008	Eagle-Tripati lab[c]
Cuona Lake	32.0	91.5	-1.1	15.7	2.6	2.2	-9.5	0.643	0.004	Eagle-Tripati lab[c]
Pung Co	31.5	91.0	0.4	15.7	2.6	4.8	-4.1	0.664	0.003	Eagle-Tripati lab[c]
Jiang Co	31.5	90.8	0.4	13.1	2.5	3.2	-5.6	0.659	0.006	Eagle-Tripati lab[c]
Bam Co	31.2	90.5	-1.7	12	2.5	3.2	-6.2	0.643	0.014	Eagle-Tripati lab[c]
Shen Co	31.0	90.5	-1.7	12.2	2.6	3.9	-5.8	0.656	0.004	Eagle-Tripati lab[c]
Selin Co	31.6	89.1	1.7	12.2	2.6	5.0	-3.5	0.651	0.016	Eagle-Tripati lab[c]
Dagze Co	31.8	87.6	1.0	12.2	2.6	2.0	-8.6	0.653	0.009	Eagle-Tripati lab[c]
Zharinanmu Co	31.1	85.4	0.2	14.5	2.6	4.4	-6.6	0.645	0.015	Eagle-Tripati lab[c]
Dajia Co	29.9	85.7	-2.9	9.8	2.6	3.9	-7.4	0.652	0.007	Eagle-Tripati lab[c]
Angrenjin Co	29.3	87.2	2.3	15.7	2.6	0.6	-7.4	0.634	0.020	Eagle-Tripati lab[c]
Lang Co	29.2	87.4	2.3	15.3	2.5	2.9	-5.5	0.634	0.016	Eagle-Tripati lab[c]
Sailimu Lake	44.6	81.2	-1.5	18.7	2.6	2.7	-1.5	0.641	0.009	Eagle-Tripati lab[c]
Ailike Lake	45.9	85.8	7.2	25.6	2.5	-3.1	-6.7	0.596	0.009	Eagle-Tripati lab[c]
Wulungu Lake	47.1	87.2	7.0	21.7	2.6	0.8	-5.1	0.605	0.003	Eagle-Tripati lab[c]
Sugan Lake	38.9	93.9	0.4	15.7	2.6	0.8	4.4	0.645	0.005	Eagle-Tripati lab[c]
Blue Eagle Lake	39.8	-106.8	5.4	15.6	3.1	-4.4	-14.0	0.663	0.014	Eiler lab[d]
Emerald Lake	39.1	-111.5	5.4	12.5	3.1	-0.3	-11.4	0.663	0.011	Eiler lab[d]
South Grizzly Lake	39.7	-107.3	2.5	11.6	3.1	-3.2	-14.1	0.675	0.021	Eiler lab[d]
Microbialites										

Laguna Bacalar	18.7	-88.4	27.0	29	2.0	-1.8	-6.0	0.585	0.009	Eagle-Tripati lab (this study)
Lago Sarmiento	-51.1	-72.7	6.5	12.2	2.0	4.9	-1.3	0.633	0.016	Eagle-Tripati lab (this study)
South Arm, Great Salt Lake	41.0	-112.2	8.5	26.1	2.0	3.6	-4.9	0.600	0.003	Eagle-Tripati lab (this study)
North Arm, Great Salt Lake	41.4	-112.7	11.0	27.7	2.0	4.6	-4.8	0.605	0.006	Eagle-Tripati lab (this study)
Kelly Lake	51.0	-121.8	3.5	17	2.0	-2.5	-16.5	0.636	0.006	Eiler lab[e]
Pavillion Lake	50.9	-121.7	3.5	19	2.0	0.6	-11.3	0.630	0.007	Eiler lab[e]
Ooids										
South Arm, Great Salt Lake	41.4	-112.7	8.5	27.7	2.0	4.0	-4.4	0.599	0.006	Eagle-Tripati lab (this study)
North Arm, Great Salt Lake	41.0	-112.2	11.0	26.1	2.0	4.3	-4.2	0.603	0.006	Eagle-Tripati lab (this study)
Tufas										
Lake Surprise	41.5	-120.1	5.6	19	3.8	3.6	-2.7	0.630	0.005	Eagle-Tripati lab[f]
Walker Lake	38.7	-118.8	13.0	24.1	4.2	0.4	-2.8	0.602	0.003	Eagle-Tripati lab (this study)
Cannatoppa*	43.3	11.6	14.4	11	2.0	-4.0	-5.4	0.653	0.006	ETH[g]
						-4.1	-5.4	0.628	0.013	MIT
La Pigna*	43.1	11.3	14.4	12.5	2.0	-11.3	-5.7	0.643	0.008	ETH[g]
						-11.4	-5.5	0.621	0.012	MIT
Sarteano*	43.0	11.9	14.2	20.7	2.0	0.6	-7.4	0.609	0.006	ETH[g]
						0.4	-7.3	0.594	0.012	MIT
Szalajka	48.1	20.4	9.5	12.1	2.0	-9.4	-9.3	0.666	0.007	ETH[g]
Szalajka*	48.1	20.4	9.5	11	2.0	-10.2	-8.5	0.642	0.007	ETH[g]
						-10.3	-8.3	0.654	0.012	MIT
Szalajka	48.1	20.4	9.5	10.1	2.0	-9.9	-8.7	0.664	0.006	ETH[g]
Kailas	31.7	82.7	-1.2	15	2.0	1.8	-5.2	0.596	0.006	Eiler lab[b]
Lake Crowley	37.6	-118.7	8.4	18.5	3.0	-1.2	-14.9	0.638	0.019	Eiler lab[d]
Lake Mead	36.3	-114.4	17.7	28.2	3.0	-8.9	-8.9	0.622	0.000	Eiler lab[d]
Mono Lake	37.9	-119.0	8.4	19.4	3.0	6.9	-2.2	0.607	0.002	Eiler lab[d]
Travertines										
Aqua Borra*	43.3	11.4	14.4	36.1	2.0	2.3	-8.1	0.565	0.012	ETH[g]
						1.7	8.4	0.577	0.011	MIT
Bagnoli	43.4	11.1	14.8	23.7	2.0	5.5	-7.6	0.591	0.008	ETH[g]
BSF Fosso Bianco	42.9	11.7	14.4	44.6	2.0	7.4	-9.9	0.542	0.006	ETH[g]
Bük*	47.4	16.8	10.6	54.9	2.0	2.2	-15.1	0.530	0.008	ETH[g]
						2.2	-15.0	0.541	0.012	MIT
Madre del Agua*	28.2	-16.6	-	33.8	2.0	0.2	-10.3	0.566	0.010	ETH[g]

						0.1	-10.2	0.584	0.013	MIT
Igal*	46.5	17.9	10.7	75.0	2.0	0.7	-13.6	0.469	0.007	ETH[g]
						0.6	-13.5	0.475	0.011	MIT
Köröm	48.0	21.0	10.2	79.2	2.0	3.6	-22.0	0.461	0.006	ETH[g]
Baishuitai - summer*	27.5	100.0	7.2	12.0	2.0	5.5	-14.3	0.637	0.006	ETH[g]
						5.4	-14.3	0.633	0.012	MIT
Baishuitai - winter*	27.5	100.0	7.2	5.0	2.0	5.2	-12.8	0.637	0.008	ETH[g]
						5.1	-12.7	0.635	0.011	MIT
Piscine Carletti	42.4	12.1	14.5	57.9	2.0	7.3	-12.4	0.511	0.007	ETH[g]
Rapolano Terme	43.3	11.6	14.4	28.0	2.0	3.8	-7.5	0.574	0.009	ETH[g]
Szèchenyi Spa	47.5	19.1	11.0	70.9	2.0	2.9	-20.5	0.473	0.008	ETH[g]
Terme Sangiovanni	43.3	11.6	14.4	41.2	2.0	2.6	-8.9	0.580	0.006	ETH[g]
Tura*	47.6	19.6	9.9	95.0	2.0	3.7	-23.3	0.416	0.011	ETH[g]
						3.7	-23.2	0.409	0.012	MIT
Narrow Gauge, Yellowstone*	44.6	-110.4	0.0	60.4	2.0	3.8	-24.5	0.504	0.006	ETH[g]
						3.6	-24.6	0.505	0.012	MIT

Table 1.1: Site information and stable and clumped isotope results for freshwater carbonates used in this study. T_w is the independently measured water temperature. $\delta^{13}C$ and $\delta^{18}O$ values are presented relative to the Vienna Pee Dee Belemnite (VPBD) and Δ_{47} is presented in the I-CDES reference frame. Mean annual air temperatures (MAAT) are averages of the long-term monthly means from each of our sites from 1981-2010, using the University of Delaware's high resolution gridded air temperature dataset (Willmott and Matsuura, 2001) provided by NOAA (https://psl.noaa.gov/data/gridded/data.UDel_AirT_Precip.html). Samples from the Eiler Lab at Caltech were processed in the CDES reference frame and projected into I-CDES following the methodology described in Bernasconi et al. (2021).

*Data from the Bernasconi Lab at ETH was recalculated using the methodology described in Bernasconi et al. (2021) and data from the Bergmann Lab at MIT was taken from Anderson et al. (2021).

[a] Recalculated from Wang et al. (2021)

[b] Recalculated from Huntington et al. (2015)

[c] Recalculated from Li et al. (2021)

[d] Recalculated from Huntington et al. (2010)

[e] Recalculated from Petryshyn et al. (2015)
[f] Recalculated from Santi et al. (2020)
[g] Recalculated from Bernasconi et al. (2018)

	n	Slope ± 1 s.e.			Intercept ± 1 s.e.			r^2	p
Composite	108	0.0420	±	0.0013	0.1270	±	0.0152	0.9053	<0.0001
Biogenic	23	0.0371	±	0.0043	0.1739	±	0.0510	0.7811	<0.0001
Fine-grained	38	0.0462	±	0.0074	0.0844	±	0.0890	0.5170	<0.0001
Bio-mediated	22	0.0345	±	0.0067	0.2164	±	0.0798	0.5669	<0.0001
Travertine	23	0.0398	±	0.0020	0.1450	±	0.0203	0.9487	<0.0001

Table 1.2: Derived regression parameters for all freshwater calibration data and material specific calibration data using linear, ordinary least squares regression.

Regression parameter: slope

	This study: composite	This study: biogenic	This study: fine-grained	This study: bio-mediated*	This study: travertine	Petersen et al. (2019)[a]	Anderson et al. (2021)[b]
This study: composite						0.0036	0.0334
This study: biogenic			0.4880	0.7463	0.6730	0.9456	0.7660
This study: fine-grained		0.4880		0.3785	0.6114	0.4590	0.4880
This study: bio-mediated*		0.7463	0.3785		0.4580	0.6770	0.4852
This study: travertine		0.6730	0.6114	0.4580		0.3620	0.6320
Petersen et al. (2019)[a]	0.0036	0.9456	0.4590	0.6770	0.3620		0.2078
Anderson et al. (2021)[b]	0.0334	0.7660	0.4880	0.4852	0.6320	0.2078	

Regression parameter: intercept

	This study: composite[a]	This study: biogenic	This study: fine-grained	This study: bio-mediated[a]	This study: travertine	Petersen et al. (2019)[b]	Anderson et al. (2021)[a]
This study: composite[a]							
This study: biogenic			0.0000	0.0047	0.6320	0.0728	0.2710
This study: fine-grained		0.0000		0.0379	0.0050	0.0000	0.0000
This study: bio-mediated[a]		0.0047	0.0379		0.1140	0.2540	0.0542
This study: travertine		0.6320	0.0050	0.1140		0.0354	0.4440
Petersen et al. (2019)[b]		0.0728	0.0000	0.2540	0.0354		0.0835
Anderson et al. (2021)[a]		0.2710	0.0000	0.0542	0.4440	0.0835	

Table 1.3: **Results of the ANCOVA test for calibration-pairs for slope and intercept.** Red shading indicates differences in parameters with 95% confidence ($p < 0.05$), yellow shading indicates differences in parameters with 90% confidence ($0.05 < p < 0.10$), and no shading indicates no statistically significant difference between parameters. Top: ANCOVA results for slope. 27 pairs have a p value > 0.1, demonstrating a convergence of slope when looking at material-specific groups of data. Bottom: Results of the ANCOVA test for calibration-pairs for intercept. This analysis is only performed on calibration pairs that had p-values exceeding 0.1 for the slope analysis. Differences in intercepts between different groups of data in this study were prevalent in 4 pairwise comparisons ($p < 0.05$), thus, material specific calibrations may be appropriate for climate reconstructions.

[a]Composite and biologically mediated regression excludes low temperature/high pH microbialites from Anderson et al. (2021).

[b]Δ_{47} values were corrected to a 90°C reference frame using AFF presented in Petersen et al. (2019).

Hydroclimate reconstruction at Lake Surprise, CA				
(41.5°N, 120.0°W)	T_w (°C)		$\delta^{18}O$ (‰)	
	LGM	Deglacial	LGM	Deglacial
This study - material-specific	11.2 ± 6.7	10.5 ± 4.4	-4.0 ± 2.0	-4.1 ± 1.4
This study - composite	12.1 ± 5.4	11.6 ± 3.6	-3.8 ± 1.6	-3.8 ± 1.2
Anderson et al. (2021)	9.6 ± 6.0	9.0 ± 4.0	-4.4 ± 1.2	-4.3 ± 1.6
Santi et al. (2020)	11.3 ± 4.5	10.8 ± 3.0	-4.0 ± 1.3	-4.0 ± 1.0

Elevation reconstruction in Nangqian Basin, Tibetan Plateau						
(32.2°N, 96.5°E)	Unit 1 (mid Cretaceous)		Unit 3 (mid Paleogene; >38 Ma)		Unit 4 (38-37 Ma)	
	T_w (°C)	$\delta^{18}O_w$ (‰)	T_w (°C)	$\delta^{18}O_w$ (‰)	Tw (°C)	$\delta^{18}O_w$ (‰)
This study - material-specific	25.1 ± 3.0	-6.0 ± 1.2	39.0 ± 3.7	-5.0 ± 0.8	30.3 ± 3.5	-6.2 ± 1.1
This study - composite	23.7 ± 3.3	-6.3 ± 1.0	38.8 ± 4.1	-5.0 ± 0.7	27.9 ± 3.8	-6.5 ± 1.0
Anderson et al. (2021)	21.7 ± 3.4	-6.7 ± 1.0	37.7 ± 4.4	-5.2 ± 0.8	26.1 ± 4.0	-6.8 ± 1.0
Li et al. (2019)	24.9 ± 2.8	-6.2 ± 1.5	40.9 ± 4.1	-4.6 ± 0.9	29.7 ± 3.7	-6.2 ± 1.4

Table 1.4: Comparison of recalculated Δ_{47}-based reconstructions derived from the material-specific, composite freshwater, and calibration from Anderson et al. (2021) to published values. Top: Comparison of water temperature and water $\delta^{18}O$ at Lake Surprise, CA to published values from Santi et al. (2020). Bottom: Comparison of clumped isotope derived water temperature and water $\delta^{18}O$ for samples run for clumped isotope analysis from the Nangquian Basin to published values from Li et al. (2019).

8. Supplement

Text S1: Seasonality of freshwater carbonate formation

Carbonates precipitate in many lakes and can form in various freshwater environments with the extent and depth of carbonate deposition determined by seasonal changes in water chemistry, as well as water depth, slope gradient, and circulation within the basin (Platt and Wright, 2009; Gierlowski-Kordesch, 2010). Carbonates that form at the lake margin include ooids, beach rock, shelly accumulations of gastropods and bivalves, microbialites, and tufa, while deep-water deposits are comprised largely of carbonate muds and grains (such as ostracods) that accumulate below the storm wave base (Platt and Wright, 2009). In most cases, carbonate accumulation is controlled by seasonal changes in saturation (Kelts and Hsü, 1978; Anadón *et al.*, 2009; Hren and Sheldon, 2012; Street-Perrott and Harrison, 2013).

Different types of carbonates have different factors that promote mineral growth, and thus, different biases for seasonality of growth. For example, biogenic taxa precipitate most of the shell material during a well-defined "growing" season, typically initiating shell calcification during the spring, as long as food availability and water temperature exceed a species-specific threshold value (Wilbur and Watabe, 1963; Platt and Wright, 2009; Gierlowski-Kordesch, 2010; Versteegh *et al.*, 2010; Hren and Sheldon, 2012). Prior research has shown that in the Northern Hemisphere, the April-October interval has been shown to encompass a majority of shell growth for freshwater mollusks (Versteegh *et al.*, 2010; Apolinarska *et al.*, 2015). However, most individual species have a restricted range of water temperatures that they can tolerate and that allows shell formation, thus, it is likely that calcification occurs within a narrower interval sometime between spring and early summer, when water temperatures fall within the species-specific temperature range (Versteegh *et al.*, 2010; Hren and Sheldon, 2012).

Abiotic authigenic carbonate precipitation is typically biased towards the warmest period of the year, when carbonate precipitation is enhanced due to evaporation increasing carbonate saturation and photosynthetic uptake lowering pCO_2, thereby increasing water pH (Oviatt *et al.*, 1994; Platt and Wright, 2009; Hren and Sheldon, 2012). In the subtropical and polar Northern Hemisphere this corresponds to June – August, while tropical lakes have less variability in lake temperature resulting from decreased seasonality. Although tropical lakes experience decreased seasonality, seasonal changes in rainfall and evaporation within tropical lakes can also play a role in influencing carbonate saturation state.

Biologically mediated carbonates, including tufas and microbialites, precipitate as a result of local changes in water conditions and biological productivity (Capezzuoli *et al.*, 2014). These carbonates are formed by both abiogenic and biogenic processes, with algae and other aquatic plants influencing their precipitation on organic and inorganic substrates (Flügel, 2004; Capezzuoli *et al.*, 2014). Microbial activity within carbonates can increase rates of photosynthesis, thereby lowering pCO_2 and increasing carbonate saturation state making carbonate mineral precipitation more favorable (Platt and Wright, 2009; Solari *et al.*, 2010a; Pacton *et al.*, 2015). Additionally, microbial biomass provides a negatively charged surface to which ions may adhere, which locally increases calcium concentration and promotes the supersaturation of carbonates (Fein, 2017). These conditions are enhanced during the warmest interval of the year, when evaporation also plays a role in increasing carbonate saturation, eventually inducing precipitation of shoreline carbonates. Recent field studies of modern tufas and microbialites have shown elevated growth rates during warmer water temperature conditions (Pedley, 1990; Brady *et al.*, 2014; Marić *et al.*, 2020).

Text S2: Evaluation of potential disequilibrium in freshwater carbonates

No statistically significant relationships are observed between $\delta^{18}O_{carb}$ and Δ_{47} for biogenic, fine-grained, and biologically mediated carbonates. Travertines do exhibit a statistically significant positive relationship between $\delta^{18}O_{carb}$ and Δ_{47} (slope = 0.0052; p = 0.0049; Figure 1.A.2).

To gauge the extent of potential disequilibrium in our dataset, we calculated both Δ_{47} offsets ($\Delta\Delta_{47}$: Measured Δ_{47} - Calculated Δ_{47}) and $\delta^{18}O_{carb}$ offsets ($\Delta\delta^{18}O_{carb}$: Measured $\delta^{18}O_{carb}$ - Calculated $\delta^{18}O_{carb}$) relative to our data from calculated equilibrium values. We calculated the theoretical equilibrium Δ_{47} by using the equilibrium Δ_{47}-T equation from Lucarelli et al. (2023) in concert with independently derived water temperature estimates in this study. To constrain theoretical $\delta^{18}O_{carb}$ values, we used the equations of Tremaine et al. (2011) for travertine and biologically mediated carbonates (as suggested by Kele et al. (2015)), White et al. (1999) for biogenic carbonates, and Kim et al (2007) (aragonite) and Kim and O'Neil (1997) (calcite) for the remaining carbonates, depending on their mineralogy. Temperature inputs were provided from the independently measured water temperatures (Table 1.1) and water $\delta^{18}O$ (Table 1.A.5). Due to the limitation of having measured water $\delta^{18}O$ values, we were not able to calculate the theoretical carbonate composition for the complete dataset. Figure 1.A.3 shows no significant relationship between $\Delta\Delta_{47}$ and $\Delta\delta^{18}O_{carb}$ for any of our carbonate types. A positive offset is observed in $\Delta\Delta_{47}$ values of fine-grained carbonates, with an average value of 0.018‰, while average $\Delta\Delta_{47}$ values for other carbonate groups are centered around 0.

In order to probe disequilibrium data Δ_{47} within our dataset and how data at disequilibrium could influence our dataset, we applied a threshold of 0.030‰ relative to the equilibrium values estimated from Lucarelli et al. (2023) using our independently measured water temperatures. When using this threshold, the dataset excludes 10 points that are not

reflecting theoretical equilibrium conditions (7 fine-grained carbonates, 2 biologically mediated carbonates, and 1 travertines).

Partitioning our dataset into material specific subgroups based on this criteria reduce the sample size, ranging from 22-31 samples for each analysis. Regression parameters remain consistent for biogenic and biologically mediated carbonates. Given the Δ_{47} values in fine-grained carbonates in our study can be influenced by a number of factors, for example, mixing of sources of authigenic, detrital, and/or biogenic origin (see Section 4.1.3), it is unsurprising that this group had the maximum number of points excluded. Due to the number of excluded points, the regression parameters for fine-grained carbonates demonstrate the largest change when excluding disequilibrium values (Table 1.A.8). As expected, r^2 values show improvement relative to the original study with all data (Figure 1.A.6), but not to the same extent as the smaller threshold, with values ranging from 0.6206 to 0.9460.

Regression slopes are reduced in almost every case (with the exception of biologically mediated carbonates, which is identical despite the exclusion of 5 samples) and range from 0.0353 to 0.408. Similar to our full analysis, an ANCOVA detects no statistical difference between material-specific slopes in our study and suggests differences in intercepts between material-specific groups (Table 1.A.8). Statistically significant differences are detected between biogenic carbonates and fine-grained carbonates, biogenic carbonates and biologically mediated carbonates, and fine-grained carbonates and travertines. Overall, the only difference between the conclusions from our dataset and removing potential disequilibrium data is that a statistically significant difference in intercepts is no longer found between fine-grained carbonates and biologically mediated carbonates, due to the increase in estimated intercept for fine-grained carbonates.

Text S3: Hydroclimate modeling methodology for Lake Surprise, CA

More detailed methodology regarding modeling hydroclimate parameters can be found in Santi et al. (2020). In brief, the equation derived in Linacre (1993) was used to estimate lake evaporation rates. This equation (Eq. 1) utilizes elevation (Z), latitude (Lat), mean annual air temperature (T), and dew point temperature (T_d) as inputs to derive estimates of past lake evaporation at Lake Surprise. Mean annual air temperature was estimated using the water-to-air temperature transfer functions outlined in Hren and Sheldon (2012) in concert with water temperatures derived from clumped isotope analysis.

$$E_L = [0.015 + 4 \times 10^{-4} T + 10^{-6} z] \times [\frac{480(T + 0.006z)}{(84 - L)} - 40 + 2.3u(T - Td)] \quad (1)$$

Following evaporation, past precipitation rates were estimated using an isotope mass balance equation from Santi et al. (2020), based on lake water $\delta^{18}O$ ($\delta^{18}O_L$) using temperatures derived from clumped isotope analysis (Eq. 2). This built on an isotope mass balance equation developed in Ibarra et al. (2014) that factors in water balance and basin hypsometry. The precipitation equation utilizes lake evaporation (E_L), a runoff coefficient (k_{run}), lake (A_L) and tributary (A_W) area, along with the oxygen isotopic composition of evaporation, rainfall, and lake water ($\delta^{18}O_E$, $\delta^{18}O_W$, $\delta^{18}O_L$, respectively).

$$P = \frac{E_L}{\left(1+\frac{K_{run}}{HI}\right)} \times \frac{(\delta^{18}O_E - \delta^{18}O_L)}{(\delta^{18}O_W - \delta^{18}O_L)} \quad (2)$$

Santi et al. (2020) used a seasonal lake-to-mean annual air temperature (MAAT) transfer function from Hren and Sheldon (2012) to use lake water temperature estimates derived from clumped isotopes to estimate past MAAT. The temperature of water in the empirical equation is directly proportional to MAAT, thus, similar increases or decreases observed in water

temperatures will be reflected in the estimated MAAT. Lake evaporation rates were estimated in Santi et al. (2020) using a modified Linacre equation. In this equation, evaporation rates are directly related to air temperature (see Equation 1), thus, if a calibration resulted in lower (higher) air temperatures the resulting evaporation rate would be lower (higher). Precipitation rates were estimated using an isotope mass balance equation, which considers the derived evaporation rate and the oxygen isotopic composition of lake water (see Equation 2). Since evaporation and precipitation are directly proportional in the derived isotope mass balancing equation, evaporation increases (decreases) with increasing (decreasing) temperature would also mean an increase (decrease) in derived precipitation rates. We note that this is a first-order approximation of changes in hydroclimate based on changes in clumped-isotope derived parameters based on different calibration methods.

Supplementary Figures

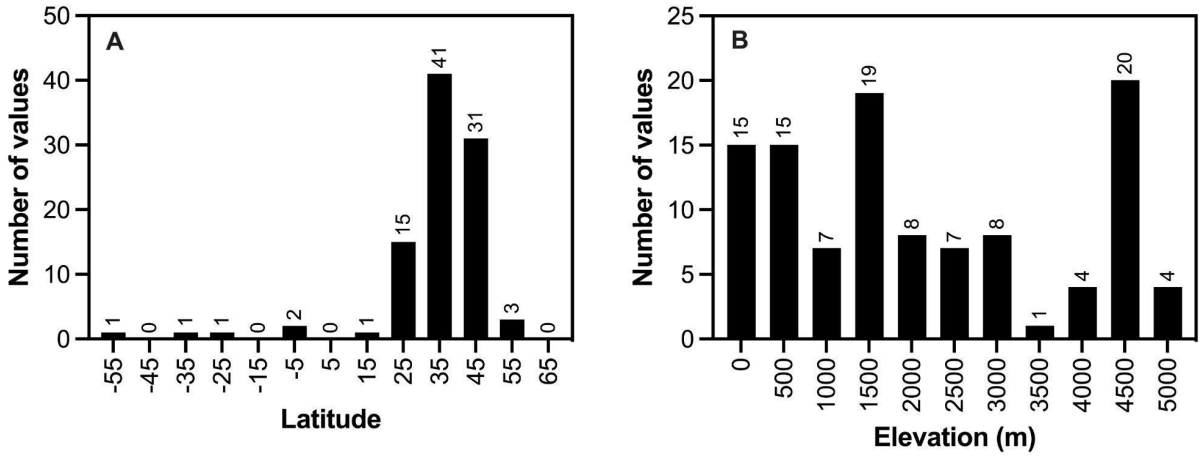

Figure 1.A.1: Histograms of latitude (A) and elevation (B) for sample sites in this study. Numbers on top of the bar represent the number of values in that bin.

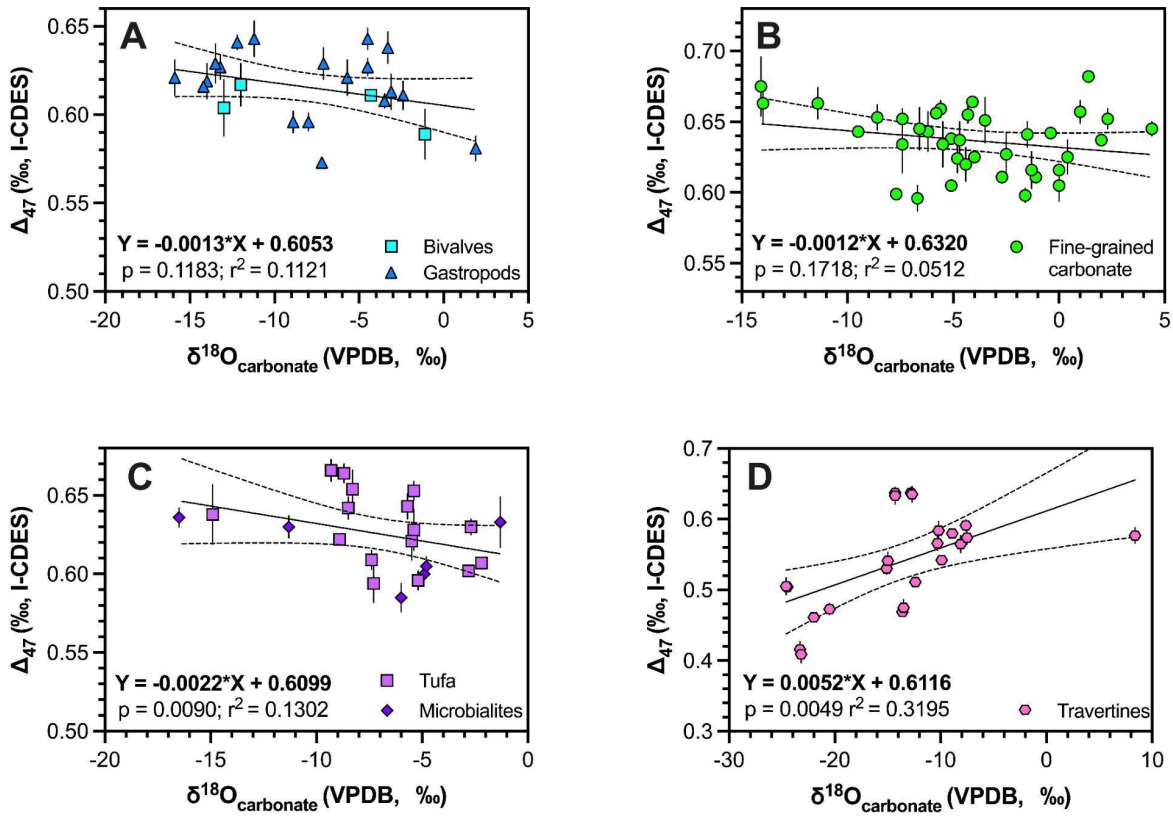

Figure 1.A.2: Relationship between $\delta^{18}O_{carb}$ and Δ_{47} for A) biogenic, B) fine-grained, C) biologically mediated, and D) travertine carbonate types in this study.

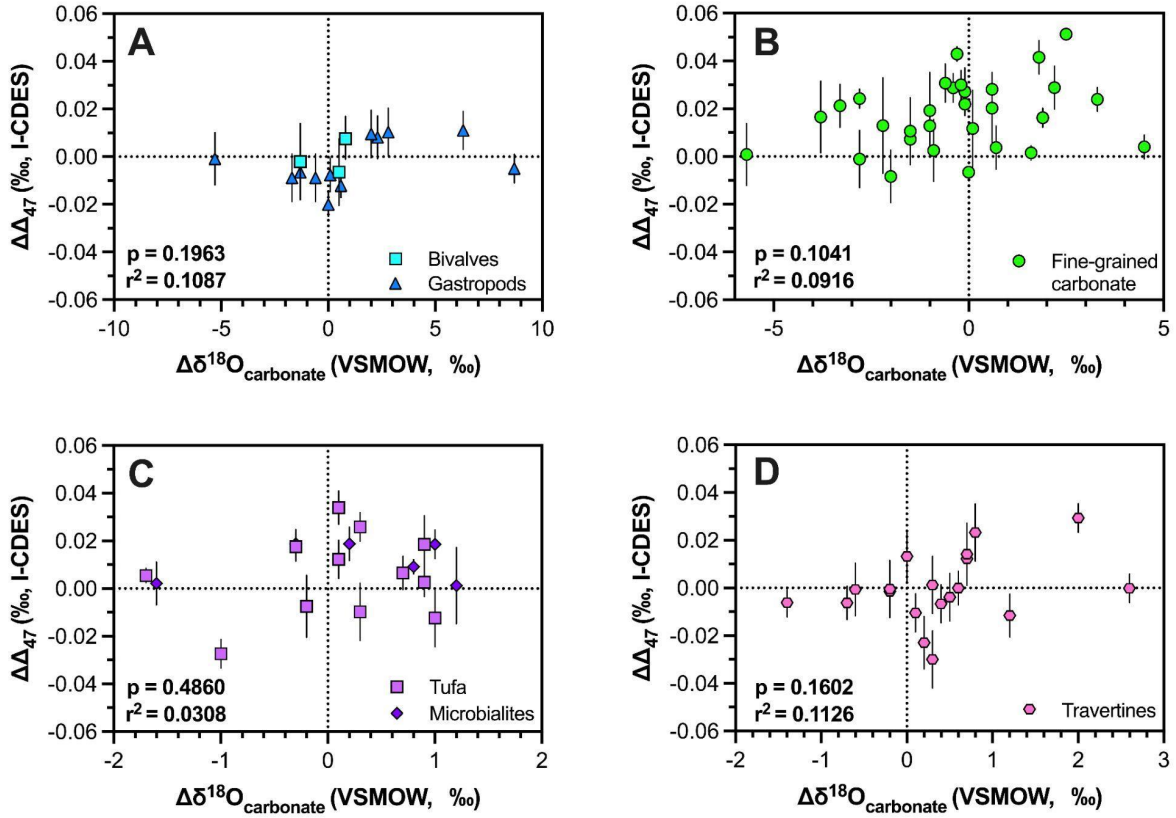

Figure 1.A.3: Δ_{47} and $\delta^{18}O_{carb}$ residual (measured - calculated) for A) biogenic, B) fine-grained, C) biologically mediated, and D) travertine carbonate in this study. Δ_{47} equilibrium values are calculated using independently measured water temperatures and the equation from Lucarelli et al. (2023). $\delta^{18}O_{carb}$ equilibrium values are calculated using the equation from White et al. (1999) for biogenic carbonates, the equations of Kim et al. (2007) (aragonite) and Kim and O'Neil (1997) (calcite) for fine-grained carbonates, and the equation of Tremaine et al. (2011) for biologically mediated carbonates and travertines.

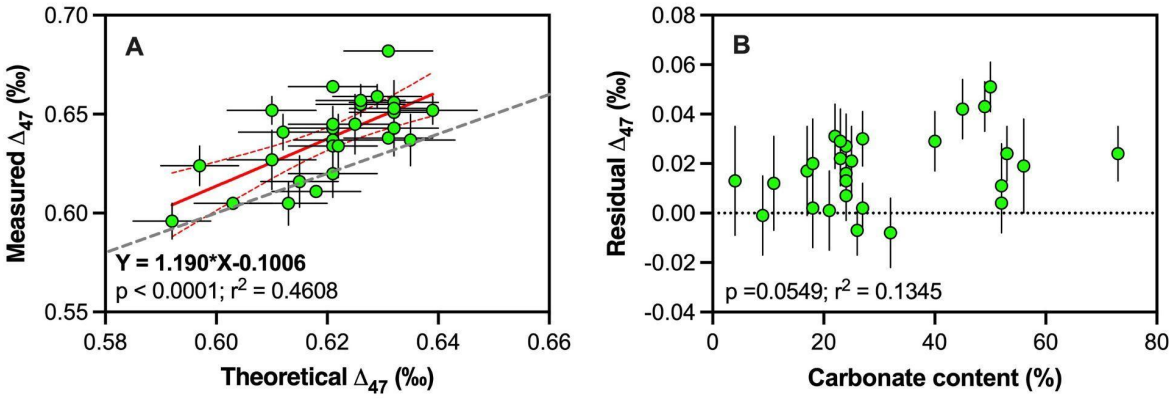

Figure 1.A.4: A) Comparison between measured Δ_{47} (from this study) and theoretical Δ_{47} based on independently measured water temperatures used in this study (calculated using the equation in Lucarelli et al. (2023)) for fine-grained carbonates. Gray dashed line represents the 1:1 line. Correlation is observed between measured and predicted values (r^2 = 0.4608), with RMSE of 0.023‰. **B) Residual Δ_{47} (measured - theoretical) and carbonate content for fine-grained carbonates.** No significant relationship and low correlation are found between carbonate content and Δ_{47} residuals (r^2 = 0.1345, p = 0.0549).

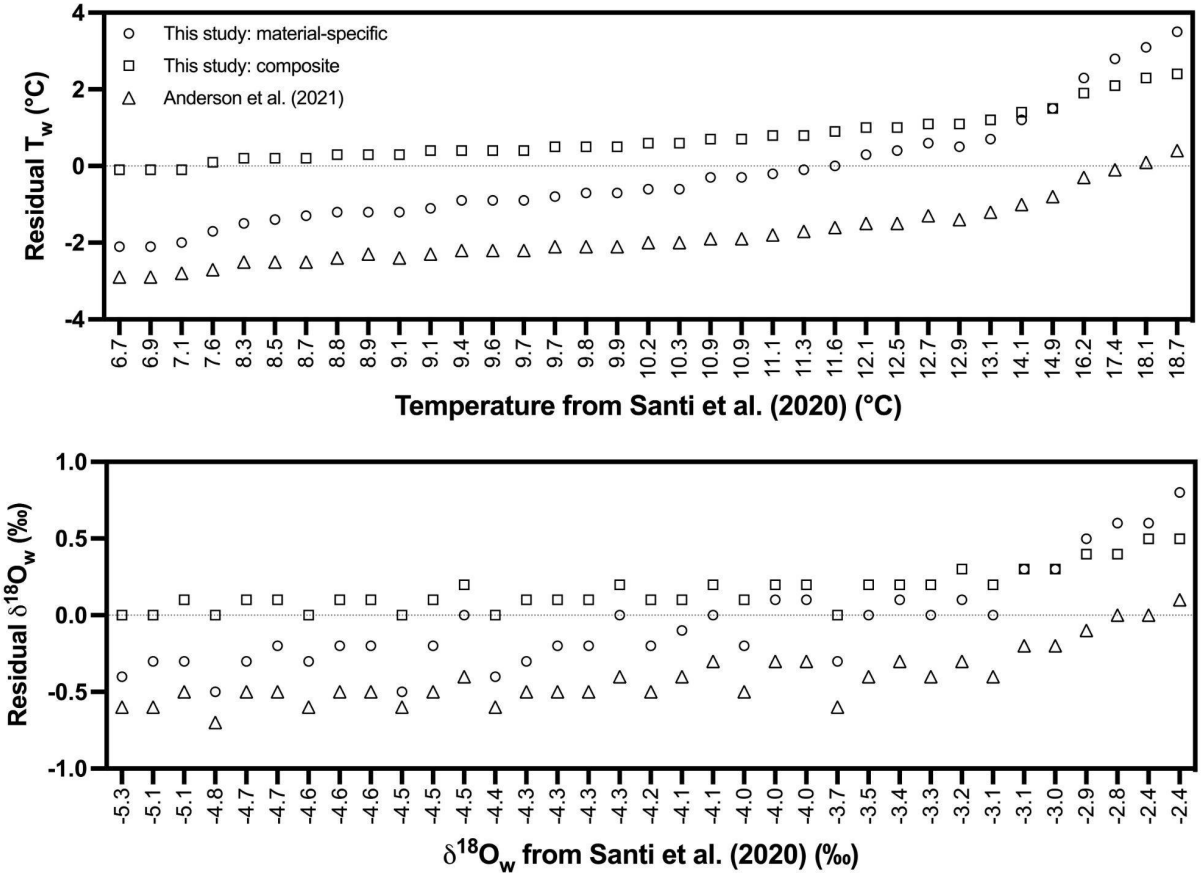

Figure 1.A.5: Residuals of reconstructed temperature and $\delta^{18}O_{water}$ for data from Lake Surprise, California. Residuals (published - new reconstructed values) are calculated relative to the clumped isotope-derived estimates presented in Santi et al. (2020).

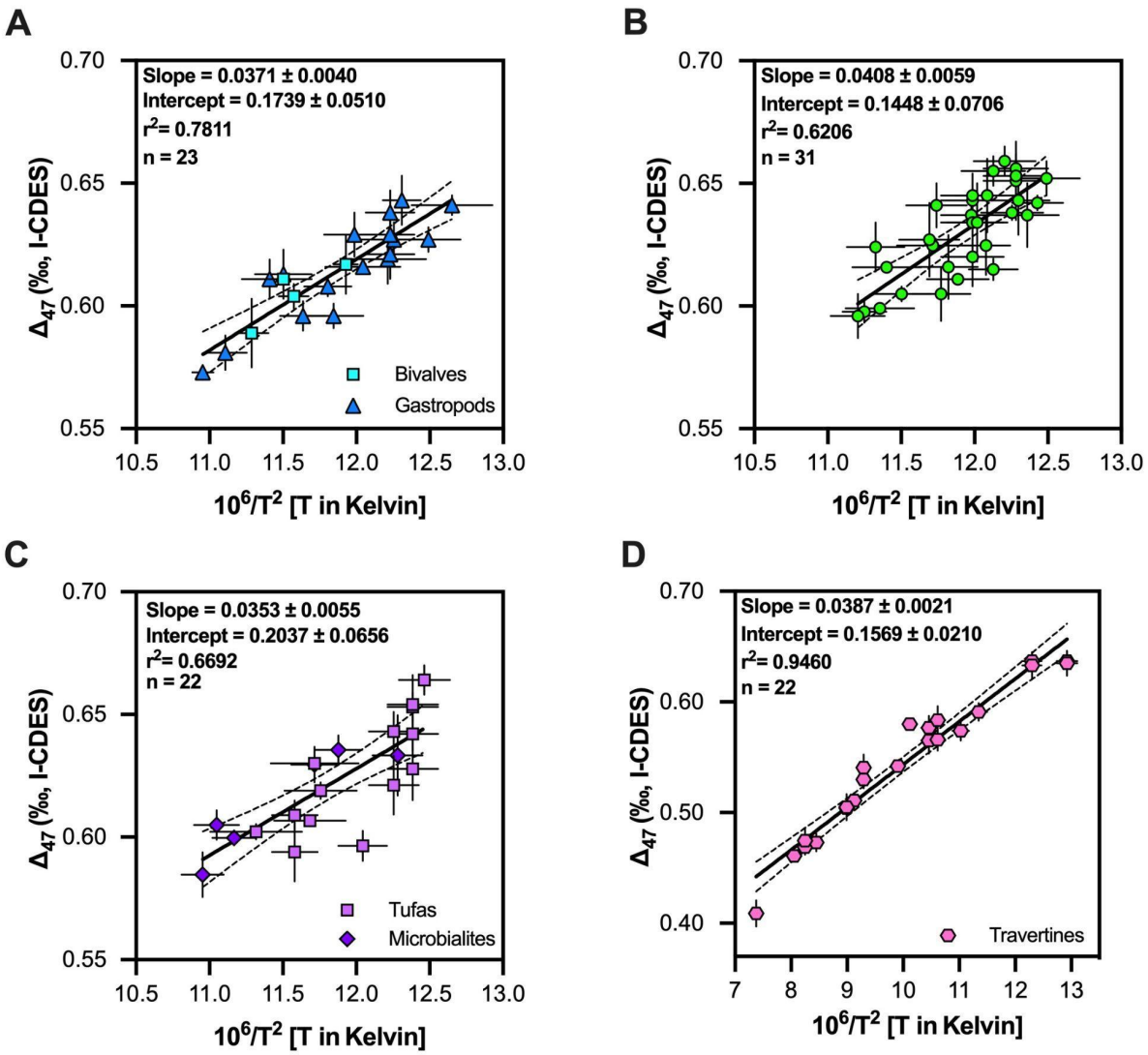

Figure 1.A.6: Δ_{47}-temperature relationships derived for A) biogenic, B) fine-grained, C) biologically mediated, and D) travertine carbonate when applying a disequilibrium threshold of $\Delta\Delta_{47} < 0.030$‰ based on estimated equilibrium estimates from Lucarelli et al. (2023).

Supplementary Tables

Sample Name	No. of Samples	No. of Analyses	Elevation (m)	System	Water Temperature Data Source	Timescale of measurement
Bivalves						
Red Rock	1	7	1207	River	U.S.G.S, 2018 - Stn. 09504440	~Monthly measurement (1978-1983; 1986-1992)
Colorado River	4	12	38	River	U.S.G.S, 2018 - Stn. 09522000	~Monthly measurement (1972-2014)
Vail Lake	2	6	432	Lake	Preszler, 2018	~Monthly measurement (2015)
Wulungu Lake	1	2	482	Lake	Li et al., 2020	Point measurement + regression analysis
Gastropods						
Santa Clara River	1	4	2123	Spring	U.S.G.S, 2018 - Stn. 09409100	~Monthly measurement (1989-2015)
Painter Spring	1	4	1633	Spring	Stephens, 1977	Point measurement
Lake Warner	1	3	1367	Lake	Phillips and Van Denburgh, 1971	Point measurements (1961 - 1963)
Clear Lake	2	8	1401	Lake	Hovingh, personal communication	Point measurement
Lake Tanganyika	6	16	774	Lake	Crul, 1997	~Weekly measurement (1955-1957)
Lake Towuti	3	15	293	Lake	Tierney and Russell, 2009	Point measurement
Nimgun Lake	3	5	320	Lake	MacDonald, 1996	Point measurements (1984-1989)
Fuxian Lake	1	6	1722	Lake	De Cui et al., 2008	~Bimonthly (2002-2003)
Lake Manasarovar	1	14	4600	Lake	Huntington et al., 2015	Daily measurement (2010-2011)
Yamdrok Yumco	1	3	4430	Lake	Yu et al., 2011	Monthly measurement (1978-1995)
Yamdrok Yumco	1	11	4435	Lake	Yu et al., 2011	Monthly measurement (1978-1995)
Tso Nag	1	1	4810	Lake	Huntington et al., 2015	Daily measurement (2010-2011)
Tsangpo	1	1	4580	Creek	Huntington et al., 2015	Daily measurement (2010-2011)
Zhongba	1	1	4570	Interdune pool	Huntington et al., 2015	Daily measurement (2010-2011)
Bosten Lake	1	5	1044	Lake	Li et al., 2020	Point measurement + regression analysis
Cuona Lake	1	4	4592	Lake	Li et al., 2020	Point measurement + regression analysis
Dajia Co	1	3	5156	Lake	Li et al., 2020	Point measurement + regression analysis

Jinzihai Lake	1	4	2985	Lake	Li et al., 2020	Daily measurement (2016-2017)
Wulungu Lake	1	2	482	Lake	Li et al., 2020	Point measurement + regression analysis
Fine-grained carbonate						
Laguna Pozuelos	1	1	3600	Lake	Ferrero et al., 2004	Point measurement
Mar Chiquita	1	3	68	Lake	Reati et al., 1997	Point measurement
El Potosi	2	7	1880	Lake	Roy et al., 2016	Point measurement
Kusai	2	6	4475	Lake	Zhang et al. 2020	Point measurement
Laguna La Salada	2	4	2035	Lake	Roy et al., 2014	Point measurement
Laguna Las Cruces	1	4	2106	Lake	Roy et al., 2013	Point measurement
Zaca Lake	1	5	730	Lake	Dickman, 1987	Point measurements (1984)
Pipahai Lake	1	2	1770	Lake	Li et al., 2020	Point measurement + regression analysis
Chagan Lake	1	2	1021	Lake	Li et al., 2020	Point measurement + regression analysis
Gahai Lake	1	1	3192	Lake	Li et al., 2020	Daily measurement (2016-2017)
Qinghai Lake	1	2	3196	Lake	Li et al., 2020	Point measurement + regression analysis
Kuhai Lake	1	2	4133	Lake	Li et al., 2020	Daily measurement (2016-2017)
Eling Lake	1	2	4272	Lake	Li et al., 2020	Point measurement + regression analysis
Zhaling Lake	1	2	4298	Lake	Li et al., 2020	Point measurement + regression analysis
Xingxinghai Lake	1	2	4224	Lake	Li et al., 2020	Point measurement + regression analysis
Koucha Lake	1	4	4537	Lake	Li et al., 2020	Daily measurement (2016-2017)
Donggi Cona Lake	1	1	4092	Lake	Li et al., 2020	Daily measurement (2016-2017)
Gahai Lake2	1	1	2859	Lake	Li et al., 2020	Daily measurement (2016-2017)
Tuosu Lake	1	3	2804	Lake	Li et al., 2020	Daily measurement (2016-2017)
Hala Lake	1	3	4081	Lake	Li et al., 2020	Point measurement + regression analysis
Cuona Lake	1	3	4592	Lake	Li et al., 2020	Point measurement + regression analysis
Pung Co	1	4	4540	Lake	Li et al., 2020	Point measurement + regression analysis
Jiang Co	1	2	4616	Lake	Li et al., 2020	Daily measurement (2016-2017)
Bam Co	1	3	4575	Lake	Li et al., 2020	Daily measurement (2016-2017)
Shen Co	1	6	4744	Lake	Li et al., 2020	Point measurement + regression analysis

Selin Co	1	4	4553	Lake	Li et al., 2020	Point measurement + regression analysis
Dagze Co	1	4	4480	Lake	Li et al., 2020	Point measurement + regression analysis
Zharinanmu Co	1	3	4629	Lake	Li et al., 2020	Point measurement + regression analysis
Dajia Co	1	3	5156	Lake	Li et al., 2020	Point measurement + regression analysis
Angrenjin Co	1	2	4295	Lake	Li et al., 2020	Point measurement + regression analysis
Lang Co	1	3	4303	Lake	Li et al., 2020	Daily measurement (2016-2017)
Sailimu Lake	1	4	2078	Lake	Li et al., 2020	Point measurement + regression analysis
Ailike Lake	1	3	270	Lake	Li et al., 2020	Daily measurement (2016-2017)
Wulungu Lake	1	3	482	Lake	Li et al., 2020	Point measurement + regression analysis
Sugan Lake	1	5	3000	Lake	Li et al., 2020	Point measurement + regression analysis
Blue Eagle Lake	1	4	2552	Lake	Huntington et al., 2010	Point measurement + regression analysis
Emerald Lake	1	4	3093	Lake	Huntington et al., 2010	Point measurement + regression analysis
South Grizzly Lake	1	3	3242	Lake	Huntington et al., 2010	Point measurement + regression analysis
Microbialites						
Laguna Bacalar	1	3	2	Lake	Tobón Velázquez, 2017	Point measurements (2006)
Lago Sarmiento	1	3	77	Lake	Airo, 2010	Daily measurement (2003-2004)
South Arm, Great Salt Lake	1	3	1280	Lake	Gwynn, J.W., 2007	Daily measurement (1966-2006)
North Arm, Great Salt Lake	1	2	1280	Lake	Gwynn, J.W., 2007	Daily measurement (1966-2006)
Kelly Lake	1	3	1070	Lake	Petryshyn et al., 2015	Point measurement (2004 - 2010)
Pavillion Lake	1	3	823	Lake	Petryshyn et al., 2015	Point measurement (2004 - 2010)
Ooids						
South Arm, Great Salt Lake	7	19	1280	Lake	Gwynn, J.W., 2007	Daily measurement (1966-2006)
North Arm, Great Salt Lake	4	14	1280	Lake	Gwynn, J.W., 2007	Daily measurement (1966-2006)
Tufas						
Lake Surprise	1	1	1363.5	Lake	Costa et al., 2008	Point measurement
Walker Lake	1	11	1190	Lake	Petryshyn et al., 2015	Monthly measurement (1992-1993; 1995-1996)
Cannatoppa*	1	29	254	Stream	Kele et al., 2015	Point measurement

Cannatoppa^	1	8	254	Stream	Kele et al., 2015	Point measurement
La Pigna*	1	31	1359	Stream	Kele et al., 2015	Point measurement
La Pigna^	1	9	1359	Stream	Kele et al., 2015	Point measurement
Sarteano*	1	29	1400	Stream	Kele et al., 2015	Point measurement
Sarteano^	1	9	1400	Stream	Kele et al., 2015	Point measurement
Szalajka	1	30	1414	Stream	Kele et al., 2015	Point measurement
Szalajka*	1	29	1414	Stream	Kele et al., 2015	Point measurement
Szalajka^	1	9	1414	Stream	Kele et al., 2015	Point measurement
Szalajka	1	29	1414	Stream	Kele et al., 2015	Point measurement
Kailas	2	6	4780	Lake	Huntington et al., 2015	Daily measurement (2010-2011)
Lake Crowley	1	3	2058	Lake	Huntington et al., 2010	Point measurement + regression analysis
Lake Mead	1	3	372	Lake	Huntington et al., 2010	Point measurement + regression analysis
Mono Lake	1	2	1899	Lake	Huntington et al., 2010	Point measurement + regression analysis
Travertines						
Aqua Borra*	1	30	192	Natural spring	Kele et al., 2015	Point measurement
Aqua Borra^	1	11	192	Natural spring	Kele et al., 2015	Point measurement
Bagnoli	1	32	178	Natural spring	Kele et al., 2015	Point measurement
BSF Fosso Bianco	1	30	526	Natural spring	Kele et al., 2015	Point measurement
Bük*	1	28	169	Thermal well	Kele et al., 2015	Point measurement
Bük^	1	9	169	Thermal well	Kele et al., 2015	Point measurement
Madre del Agua*	1	29	1629	Natural spring	Kele et al., 2015	Point measurement
Madre del Agua^	1	8	1629	Natural spring	Kele et al., 2015	Point measurement
Igal*	1	30	172	Thermal well	Kele et al., 2015	Point measurement
Igal^	1	10	172	Thermal well	Kele et al., 2015	Point measurement
Köröm	1	36	99	Thermal well	Kele et al., 2015	Point measurement
Baishuitai - summer*	1	38	2688	Natural spring	Kele et al., 2015	Point measurement
Baishuitai - summer^	1	9	2688	Natural spring	Kele et al., 2015	Point measurement
Baishuitai - winter*	1	43	2688	Natural spring	Kele et al., 2015	Point measurement

Baishuitai - winter^	1	10	2688	Natural spring	Kele et al., 2015	Point measurement
Piscine Carletti	1	29	275	Natural spring	Kele et al., 2015	Point measurement
Rapolano Terme	1	28	257	Thermal well	Kele et al., 2015	Point measurement
Szèchenyi Spa	1	28	107	Thermal well	Kele et al., 2015	Point measurement
Terme Sangiovanni	1	28	258	Natural spring	Kele et al., 2015	Point measurement
Tura*	1	30	135	Thermal well	Kele et al., 2015	Point measurement
Tura^	1	9	135	Thermal well	Kele et al., 2015	Point measurement
Narrow Gauge, Yellowstone*	1	29	2632	Natural spring	Kele et al., 2015	Point measurement
Narrow Gauge, Yellowstone^	1	9	2632	Natural spring	Kele et al., 2015	Point measurement

Table 1.A.1. Sample site, analyses, and temperature data source for freshwater carbonates included in this study.
*Denotes sample run at ETH.
^Denotes sample run at MIT.

UCLA Standards

Standard	Type	N	$\delta^{13}C$ (‰,VPDB)	$\delta^{18}O$ (‰,VPDB)	Δ_{47} (‰, I-CDES)
Bonedry Tank CO_2	25°C gas breakseal	-	-	-	25°C equilibration
Bonedry Tank CO_2	1000°C gas breakseal	-	-	-	Stochastic
Carmel Chalk	Carbonate	178	-2.2 ± 0.1	-4.0 ± 0.1	0.594 ± 0.001
Carrara Marble	Carbonate	63	2.1 ± 0.0	-1.5 ± 0.1	0.313 ± 0.003
Carrara Marble - CIT	Carbonate	97	2.3 ± 0.0	-1.8 ± 0.1	0.312 ± 0.002
CM Tile	Carbonate	45	2.0 ± 0.0	-1.5 ± 0.1	0.313 ± 0.002
ETH-1	Carbonate	63	2.0 ± 0.1	-2.2 ± 0.1	0.210 ± 0.003
ETH-2	Carbonate	47	-10.2 ± 0.0	-18.7 ± 0.1	0.206 ± 0.003
ETH-3	Carbonate	38	1.7 ± 0.1	-1.8 ± 0.1	0.618 ± 0.004
ETH-4	Carbonate	47	-10.2 ± 0.1	-18.8 ± 0.1	0.448 ± 0.002
Evap DI + Carrera Marble CO_2	25°C gas breakseal	-	-	-	25°C equilibration
Evap DI + Carrera Marble CO_2	1000°C gas breakseal	-	-	-	Stochastic
IAEA-C1	Carbonate	11	2.4 ± 0.1	-2.3 ± 0.1	0.302 ± 0.004
IAEA-C2	Carbonate	10	-8.1 ± 0.1	-8.8 ± 0.1	0.631 ± 0.005
MERCK	Carbonate	7	-41.9 ± 0.1	-15.6 ± 0.1	0.526 ± 0.011
Spel 2-8-E	Carbonate	14	-9.4 ± 0.4	-6.1 ± 0.1	0.617 ± 0.009
TV01	Carbonate	4	2.5 ± 0.1	-8.3 ± 0.1	0.628 ± 0.007
TV03	Carbonate	21	2.6 ± 0.1	-8.4 ± 0.1	0.620 ± 0.005
TV03 - CIT	Carbonate	26	3.3 ± 0.1	-8.2 ± 0.3	0.624 ± 0.003
Veinstrom	Carbonate	104	-6.2 ± 0.1	-12.6 ± 0.1	0.632 ± 0.002
102-GC-AZ01	Carbonate	9	0.4 ± 0.1	-13.9 ± 0.3	0.630 ± 0.019

Caltech Standards

Standard	Type	N	$\delta^{13}C$ (‰,VPDB)	$\delta^{18}O$ (‰,VPDB)	Δ_{47} (‰, I-CDES$_{90}$)
BOC	25°C gas breakseal	-	-	-	25°C equilibration
BOC	1000°C gas breakseal	-	-	-	Stochastic
Cararra Marble	Carbonate	78	2.3 ± 0.1	-1.9 ± 0.1	0.301 ± 0.002
Enriched BOC	25°C gas breakseal		-	-	25°C equilibration
Enriched BOC	1000°C gas breakseal		-	-	Stochastic
NBS-19	Carbonate	10	1.9 ± 0.0	-2.2 ± 0.1	0.298 ± 0.009
Spel 2-8-E	Carbonate	15	-8.1 ± 1.3	-6.3 ± 0.1	0.555 ± 0.054
TV01	Carbonate	59	2.4 ± 0.1	-8.5 ± 0.1	0.627 ± 0.003
102-GC-AZ01	Carbonate	13	0.5 ± 0.0	-14.4 ± 0.1	0.559 ± 0.058

Table 1.A.2. Stable and clumped isotope results for standards used for processing UCLA data and Caltech data based on best practices outlined in Upadhyay et al. (2021). $\delta^{13}C$ and $\delta^{18}O$ data are presented with one standard deviation, while Δ_{47} data is presented with one standard error.

Regression parameter: slope

	This study: biologic	This study: fine-grained	This study: bio-mediated	Petersen et al. (2019)[a]	Anderson et al. (2021)
This study: composite				0.5266	0.6260
This study: biologic		0.4560	0.5727	0.9540	0.9130
This study: fine-grained	0.4560		0.3750	0.4140	0.3910
This study: bio-mediated	0.5727	0.3750		0.7602	0.6020

Regression parameter: intercept

	This study: biologic	This study: fine-grained	This study: bio-mediated	Petersen et al. (2019)[a]	Anderson et al. (2021)
This study: composite				0.0396	0.0087
This study: biologic		<0.001	0.0087	0.1260	0.3900
This study: fine-grained	<0.001		0.6080	0.0004	<0.001
This study: bio-mediated	0.0087	0.6080		0.3320	0.0531

Table 1.A.3: Results of the ANCOVA test for calibration-pairs for slope and intercept using only UCLA-measured carbonates. Red shading indicates differences in parameters with 95% confidence ($p < 0.05$), yellow shading indicates differences in parameters with 90% confidence ($0.05 < p < 0.10$), and no shading indicates no statistically significant difference between parameters.

[a]Δ_{47} values were corrected to a 90°C reference frame using AFF presented in Petersen et al. (2019).

	Water Temperature (°C)						
Δ_{47} (‰, I-CDES)	**Composite**	**Biogenic**	**Fine-grained**	**Bio-mediated**	**Travertine**	**Anderson et al. (2021)**	**Petersen et al. (2019)[a]**
0.550	42.0	40.9	41.9	48.7	40.3	41.1	44.3
0.575	33.1	31.0	33.7	37.0	31.1	31.6	34.4
0.600	24.9	21.9	26.2	26.7	22.6	22.9	25.3
0.625	17.3	13.6	19.2	17.4	14.8	15.0	17.0
0.650	10.3	6.0	12.7	8.9	7.6	7.6	9.3
0.675	3.8	-1.1	6.5	1.1	0.9	0.8	2.2
0.700	-2.3	-7.6	0.8	-6.1	-5.4	-5.5	-4.3

Table 1.A.4: Comparison of derived temperatures using regressions derived within this study to a recently published calibration (Anderson et al., 2021) and a 'universal' calibration (Petersen et al., 2019).

[a]Data is presented in $CDES_{90}$ using AFF in Petersen et al. (2019)

Sample Name	Measured $\delta^{18}O_w$ (‰, VSMOW)	$\delta^{18}O_w$ Data Source	Timescale of measurement
Bivalves			
Red Rock	-11.6	U.S.G.S, 2018 - Stn. 9504420	Multiple measurements (2009-2014)
Colorado River	-11.8	U.S.G.S, 2018 - Stn. 09522000	Multiple measurements (1997-2000; 2009-2010)
Vail Lake	-0.6	U.S.G.S, 2018 - Stn. 11042510	Point measurements (August 2011; September 2012)
Wulungu Lake	-4.7	Li et al., 2020	Point measurement (June - August)
Gastropods			
Lake Tanganyika	3.4	Dettman et al., 2005	Multiple measurements (1985-1999)
Fuxian Lake	-2.5	Roy et al., 2019	Multiple measurements (2013-2016)
Lake Manasarovar	-6.9	Roy et al., 2020	Point measurement (August 2007)
Yamdrok Yumco	-15.8	Yang et al., 2020	Point measurement (August 2013)
Tso Nag	-5.4	Huntington et al., 2015	Point measurement (mid-June)
Tsangpo	-17.0	Huntington et al., 2015	Point measurement (mid-June)
Zhongba	-9.9	Huntington et al., 2015	Point measurement (mid-June)
Bosten Lake	-8.0	Li et al., 2020	Point measurement (June - August)
Cuona Lake	-8.8	Li et al., 2020	Point measurement (June - August)
Dajia Co	-7.1	Li et al., 2020	Point measurement (June - August)
Jinzihai Lake	-8.6	Li et al., 2020	Point measurement (June - August)
Wulungu Lake	-4.7	Li et al., 2020	Point measurement (June - August)
Micrite			
Mar Chiquita	1.1	Piovano et al., 2001	Point measurement (Summer, 2 measurements)
Zaca Lake	-3.3	Feakins et al., 2014	Multiple measurements (2009-2012)
Pipahai Lake	2.9	Li et al., 2020	Point measurement (June - August)
Chagan Lake	-2.2	Li et al., 2020	Point measurement (June - August)
Gahai Lake	1.1	Li et al., 2020	Point measurement (June - August)

Qinghai Lake	1.4	Li et al., 2020	Point measurement (June - August)
Kuhai Lake	-0.9	Li et al., 2020	Point measurement (June - August)
Eling Lake	-3.5	Li et al., 2020	Point measurement (June - August)
Zhaling Lake	-1.6	Li et al., 2020	Point measurement (June - August)
Xingxinghai Lake	-0.8	Li et al., 2020	Point measurement (June - August)
Koucha Lake	-3.6	Li et al., 2020	Point measurement (June - August)
Donggi Cona Lake	-4.0	Li et al., 2020	Point measurement (June - August)
Gahai Lake2	3.5	Li et al., 2020	Point measurement (June - August)
Tuosu Lake	5.7	Li et al., 2020	Point measurement (June - August)
Hala Lake	1.5	Li et al., 2020	Point measurement (June - August)
Cuona Lake	-8.8	Li et al., 2020	Point measurement (June - August)
Pung Co	-3.7	Li et al., 2020	Point measurement (June - August)
Jiang Co	-6.0	Li et al., 2020	Point measurement (June - August)
Bam Co	-5.6	Li et al., 2020	Point measurement (June - August)
Shen Co	-3.8	Li et al., 2020	Point measurement (June - August)
Selin Co	-3.2	Li et al., 2020	Point measurement (June - August)
Dagze Co	-5.5	Li et al., 2020	Point measurement (June - August)
Zharinanmu Co	-7.5	Li et al., 2020	Point measurement (June - August)
Dajia Co	-7.1	Li et al., 2020	Point measurement (June - August)
Angrenjin Co	-4.5	Li et al., 2020	Point measurement (June - August)
Lang Co	-5.7	Li et al., 2020	Point measurement (June - August)
Sailimu Lake	-2.2	Li et al., 2020	Point measurement (June - August)
Ailike Lake	-4.6	Li et al., 2020	Point measurement (June - August)
Wulungu Lake	-4.7	Li et al., 2020	Point measurement (June - August)
Sugan Lake	2.1	Li et al., 2020	Point measurement (June - August)
Microbialites			
Laguna Bacalar	-2.4	Pérez et al., 2011	Point measurement (November - March)
Lago Sarmiento	-3.5	Solari et al., 2010	Biannual measurement (January/September)

South Arm, Great Salt Lake	-4.1	Pedone et al., 2002	Annual measurement (3 years; winter and summer)
North Arm, Great Salt Lake	-4.0	Pedone et al., 2002	Annual measurement (3 years; winter and summer)
Kelly Lake	-16.7	Petryshyn et al., 2015	Annual measurement (3 years; summer)
Pavillion Lake	-11.4	Petryshyn et al., 2015	Annual measurement (3 years; summer)
Ooids			
South Arm, Great Salt Lake	-4.0	Pedone et al., 2002	Annual measurement (3 years; winter and summer)
North Arm, Great Salt Lake	-2.0	Pedone et al., 2002	Annual measurement (3 years; winter and summer)
Tufas			
Walker Lake	0.2	Yuan et al., 2006	Point measurement (1985-1994)
Cannatoppa*	-6.5	Kele et al., 2015	Point measurement (October)
La Pigna*	-6.8	Kele et al., 2015	Point measurement (October)
Sarteano	-7.8	Kele et al., 2015	Point measurement (October)
Szalajka	-10.6	Kele et al., 2015	Point measurement (October)
Szalajka*	-10.6	Kele et al., 2015	Point measurement (October)
Szalajka	-10.7	Kele et al., 2015	Point measurement (October)
Kailas	-4.7	Huntington et al., 2015	Point measurement (mid-June)
Travertines			
Aqua Borra*	-5.2	Kele et al., 2015	Point measurement
Bagnoli	-7.0	Kele et al., 2015	Point measurement
BSF Fosso Bianco	-7.9	Kele et al., 2015	Point measurement
Bük*	-9.9	Kele et al., 2015	Point measurement
Madre del Agua*	-8.1	Kele et al., 2015	Point measurement
Igal*	-4.0	Kele et al., 2015	Point measurement
Köröm	-11.5	Kele et al., 2015	Point measurement
Piscine Carletti	-6.5	Kele et al., 2015	Point measurement
Rapolano Terme	-6.9	Kele et al., 2015	Point measurement
Szèchenyi Spa	-12.6	Kele et al., 2015	Point measurement
Terme Sangiovanni	-6.9	Kele et al., 2015	Point measurement

Tura*	-12.4	Kele et al., 2015	Point measurement
Narrow Gauge, Yellowstone*	-17.9	Kele et al., 2015	Point measurement

Table 1.A.5. Measured $\delta^{18}O$ values for selected sites and their respective sources

Sample Name	Type	Age	Error	Mineralogy	n	$\delta^{13}C$ (‰, VPDB)	1 s.d.	$\delta^{18}O$ (‰, VPDB)	1 s.d.	Δ_{47} (‰, I-CDES)	1 s.e.
AIN4-CI1	Travertine	14.23	0.08	Aragonite	4	1.0	0.1	-10.8	0.1	0.645	0.01
AIN4-Cl2	Travertine	14.21	0.08	Calcite	6	-1.5	0.1	-11.6	0.1	0.631	0.011
AIN5-Cl1	Travertine	14.33	0.06	Aragonite	4	0.2	0.5	-11.0	0.2	0.624	0.005
AIN7-CI1	Tufa	13.4	1.04	Calcite	7	-2.9	0.6	-11.2	0.3	0.645	0.006
AIN8-Cl1	Travertine	13.87	0.08	Aragonite	6	-2.1	0.5	-11.5	0.1	0.628	0.006

Table 1.A.6. Δ_{47} results for a travertine sequence in Austria. Δ_{47} is presented in I-CDES and $\delta^{18}O_w$ relative to VSMOW.

	Kelson et al. (2017)				This study - MS				This study - C				Anderson et al. (2021)			
Sample Name	**T_w (°C)**	**s.e.**	**$\delta^{18}O_w$ (‰)**	**s.e.**	**T_w (°C)**	**s.e.**	**$\delta^{18}O_w$ (‰)**	**s.e.**	**T_w (°C)**	**s.e.**	**$\delta^{18}O_w$ (‰)**	**s.e.**	**T_w (°C)**	**s.e.**	**$\delta^{18}O_w$ (‰)**	**s.e.**
'16NQ02'	28.1	1.6	-7.3	0.3	29.1	1.9	-7.2	0.3	26.6	2.1	-7.7	0.4	24.8	2.2	-8.0	0.4
'16NQ04'	26.0	0.8	-9.2	0.2	28.1	1.8	-8.8	0.4	25.5	1.9	-9.3	0.4	23.6	2.0	-9.7	0.4
'16NQ05'	20.5	0.9	-5.9	0.2	20.5	0.9	-5.8	0.3	17.4	1.0	-6.4	0.4	15.1	1.0	-6.9	0.4
'16NQ08'	24.7	2.0	-2.2	0.4	27.8	1.5	-1.2	0.2	25.1	1.6	-1.8	0.2	23.2	1.7	-2.2	0.3
'16NQ19'	56.5	1.4	-1.8	0.2	52.5	2.3	-2.5	0.4	51.9	2.5	-2.6	0.5	51.7	2.7	-2.7	0.5
'16NQ20'	76.5	3.5	0.8	0.5	69.7	3.4	-0.3	0.5	70.9	3.8	-0.2	0.5	72.2	4.1	0.0	0.6
'16NQ21'	68.5	2.1	0.9	0.3	64.7	2.0	0.3	0.2	65.2	2.2	0.3	0.2	66.0	2.4	0.5	0.3
'16NQ22'	48.1	1.5	-3.3	0.3	45.8	1.6	-3.7	0.3	44.5	1.7	-3.9	0.3	43.8	1.8	-4.1	0.3
'16NQ23'	45.4	1.7	-3.6	0.5	45.4	1.7	-3.6	0.2	44.1	1.8	-3.8	0.3	43.4	2.0	-3.9	0.3
'16NQ25'	35.0	2.5	-7.3	0.9	33.7	2.1	-7.6	0.4	31.5	2.3	-8.0	0.4	30.0	2.4	-8.3	0.4
'16NQ26'	35.2	1.8	-4.2	0.6	37.0	1.7	-3.9	0.3	35.0	1.9	-4.3	0.4	33.7	2.0	-4.6	0.4
'16NQ34'	28.8	1.2	-9.1	0.5	28.7	1.2	-9.2	0.3	26.1	1.3	-9.7	0.3	24.3	1.4	-10.0	0.4
'16NQ35'	27.9	1.9	-3.0	0.7	28.6	1.5	-2.5	0.3	26.0	1.6	-3.0	0.3	24.2	1.7	-3.4	0.4
'16NQ36'	35.1	1.8	-5.0	0.5	34.1	2.5	-5.3	0.4	31.9	2.7	-5.7	0.4	30.4	2.9	-6.0	0.5
'16NQ37'	27.0	2.1	-7.6	0.6	29.9	1.8	-7.0	0.4	27.4	1.9	-7.5	0.4	25.7	2.0	-7.8	0.4

Table 1.A.7. Comparison of derived water temperatures and water $\delta^{18}O$ published in Li et al (2019) from the Nangqian Basin using material specific (MS), composite freshwater (C), and Anderson et al. (2021) to estimates derived in the original publication used the calibration of Kelson et al. (2017). $\delta^{18}O_w$ is measured relative to VSMOW.

Regression parameter: slope

	This study: biologic	This study: fine-grained	This study: bio-mediated	This study: travertine
This study: biologic		0.6257	0.8076	0.7980
This study: fine-grained	0.6257		0.5119	0.7697
This study: bio-mediated	0.8076	0.5119		0.6047
This study: travertine	0.7980	0.7697	0.6047	

Regression parameter: intercept

	This study: biologic	This study: fine-grained	This study: bio-mediated	This study: travertine
This study: biologic		<0.0001	0.0090	0.7552
This study: fine-grained	<0.0001		0.1784	0.0178
This study: bio-mediated	0.0090	0.1784		0.1285
This study: travertine	0.7552	0.0178	0.1285	

Table 1.A.8: ANCOVA between material-specific parameter estimates when applying a threshold of $\Delta\Delta_{47}$ < 0.030‰ based on estimated equilibrium estimates from Lucarelli et al. (2023). Red shading indicates statistically significant differences in intercept, where $p < 0.05$.

Supplementary References

Airo, A. (2010) *Biotic and abiotic controls on the morphological and textural development of modern microbialites at Lago Sarmiento, Chile*. Ph.D. Thesis. Stanford University.

Anadón, P., Cabrera, L. and Kelts, K. (2009) *Lacustrine facies analysis*. John Wiley & Sons.

Anderson, N.T., Kelson, J.R., Kele, S., Daëron, M., Bonifacie, M., Horita, J., Mackey, T.J., John, C.M., Kluge, T., Petschnig, P., Jost, A.B., Huntington, K.W., Bernasconi, S.M. and Bergmann, K.D. (2021) 'A Unified Clumped Isotope Thermometer Calibration (0.5–1,100°C) Using Carbonate-Based Standardization', *Geophysical Research Letters*, 48(7), p. e2020GL092069. Available at: https://doi.org/10.1029/2020GL092069.

Apolinarska, K., Pełechaty, M. and Noskowiak, D. (2015) 'Differences in stable isotope compositions of freshwater snails from surface sediments of two Polish shallow lakes', *Limnologica*, 53, pp. 95–105. Available at: https://doi.org/10.1016/j.limno.2015.06.003.

Brady, A.L., Laval, B., Lim, D.S.S. and Slater, G.F. (2014) 'Autotrophic and heterotrophic associated biosignatures in modern freshwater microbialites over seasonal and spatial gradients', *Organic Geochemistry*, 67, pp. 8–18. Available at: https://doi.org/10.1016/j.orggeochem.2013.11.013.

Capezzuoli, E., Gandin, A. and Pedley, M. (2014) 'Decoding tufa and travertine (fresh water carbonates) in the sedimentary record: The state of the art', *Sedimentology*, 61(1), pp. 1–21. Available at: https://doi.org/10.1111/sed.12075.

Costa, K.C., Hallmark, J., Navarro, J.B., Hedlund, B.P., Moser, D.P., Labahn, S. and Soukup, D. (2008) 'Geomicrobiological Changes in Two Ephemeral Desert Playa Lakes in the

Western United States', *Geomicrobiology Journal*, 25(5), pp. 250–259. Available at: https://doi.org/10.1080/01490450802153033.

Crul, R. (1997) 'Limnology and hydrology of Lakes Tanganyika and Malawi', *Studies and Reports in Hydrology*, 54.

Cui, Y.-D., Liu, X.-Q. and Wang, H.-Z. (2008) 'Macrozoobenthic community of Fuxian Lake, the deepest lake of southwest China', *Limnologica*, 38(2), pp. 116–125. Available at: https://doi.org/10.1016/j.limno.2007.10.003.

Dettman, D.L., Palacios-Fest, M.R., Nkotagu, H.H. and Cohen, A.S. (2005) 'Paleolimnological investigations of anthropogenic environmental change in Lake Tanganyika: VII. Carbonate isotope geochemistry as a record of riverine runoff', *Journal of Paleolimnology*, 34(1), pp. 93–105. Available at: https://doi.org/10.1007/s10933-005-2400-x.

Dickman, M. (1987) 'Lake sediment microlaminae and annual mortalities of photosynthetic bacteria in an oligomictic lake', *Freshwater Biology*, 18(1), pp. 151–164. Available at: https://doi.org/10.1111/j.1365-2427.1987.tb01303.x.

Feakins, S.J., Kirby, M.E., Cheetham, M.I., Ibarra, Y. and Zimmerman, S.R.H. (2014) 'Fluctuation in leaf wax D/H ratio from a southern California lake records significant variability in isotopes in precipitation during the late Holocene', *Organic Geochemistry*, 66, pp. 48–59. Available at: https://doi.org/10.1016/j.orggeochem.2013.10.015.

Fein, J.B. (2017) ‘Advanced biotic ligand models: Using surface complexation modeling to quantify metal bioavailability to bacteria in geologic systems’, *Chemical Geology*, 464, pp. 127–136. Available at: https://doi.org/10.1016/j.chemgeo.2016.10.001.

Ferrero, M., Farías, M.E. and Siñeriz, F. (2004) ‘Preliminary characterization of microbial communities in high altitude wetlands of northwestern Argentina by determining terminal restriction fragment length polymorphisms’, *Revista latinoamericana de microbiologia*, 46(3–4), pp. 72–80.

Flügel, E. (2004) *Microfacies of carbonate rocks: analysis, interpretation and application*. Springer Science & Business Media.

Gierlowski-Kordesch, E.H. (2010) ‘Lacustrine carbonates’, *Developments in sedimentology*, 61, pp. 1–101.

Gwynn, J.W. (2007) *Great Salt Lake Brine Chemistry Databases and Reports, 1966-2006*. Utah Geological Survey Salt Lake City, UT.

Hren, M.T. and Sheldon, N.D. (2012) ‘Temporal variations in lake water temperature: Paleoenvironmental implications of lake carbonate δ18O and temperature records’, *Earth and Planetary Science Letters*, 337, pp. 77–84. Available at: https://doi.org/10.1016/j.epsl.2012.05.019.

Huntington, K.W., Saylor, J., Quade, J. and Hudson, A.M. (2015) ‘High late Miocene–Pliocene elevation of the Zhada Basin, southwestern Tibetan Plateau, from carbonate clumped isotope thermometry’, *Geological Society of America Bulletin*, 127(1–2), pp. 181–199. Available at: https://doi.org/10.1130/B31000.1.

Huntington, K.W., Wernicke, B.P. and Eiler, J.M. (2010) 'Influence of climate change and uplift on Colorado Plateau paleotemperatures from carbonate clumped isotope thermometry: COLORADO PLATEAU CARBONATES', *Tectonics*, 29(3). Available at: https://doi.org/10.1029/2009TC002449.

Ibarra, D.E., Egger, A.E., Weaver, K.L., Harris, C.R. and Maher, K. (2014) 'Rise and fall of late Pleistocene pluvial lakes in response to reduced evaporation and precipitation: Evidence from Lake Surprise, California', *GSA Bulletin*, 126(11–12), pp. 1387–1415. Available at: https://doi.org/10.1130/B31014.1.

Kele, S., Breitenbach, S.F.M., Capezzuoli, E., Meckler, A.N., Ziegler, M., Millan, I.M., Kluge, T., Deák, J., Hanselmann, K., John, C.M., Yan, H., Liu, Z. and Bernasconi, S.M. (2015) 'Temperature dependence of oxygen- and clumped isotope fractionation in carbonates: A study of travertines and tufas in the 6–95°C temperature range', *Geochimica et Cosmochimica Acta*, 168, pp. 172–192. Available at: https://doi.org/10.1016/j.gca.2015.06.032.

Kelson, J.R., Huntington, K.W., Schauer, A.J., Saenger, C. and Lechler, A.R. (2017) 'Toward a universal carbonate clumped isotope calibration: Diverse synthesis and preparatory methods suggest a single temperature relationship', *Geochimica et Cosmochimica Acta*, 197, pp. 104–131. Available at: https://doi.org/10.1016/j.gca.2016.10.010.

Kelts, K. and Hsü, K.J. (1978) 'Freshwater Carbonate Sedimentation', in A. Lerman (ed.) *Lakes: Chemistry, Geology, Physics*. New York, NY: Springer New York, pp. 295–323. Available at: https://doi.org/10.1007/978-1-4757-1152-3_9.

Kim, S.-T. and O'Neil, J.R. (1997) 'Equilibrium and nonequilibrium oxygen isotope effects in synthetic carbonates', *Geochimica et Cosmochimica Acta*, 61(16), pp. 3461–3475. Available at: https://doi.org/10.1016/S0016-7037(97)00169-5.

Kim, S.-T., O'Neil, J.R., Hillaire-Marcel, C. and Mucci, A. (2007) 'Oxygen isotope fractionation between synthetic aragonite and water: Influence of temperature and Mg2+ concentration', *Geochimica et Cosmochimica Acta*, 71(19), pp. 4704–4715. Available at: https://doi.org/10.1016/j.gca.2007.04.019.

Li, H., Liu, X., Arnold, A., Elliott, B., Flores, R., Kelley, A.M. and Tripati, A. (2021) 'Mass 47 clumped isotope signatures in modern lacustrine authigenic carbonates in Western China and other regions and implications for paleotemperature and paleoelevation reconstructions', *Earth and Planetary Science Letters*, 562, p. 116840. Available at: https://doi.org/10.1016/j.epsl.2021.116840.

Li, H., Liu, X., Tripati, A., Feng, S., Elliott, B., Whicker, C., Arnold, A. and Kelley, A.M. (2020) 'Factors controlling the oxygen isotopic composition of lacustrine authigenic carbonates in Western China: implications for paleoclimate reconstructions', *Scientific Reports*, 10(1), p. 16370. Available at: https://doi.org/10.1038/s41598-020-73422-4.

Li, L., Fan, M., Davila, N., Jesmok, G., Mitsunaga, B., Tripati, A. and Orme, D. (2019) 'Carbonate stable and clumped isotopic evidence for late Eocene moderate to high elevation of the east-central Tibetan Plateau and its geodynamic implications', *GSA Bulletin*, 131(5–6), pp. 831–844. Available at: https://doi.org/10.1130/B32060.1.

Linacre, E.T. (1993) ‘Data-sparse estimation of lake evaporation, using a simplified Penman equation’, *Agricultural and Forest Meteorology*, 64(3–4), pp. 237–256. Available at: https://doi.org/10.1016/0168-1923(93)90031-C.

Lucarelli, J.K., Carroll, H.M., Ulrich, R.N., Elliott, B.M., Coplen, T.B., Eagle, R.A. and Tripati, A. (2023) ‘Equilibrated Gas and Carbonate Standard-Derived Dual (Δ47 and Δ48) Clumped Isotope Values’, *Geochemistry, Geophysics, Geosystems*, 24(2), p. e2022GC010458. Available at: https://doi.org/10.1029/2022GC010458.

MacDonald, R. (1996) *Baseline physical, biological and chemical parameters of 21 lakes, Togiak National Wildlife Refuge, 1984-1990*. Togiak National Wildlife Refuge, US Fish and Wildlife Service.

Marić, I., Šiljeg, A., Cukrov, N., Roland, V. and Domazetović, F. (2020) ‘How fast does tufa grow? Very high-resolution measurement of the tufa growth rate on artificial substrates by the development of a contactless image-based modelling device’, *Earth Surface Processes and Landforms*, 45(10), pp. 2331–2349. Available at: https://doi.org/10.1002/esp.4883.

Oviatt, C.G., Habiger, G.D. and Hay, J.E. (1994) ‘Variation in the composition of Lake Bonneville marl: a potential key to lake-level fluctuations and paleoclimate’, *Journal of Paleolimnology*, 11(1), pp. 19–30. Available at: https://doi.org/10.1007/BF00683268.

Pacton, M., Hunger, G., Martinuzzi, V., Cusminsky, G., Burdin, B., Barmettler, K., Vasconcelos, C. and Ariztegui, D. (2015) ‘Organomineralization processes in freshwater stromatolites:

a living example from eastern Patagonia', *The Depositional Record*, 1(2), pp. 130–146. Available at: https://doi.org/10.1002/dep2.7.

Pedley, H.M. (1990) 'Classification and environmental models of cool freshwater tufas', *Sedimentary Geology*, 68(1–2), pp. 143–154. Available at: https://doi.org/10.1016/0037-0738(90)90124-C.

Pedone, V.A. (2002) 'Oxygen-isotope composition of Great Salt Lake, 1979 to 1996', *Great Salt Lake: An Overview of Change*, pp. 121–126.

Pérez, L., Bugja, R., Lorenschat, J., Brenner, M., Curtis, J., Hoelzmann, P., Islebe, G., Scharf, B. and Schwalb, A. (2011) 'Aquatic ecosystems of the Yucatan peninsula (Mexico), Belize, and Guatemala', *Hydrobiologia*, 661(1), pp. 407–433. Available at: https://doi.org/10.1007/s10750-010-0552-9.

Petersen, S.V., Defliese, W.F., Saenger, C., Daëron, M., Huntington, K.W., John, C.M., Kelson, J.R., Bernasconi, S.M., Colman, A.S., Kluge, T., Olack, G.A., Schauer, A.J., Bajnai, D., Bonifacie, M., Breitenbach, S.F.M., Fiebig, J., Fernandez, A.B., Henkes, G.A., Hodell, D., Katz, A., Kele, S., Lohmann, K.C., Passey, B.H., Peral, M.Y., Petrizzo, D.A., Rosenheim, B.E., Tripati, A., Venturelli, R., Young, E.D. and Winkelstern, I.Z. (2019) 'Effects of Improved 17O Correction on Interlaboratory Agreement in Clumped Isotope Calibrations, Estimates of Mineral-Specific Offsets, and Temperature Dependence of Acid Digestion Fractionation', *Geochemistry, Geophysics, Geosystems*, 20(7), pp. 3495–3519. Available at: https://doi.org/10.1029/2018GC008127.

Petryshyn, V.A., Juarez Rivera, M., Agić, H., Frantz, C.M., Corsetti, F.A. and Tripati, A.E. (2016) 'Stromatolites in Walker Lake (Nevada, Great Basin, USA) record climate and lake level changes ~35,000years ago', *Palaeogeography, Palaeoclimatology, Palaeoecology*, 451, pp. 140–151. Available at: https://doi.org/10.1016/j.palaeo.2016.02.054.

Petryshyn, V.A., Lim, D., Laval, B.L., Brady, A., Slater, G. and Tripati, A.K. (2015) 'Reconstruction of limnology and microbialite formation conditions from carbonate clumped isotope thermometry', *Geobiology*, 13(1), pp. 53–67. Available at: https://doi.org/10.1111/gbi.12121.

Phillips, K.N. and Van Denburgh, A.S. (1971) *Hydrology and geochemistry of Abert, Summer, and Goose Lakes and other closed-basin lakes in south-central Oregon*. US Government Printing Office.

Piovano, E.L., Ariztegui, D., Bernasconi, S.M. and McKenzie, J.A. (2004) 'Stable isotopic record of hydrological changes in subtropical Laguna Mar Chiquita (Argentina) over the last 230 years', *The holocene*, 14(4), pp. 525–535. Available at: https://doi.org/10.1191/0959683604hl729rp.

Platt, N.H. and Wright, V.P. (2009) 'Lacustrine Carbonates: Facies Models, Facies Distributions and Hydrocarbon Aspects', in *Lacustrine Facies Analysis*. John Wiley & Sons, Ltd, pp. 57–74. Available at: https://doi.org/10.1002/9781444303919.ch3.

Reati, G.J., Florín, M., Fernández, G.J. and Montes, C. (1996) 'The Laguna de Mar Chiquita (Córdoba, Argentina): A little known, secularly fluctuating, saline lake', *International*

Journal of Salt Lake Research, 5(3), pp. 187–219. Available at: https://doi.org/10.1007/BF01997137.

Roy, P.D., Charles-Polo, M.P., Lopez-Balbiaux, N., Pi-Puig, T., Sankar, G.M., Lozano-Santacruz, R., Lozano-García, S. and Romero, F.M. (2014) 'Last glacial hydrological variations at the southern margin of sub-tropical North America and a regional comparison', *Journal of Quaternary Science*, 29(5), pp. 495–505. Available at: https://doi.org/10.1002/jqs.2718.

Roy, P.D., Rivero-Navarette, A., Lopez-Balbiaux, N., Pérez-Cruz, L.L., Metcalfe, S.E., Sankar, G.M. and Sánchez-Zavala, J.L. (2013) 'A record of Holocene summer-season palaeohydrological changes from the southern margin of Chihuahua Desert (Mexico) and possible forcings', *The Holocene*, 23(8), pp. 1105–1114. Available at: https://doi.org/10.1177/0959683613483619.

Roy, P.D., Rivero-Navarrete, A., Sánchez-Zavala, J.L., Beramendi-Orosco, L.E., Muthu-Sankar, G. and Lozano-Santacruz, R. (2016) 'Atlantic Ocean modulated hydroclimate of the subtropical northeastern Mexico since the last glacial maximum and comparison with the southern US', *Earth and Planetary Science Letters*, 434, pp. 141–150. Available at: https://doi.org/10.1016/j.epsl.2015.11.048.

Roy, R., Wang, Y. and Jiang, S. (2019) 'Growth pattern and oxygen isotopic systematics of modern freshwater mollusks along an elevation transect: Implications for paleoclimate reconstruction', *Palaeogeography, Palaeoclimatology, Palaeoecology*, 532, p. 109243. Available at: https://doi.org/10.1016/j.palaeo.2019.109243.

Santi, Arnold, A.J., Ibarra, D.E., Whicker, C.A., Mering, J.A., Lomarda, R.B., Lora, J.M. and Tripati, A. (2020) 'Clumped isotope constraints on changes in latest Pleistocene hydroclimate in the northwestern Great Basin: Lake Surprise, California', *GSA Bulletin*, 132(11–12), pp. 2669–2683. Available at: https://doi.org/10.1130/B35484.1.

Solari, M.A., Hervé, F., Le Roux, J.P., Airo, A. and Sial, A.N. (2010) 'Paleoclimatic significance of lacustrine microbialites: A stable isotope case study of two lakes at Torres del Paine, southern Chile', *Palaeogeography, Palaeoclimatology, Palaeoecology*, 297(1), pp. 70–82. Available at: https://doi.org/10.1016/j.palaeo.2010.07.016.

Stephens, J.C. (1977) 'Hydrologic Reconnaissance of the Tule Valley Drainage Basin, Juab and Millard Counties, Utah', *State of Utah, Department of Natural Resources*, Technical Publication No. 56.

Street-Perrott, F.A. and Harrison, S.P. (2013) 'Temporal Variations in Lake Levels Since 30,000 YR BP—An Index of the Global Hydrological Cycle', in *Climate Processes and Climate Sensitivity*. American Geophysical Union (AGU), pp. 118–129. Available at: https://doi.org/10.1029/GM029p0118.

Tierney, J.E. and Russell, J.M. (2009) 'Distributions of branched GDGTs in a tropical lake system: implications for lacustrine application of the MBT/CBT paleoproxy', *Organic Geochemistry*, 40(9), pp. 1032–1036. Available at: https://doi.org/10.1016/j.orggeochem.2009.04.014.

Tremaine, D.M., Froelich, P.N. and Wang, Y. (2011) 'Speleothem calcite farmed in situ: Modern calibration of δ18O and δ13C paleoclimate proxies in a continuously-monitored natural

cave system', *Geochimica et Cosmochimica Acta*, 75(17), pp. 4929–4950. Available at: https://doi.org/10.1016/j.gca.2011.06.005.

Upadhyay, D., Lucarelli, J., Arnold, A., Flores, R., Bricker, H., Ulrich, R.N., Jesmok, G., Santi, L., Defliese, W., Eagle, R.A., Carroll, H.M., Bateman, J.B., Petryshyn, V., Loyd, S.J., Tang, J., Priyadarshi, A., Elliott, B. and Tripati, A. (2021) 'Carbonate clumped isotope analysis (Δ47) of 21 carbonate standards determined via gas-source isotope-ratio mass spectrometry on four instrumental configurations using carbonate-based standardization and multiyear data sets', *Rapid Communications in Mass Spectrometry*, 35(17), p. e9143. Available at: https://doi.org/10.1002/rcm.9143.

U.S. Geological Survey (2022a) *National Water Information System data available on the World Wide Web (USGS Water Data for the Nation)*, *OAK CREEK AT RED ROCK CROSSING NR SEDONA, AZ (USGS-09504440) site data in the Water Quality Portal*. Available at: https://www.waterqualitydata.us/provider/NWIS/USGS-AZ/USGS-09504440/.

U.S. Geological Survey (2022b) *National Water Information System data available on the World Wide Web (USGS Water Data for the Nation)*, *USGS 11042510 VAIL LK NR TEMECULA CA*. Available at: https://waterdata.usgs.gov/nwis/inventory/?site_no=11042510&agency_cd=USGS.

U.S. Geological Survey (2022c) *National Water Information System data available on the World Wide Web (USGS Water Data for the Nation)*, *USGS 09522000 COLORADO RIVER AT NIB, ABOVE MORELOS DAM, AZ*. Available at: https://waterdata.usgs.gov/nwis/inventory/?site_no=09522000.

U.S. Geological Survey (2022d) *National Water Information System data available on the World Wide Web (USGS Water Data for the Nation)*, *SANTA CLARA RIVER ABV BAKER RES, NR CENTRAL, UT (USGS-09409100)*. Available at: https://www.waterqualitydata.us/provider/NWIS/USGS-UT/USGS-09409100/.

Velázquez, N.I.T. (2017) 'Paleohydrology record of the stromatolites of the Bacalar Lagoon: new insight for climate change assessment in the Mexican Caribbean', in *XVI World Water Congress*.

Versteegh, E.A., Vonhof, H.B., Troelstra, S.R., Kaandorp, R.J. and Kroon, D. (2010) 'Seasonally resolved growth of freshwater bivalves determined by oxygen and carbon isotope shell chemistry', *Geochemistry, Geophysics, Geosystems*, 11(8). Available at: https://doi.org/10.1029/2009GC002961.

Wang, Y., Passey, B., Roy, R., Deng, T., Jiang, S., Hannold, C., Wang, X., Lochner, E. and Tripati, A. (2021) 'Clumped isotope thermometry of modern and fossil snail shells from the Himalayan-Tibetan Plateau: Implications for paleoclimate and paleoelevation reconstructions', *GSA Bulletin*, 133(7–8), pp. 1370–1380. Available at: https://doi.org/10.1130/B35784.1.

White, R., Dennis, P. and Atkinson, T. (1999) 'Experimental calibration and field investigation of the oxygen isotopic fractionation between biogenic aragonite and water', *Rapid Communications in Mass Spectrometry*, 13(13), pp. 1242–1247. Available at: https://doi.org/10.1002/(SICI)1097-0231(19990715)13:13<1242::AID-RCM627>3.0.CO;2-F.

Wilbur, K.M. and Watabe, N. (1963) ‘Experimental Studies on Calcification in Molluscs and the Alga Coccolithus Huxleyi’, *Annals of the New York Academy of Sciences*, 109(1), pp. 82–112. Available at: https://doi.org/10.1111/j.1749-6632.1963.tb13463.x.

Yu, S., Liu, J., Xu, J. and Wang, H. (2011) ‘Evaporation and energy balance estimates over a large inland lake in the Tibet-Himalaya’, *Environmental Earth Sciences*, 64(4), pp. 1169–1176. Available at: https://doi.org/10.1007/s12665-011-0933-z.

Yuan, F., Linsley, B.K. and Howe, S.S. (2006) ‘Evaluating sedimentary geochemical lake-level tracers in Walker Lake, Nevada, over the last 200 years’, *Journal of Paleolimnology*, 36(1), pp. 37–54. Available at: https://doi.org/10.1007/s10933-006-0004-8.

Zhang, Q., Liu, X. and Li, H. (2021) ‘Impact of hydrological conditions on the radiocarbon reservoir effect in lake sediment 14C dating: the case of Kusai Lake on the northern Qinghai-Tibet Plateau’, *Quaternary Geochronology*, 62, p. 101149. Available at: https://doi.org/10.1016/j.quageo.2020.101149.

9. References

Anderson, N.T., Kelson, J.R., Kele, S., Daëron, M., Bonifacie, M., Horita, J., Mackey, T.J., John, C.M., Kluge, T., Petschnig, P., Jost, A.B., Huntington, K.W., Bernasconi, S.M. and Bergmann, K.D. (2021) 'A Unified Clumped Isotope Thermometer Calibration (0.5–1,100°C) Using Carbonate-Based Standardization', *Geophysical Research Letters*, 48(7), p. e2020GL092069. Available at: https://doi.org/10.1029/2020GL092069.

Aravena, R., Warner, B.G., MacDonald, G.M. and Hanf, K.I. (1992) 'Carbon isotope composition of lake sediments in relation to lake productivity and radiocarbon dating', *Quaternary Research*, 37(3), pp. 333–345. Available at: https://doi.org/10.1016/0033-5894(92)90071-P.

Arenas-Abad, C., Vázquez-Urbez, M., Pardo-Tirapu, G. and Sancho-Marcén, C. (2010) 'Fluvial and associated carbonate deposits', *Developments in Sedimentology*, 61, pp. 133–175. Available at: https://doi.org/10.1016/S0070-4571(09)06103-2.

Beck, W.C., Grossman, E.L. and Morse, J.W. (2005) 'Experimental studies of oxygen isotope fractionation in the carbonic acid system at 15, 25, and 40 C', *Geochimica et Cosmochimica Acta*, 69(14), pp. 3493–3503. Available at: https://doi.org/10.1016/j.gca.2005.02.003.

Bernasconi, S.M., Daëron, M., Bergmann, K.D., Bonifacie, M., Meckler, A.N., Affek, H.P., Anderson, N., Bajnai, D., Barkan, E., Beverly, E., Blamart, D., Burgener, L., Calmels, D., Chaduteau, C., Clog, M., Davidheiser-Kroll, B., Davies, A., Dux, F., Eiler, J., Elliott, B., Fetrow, A.C., Fiebig, J., Goldberg, S., Hermoso, M., Huntington, K.W., Hyland, E.,

Ingalls, M., Jaggi, M., John, C.M., Jost, A.B., Katz, S., Kelson, J., Kluge, T., Kocken, I.J., Laskar, A., Leutert, T.J., Liang, D., Lucarelli, J., Mackey, T.J., Mangenot, X., Meinicke, N., Modestou, S.E., Müller, I.A., Murray, S., Neary, A., Packard, N., Passey, B.H., Pelletier, E., Petersen, S., Piasecki, A., Schauer, A., Snell, K.E., Swart, P.K., Tripati, A., Upadhyay, D., Vennemann, T., Winkelstern, I., Yarian, D., Yoshida, N., Zhang, N. and Ziegler, M. (2021) 'InterCarb: A Community Effort to Improve Interlaboratory Standardization of the Carbonate Clumped Isotope Thermometer Using Carbonate Standards', *Geochemistry, Geophysics, Geosystems*, 22(5), p. e2020GC009588. Available at: https://doi.org/10.1029/2020GC009588.

Bernasconi, S.M., Müller, I.A., Bergmann, K.D., Breitenbach, S.F.M., Fernandez, A., Hodell, D.A., Jaggi, M., Meckler, A.N., Millan, I. and Ziegler, M. (2018) 'Reducing Uncertainties in Carbonate Clumped Isotope Analysis Through Consistent Carbonate-Based Standardization', *Geochemistry, Geophysics, Geosystems*, 19(9), pp. 2895–2914. Available at: https://doi.org/10.1029/2017GC007385.

Boch, R., Spötl, C., Reitner, J.M. and Kramers, J. (2005) 'A lateglacial travertine deposit in Eastern Tyrol (Austria)', *Austrian Journal of Earth Sciences*, 98, pp. 78–91.

Boch, R., Wang, X., Kluge, T., Leis, A., Lin, K., Pluch, H., Mittermayr, F., Baldermann, A., Boettcher, M.E. and Dietzel, M. (2019) 'Aragonite–calcite veins of the 'Erzberg'iron ore deposit (Austria): Environmental implications from young fractures', *Sedimentology*, 66(2), pp. 604–635. Available at: https://doi.org/10.1111/sed.12500.

Brenner, M., Whitmore, T.J., Curtis, J.H., Hodell, D.A. and Schelske, C.L. (1999) 'Stable isotope (δ13C and δ15N) signatures of sedimented organic matter as indicators of historic

lake trophic state', *Journal of Paleolimnology*, 22(2), pp. 205–221. Available at: https://doi.org/10.1023/A:1008078222806.

Chamberlain, C.P. and Poage, M.A. (2000) 'Reconstructing the paleotopography of mountain belts from the isotopic composition of authigenic minerals', *Geology*, 28(2), pp. 115–118. Available at: https://doi.org/10.1130/0091-7613(2000)28<115:RTPOMB>2.0.CO;2.

Cheng, F., Garzione, C., Li, X., Salzmann, U., Schwarz, F., Haywood, A.M., Tindall, J., Nie, J., Li, L. and Wang, L. (2022) 'Alpine permafrost could account for a quarter of thawed carbon based on Plio-Pleistocene paleoclimate analogue', *Nature communications*, 13(1), pp. 1–12. Available at: https://doi.org/10.1038/s41467-022-29011-2.

Csank, A.Z., Tripati, A.K., Patterson, W.P., Eagle, R.A., Rybczynski, N., Ballantyne, A.P. and Eiler, J.M. (2011) 'Estimates of Arctic land surface temperatures during the early Pliocene from two novel proxies', *Earth and Planetary Science Letters*, 304(3–4), pp. 291–299. Available at: https://doi.org/10.1016/j.epsl.2011.02.030.

Daëron, M. (2021) 'Full propagation of analytical uncertainties in Δ47 measurements', *Geochemistry, Geophysics, Geosystems*, 22(5), p. e2020GC009592. Available at: https://doi.org/10.1029/2020GC009592.

Daëron, M., Blamart, D., Peral, M. and Affek, H.P. (2016) 'Absolute isotopic abundance ratios and the accuracy of Δ47 measurements', *Chemical Geology*, 442, pp. 83–96. Available at: https://doi.org/10.1016/j.chemgeo.2016.08.014.

Das, O., Wang, Y., Donoghue, J., Xu, X., Coor, J., Elsner, J. and Xu, Y. (2013) 'Reconstruction of paleostorms and paleoenvironment using geochemical proxies archived in the

sediments of two coastal lakes in northwest Florida', *Quaternary Science Reviews*, 68, pp. 142–153. Available at: https://doi.org/10.1016/j.quascirev.2013.02.014.

Davies, A.J. and John, C.M. (2019) 'The clumped (13C18O) isotope composition of echinoid calcite: Further evidence for "vital effects" in the clumped isotope proxy', *Geochimica et Cosmochimica Acta*, 245, pp. 172–189. Available at: https://doi.org/10.1016/j.gca.2018.07.038.

Eagle, R.A., Eiler, J.M., Tripati, A.K., Ries, J.B., Freitas, P.S., Hiebenthal, C., Wanamaker, A.D., Taviani, M., Elliot, M., Marenssi, S., Nakamura, K., Ramirez, P. and Roy, K. (2013) 'The influence of temperature and seawater carbonate saturation state on 13C–18O bond ordering in bivalve mollusks', *Biogeosciences*, 10(7), pp. 4591–4606. Available at: https://doi.org/10.5194/bg-10-4591-2013.

Eagle, R.A., Risi, C., Mitchell, J.L., Eiler, J.M., Seibt, U., Neelin, J.D., Li, G. and Tripati, A.K. (2013) 'High regional climate sensitivity over continental China constrained by glacial-recent changes in temperature and the hydrological cycle', *Proceedings of the National Academy of Sciences*, 110(22), pp. 8813–8818. Available at: https://doi.org/10.1073/pnas.1213366110.

Egger, A.E., Ibarra, D.E., Weldon, R., Langridge, R.M., Marion, B., Hall, J., Starratt, S.W. and Rosen, M.R. (2018) 'Influence of pluvial lake cycles on earthquake recurrence in the northwestern Basin and Range, USA', *Geological Society of America Special Paper*, 536, pp. 1–28. Available at: https://doi.org/doi:10.1130/2018.2536(07).

Epstein, S., Buchsbaum, R., Lowenstam, H.A. and Urey, H.C. (1953) 'Revised carbonate-water isotopic temperature scale', *Geological Society of America Bulletin*, 64(11), pp. 1315–1326. Available at: https://doi.org/10.1130/0016-7606(1953)64[1315:RCITS]2.0.CO;2.

Esper, J., St. George, S., Anchukaitis, K., D'Arrigo, R., Ljungqvist, F.C., Luterbacher, J., Schneider, L., Stoffel, M., Wilson, R. and Büntgen, U. (2018) 'Large-scale, millennial-length temperature reconstructions from tree-rings', *Dendrochronologia*, 50, pp. 81–90. Available at: https://doi.org/10.1016/j.dendro.2018.06.001.

Gallagher, T.M. and Sheldon, N.D. (2013) 'A new paleothermometer for forest paleosols and its implications for Cenozoic climate', *Geology*, 41(6), pp. 647–650. Available at: https://doi.org/10.1130/G34074.1.

Ghosh, P., Adkins, J., Affek, H., Balta, B., Guo, W., Schauble, E.A., Schrag, D. and Eiler, J.M. (2006) '13C–18O bonds in carbonate minerals: a new kind of paleothermometer', *Geochimica et Cosmochimica Acta*, 70(6), pp. 1439–1456. Available at: https://doi.org/10.1016/j.gca.2005.11.014.

Ghosh, P., Garzione, C.N. and Eiler, J.M. (2006) 'Rapid Uplift of the Altiplano Revealed Through 13C-18O Bonds in Paleosol Carbonates', *Science*, 311(5760), pp. 511–515. Available at: https://doi.org/10.1126/science.1119365.

Gierlowski-Kordesch, E.H. (2010) 'Lacustrine carbonates', *Developments in sedimentology*, 61, pp. 1–101.

Grauel, A.-L., Hodell, D.A. and Bernasconi, S.M. (2016) 'Quantitative estimates of tropical temperature change in lowland Central America during the last 42 ka', *Earth and*

Planetary Science Letters, 438, pp. 37–46. Available at: https://doi.org/10.1016/j.epsl.2016.01.001.

Gwynn, J.W. (2007) *Great Salt Lake Brine Chemistry Databases and Reports, 1966-2006*. Utah Geological Survey Salt Lake City, UT.

Hansen, J., Satoa, M., Kharechaa, P., Beerlingc, D., Bernerd, R., Masson-delmottee, V., Paganid, M., Raymof, M., Royerg, D.L. and Zachosh, J.C. (2008) 'Target Atmospheric CO2: Where Should Humanity Aim?" The Open Atmospheric Science Journal'. Available at: https://doi.org/10.2174/1874282300802010217.

Hill, P.S., Schauble, E.A. and Tripati, A. (2020) 'Theoretical constraints on the effects of added cations on clumped, oxygen, and carbon isotope signatures of dissolved inorganic carbon species and minerals', *Geochimica et Cosmochimica Acta*, 269, pp. 496–539. Available at: https://doi.org/10.1016/j.gca.2019.10.016.

Hill, P.S., Tripati, A.K. and Schauble, E.A. (2014) 'Theoretical constraints on the effects of pH, salinity, and temperature on clumped isotope signatures of dissolved inorganic carbon species and precipitating carbonate minerals', *Geochimica et Cosmochimica Acta*, 125, pp. 610–652. Available at: https://doi.org/10.1016/j.gca.2013.06.018.

Horton, T.W., Defliese, W.F., Tripati, A.K. and Oze, C. (2016) 'Evaporation induced 18O and 13C enrichment in lake systems: A global perspective on hydrologic balance effects', *Quaternary Science Reviews*, 131, pp. 365–379. Available at: https://doi.org/10.1016/j.quascirev.2015.06.030.

Hren, M.T. and Sheldon, N.D. (2012) 'Temporal variations in lake water temperature: Paleoenvironmental implications of lake carbonate δ18O and temperature records', *Earth and Planetary Science Letters*, 337, pp. 77–84. Available at: https://doi.org/10.1016/j.epsl.2012.05.019.

Hren, M.T., Sheldon, N.D., Grimes, S.T., Collinson, M.E., Hooker, J.J., Bugler, M. and Lohmann, K.C. (2013) 'Terrestrial cooling in Northern Europe during the Eocene–Oligocene transition', *Proceedings of the National Academy of Sciences*, 110(19), pp. 7562–7567. Available at: https://doi.org/10.1073/pnas.1210930110.

Hudson, A.M., Quade, J., Ali, G., Boyle, D., Bassett, S., Huntington, K.W., De los Santos, M.G., Cohen, A.S., Lin, K. and Wang, X. (2017) 'Stable C, O and clumped isotope systematics and 14C geochronology of carbonates from the Quaternary Chewaucan closed-basin lake system, Great Basin, USA: Implications for paleoenvironmental reconstructions using carbonates', *Geochimica et Cosmochimica Acta*, 212, pp. 274–302. Available at: https://doi.org/10.1016/j.gca.2017.06.024.

Huntington, K.W. and Lechler, A.R. (2015) 'Carbonate clumped isotope thermometry in continental tectonics', *Tectonophysics*, 647–648, pp. 1–20. Available at: https://doi.org/10.1016/j.tecto.2015.02.019.

Huntington, K.W., Saylor, J., Quade, J. and Hudson, A.M. (2015) 'High late Miocene–Pliocene elevation of the Zhada Basin, southwestern Tibetan Plateau, from carbonate clumped isotope thermometry', *Geological Society of America Bulletin*, 127(1–2), pp. 181–199. Available at: https://doi.org/10.1130/B31000.1.

Huntington, K.W., Wernicke, B.P. and Eiler, J.M. (2010) 'Influence of climate change and uplift on Colorado Plateau paleotemperatures from carbonate clumped isotope thermometry: COLORADO PLATEAU CARBONATES', *Tectonics*, 29(3). Available at: https://doi.org/10.1029/2009TC002449.

Ibarra, D.E., Egger, A.E., Weaver, K.L., Harris, C.R. and Maher, K. (2014) 'Rise and fall of late Pleistocene pluvial lakes in response to reduced evaporation and precipitation: Evidence from Lake Surprise, California', *GSA Bulletin*, 126(11–12), pp. 1387–1415. Available at: https://doi.org/10.1130/B31014.1.

Ingalls, M., Frantz, C.M., Snell, K.E. and Trower, E.J. (2020) 'Carbonate facies-specific stable isotope data record climate, hydrology, and microbial communities in Great Salt Lake, UT', *Geobiology*, 18(5), pp. 566–593. Available at: https://doi.org/10.1111/gbi.12386.

Ingalls, M., Rowley, D., Olack, G., Currie, B., Li, S., Schmidt, J., Tremblay, M., Polissar, P., Shuster, D.L., Lin, D. and Colman, A. (2017) 'Paleocene to Pliocene low-latitude, high-elevation basins of southern Tibet: Implications for tectonic models of India-Asia collision, Cenozoic climate, and geochemical weathering', *GSA Bulletin*, 130(1–2), pp. 307–330. Available at: https://doi.org/10.1130/B31723.1.

John, C.M. and Bowen, D. (2016) 'Community software for challenging isotope analysis: First applications of "Easotope" to clumped isotopes: Community software for challenging isotope analysis', *Rapid Communications in Mass Spectrometry*, 30(21), pp. 2285–2300. Available at: https://doi.org/10.1002/rcm.7720.

Kato, H., Amekawa, S., Kano, A., Mori, T., Kuwahara, Y. and Quade, J. (2019) 'Seasonal temperature changes obtained from carbonate clumped isotopes of annually laminated tufas from Japan: Discrepancy between natural and synthetic calcites', *Geochimica et Cosmochimica Acta*, 244, pp. 548–564. Available at: https://doi.org/10.1016/j.gca.2018.10.016.

Kaufman, D., McKay, N., Routson, C., Erb, M., Davis, B., Heiri, O., Jaccard, S., Tierney, J., Dätwyler, C. and Axford, Y. (2020) 'A global database of Holocene paleotemperature records', *Scientific data*, 7(1), pp. 1–34. Available at: https://doi.org/10.1038/s41597-020-0445-3.

Kele, S., Breitenbach, S.F.M., Capezzuoli, E., Meckler, A.N., Ziegler, M., Millan, I.M., Kluge, T., Deák, J., Hanselmann, K., John, C.M., Yan, H., Liu, Z. and Bernasconi, S.M. (2015) 'Temperature dependence of oxygen- and clumped isotope fractionation in carbonates: A study of travertines and tufas in the 6–95°C temperature range', *Geochimica et Cosmochimica Acta*, 168, pp. 172–192. Available at: https://doi.org/10.1016/j.gca.2015.06.032.

Kim, S.-T. and O'Neil, J.R. (1997) 'Equilibrium and nonequilibrium oxygen isotope effects in synthetic carbonates', *Geochimica et Cosmochimica Acta*, 61(16), pp. 3461–3475. Available at: https://doi.org/10.1016/S0016-7037(97)00169-5.

Kim, S.-T., O'Neil, J.R., Hillaire-Marcel, C. and Mucci, A. (2007) 'Oxygen isotope fractionation between synthetic aragonite and water: Influence of temperature and Mg2+ concentration', *Geochimica et Cosmochimica Acta*, 71(19), pp. 4704–4715. Available at: https://doi.org/10.1016/j.gca.2007.04.019.

Kimball, J., Eagle, R. and Dunbar, R. (2016) 'Carbonate "clumped" isotope signatures in aragonitic scleractinian and calcitic gorgonian deep-sea corals', *Biogeosciences*, 13(23), pp. 6487–6505. Available at: https://doi.org/10.5194/bg-13-6487-2016.

Li, H., Liu, X., Arnold, A., Elliott, B., Flores, R., Kelley, A.M. and Tripati, A. (2021) 'Mass 47 clumped isotope signatures in modern lacustrine authigenic carbonates in Western China and other regions and implications for paleotemperature and paleoelevation reconstructions', *Earth and Planetary Science Letters*, 562, p. 116840. Available at: https://doi.org/10.1016/j.epsl.2021.116840.

Li, H., Liu, X., Tripati, A., Feng, S., Elliott, B., Whicker, C., Arnold, A. and Kelley, A.M. (2020) 'Factors controlling the oxygen isotopic composition of lacustrine authigenic carbonates in Western China: implications for paleoclimate reconstructions', *Scientific Reports*, 10(1), p. 16370. Available at: https://doi.org/10.1038/s41598-020-73422-4.

Li, L., Fan, M., Davila, N., Jesmok, G., Mitsunaga, B., Tripati, A. and Orme, D. (2019) 'Carbonate stable and clumped isotopic evidence for late Eocene moderate to high elevation of the east-central Tibetan Plateau and its geodynamic implications', *GSA Bulletin*, 131(5–6), pp. 831–844. Available at: https://doi.org/10.1130/B32060.1.

Li, X., Zhou, X., Liu, W., Wang, Z., He, Y. and Xu, L. (2016) 'Carbon and oxygen isotopic records from Lake Tuosu over the last 120 years in the Qaidam Basin, Northwestern China: The implications for paleoenvironmental reconstruction', *Global and Planetary Change*, 141, pp. 54–62. Available at: https://doi.org/10.1016/j.gloplacha.2016.04.006.

Lucarelli, J.K., Carroll, H.M., Ulrich, R.N., Elliott, B.M., Coplen, T.B., Eagle, R.A. and Tripati, A. (2023) 'Equilibrated Gas and Carbonate Standard-Derived Dual (Δ47 and Δ48) Clumped Isotope Values', *Geochemistry, Geophysics, Geosystems*, 24(2), p. e2022GC010458. Available at: https://doi.org/10.1029/2022GC010458.

Mackey, T.J., Sumner, D.Y., Hawes, I., Leidman, S.Z., Andersen, D.T. and Jungblut, A.D. (2018) 'Stromatolite records of environmental change in perennially ice-covered Lake Joyce, McMurdo Dry Valleys, Antarctica', *Biogeochemistry*, 137(1), pp. 73–92. Available at: https://doi.org/10.1007/s10533-017-0402-1.

Meckler, A.N., Vonhof, H. and Martínez-García, A. (2021) 'Temperature Reconstructions Using Speleothems', *Elements*, 17(2), pp. 101–106. Available at: https://doi.org/10.2138/gselements.17.2.101.

Pace, A., Bourillot, R., Bouton, A., Vennin, E., Galaup, S., Bundeleva, I., Patrier, P., Dupraz, C., Thomazo, C., Sansjofre, P., Yokoyama, Y., Franceschi, M., Anguy, Y., Pigot, L., Virgone, A. and Visscher, P.T. (2016) 'Microbial and diagenetic steps leading to the mineralisation of Great Salt Lake microbialites', *Scientific Reports*, 6(1), p. 31495. Available at: https://doi.org/10.1038/srep31495.

Paradis, O.P. (2019) *Great Salt Lake ooids: Insights into rate of formation, potential as paleoenvironmental archives, and biogenicity*. Ph.D. Thesis. University of Southern California.

Passey, B.H., Levin, N.E., Cerling, T.E., Brown, F.H. and Eiler, J.M. (2010) 'High-temperature environments of human evolution in East Africa based on bond ordering in paleosol

carbonates', *Proceedings of the National Academy of Sciences*, 107(25), pp. 11245–11249. Available at: https://doi.org/10.1073/pnas.1001824107.

Petersen, S.V., Defliese, W.F., Saenger, C., Daëron, M., Huntington, K.W., John, C.M., Kelson, J.R., Bernasconi, S.M., Colman, A.S., Kluge, T., Olack, G.A., Schauer, A.J., Bajnai, D., Bonifacie, M., Breitenbach, S.F.M., Fiebig, J., Fernandez, A.B., Henkes, G.A., Hodell, D., Katz, A., Kele, S., Lohmann, K.C., Passey, B.H., Peral, M.Y., Petrizzo, D.A., Rosenheim, B.E., Tripati, A., Venturelli, R., Young, E.D. and Winkelstern, I.Z. (2019) 'Effects of Improved 17O Correction on Interlaboratory Agreement in Clumped Isotope Calibrations, Estimates of Mineral-Specific Offsets, and Temperature Dependence of Acid Digestion Fractionation', *Geochemistry, Geophysics, Geosystems*, 20(7), pp. 3495–3519. Available at: https://doi.org/10.1029/2018GC008127.

Petryshyn, V.A., Lim, D., Laval, B.L., Brady, A., Slater, G. and Tripati, A.K. (2015) 'Reconstruction of limnology and microbialite formation conditions from carbonate clumped isotope thermometry', *Geobiology*, 13(1), pp. 53–67. Available at: https://doi.org/10.1111/gbi.12121.

Platt, N.H. and Wright, V.P. (2009) 'Lacustrine Carbonates: Facies Models, Facies Distributions and Hydrocarbon Aspects', in *Lacustrine Facies Analysis*. John Wiley & Sons, Ltd, pp. 57–74. Available at: https://doi.org/10.1002/9781444303919.ch3.

Poage, M.A. and Chamberlain, C.P. (2001) 'Empirical Relationships Between Elevation and the Stable Isotope Composition of Precipitation and Surface Waters: Considerations for Studies of Paleoelevation Change', *American Journal of Science*, 301(1), pp. 1–15. Available at: https://doi.org/10.2475/ajs.301.1.1.

Powers, L., Werne, J.P., Vanderwoude, A.J., Sinninghe Damsté, J.S., Hopmans, E.C. and Schouten, S. (2010) 'Applicability and calibration of the TEX86 paleothermometer in lakes', *Organic Geochemistry*, 41(4), pp. 404–413. Available at: https://doi.org/10.1016/j.orggeochem.2009.11.009.

Quade, J., Eiler, J., Daëron, M. and Achyuthan, H. (2013) 'The clumped isotope geothermometer in soil and paleosol carbonate', *Geochimica et Cosmochimica Acta*, 105, pp. 92–107. Available at: https://doi.org/10.1016/j.gca.2012.11.031.

R Core Team (2022) 'R: A language and environment for statistical computing.' Vienna, Austria: R Foundation for Statistical Computing. Available at: https://www.R-project.org/.

Richter, F., Garzione, C.N., Liu, W., Qiang, X., Chang, H., Cheng, F., Li, X. and Tripati, A. (2022) 'Plio-Pleistocene cooling of the northeastern Tibetan Plateau due to global climate change and surface uplift', *GSA Bulletin*, 135(5–6), pp. 1327–1343. Available at: https://doi.org/10.1130/B36302.1.

Román Palacios, C., Carroll, H., Arnold, A., Flores, R., Petersen, S., McKinnon, K. and Tripati, A. (2021) 'BayClump: Bayesian Calibration and Temperature Reconstructions for Clumped Isotope Thermometry'. Available at: https://www.essoar.org/doi/10.1002/essoar.10507995.1.

Rowley, D.B. and Garzione, C.N. (2007) 'Stable Isotope-Based Paleoaltimetry', *Annual Review of Earth and Planetary Sciences*, 35(1), pp. 463–508. Available at: https://doi.org/10.1146/annurev.earth.35.031306.140155.

Saenger, C., Affek, H.P., Felis, T., Thiagarajan, N., Lough, J.M. and Holcomb, M. (2012) 'Carbonate clumped isotope variability in shallow water corals: Temperature dependence and growth-related vital effects', *Geochimica et Cosmochimica Acta*, 99, pp. 224–242. Available at: https://doi.org/10.1016/j.gca.2012.09.035.

Santi, L., Arnold, A., Mering, J., Arnold, D., Tripati, A., Whicker, C. and Oviatt, C.G. (2019) 'Lake level fluctuations in the Northern Great Basin for the last 25,000 years', *Exploring Ends of Eras in the Eastern Mojave Desert: 2019 Desert Symposium Field Guide and Proceedings*, pp. 176–186. Available at: https://doi.org/10.31223/osf.io/6as7t.

Santi, L., Arnold, A.J., Ibarra, D.E., Whicker, C.A., Mering, J.A., Lomarda, R.B., Lora, J.M. and Tripati, A. (2020) 'Clumped isotope constraints on changes in latest Pleistocene hydroclimate in the northwestern Great Basin: Lake Surprise, California', *GSA Bulletin*, 132(11–12), pp. 2669–2683. Available at: https://doi.org/10.1130/B35484.1.

Schauble, E.A., Ghosh, P. and Eiler, J.M. (2006) 'Preferential formation of 13C–18O bonds in carbonate minerals, estimated using first-principles lattice dynamics', *Geochimica et Cosmochimica Acta*, 70(10), pp. 2510–2529. Available at: https://doi.org/10.1016/j.gca.2006.02.011.

Schelske, C.L. and Hodell, D.A. (1995) 'Using carbon isotopes of bulk sedimentary organic matter to reconstruct the history of nutrient loading and eutrophication in Lake Erie', *Limnology and Oceanography*, 40(5), pp. 918–929. Available at: https://doi.org/10.4319/lo.1995.40.5.0918.

Spencer, C. and Kim, S.-T. (2015) ‘Carbonate clumped isotope paleothermometry: a review of recent advances in CO2 gas evolution, purification, measurement and standardization techniques’, *Geosciences Journal*, 19(2), pp. 357–374. Available at: https://doi.org/10.1007/s12303-015-0018-1.

Spooner, P.T., Guo, W., Robinson, L.F., Thiagarajan, N., Hendry, K.R., Rosenheim, B.E. and Leng, M.J. (2016) ‘Clumped isotope composition of cold-water corals: A role for vital effects?’, *Geochimica et Cosmochimica Acta*, 179, pp. 123–141. Available at: https://doi.org/10.1016/j.gca.2016.01.023.

Stuiver, M. and Grootes, P.M. (2000) ‘GISP2 oxygen isotope ratios’, *Quaternary Research*, 53(3), pp. 277–284. Available at: https://doi.org/10.1006/qres.2000.2127.

Stute, M. and Schlosser, P. (2000) ‘Atmospheric Noble Gases’, in P.G. Cook and A.L. Herczeg (eds) *Environmental Tracers in Subsurface Hydrology*. Boston, MA: Springer US, pp. 349–377. Available at: https://doi.org/10.1007/978-1-4615-4557-6_11.

Swart, P.K., Burns, S.J. and Leder, J.J. (1991) ‘Fractionation of the stable isotopes of oxygen and carbon in carbon dioxide during the reaction of calcite with phosphoric acid as a function of temperature and technique’, *Chemical Geology: Isotope Geoscience section*, 86(2), pp. 89–96. Available at: https://doi.org/10.1016/0168-9622(91)90055-2.

Tang, J., Dietzel, M., Fernandez, A., Tripati, A.K. and Rosenheim, B.E. (2014) ‘Evaluation of kinetic effects on clumped isotope fractionation (Δ47) during inorganic calcite precipitation’, *Geochimica et Cosmochimica Acta*, 134, pp. 120–136. Available at: https://doi.org/10.1016/j.gca.2014.03.005.

Tripati, A.K., Eagle, R.A., Thiagarajan, N., Gagnon, A.C., Bauch, H., Halloran, P.R. and Eiler, J.M. (2010) '13C–18O isotope signatures and "clumped isotope" thermometry in foraminifera and coccoliths', *Geochimica et Cosmochimica Acta*, 74(20), pp. 5697–5717. Available at: https://doi.org/10.1016/j.gca.2010.07.006.

Tripati, A.K., Hill, P.S., Eagle, R.A., Mosenfelder, J.L., Tang, J., Schauble, E.A., Eiler, J.M., Zeebe, R.E., Uchikawa, J., Coplen, T.B., Ries, J.B. and Henry, D. (2015) 'Beyond temperature: Clumped isotope signatures in dissolved inorganic carbon species and the influence of solution chemistry on carbonate mineral composition', *Geochimica et Cosmochimica Acta*, 166, pp. 344–371. Available at: https://doi.org/10.1016/j.gca.2015.06.021.

Tripati, A.K., Sahany, S., Pittman, D., Eagle, R.A., Neelin, J.D., Mitchell, J.L. and Beaufort, L. (2014) 'Modern and glacial tropical snowlines controlled by sea surface temperature and atmospheric mixing', *Nature Geoscience*, 7(3), pp. 205–209. Available at: https://doi.org/10.1038/ngeo2082.

Upadhyay, D., Lucarelli, J., Arnold, A., Flores, R., Bricker, H., Ulrich, R.N., Jesmok, G., Santi, L., Defliese, W., Eagle, R.A., Carroll, H.M., Bateman, J.B., Petryshyn, V., Loyd, S.J., Tang, J., Priyadarshi, A., Elliott, B. and Tripati, A. (2021) 'Carbonate clumped isotope analysis (Δ47) of 21 carbonate standards determined via gas-source isotope-ratio mass spectrometry on four instrumental configurations using carbonate-based standardization and multiyear data sets', *Rapid Communications in Mass Spectrometry*, 35(17), p. e9143. Available at: https://doi.org/10.1002/rcm.9143.

Urey, H.C. (1947) ‘The thermodynamic properties of isotopic substances’, *Journal of the Chemical Society (Resumed)*, (0), pp. 562–581. Available at: https://doi.org/10.1039/JR9470000562.

Vasconcelos, C., McKenzie, J.A., Warthmann, R. and Bernasconi, S.M. (2005) ‘Calibration of the δ18O paleothermometer for dolomite precipitated in microbial cultures and natural environments’, *Geology*, 33(4), pp. 317–320. Available at: https://doi.org/10.1130/G20992.1.

Versteegh, E.A., Vonhof, H.B., Troelstra, S.R., Kaandorp, R.J. and Kroon, D. (2010) ‘Seasonally resolved growth of freshwater bivalves determined by oxygen and carbon isotope shell chemistry’, *Geochemistry, Geophysics, Geosystems*, 11(8). Available at: https://doi.org/10.1029/2009GC002961.

Wang, Y., Passey, B., Roy, R., Deng, T., Jiang, S., Hannold, C., Wang, X., Lochner, E. and Tripati, A. (2021) ‘Clumped isotope thermometry of modern and fossil snail shells from the Himalayan-Tibetan Plateau: Implications for paleoclimate and paleoelevation reconstructions’, *GSA Bulletin*, 133(7–8), pp. 1370–1380. Available at: https://doi.org/10.1130/B35784.1.

Wilf, P. (1997) ‘When are leaves good thermometers? A new case for Leaf Margin Analysis’, *Paleobiology*, 23(3), pp. 373–390. Available at: https://doi.org/10.1017/S0094837300019746.

Willmott, Cort J. and Matsuura, K. (2001) *Terrestrial Air Temperature and Precipitation: Monthly and Annual Time Series (1950 - 1999)*. Available at:

http://climate.geog.udel.edu/~climate/html_pages/README.ghcn_ts2.html (Accessed: 26 April 2022).

Wrozyna, C., Meyer, J., Dietzel, M. and Piller, W.E. (2022) 'Neotropical ostracode oxygen and carbon isotope signatures: implications for calcification conditions', *Biogeochemistry*, 159(1), pp. 103–138. Available at: https://doi.org/10.1007/s10533-022-00917-9.

Xu, H., Ai, L., Tan, L. and An, Z. (2006) 'Stable isotopes in bulk carbonates and organic matter in recent sediments of Lake Qinghai and their climatic implications', *Chemical Geology*, 235(3), pp. 262–275. Available at: https://doi.org/10.1016/j.chemgeo.2006.07.005.

Zaarur, S., Affek, H.P. and Stein, M. (2016) 'Last glacial-Holocene temperatures and hydrology of the Sea of Galilee and Hula Valley from clumped isotopes in Melanopsis shells', *Geochimica et Cosmochimica Acta*, 179, pp. 142–155. Available at: https://doi.org/10.1016/j.gca.2015.12.034.

CHAPTER 2

Rainfall or Evaporation? Controls on Great Lake Bonneville

Alexandrea J. Arnold*, John Mering*, Lauren Santi, Hung-I Lee, Jory Lerback, Victoria Petryshyn, Daniel E. Ibarra, Charles Oviatt, Juan Lora, Steve Nelson, Aradhna Tripati

*AA and JM contributed equally to this work and are listed based on alphabetical ordering.

Abstract

Lake Bonneville was the largest Pleistocene lake within Western North America, reaching a maximum surface area of roughly 50,000 km^2 during the last ice age, and eventually shrank dramatically and became what is now known as the Great Salt Lake. Multiple studies have identified precipitation as the main factor associated with the lake highstand. However, the factors associated with the size, growth, and retreat of the lake are uncertain as most proxies cannot resolve precipitation from evaporation, but yield net precipitation. Here, we use the thermodynamically-based carbonate clumped isotope thermometer to estimate past temperature, temperature-driven evaporation rates, precipitation rates, and lapse rates from 23,000 to 16,000 years ago (ka). At the maximum extent (17.5 ka), precipitation was similar to modern, but evaporation was suppressed by ~60%. Our work emphasizes the importance of temperature as a primary driver in shaping the water balance of the region, in contrast to some prior findings.

1. Introduction

During the late Pleistocene, lakes expanded throughout the Great Basin, from southern Oregon to Mexico, with highstands between 25 and 15 ka (Gilbert, 1890; Hostetler et al., 1994; Reheis et al., 2014). Lake Bonneville was the largest pluvial lake within the Great Basin during

the late Pleistocene, reaching a maximum extent of 52,110 km^2 shortly after the Last Glacial Maximum (LGM; 21 ± 2 ka) (Adams & Bills, 2016), and is on the traditional lands of the Goshute. Due to the sheer size of the ancient lake as indicated by lacustrine geomorphic features, Bonneville has been of longstanding interest, with the first publication reporting it by Gilbert (1890). Despite over a century of study, the hydrologic factors that sustained the size of the lake, or associated with the lake's growth and subsequent regression to the modern Great Salt Lake remain ambiguous.

Lake Bonneville began its transgression from a saline, ephemeral body to a large, freshwater lake around 24 ka (Oviatt & Pedone, 2024). The hydrographically closed basin filled to 1370 meters above sea level (m.a.s.l.) by ~23 ka, leaving the Stansbury shoreline (Oviatt & Pedone, 2024); by ~17.5 ka, it reached a maximum elevation of 1552 m.a.s.l with depths of over 300 meters in some locations, in a pluvial maximum termed the Bonneville highstand, when there was a short-lived outlet for the lake (Oviatt, 2015). The Bonneville flood at ~17.5 ka was a catastrophic landslide associated with the newly formed outlet that caused the loss of a large volume of water, with a 100 m lake level drop and a transition to a hydrologically-open basin, as well as the Provo shoreline (Oviatt, 2015). Lake Bonneville has continued to shrink (Hart et al., 2022) with its final remnants called the Great Salt Lake (1277 m.a.s.l).

Climate model analysis has been used to argue that synoptic-scale moisture transport was the primary factor causing the large size of Lake Bonneville, and associated lake effect precipitation (Hostetler et al., 1994). Antevs (1948) suggested winter rainfall across Western North America was enhanced during stadial intervals because the mean position of the mid-latitude jet stream was deflected south by the Laurentide Ice Sheet. An alternative hypothesis holds that the timing of lake level highstands reflect enhanced rainfall due to both the mean

position of the jet and the position of the jet during temporary excursions (Munroe & Laabs, 2013). The existence of a possible teleconnection with the North Atlantic that affected precipitation in the region could explain why montane glaciers in the Wasatch and Uinta Mountains, east of the Bonneville Basin, also retreated and advanced contemporaneously with the Laurentide Ice Sheet (Clark & Bartlein, 1995). However, recent analyses of deglacial climate simulations suggests that western North American precipitation and the mid-latitude jet are not always collocated, and that their relationship changed through the deglaciation (Lora et al., 2016).

However, not all studies identify winter storms as the most likely cause for lake highstands in the region. Lyle et al. (2012) reported that many lakes in the northern Great Basin did not achieve highstands until after the LGM, while lakes in the southern Great Basin expanded before and during the LGM, and identified the Sierra Nevada and Cascade Mountains as strong barriers that would have inhibited transport of moisture inland from the coast into the central and northern Great Basin. They argued a strengthened summer monsoon from the tropical East Pacific could have penetrated further north, providing additional moisture to advance lakes, however, they do not provide a mechanism for increased northwards monsoon activity (Lyle et al., 2012). Lora et al. (2017) demonstrate that during the LGM, North Pacific atmospheric rivers preferentially occurred southeast of their modern climatological location, in association with a weakened North Pacific High and strengthened Aleutian Low, which would likely increase winter precipitation delivered by atmospheric rivers to the southwest coast of North America. However, it is not clear whether atmospheric rivers could have been responsible for substantially increased moisture delivery to Lake Bonneville, due to orographic effects imposed by the Sierra Nevada and Cascade ranges. Additionally, although much work has focused on precipitation in

the water budgets in the Great Basin, diminished evaporative loss during cooler stadial summers has also been identified as a driver for the advance of many lake systems across the region (Ibarra et al., 2014; Kaufman, 2003; Lemons et al., 1996).

Critical for resolving the factors influencing the hydrologic budget of the lake are unambiguous proxy data. Yet most terrestrial proxies reflect net precipitation (e.g., lake level), are subject to multiple assumptions (e.g., $\delta^{18}O$ and δD-based reconstructions), and/or are sensitive to changes in species-composition (e.g., pollen). As such, the climatic conditions required to sustain large lakes in the Great Basin remain under-defined.

Here, we utilize a thermodynamically-based proxy to evaluate the paleohydrologic framework for Lake Bonneville. Clumped isotopes have been shown to provide a direct constraint on the temperature of lacustrine carbonate mineral formation, which cannot accurately be quantified using conventional oxygen isotope techniques alone (Cheng et al., 2022; Li et al., 2021; Petryshyn et al., 2015). We apply the carbonate clumped isotope proxy to lacustrine archives and reconstruct lake surface temperatures, which then are used to calculate annual air temperature, evaporation, and precipitation rates, and determine controls on lake water balance.

2. Methods

2.1 Sample collection

Field sample collection was carried out at sites within the Bonneville Basin and Sevier Subbasin in October 2012 (Fig. 2.1; Table 2.1 and 2.2). Gastropods were collected from sand and gravel strata that correspond with littoral conditions. Based on sequence stratigraphic interpretations, the localities sampled record the initial transgression of the lake to a given shorezone. Lacustrine marl was collected from above the sandy gastropod-bearing beds. Samples

of lacustrine tufa representing the Stansbury, Bonneville, and Provo shore zones were selected from the collection of Steve Nelson at Brigham Young University. These samples are from sites at the Pilot Valley Subbasin at the west end of the lake (Fig. 2.1). Oxygen and carbon stable isotope values were previously reported for these samples (Nelson et al., 2005), but clumped isotope abundances were not measured. Tufa samples varied in texture. Some materials were porous and contained micrite and spar, while others were dense and lacked void spaces.

2.2 Sample preparation

Aragonitic gastropod shells were separated by taxa. Shells were broken into pieces, sonicated in Milli-Q deionized water until clean, dried overnight at 50°C, and powdered using a mortar and pestle. For a given study site, 4-10 individual gastropod shells were analyzed 1-4 times each, depending on sample limitations. Replicate analyses of individual shells served to test the reproducibility of isotope results. Individual gastropod shells represent short time scales, thus analyses of multiple shells at a given site allowed for compilation of a statistically significant climatic signal.

2-6 individual blocks of marl were selected for clumped isotope analysis at each sampling site in order to ensure that reconstructed water temperatures encompassed the broadest interval of lake history. Sample blocks were disaggregated in Milli-Q water and poured through a 212 μm steel mesh filter to exclude particles coarser than fine sand (e.g. detrital clasts, charcoal, root, and biogenic shell fragments). Following sieving at 212 μm, the resultant slurry was allowed to settle for 5-10 minutes. The residue coming out of suspension was isolated by pouring the slurry into a second beaker. This process was repeated until virtually no settling occurred. The final suspension was treated with dilute hydrogen peroxide (1.5-3%) for 20-60

minutes to remove residual organic material (Eagle, Risi, et al., 2013). Carbonate was collected on 0.45 μm cellulose nitrate filter membranes and dried overnight at 50° C.

Tufas and cements were cut perpendicular to laminae. Areas containing spar, or evidence of regrowth, were selected against. Powders were extracted by crushing rock chips to fine sand grain size, following methodology in Nelson et al. (2005). Powdered tufa samples were reacted in 3% H_2O_2 for 60 minutes to remove organic materials. Following peroxide treatment, samples were rinsed in Milli-Q deionized water and dried for 12 hours at 50°C. Cleaned powders were weighed out in 5 to 15 mg increments, depending on carbonate content and instrument sensitivity at the time of analysis.

2.3 Analytical procedure for stable and clumped Isotopes

Samples were reacted for 20 minutes on a 90°C common phosphoric acid bath system in the Tripati Lab at UCLA. For samples containing greater than 90% carbonate (i.e. gastropod shell), sufficient CO_2 gas was obtained from acid digestion of 5-10 mg of material. In the case of samples with lower carbonate content (e.g. carbonate muds), 10-50 mg samples were reacted to generate sufficient CO_2 gas. Samples were run for at least three replicates, unless there was insufficient material for analysis. The acid bath was maintained at constant temperature through use of a cylindrical heating block with a thermocouple feedback system. The temperature of the acid bath was physically measured with a glass thermometer daily and found to be at 90°C. CO_2 was cryogenically purified using an automated vacuum line that was modeled on a system at the California Institute of Technology (Passey et al., 2010). Organic compounds were removed with a Porapak column installed on a Thermo Trace GC Ultra gas chromatograph. $\delta^{13}C$, $\delta^{18}O$, Δ_{47}, and Δ_{48} were determined using a Thermo 253 Gas Source isotope ratio mass spectrometer.

During 2013 and the first half of 2014, samples were run for 8 acquisition cycles consisting of 10 measurements of sample and reference gas. During the latter half of 2014 and onwards, samples were run for 9 acquisition cycles consisting of 10 measurements of sample and reference gas. During each acquisition, sample gas voltages were compared to high purity Oztech brand CO_2 reference gas ($\delta^{18}O$ = 25.03‰ V-SMOW, $\delta^{13}C$ = -3.60‰ V-PDB). CO_2 gas standards, and carbonate standards of known isotopic compositions, were run every 4-5 analyses.

Data was processed using the Easotope software using the Brand parameter set (Brand et al., 2010; John & Bowen, 2016). Results were normalized following the Absolute Reference Frame correction and standardization process (Dennis et al., 2011). Signal interference due to electron backscattering in the source of the mass spectrometer was quantified and corrected for using equilibrated gases with two different bulk isotopic signatures at two different temperatures (25 and 1000°C) and ETH-1 and ETH-2 from the ETH suite of standards (Bernasconi et al., 2021). Aliquots of gas were cryogenically purified on a manual vacuum line system and collected in borosilicate breakseal tubes. Changes in slope of δ_{47} vs. Δ_{47} were attributed to shifting conditions in the source of the mass spectrometer, and occasionally to the presence of organic contaminants. Samples were strictly run during periods of time in which the calculated slopes of regressions, relating δ_{47} vs. Δ_{47}, did not change. ETH-1 to ETH-3 along with internal standards were used to create an empirical transfer function to convert values to the carbon dioxide equilibrium scale to calculate the final Δ_{47} value. Δ_{47} values for sample and standard runs are presented in Table 2.A.1.

2.4 Elevation and age control

Sample altitude was corrected for using the following relationship (Oviatt et al., 1992),

where Z_a is the rebound-free adjusted altitude, Z_r is the modern mapped altitude of the sample, Z_b is the local altitude of the Bonneville shoreline, and 1552 and 1200 are the average unrebounded altitude of Bonneville shoreline and basin floor altitude at the beginning of the Bonneville lake cycle, respectively and all elevations are in meters:

$$Z_a = Z_r - [\frac{(Z_r - 1200)}{(Z_b - 1200)}] \times [Z_b - 1552]$$

The paleoshoreline age for a sample was determined by interpolation along the lake hydrograph of Oviatt and Pedone (2024) (Fig. 2.2E) using the rebound-adjusted altitude. The Bonneville hydrograph represents a compilation of radiocarbon dates from lacustrine carbonates, charcoal, wood, and bone from shore zones.

2.5 Δ_{47}-temperature dependence

The clumped isotope value (Δ_{47}) can be related to the temperature of ambient waters at the time of mineralization, where lower temperatures are associated with a greater abundance of ^{13}C-^{18}O bonds (Csank et al., 2011; Eagle, Eiler, et al., 2013; Ghosh et al., 2006; Schauble et al., 2006; Tripati et al., 2010, 2014). Clumped isotope measurements (Δ_{47}) were converted to water temperatures using the material-specific calibrations of Arnold et al. (2023) with the following equations used for each type of carbonate:

$$\Delta_{47}\,(gastropods) = (0.0371 \pm 0.004) \times 10^6/T^2 + (0.174 \pm 0.051)$$

$$\Delta_{47}\,(tufas) = (0.0345 \pm 0.007) \times 10^6/T^2 + (0.216 \pm 0.080)$$

$$\Delta_{47}\,(marls) = (0.0462 \pm 0.007) \times 10^6/T^2 + (0.084 \pm 0.089)$$

2.6 Calculation of water $\delta^{18}O$

The relationship between mineralization temperature (provided by clumped isotope analysis), $\delta^{18}O_{water}$, values were calculated using estimations of mineralization temperatures and $\delta^{18}O_{carbonate}$ values from clumped isotope analysis, in concert with using mineral specific fractionation values calcite (Kim & O'Neil, 1997) and aragonite (Kim et al., 2007). In order to account for digestion in a common acid bath, a fractionation factor of 1.007954 for calcite and 1.00854 for aragonite was applied, following Swart et al. (1991) and Kim et al. (2007), respectively. Reconstructions in this work were reported with an ice-volume correction applied to account for enrichment of ^{18}O in the glacial ocean during the LGM (Tripati et al., 2014).

2.7 Mean annual air temperature

Evaluation of seasonal relationships between air and water temperature in modern lakes indicate that lake surface temperature will closely match air temperature (Hren & Sheldon, 2012; Terrazas et al., 2023). In order to reconstruct air temperature at study sites, transfer functions using Model 4 in Terrazas et al. (2023) were applied to relate water surface temperature, latitude, and elevation to mean annual air temperature, assuming a seasonal dependence of carbonate formation. Gastropod shells were assigned April-June transfer functions due to primary shell formation occurring in unison with peak photosynthetic activity in the mid-to-high latitudes (Versteegh et al., 2010). Calcification of tufa is dependent on photosynthetic activity, wave action, and evaporation, thus, was assigned a larger growth season (April-October) for our analyses (Felton et al., 2006; Nelson et al., 2005). Due to the temperature dependence of evaporation promoting carbonate saturation state within the lake, marls in this study were assigned a June-August transfer function to represent the warmest interval of the year (Hren &

Sheldon, 2012). Site-specific modern mean annual air temperatures used to calculate anomalies are in Table 2.A.3.

2.8 Evaporation modeling

We reconstructed estimates of annual evaporation (E_L) using the modified Penman equation from Linacre (1993) (Linacre, 1993). This method has inputs of mean annual air temperature (T), elevation (z), latitude (L), wind speed (u), and dew point temperature (T_d).

$$E_L = [0.015 + 4 \times 10^{-4} T + 10^{-6} z] \times [\frac{480(T + 0.006z)}{(84 - L)} - 40 + 2.3u(T - Td)]$$

Mean annual air temperature was calculated using clumped isotope estimates of water temperature applied to transfer functions in Hren and Sheldon (2012). Dewpoint (T_d) temperature and wind speed (u) was estimated by using modern reanalysis data over the modern Bonneville basin and assumed to be similar to modern during the LGM. T_d values for the LGM were assumed to change by magnitudes equal to shifts in air temperature from present (Ibarra et al., 2014; Jones et al., 2007). Average pan evaporation rates (1443 mm/yr) were calculated using 13 modern sites in the Bonneville basin (Table 2.A.2; Desert Research Institute, 2021). Average modern lake evaporation rates were estimated using a pan coefficient of 0.7 from Linacre et al. (1994) (Linacre, 1994).

2.9 Precipitation modeling

Estimates of precipitation were constrained using the modeling framework described within Santi et al. (2020). This method combines $\delta^{18}O$ isotope mass balance, time-varying water

balance, and basin hypsometry to create a function to estimate annual precipitation rates:

$$P = \frac{E_L}{\left(1 + \frac{K_{run}}{HI}\right)} \times \frac{(\delta^{18}O_E - \delta^{18}O_L)}{(\delta^{18}O_W - \delta^{18}O_L)}$$

Evaporation (E_L) is estimated using the equation in the prior section. Runoff coefficient (k_{run}) is estimated using the ω values from nearby basins determined in Greve et al., 2015. Basin hypsometry is included through the hydrologic index (HI), which is the ratio of lake area to tributary area. The oxygen isotopic composition of the lake ($\delta^{18}O_L$) was determined using clumped isotope derived estimates of temperature and measured oxygen composition of the carbonate. The evaporating water vapor ($\delta^{18}O_E$) is estimated using the evaporation model from Craig and Gordon (1965)(Craig & Gordon, 1965). The average composition of the incoming meteoric water ($\delta^{18}O_W$) was estimated using modern values for all sample sites (Table 2.A.3; -13.3 ± 1.3‰ VSMOW) and is interpolated to pre-rebound elevations and corrected for LGM ^{18}O enrichment (Bowen, 2023; Bowen & Revenaugh, 2003; Tripati et al., 2014). We utilize a monte carlo simulation with 2500 iterations to estimate hydroclimatic variables, with all variables sampled from a normal distribution using the mean and standard deviation for each variable. Factor change in precipitation rates are calculated using the basin-average 30-year normal modern value of 344 mm/yr (PRISM Climate Group, 2024)

2.10 Evapotranspiration and weighted evaporation modeling

To allow our results to be comparable with land-surface evapotranspiration rates from climate model output, we calculate evapotranspiration (ET) using precipitation (P) and the runoff coefficient (k_{run}) derived in our hydroclimate modeling using the following equation:

$$ET = P \times (1 - k_{run})$$

We calculate a weighted evaporation (*WE*) rate to scale lake evaporation (E_l) occurring over the lake area (A_l), and evapotranspiration occurring in the tributary area (A_t) using the following equation:

$$WE = \frac{(P - K_{run} \times A_t) + E_l \times A_l}{A_t + A_l}$$

2.11 Partitioning thermodynamic and dynamical controls on lake level

To partition the thermodynamic and dynamic influences on lake levels, we utilize weighted evaporation ($E_{weighted}$) and precipitation (P) estimates from this study, along with modern precipitation (P_{modern}) measurements. To estimate thermodynamic control on lake level, we assume that thermodynamic contributions are governed by changes in temperature causing changes in evaporation. Thus, we derive the thermodynamic contribution by compare the anomalies for weighted evaporation to the total anomaly (WE and P anomalies) in the following equation, using an assumption of steady state for modern weighted evaporation rates ($E_{weighted, modern} = P_{modern}$):

$$Thermodynamic\ Component\ (\%) = 100 \times \frac{(e_{weighted} - P_{modern})}{(e_{weighted} - P_{modern}) + (P - P_{modern})}$$

For the dynamic component, we assume that changes in precipitation are delivered by dynamic mechanisms. The dynamic contribution compares the precipitation anomaly to the total anomaly in the following equation:

$$Dynamic\ Component\ (\%) = 100\ \times \frac{(P - P_{modern})}{(e_{weighted} - P_{modern}) + (P - P_{modern})}$$

We do not report values for samples with a negative thermodynamic component (n=2), which occurs when samples have high formation temperatures.

2.12 Climate model evaluation

PMIP models were compared to gridded modern climate data extracted from the PRISM dataset, which has 800 m cell resolution, and 30-year climate averages downloaded from the NCDC. Approximately 0.9°C of temperature discrepancy between modern climate and PMIP controls can be attributed to anthropogenic emissions since the industrial revolution (IPCC, 2013). Because the boundary conditions are not well matched in the Bonneville Basin, the most suitable method for evaluation of clumped isotope temperature data against the PMIP archive is through comparison of differences between late Pleistocene and modern states.

We compare the results derived in this study to climate model output from the Paleoclimate Modeling Intercomparison Project (PMIP) phase 3 models. We utilize near-surface air temperature (*tas*), precipitation (*pr*), and evapotranspiration (*evspbl*) climatological monthly means to compare to our data. Temperature and precipitation anomalies were compared to results from PMIP3 models and the ensemble mean, and evaluated using was computed using the skill score metric (Hargreaves et al., 2013; Lora & Ibarra, 2019), where m_i is the results from the model, n_i is the reference state (assumed to be zero, or no change between the LGM and present), and o_i and e_i are the observations and their respective errors (derived from clumped isotope analysis):

$$SS = 1 - \sqrt{\frac{\sum(m_i - o_i)^2 - \sum(e_i)^2}{\sum(n_i - o_i)^2 - \sum(e_i)^2}}$$

3. Results and discussion

3.1 Stable and clumped isotope analysis of shoreline sediments

Samples of 36 individual gastropod shells from six sites, representing two species (*Pyrgulopsis bonnevillensis* and *Stagnicola bonnevillensis*), two marl samples, and eleven tufa samples spanning the Stansbury, Bonneville, and Provo shorelines (Figure 2.1) were analyzed for $\delta^{13}C$, $\delta^{18}O$, and clumped isotope composition, Δ_{47} (see Methods). Table 2.1 contains all geochemical data for the sample set. Δ_{47}-derived water temperatures were used in concert with a transfer function to construct mean annual air temperature (MAAT) estimates and used within a hydrologic modeling framework to calculate precipitation and evaporation rates (see Methods). Oxygen isotopic composition of lake water ($\delta^{18}O_{water}$) was calculated using temperatures derived from Δ_{47} analysis, measured carbonate $\delta^{18}O$, and a mineralogy dependent equilibrium temperature. All $\delta^{18}O_{water}$ values are reported relative to the V-SMOW standard, and water isotope reconstructions in this work are reported with a correction applied to account for enrichment of ^{18}O in the glacial ocean during the LGM (Tripati et al., 2014). We utilize results of hydroclimatic change at Lake Bonneville to partition the thermodynamic and dynamic contributions to lake level changes (see Methods) and compare to climate model output.

3.2 Mean annual air temperature at Lake Bonneville

Figure 2.2A shows the evolution of Δ_{47}-T at Lake Bonneville. Cooling was associated with the growth of Lake Bonneville ~23.4 to 22.8 ka (i.e., the transgressive phase of the Stansbury Oscillation). Tufa estimates of the MAAT anomaly associated the Stansbury highstand are 9.4 ± 1.6°C, in agreement with gastropod Δ_{47}-T (7.8 ± 0.5 °C and 9.2 ± 1.3 °C below modern

for the Bonneville basin and Sevier subbasin, respectively). Two slightly younger marl samples in the Bonneville basin show similar decreases in temperature (8.5 and 9.7°C). Cooling continues through ~18.4 to 17.4 ka (the Lateglacial Bonneville highstand) with ~4.0°C warming from ~17.4 to 16.2 ka (the Provo highstand). Mean annual air temperatures were consistently depressed across much of the Bonneville lake cycle, both before, during the closed-basin and post-LGM open basin phases of the lake (Fig. 2.2A; Table 2.2).

These Δ_{47}-T reconstructions estimate slightly more cooling than vegetation-based proxies (6-7°C; Madsen et al., 2001) and packrat midden macrofossil reconstructions (6.2°C; Harbert & Nixon, 2018). Amino acid racemization indicates a decrease of 10°C (Kaufman, 2003).

3.3 Climate parameter reconstructions

While prior work has indicated that evaporation rates were reduced due to temperature depression during the LGM and deglacial, and that highstands during the LGM and Heinrich Stadial 1 were associated with increased effective precipitation, our results allow us to confidently quantify changes in temperature, precipitation, and evaporation rates, and separate out controls on effective precipitation. Table 2.2 contains Δ_{47}-derived values for hydroclimatic variables for each site we examined at Lake Bonneville. For comparison, modern evaporation rates are 1434 and precipitation rates are ~344 mm/yr (Desert Research Institute, 2021; PRISM Climate Group, 2024). Clumped isotope results suggest that evaporation rates were consistently reduced to at least half of modern values, were the dominant factor driving Lake Bonneville's growth and regional lake and glacial maxima, and that there were two temporal precipitation maxima of ~1.6-2x modern at ~23-22 ka and ~1.5x at 16 ka.

Stansbury shorezone tufa (~23 ka) indicates early LGM precipitation rates were similar to

modern (9% decrease relative to modern), while lake evaporation rates were substantially (~37%) lower than modern (Figure 2.2B and 2.2C). This suggests that, at least initially, decreased temperatures that suppressed evaporation, instead of large increases in precipitation, were the dominant factor that led to Lake Bonneville's growth. During the subsequent LGM transgression from ~23-22 ka of ~150 m over ~1.7 ka (Oviatt and Pedone, 2024), gastropod-derived values support almost a doubling of precipitation values to modern (~92-107% increase relative to modern) while evaporation rates remained consistent, at 30-37% lower than modern (Figure 2.2E). Thus, increased evaporative suppression was a factor contributing to lake growth, while coupled increases in precipitation contributed to large lake area increases during the LGM. Estimates from slightly younger marls from the same site suggest a slightly higher degree of evaporation suppression (37% lower than modern), and a less extensive increase in precipitation rates (61% increase relative to modern); we note that gastropods may reflect shorter-term changes in precipitation in comparison to tufa and marls, which integrate over the longer time intervals during which they form. Thus, we suggest increases in precipitation were integral to lake growth in the early-LGM.

Results for tufas formed along the Bonneville shoreline (~17.5 ka) do not support enhanced moisture transport and delivery into the watershed during this time, with the highest lake levels coinciding with Δ_{47}-derived precipitation estimates near modern (~2% less) and maximum evaporation suppression (56% less than modern lake evaporation). Thus, short-lived increases in precipitation coupled with a temperature-driven reduction in evaporation was critical for the dramatic growth of Lake Bonneville during its transgression.

During the LGM, when our Δ_{47}-estimates of temperature indicate that Lake Bonneville evaporation rates were reduced by 37-56%, other lakes in the Great Basin are hypothesized to

have experienced reduced evaporation rates due to temperature depression (Hostetler & Benson, 1990; Ibarra et al., 2014; Kaufman, 2003; Lemons et al., 1996; Quirk et al., 2020; Santi et al., 2020). Regional glacial maxima are ~19.8 ka, based on a synthesis of glacial modeling in nine mountain ranges (Walter, 2022), and can be reconciled with a large temperature depression of ~10°C (Quirk et al., 2020; Walter, 2022), similar to our results. Our LGM-age Bonneville shoreline tufas indicate ~10.7°C magnitude of temperature depression, and dry conditions throughout the lake highstand (Fig. 2.2A; 2.2C; 2.2G). Cold and dry conditions during this interval would allow for glacial accumulation and a gradual transgression of lake elevation due to temperature suppression (Fig. 2.2E). During the regressive phase of the lake around 16 ka as recorded by the Provo tufa, although there is evidence for increased precipitation (47% greater than modern), increasing lake evaporation rates (80% of modern values) were critical for setting the water balance. Thus, our results indicate that reduced evaporation was critical for the large size of the lake, but that a short-lived wetter state persisted during the early LGM and following the highstand.

3.4 Temporal evolution of $\delta^{18}O_{water}$

Figure 2.2D shows the temporal evolution of lake water oxygen isotopic composition of Lake Bonneville. Throughout our study interval, Lake Bonneville exhibited ~3.1‰ of variability. Average $\delta^{18}O_{water}$ values for Stansbury-aged tufa (~23 ka) are -4.9 ± 0.3‰. Average $\delta^{18}O_{water}$ estimates decrease during the Stansbury Oscillation (~23-22 ka) for Bonneville basin gastropods and marls (-7.3 ± 0.6‰ and -7.2 ± 0.6‰, respectively) and the Sevier Subbasin gastropods (-7.9 ± 0.4‰). $\delta^{18}O_{water}$ increases towards the Bonneville Highstand (~17.5 ka), with estimates from a suite of tufas resulting in a composition of -5.4 ± 0.5‰, and remains similar

throughout the Provo highstand (~16 ka; -5.3 ± 0.3‰).

We observe the largest change in $\delta^{18}O_{water}$ between the Stansbury highstand and gastropod and marl samples from the lake's transgression following the Stansbury Oscillation (between 23-22 ka). During the Stansbury highstand (~23 ka), the lake was shallow (1380 m.a.s.l.) but the extent of the lake was still widespread (24,086 km^2; Nelson et al., 2005), which may have led evaporative enrichment to play a larger role due to regional geomorphic constraints in Pilot Valley, where the tufa samples were collected, and elsewhere throughout the basin ((Nelson & Rey, 2018; Fig. 2.1). Elevated $\delta^{18}O_{water}$ estimates derived for tufas relative to marl and gastropods samples are likely to have increased interaction with waters impacted by evaporation and atmospheric exchange (Figure 2.2A, (Nelson et al., 2005). In the early LGM, we reconstruct a coeval reduction in $\delta^{18}O_{water}$ without significant changes in Δ_{47}-MAAT, suggestive of dynamical changes being the primary driver of precipitation delivery into the basin (Figure 2D).

Figure 2.2A also shows a comparison of our new, shallow water record relative to a record derived from deep water carbonate deposits formed in Craners and Cathedral Caves in the Bonneville basin (McGee et al., 2012). Tufas from our record are comparatively enriched relative to the cave record, while gastropod and marl samples are lower than $\delta^{18}O_{water}$ values estimated in cave deposits. Results from early-LGM tufas compared to gastropods and marls during the transgressive phase of the lake estimate similar MAAT's, but show decreases in reconstructed $\delta^{18}O_{water}$ values, which could be interpreted as increases in precipitation or runoff rates, or changes in dominant moisture source, with moisture from the North Pacific Storm track being more depleted (Welker, 2012). A first-order calculation also supports the interpretation that dynamics are the dominant control on lake water balance (82-93%) (Figure 2.2F).

The deep-water carbonate deposits, which are subject to more consistent conditions, show an increase in $\delta^{18}O_{water}$ during the transition from open to closed basin between the Bonneville to the Provo phase. In contrast, our estimates of $\delta^{18}O_{water}$ derived from the Bonneville and Provo tufas remain consistent throughout the two intervals. The increase observed in deep-water carbonates during the Provo stage (~16 ka) may suggest that lake regression following the Bonneville flood and subsequent shallowing during this time could have promoted mixing from depth. The creation of an outlet at the northern margin on the lake following the Bonneville highstand would have decreased the residence time of water in the lake, however, since the area of outflow is restricted relative to the size of the basin, precipitation and evaporation are expected to still have a large effect on $\delta^{18}O_{water}$.

3.5 Regional rainfall changes

The first major precipitation forcing that we observe at Lake Bonneville occurs between 23-22 ka, as constrained by our results from gastropods and marls, is shown in comparison to other estimates of precipitation and temperature changes from other basins (Figure 2.2G). At this time, we find evidence for an increase in precipitation by a factor of 1.6 - 2.1 relative to modern, concurrent with a projected ~120 meter increase in lake level elevation using the updated hydrograph of the transgressive phase of Lake Bonneville (Oviatt & Pedone, 2024; Figure 2.2E, 2.2G). First-order calculations estimate a low thermodynamic contribution to lake level changes (9-24%) despite having large MAAT anomalies (7.8 - 9.2°C lower than modern) and a decrease in $\delta^{18}O_{water}$ values, as precipitation delivery mechanisms dominate as a driver of lake transgressions at this time. The second large precipitation forcing observed in Great Basin Lakes spans from roughly 17 to 14.5 ka (Fig. 2.2G), concurrent with Heinrich Stadial 1 (HS1: ~18-14.7

ka). During HS1, a majority of lakes in the northern Great Basin reached their highstand elevations trending from the southwest-northeast (Lyle et al., 2012; Munroe & Laabs, 2013; Santi et al., 2019) and temperatures were broadly warmer than during the LGM (Fig. 2.2G). Our results indicate a wetter state for the Provo phase of the lake at ~16 ka, with precipitation forcing of 1.5 times modern values, coincident with hypothesized post-LGM precipitation maxima for other lakes in the Great Basin derived using modeling, including Lake Bonneville (Belanger et al., 2022) although our results are ~40% larger; Jakes Lake (16.8 ka highstand; Barth et al., 2016; García & Stokes, 2006), Lake Surprise (15.2 ka highstand; Ibarra et al., 2014 and Santi et al., 2020) and Lake Lahontan (15.5 ka highstand; Benson et al., 2013; Hostetler & Benson, 1990) and from glacial modeling (Quirk et al., 2018, 2020).

3.6 Temperature and rainfall lapse rates

Here we derive LGM and deglacial lapse rates for temperature and precipitation and compare results to modern values to examine their response to past climate change. We calculate lapse rates using our results for tufa samples, which form over longer timescales and are likely to represent steady state conditions. Figure 2.3 compares Δ_{47}-temperature estimates to estimates of equilibrium line altitude (ELA) for a compilation of nearby mountain ranges in the Great Basin (Walter, 2022). Changes in the glacier ELA are most sensitive to changes in the warmest month, thus, we assume the same offset between modern MAAT and average July air temperature (15.2°C; Hren & Sheldon, 2012) to estimate LGM July average temperature. We derive a July temperature-elevation relationship for tufa samples.

The temperature lapse rates are steeper than the modern gradient (Belanger et al., 2022). The Δ_{47}-derived temperature lapse rates broadly intersect with the lower end of the range of

Great Basin ELAs, and are most similar to ELA estimates from glaciers on the Eastern margin, with the exception of the Uinta mountains, which has a higher ELA but is further away from the lake margin compared to other Eastern ranges in the Walter (2022) study. Estimates of precipitation from this study exceed modern average estimates of precipitation change with altitude and show a steeper relationship, suggesting increased precipitation delivery to lower altitudes and decreases in precipitation relative to modern at higher altitudes.

3.7 Model evaluation

We compare our Δ_{47}-results to long-term mean climatological data output from the Paleoclimate Modeling Intercomparison Project phase 3 (PMIP3) models to assess process representation in climate models during the LGM. In order to quantitatively gauge model performance using paleoclimate proxies from the LGM interval, we use skill score (SS) as a metric to assess whether or not these hindcasts are reflecting hydrologic variables accurately. Results should be interpreted as a model's skill in depicting past climatic changes with respect to the null hypothesis, of no change between the LGM and modern. A perfect simulation would have a score of 1, a score of 0 would indicate that the model and reference state (no change) perform equally well, and a negative score would indicate that model error is greater than in the case of the null hypothesis. A skill score that is undefined occurs when the model agrees with the data more closely than the errors in the data indicate should be possible, which may be a sign of overestimation in proxy error (Hargreaves et al., 2013; Lora & Ibarra, 2019). We compare results from tufa that formed over the course of the Bonneville highstand (~18 ka), along with gastropod samples in the larger Bonneville basin, further North, and the smaller, Sevier subbasin, further South. All models exhibit reasonable agreement showing a depression in temperature during the

LGM, with positive skill score values ranging from 0.52-0.91 for all models and 0.71 for the ensemble mean (Figure 2.4; Table 2.3). The models with the highest skill score are those that simulate a larger extent of cooling in the Bonneville and Sevier basins. However, most models perform more poorly with respect to evapotranspiration anomaly and precipitation forcing. Four models estimate skill scores ranging from -0.42 to -0.87 with respect to evapotranspiration anomaly, with five models having undefined skill scores (Table 2.3). The negative skill scores indicate the models fail to capture the magnitude of evaporation suppression estimated from this study. Overall, MPI-ESM-P exhibits the highest skill scores with respect to all of our proxy reconstructed hydroclimate variables and performs best with respect to our proxy reconstructions. Models underestimate the Δ_{47}-reconstructed precipitation forcing, with model skill scores for precipitation anomaly ranging from -0.93 to 0.58, with an ensemble mean of -0.14. The Δ_{47}-estimates of precipitation rates indicate a ~51 mm/yr increase in precipitation further south, in the Sevier subbasin, relative to the Bonneville basin; this increase is also observed in seven out of the nine models (Table 3). We note that model skill for precipitation and evaporation may be influenced by the lack of pluvial lakes in the LGM simulations, which can substantially modify regional climate.

3.8 Paleoclimatic lake-atmosphere interactions

We hypothesize that lake-effect precipitation feedbacks may have been an important mechanism for amplifying the precipitation maxima during the early LGM and HS1. Today, lake-effect precipitation accounts for up to 8% of regional precipitation and contributes to hydroclimate directly through precipitation over the lake and indirectly through snowpack that leads to runoff into the lake (Alcott & Steenburgh, 2013; Yeager et al., 2013). In the modern

Great Salt Lake, a minimum of 6°C temperature gradient between lake and land is needed prompt the development of a land-breeze circulation, causing air to move from the shorelines towards the center of the lake, creating low level convergence and promoting moisture uptake from the lake (Steenburgh et al., 2000). This land-water temperature gradient is commonly exceeded in modern winter months, with peaks in lake-effect precipitation between October and November, and then again from March to April (Yeager et al., 2013). In addition to the thermally-driven convergence, the complex regional terrain that surrounds the Great Salt Lake causes large-scale orographically forced convergence in the valleys, in turn funneling cold and dry air from the northwest that descends and warms, further enhancing precipitation in the downwind mountain ranges (Alcott & Steenburgh, 2013).

At its maximum extent, Lake Bonneville was comparable in size and depth to a modern Laurentian Great Lake, but was roughly ten times greater in surface area and depth compared to the modern Great Salt Lake, which might have sustained more intense lake effect precipitation. In the past and present, lake water temperatures warm over the course of the spring and summer months, but the differences in heat capacity between water and air would allow lake temperatures to cool at a slower rate than the atmosphere above it, driving thermal convergence. Deeper lakes have been shown to influence the coverage and extent of lake ice since a larger body of water typically takes longer to cool, allowing for increased lake-air interactions (Brown & Duguay, 2010; Woolway et al., 2020)**.** Further, the increased lake surface area may increase the fetch of the lake, which has been shown to inhibit or delay ice formation (Magee & Wu, 2017; Woolway et al., 2020).

As Lake Bonneville transgressed and lake area increased, air-water interactions over a larger surface area paired with the surrounding topography may have sustained an increased

lake-effect, where the thermal contrast between lake and land would promote moisture uptake and subsequent rainout due to orographic forcing (Hostetler et al., 1994). The lake-to-land temperature gradient would be greatest during the autumn months, due to the depth and extent of the lake inhibiting complete ice coverage, allowing thermal lake-atmosphere interactions to develop and enhancing lake effect precipitation.

Deposition of spits in Lake Bonneville suggest that winds had predominantly northeasterly or northwesterly flow in the LGM and deglaciation (Jewell, 2007), which is the direction of flow needed for the formation of modern LEP in the Bonneville Basin. Northwesterly winds would bring in cold, dry air from the ice sheet boundary into the Bonneville basin as the westerly storm track was diverted south, which could potentially influence moisture uptake and increase the frequency of orographically-induced lake effect precipitation in Lake Bonneville.

Early-LGM gastropod and marl samples from the Bonneville transgression show rapid increases in lake elevation paired with increases in effective moisture, with increased effective moisture observed in the southern Sevier subbasin (Fig. 2.A.2; defined as the difference between precipitation and evaporation). Unlike what is observed at Lake Bonneville, hydrographs from nearby Lake Franklin or Lake Lahontan, the second-largest late Pleistocene lake in the Great Basin, do not reflect large lake elevation/area increases during this time (Adams et al., 2008; Benson et al., 2013; Munroe & Laabs, 2013; Santi et al., 2019), thus, this precipitation forcing may have been observed only locally. Meteorological conditions conducive to lake effect precipitation during this interval may have allowed moisture generated from the lake to have fallen back as direct runoff or delayed snowmelt the following spring. The contrast between the enhanced precipitation forcing observed within this study during the transgression of Lake

Bonneville and smaller lakes within the area suggests that localized feedback may have been influential in Bonneville's initial ascent (Fig 2.2G).

A modeling study by Hostetler & Giorgi (1992) estimated that 32% of evaporation leaving Lake Bonneville was returned directly to the basin by precipitation at its maximum extent. However, results presented in this study do not find evidence for increased precipitation during the lake highstand, despite having the largest surface area during that time. We estimate 3-4°C of cooling between samples within the transgressive phase of the lake and samples from the highstand, which may have inhibited the temperature gradient necessary to prompt lake-enhanced precipitation. Additionally, as the deglaciation initiated, the meteorological conditions may have been unfavorable for increases in precipitation within the basin. Overall, our results suggest that reductions in evaporation rates were the dominant factor in reaching the lake highstand at 17.9 ka, not lake effect precipitation.

Synchronicity in lake highstands and evidence of regional deglaciation regionally demonstrates that the large-scale climate patterns were dominant in influencing hydroclimate at Lake Bonneville during the Provo phase of the lake (McGee et al., 2018; Quirk et al., 2020; Santi et al., 2019). Following the Bonneville flood after it reached the highstand elevation, lake levels rapidly dropped roughly 100 meters to form the Provo shoreline, and ice sheet and glacier retreat occurred simultaneously with lake spillover (Quirk et al., 2020). Dating of glacial moraines in the Uinta Mountains showed that peak altitude for glaciers were reached after the Bonneville highstand, demonstrating the importance of local moisture during this interval (Munroe et al., 2006). As Bonneville rapidly decreased in area, the magnitude of moisture transport from the lake effect would be hindered.

3.9 Water balance implications

In summary, clumped isotopes allow us to not only estimate temperatures but quantify the impacts of temperatures on evaporation, and show their integral role in the growth of Lake Bonneville, during the LGM and subsequent deglaciation. Our findings show that reconstructed evaporation rates decreased as lake levels at Lake Bonneville transgressed. We also quantify precipitation rates and show there were two intervals with higher than modern precipitation. During the interval, in the early LGM, moisture generated by Lake Bonneville may have been an integral contributor to the regional hydrologic budget. Prior to lake highstand, temperature and evaporation suppression paired with thermally and orographically-driven lake-effect precipitation may have been enough to allow the rapid transgression of Bonneville between 23 - 22 ka. Our results here suggest that reduced evaporation, combined with modest increases in regional precipitation, contributed to the initial growth of Lake Bonneville during this significant climatic interval. During HS1, there was both a localized response and a larger-scale regional response. We note that future work could expand this approach to look at other large lakes, and could address uncertainties in groundwater input and outflow from the lake. Areas with complex terrain near large lakes similar to Lake Bonneville (e.g. Lake Lahontan in the Great Basin or Lake Tauca in the Altiplano) may also be sensitive to lake effect precipitation effects and the influence of lake effect precipitation should be considered within palaeohydrological reconstructions.

Our results highlight the importance of temperature as a direct driver of lakes, and the role of water recycling within basins, for understanding past and future hydrologic cycle responses to changing climate forcing, especially lakes with large surface areas in mid-to-high latitude settings. Accurate simulations of how much evaporation and precipitation rates will

change as climate warms in the future is critical for forecasting the extent of lakes as a key water resource.

4. Figures

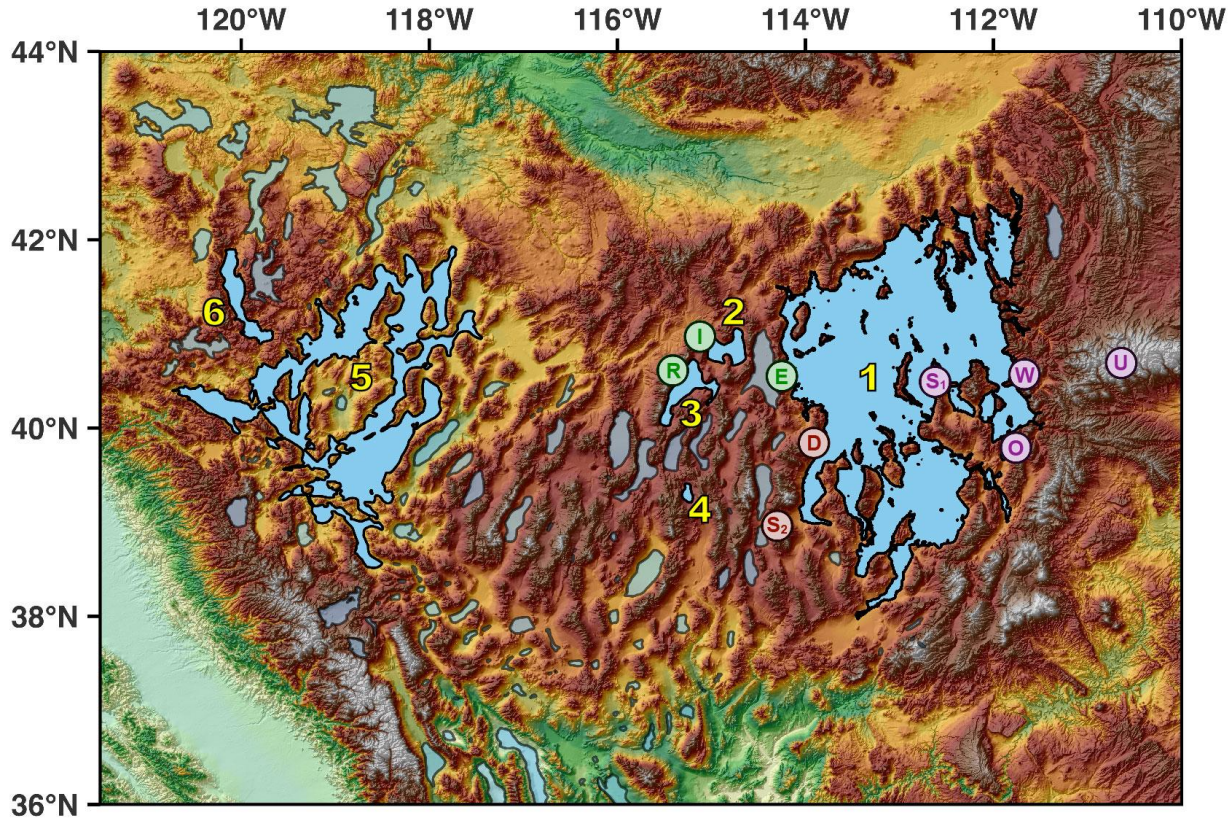

Figure 2.1: Location of Lake Bonneville and other pluvial lakes in the Great Basin at their highstands during the Pleistocene. Lakes referred to in this paper are in blue with yellow numbers (1 - Lake Bonneville, 2 - Lake Clover, 3 - Lake Franklin, 4 - Jakes Lake, 5 - Lake Lahontan, 6 - Lake Surprise). Additional pluvial lakes in the region are shown with transparent blue shading. Colored circles indicate LGM glacial moraines (Walter, 2022) (Purple - Eastern Glaciers: U - Uinta, W - Wasatch, S_1 - Stansbury, O - Oquirrh; Red - Southwestern Glaciers: D - Deep Creek, S_2 - South Snake; Green - Western Glaciers: E - East Humboldt, I - Independence, R - Ruby).

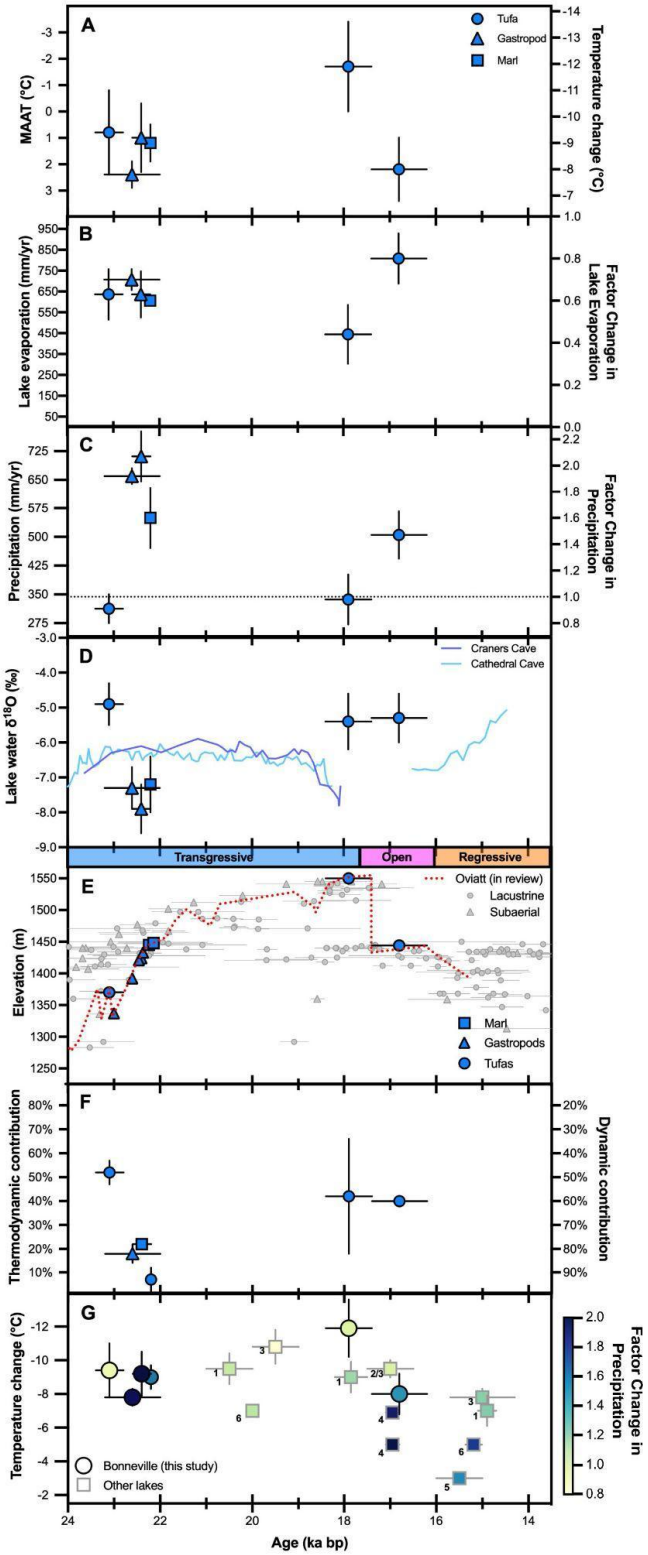
A
Tufa
Gastropod
Marl
MAAT (°C)
Temperature change (°C)
B
Lake evaporation (mm/yr)
Factor Change in Lake Evaporation
C
Precipitation (mm/yr)
Factor Change in Precipitation
D
Craners Cave
Cathedral Cave
Lake water δ18O (‰)
Transgressive
Open
Regressive
E
Oviatt (in review)
Lacustrine
Subaerial
Marl
Gastropods
Tufas
Elevation (m)
F
Thermodynamic contribution
Dynamic contribution
G
Bonneville (this study)
Other lakes
Temperature change (°C)
Factor Change in Precipitation
Age (ka bp)

Figure 2.2: Evolution of hydroclimates at Lake Bonneville from 23-15 ka. Vertical error bars = 1 s.e.; horizontal bars = age range.

(A) Δ_{47}-T anomaly for samples and reconstructed MAAT. See methods for description of calculations and errors.

(B) Δ_{47}-derived factor change in lake evaporation and lake evaporation rates.

(C) Δ_{47}-derived factor change in precipitation and precipitation rates.

(D) Δ_{47}-derived water $\delta^{18}O$, corrected for ice volume. Purple and light blue lines show lake water $\delta^{18}O$ values calculated from lacustrine cave carbonate data (McGee et al., 2012). A water temperature of 4°C applied to cave carbonates, which formed in the deep lake, reflecting the temperature at which fresh water attains maximum density.

(E) Hydrograph for Lake Bonneville based on isostatically-corrected elevations (Oviatt & Pedone, 2024).

(F) Δ_{47}-derived first-order estimates of thermodynamic and dynamic contributions to lake level changes.

(G) Adapted from Belanger et al. (2022). Δ_{47}-derived estimates of temperature and precipitation changes at Lake Bonneville from this work compared to other reconstructions. Numbers correspond to lakes named in Figure 2.1, with basins that are furthest west indicated by higher values. See methods for data sources.

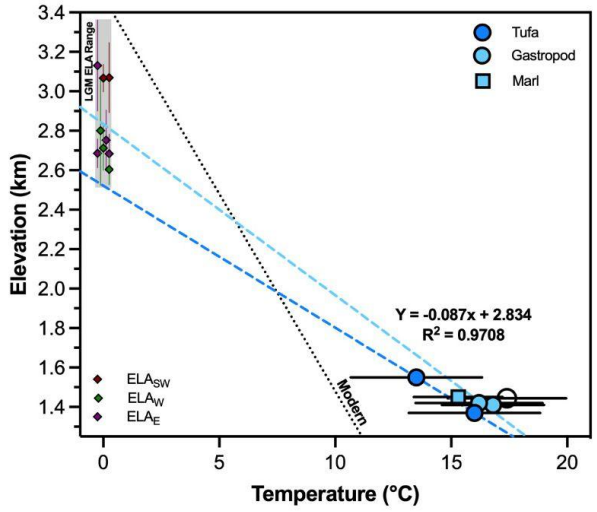
Tufa
Gastropod
Marl
LGM ELA Range
Y = -0.087x + 2.834
R² = 0.9708
Modern
ELA_SW
ELA_W
ELA_E
Elevation (km)
Temperature (°C)

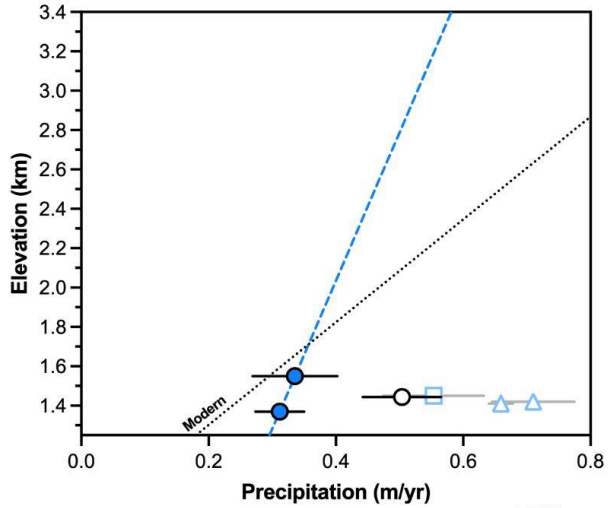
Modern
Elevation (km)
Precipitation (m/yr)

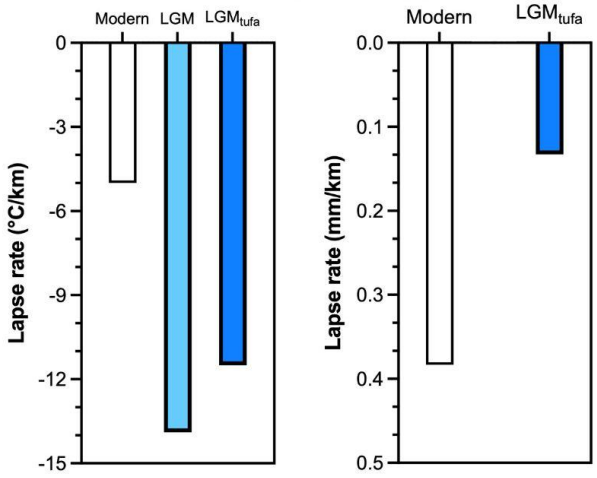
Modern
LGM
LGM_tufa
Lapse rate (°C/km)
Modern
LGM_tufa
Lapse rate (mm/km)

Figure 2.3: Constraints on lapse rates from Δ_{47} in the Bonneville Basin. Samples from this study reflect average July air temperatures by assuming a 15.2°C temperature difference between MAAT and July water temperatures (Hren & Sheldon, 2012). Paleo-MAAT used in this calculation was derived using water-to-air transfer function from Terazzas et al. (2023). Modern relationships for the Bonneville basin are represented by a dotted black line and taken from Belanger at al. (2022). ELA estimates are shown by purple diamonds for Eastern glaciers (U - Uinta, W - Wasatch, S_1 - Stansbury, O - Oquirrh), red for Southwestern glaciers (D - Deep Creek, S_2 - South Snake), and green for Western glaciers (E - East Humboldt, I - Independence, R - Ruby). Locations for glaciers can be found in Figure 2.1. Light gray bar represents the range of LGM ELA's in the Great Basin from a compilation of nine mountain ranges (Walter, 2022). Dark blue dashed line shows the relationship derived from tufa samples, which are more likely to have been formed during steady-state conditions, while the light blue line shows the relationship derived from all data from 23-17.5 ka.

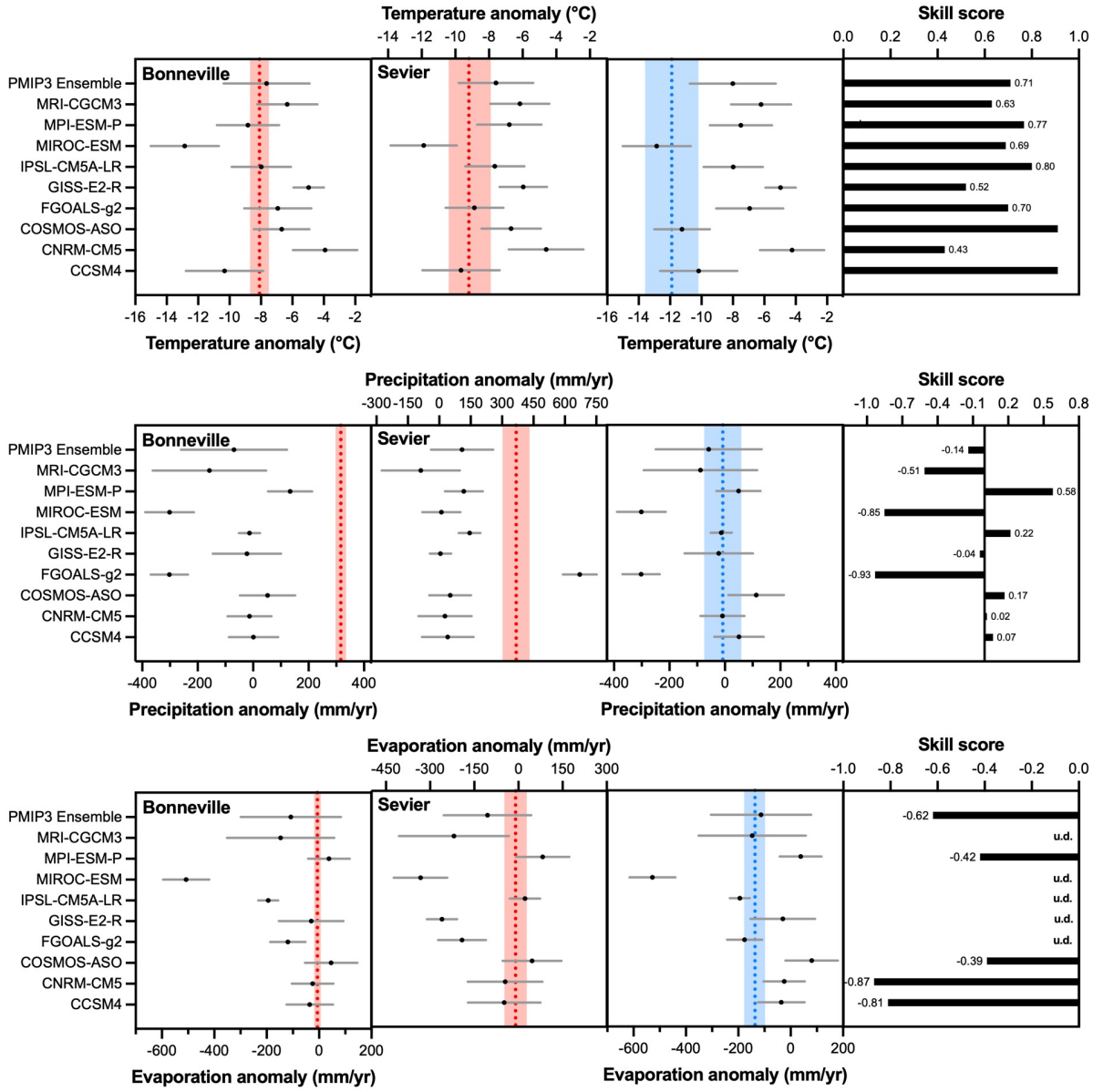

Figure 2.4: Comparison of hydroclimatic parameters derived from clumped-isotopes and output from the PMIP3 suite of climate models. Red dotted line reflects averages derived from gastropods for the Bonneville basin (30GP, FW-S, FW-P, PV, and SG) and Sevier subbasin (GSF, LRSW, OC-5B) and red shading represent uncertainty (±1 s.d.) and blue dotted line reflects average anomalies from Bonneville highstand tufas (~18 ka) and blue shading represents uncertainty. Climate model output is shown by a black circle, and 1 standard deviation is represented by gray error bars. Anomalies from the PMIP model suite are calculated as the difference between LGM and pre-industrial. Numbers represent the skill score for each model, with u.d. representing skill scores that are undefined.

(**Top**) Model-proxy comparison for temperature anomaly (LGM-PI). Modern temperature is derived from Prism Climate Group (2021). (**Middle**) Model-proxy comparison for precipitation anomaly (LGM-PI). Modern precipitation over the entire Bonneville basin is 344 mm/yr (PRISM Climate Group, 2024), comparable to values derived from reanalysis data (338 mm/yr; (Ibarra et al., 2018). (**Bottom**) Model-proxy comparison for evaporation anomaly (LGM-PI). Modern evapotranspiration rates were derived using average annual evapotranspiration from 1958-2015 (Abatzoglou et al., 2018) over the basin area.

5. Tables

Sample ID	Sample Type	Total Runs	$\delta^{13}C$ (VPDB, ‰)	$\delta^{18}O_{mineral}$ (VPDB, ‰)	Δ47 (I-CDES, ‰)	T - Lake (°C)	$\delta^{18}O_{water}$ (VSMOW, ‰)*
Stansbury Gulch - Gastropod - Stansbury Oscillation							
SG1-P-16,19	Pyrgulopsis	1	1.2	-5.1	0.646	7.2	-7.2
SG1-P-25,29,38	Pyrgulopsis	1	1.2	-5.2	0.637	9.9	-6.7
SG1-P-4,18	Pyrgulopsis	2	1.7	-5.2	0.652	5.6	-7.7
SG1-P-9,10	Pyrgulopsis	1	1.4	-5.0	0.631	11.7	-6.2
SG1-P-22,23	Pyrgulopsis	1	1.7	-5.3	0.634	10.8	-6.6
SG1-P-5,7	Pyrgulopsis	1	2.5	-4.9	0.631	11.7	-6.1
Site Average ± 1 S.E.		**7**	**1.6 ± 0.2**	**-5.1 ± 0.1**	**0.639 ± 0.004**	**9.5 ± 1.0**	**-6.8 ± 0.3**
Highway 30 Gravel Pit - Gastropod - Transgressive							
30-GP-S-1	Stagnicola	2	-0.8	-4.9	0.639	9.3	-6.6
30-GP1-S-1114A	Stagnicola	1	0.1	-4.6	0.641	8.7	-6.4
30-GP1-S-2	Stagnicola	2	-1.0	-4.9	0.648	6.7	-7.2
30-GP1-S-3	Stagnicola	1	-2.2	-4.1	0.645	7.5	-6.2
Site Average ± 1 S.E.		**6**	**-1.0 ± 0.5**	**-4.6 ± 0.2**	**0.643 ± 0.002**	**8.1 ± 0.6**	**-6.6 ± 0.2**
Pilot Valley - Gastopod - Transgressive							
PV1-S-1	Stagnicola	1	-1.4	-4.5	0.633	11.1	-5.8
PV1-S-2	Stagnicola	1	-1.4	-4.3	0.647	6.9	-6.6
PV1-S-3	Stagnicola	1	-0.5	-4.8	0.638	9.6	-6.4
PV1-S-5	Stagnicola	1	-1.1	-4.1	0.634	10.8	-5.5
PV1-S-7	Stagnicola	1	-1.6	-4.4	0.647	6.9	-6.7
PV1-S-8	Stagnicola	1	-1.1	-4.9	0.648	6.6	-7.2
Site Average ± 1 S.E.		**6**	**-1.2 ± 0.2**	**-4.5 ± 0.1**	**0.641 ± 0.003**	**8.7 ± 0.9**	**-6.4 ± 0.3**
Ferber Wash - Gastopod - Transgressive							
FW1-S-4	Stagnicola	1	-0.6	-4.4	0.633	11.1	-5.7
FW1-S-7	Stagnicola	2	-1.6	-4.1	0.649	6.3	-6.4
Site Average ± 1 S.E.		**3**	**-1.1 ± 0.5**	**-4.3 ± 0.2**	**0.641 ± 0.008**	**8.7 ± 2.4**	**-6.1 ± 0.4**
FW1-P-4,5	Pyrgulopsis	1	-0.7	-4.0	0.633	11.1	-5.3
Site Average ± 1 S.E.		**1**	**-0.7 ± 0.0**	**-4.4 ± 0.0**	**0.633 ± 0.008**	**11.1 ± 2.8**	**-5.3 ± 0.4**
Great Stone Face Gastopod - Transgressive							
GSF1-S-10	Stagnicola	2	0.3	-4.6	0.628	12.7	-5.6
GSF1-S-1114B	Stagnicola	1	-0.9	-4.5	0.623	14.3	-5.2
GSF1-S-5	Stagnicola	1	0.6	-4.5	0.634	10.8	-5.8
GSF1-S-6	Stagnicola	1	0.1	-4.5	0.646	7.2	-6.6

GSF1-S-7	Stagnicola	1	0.4	-4.7	0.643	8.1	-6.7
GSF1-S-8	Stagnicola	1	0.0	-4.9	0.651	5.7	-7.4
Site Average ± 1 S.E.		**7**	**0.1 ± 0.2**	**-4.6 ± 0.1**	**0.638 ± 0.004**	**9.8 ± 1.4**	**-6.2 ± 0.3**
DMAD Reservoir - Gastropod - Transgressive							
OC5B-P-1-2	Pyrgulopsis	1	0.8	-5.0	0.647	6.9	-7.2
OC5B-P-3	Pyrgulopsis	1	-0.4	-5.3	0.652	5.4	-7.9
OC5B-P-6	Pyrgulopsis	1	-0.3	-4.9	0.643	8.1	-6.9
OC5B-P-7	Pyrgulopsis	1	0.7	-5.1	0.656	4.3	-8.0
Site Average ± 1 S.E.		**4**	**0.2 ± 0.3**	**-5.1 ± 0.1**	**0.650 ± 0.003**	**6.2 ± 0.8**	**-7.5 ± 0.3**
Long Ridge Southwest - Gastropod - Transgressive							
LRSW3-S-1	Stagnicola	3	-0.7	-2.7	0.627	13.0	-2.2
LRSW3-S-1114-X2	Stagnicola	3	-1.0	-5.5	0.637	9.8	-5.8
LRSW3-S-1114C	Stagnicola	2	-1.0	-5.2	0.643	8.2	-5.8
LRSW3-S-1114D	Stagnicola	1	0.4	-4.6	0.639	9.3	-5.0
LRSW3-S-3	Stagnicola	2	-0.8	-5.1	0.634	11.0	-5.1
LRSW3-S-5	Stagnicola	1	-0.7	-4.9	0.629	12.4	-4.6
LRSW3-S-6	Stagnicola	1	-0.1	-5.1	0.648	6.6	-6.0
Site Average ± 1 S.E.		**13**	**-0.6 ± 0.2**	**-4.7 ± 0.4**	**0.637 ± 0.003**	**10.0 ± 0.9**	**-4.9 ± 0.5**
Highway 30 Gravel Pit - Marl - Transgressive							
30GP2-M-328	Marl	1	1.7	-8.4	0.603	25.3	-5.9
30GP2-M-1	Marl	2	1.7	-8.1	0.648	13.4	-8.2
30GP2-M-4	Marl	3	1.5	-8.3	0.608	23.8	-6.2
30GP2-M-5	Marl	2	1.4	-8.5	0.605	24.7	-6.2
Site Average ± 1 S.E.		**8**	**1.6 ± 0.1**	**-8.3 ± 0.1**	**0.616 ± 0.011**	**21.8 ± 2.8**	**-6.6 ± 0.5**
Pilot Valley - Marl - Transgressive							
PV2-M-1	Marl	1	2.6	-7.3	0.652	12.1	-7.6
PV2-M-3	Marl	4	2.7	-6.8	0.641	15.0	-6.5
PV2-M-4	Marl	1	2.1	-7.5	0.638	15.7	-7.0
PV2-M-5	Marl	1	3.0	-6.7	0.624	19.5	-5.5
Site Average ± 1 S.E.		**7**	**2.6 ± 0.2**	**-7.1 ± 0.2**	**0.639 ± 0.006**	**15.6 ± 1.5**	**-6.7 ± 0.4**
Ferber Wash - Marl - Transgressive							
FW2-M-1	Marl	1	2.2	-6.6	0.669	8.0	-7.9
FW2-M-3	Marl	1	3.5	-6.0	0.629	18.1	-5.0
FW2-M-4	Marl	2	3.8	-5.8	0.630	18.0	-4.8
FW2-M-5	Marl	1	4.8	-4.7	0.639	15.5	-4.3
Site Average ± 1 S.E.		**5**	**3.6 ± 0.5**	**-5.8 ± 0.4**	**0.642 ± 0.009**	**14.9 ± 2.4**	**-5.5 ± 0.8**
Great Stone Face - Marl - Transgressive							
GSF2-M-1	Marl	2	4.3	-4.7	0.624	19.6	-3.5
GSF2-M-2	Marl	2	4.3	-4.7	0.598	26.9	-1.9

GSF2-M-3	Marl	3	4.3	-4.7	0.619	21.1	-3.2
GSF2-M-4	Marl	2	4.4	-4.4	0.602	26.6	-1.8
GSF2-M-5	Marl	2	4.2	-4.7	0.595	27.9	-1.7
GSF2-M-6	Marl	1	4.1	-4.8	0.639	15.5	-4.4
Site Average ± 1 S.E.		**12**	**4.3 ± 0.0**	**-4.7 ± 0.1**	**0.613 ± 0.007**	**22.9 ± 2.0**	**-2.7 ± 0.4**
DMAD Reservoir - Marl - Transgressive							
OC-5B-M-1	Marl	2	2.6	-4.6	0.605	24.8	-2.3
OC-5B-M-2	Marl	1	2.4	-4.7	0.591	28.8	-1.5
Site Average ± 1 S.E.		**3**	**2.5 ± 0.1**	**-4.7 ± 0.1**	**0.598 ± 0.007**	**26.8 ± 2.0**	**-1.9 ± 0.4**
Long Ridge Southwest - Marl - Transgressive							
LRSW3-M-328	Marl	1	0.0	-5.3	0.590	29.1	-2.1
LRSW3-M-AB	Marl	1	0.7	-5.4	0.601	25.9	-2.8
LRSW3-M-D	Marl	1	0.5	-5.2	0.622	20.0	-3.9
Site Average ± 1 S.E.		**3**	**0.4 ± 0.2**	**-5.3 ± 0.1**	**0.604 ± 0.009**	**25.0 ± 2.7**	**-2.9 ± 0.5**
Pilot Valley - Tufa - Stansbury Oscillation							
CIS13	Tufa	4	5.6	-2.9	0.640	12.1	-3.2
CIS3	Tufa	5	5.6	-3.0	0.645	10.5	-3.7
CIS7	Tufa	5	5.1	-4.0	0.633	14.6	-3.8
SIS13	Tufa	2	5.2	-3.7	0.651	8.7	-4.8
Site Average ± 1 S.E.		**16**	**5.4 ± 0.1**	**-3.4 ± 0.3**	**0.642 ± 0.004**	**11.5 ± 1.3**	**-3.9 ± 0.3**
Pilot Valley - Tufa - Bonneville Shoreline							
CIB1	Tufa	5	4.4	-3.8	0.652	8.2	-5.0
SIB5	Tufa	6	5.7	-3.3	0.644	10.8	-3.9
Site Average ± 1 S.E.		**11**	**5.1 ± 0.7**	**-3.6 ± 0.3**	**0.650 ± 0.005**	**9.5 ± 1.3**	**-4.4 ± 0.5**
Pilot Valley - Tufa - Provo Shoreline							
CIP17	Tufa	5	4.1	-4.4	0.635	14.0	-4.3
CIP25	Tufa	4	4.1	-4.4	0.636	13.6	-4.4
CIP3	Tufa	5	3.8	-4.5	0.633	14.6	-4.3
SIP16	Tufa	4	3.7	-4.7	0.647	9.7	-5.5
SIP2	Tufa	2	5.6	-3.0	0.643	11.2	-3.6
Site Average ± 1 S.E.		**20**	**4.3 ± 0.3**	**-4.2 ± 0.3**	**0.639 ± 0.003**	**12.6 ± 0.9**	**-4.4 ± 0.3**

Table 2.1: Stable and clumped isotope data for Lake Bonneville carbonates included in this study. *For water oxygen isotope calculations, values do not contain correction to reflect ice cap influence on the global oxygen isotope reservoir in meteoric water.

Sample Name	Latitude	Longitude	Elevation	Modern MAAT (°C)	Estimated MAAT (°C)	MAAT Anomaly (°C)	Evaporation (mm/yr)	Evaporation anomaly (%)	Precipitation (mm/yr)	Precipitation anomaly (%)
30GP-S	41.42	-113.91	1421	8.7	0.3	-8.4	587	-59	637	85
FW-S	40.35	-114.07	1433	9.5	3.6	-5.9	885	-39	713	108
FW-P	40.35	-114.07	1433	9.5	1.1	-8.4	677	-53	668	94
SG-P	40.79	-112.52	1337	10.2	2.0	-8.2	719	-50	600	75
PV-S	40.88	-114.23	1445	8.7	1.0	-7.7	660	-54	678	97
Bonneville Basin Gastropod Average ± 1 S.E.					**1.6 ± 0.6**	**-7.8 ± 0.5**	**706 ± 50**	**-51 ± 3**	**659 ± 19**	**92 ± 6**
GSF-S	39.24	-112.75	1448	10	2.3	-7.7	772	-47	757	120
OC-5B	39.41	-112.45	1424	10.2	-1.5	-11.7	415	-71	582	69
LRSW3-S	39.03	-113.22	1392	10.2	2	-8.2	722	-50	791	130
Sevier Subbasin Gastropod Average ± 1 S.E.					**1.0 ± 1.2**	**-9.2 ± 1.3**	**637 ± 112**	**-56 ± 8**	**710 ± 65**	**107 ± 19**
FW-M	40.35	-114.07	1433	9.5	-0.2	-9.7	580	-60	474	38
PV-M	40.88	-114.23	1445	8.7	0.4	-8.3	617	-57	633	84
Bonneville Marl Average ± 1 S.E.					**0.1 ± 0.3**	**-9.0 ± 0.7**	**599 ± 19**	**-59 ± 2**	**554 ± 33**	**61 ± 23**
CIS13	41.09	-113.73	1370	10.2	1.6	-8.6	695	-52	298	-13
CIS3	41.07	-113.81	1370	10.2	-0.4	-10.6	512	-65	257	-25
CIS7	41.11	-113.78	1370	10.2	4.8	-5.4	954	-34	424	23
SIS13	40.79	-113.95	1370	10.2	-2.7	-12.9	388	-73	269	-22
Stansbury Tufa Average ± 1 S.E.					**0.8 ± 1.6**	**-9.4 ± 1.6**	**637 ± 123**	**-56 ± 9**	**312 ± 38**	**-9 ± 11**

CIB1	41.07	-113.79	1550	10.2	-3.4	-13.6	308	-79	269	-22
SIB5	40.83	-113.91	1550	10.2	0.0	-10.2	587	-59	402	17
Bonneville Tufa Average ± 1 S.E.					**-1.7 ± 1.7**	**-11.9 ± 1.7**	**448 ± 140**	**-69 ± 10**	**336 ± 67**	**-2 ± 19**
CIP25	41.08	-113.73	1450	10.2	4.0	-6.2	985	-32	598	74
CIP3	41.07	-113.8	1450	10.2	3.4	-6.8	922	-36	574	67
CIP17	41.11	-113.77	1450	10.2	4.7	-5.5	1054	-27	636	85
SIP16	40.83	-113.9	1450	10.2	-1.5	-11.7	429	-70	364	6
SIP2	40.99	-113.83	1450	10.2	0.5	-9.7	624	-57	346	1
Provo Tufa Average ± 1 S.E.					**2.2 ± 1.2**	**-8.0 ± 1.2**	**803 ± 119**	**-44 ± 8**	**504 ± 61**	**47 ± 18**

Table 2.2: Hydroclimate modeling results for sites in this study. Modern MAAT are 30-year normals from 1991-2020 (PRISM Climate Group, 2024). Precipitation anomalies were calculated using 30-year normals from 1991-2020 over the basin area were used to calculate modern precipitation of 344 mm/yr (PRISM Climate Group, 2024), which is comparable to values derived for the basin using reanalysis data (338 mm/yr; Ibarra et al., 2018). Modern lake evaporation rates used to calculate evaporation anomalies were calculated using a pan coefficient of 0.7 (Linacre, 1994) and the average modern pan evaporation rate from 13 sites located within our study area (Supplementary Table 2; Western Regional Climate Center, 2023)

PMIP3 Model		Temperature anomaly (°C)			Precipitation anomaly (mm/yr)				Evaporation anomaly (mm/yr)			
	Tufa	Gastropods		Skill Score	Tufa	Gastropods		Skill Score	Tufa	Gastropods		Skill Score
	Bonneville ΔT = -11.9	Bonneville ΔT = -8.1	Sevier ΔT= -9.2		Bonneville ΔP = -8	Bonneville ΔP = +315	Sevier ΔP = +366		Bonneville ΔE = -137	Bonneville ΔE = -7	Sevier ΔE = -10	
CCSM4	-10.2	-10.3	-9.7	0.82	51	1	40	0.06	-36	-36	-48	0.08
CNRM-CM5	-4.2	-3.9	-4.6	0.49	-9	-13	27	0.02	-25	-25	-45	0.05
COSMOS-ASO	-11.2	-6.7	-6.7	0.77	113	52	52	0.17	80	46	46	0.24
FGOALS-g2	-6.9	-6.9	-8.9	0.79	-302	-302	671	-0.63	-176	-119	-192	u.d.
GISS-E2-R	-5.0	-5.0	-6.0	0.62	-22	-22	5	-0.03	-30	-30	-260	u.d.
IPSL-CM5A-LR	-8.0	-8.0	-7.7	0.90	-13	-13	145	0.16	-194	-194	22	u.d.
MIROC-ESM	-12.9	-12.9	-11.9	0.55	-302	-302	10	-0.56	-528	-507	-333	u.d.
MPI-ESM-P	-7.5	-8.8	-6.8	0.91	49	133	117	0.41	38	38	82	0.52
MRI-CGCM3	-6.2	-6.3	-6.2	0.73	-88	-158	-88	-0.40	-147	-147	-219	u.d.
PMIP3 Ensemble	-8.0	-7.6	-7.6	0.87	-58	-69	109	0.01	-113	-108	-105	u.d.

Table 2.3: Skill score derived from PMIP3 model anomaly output and clumped-isotope derived parameters. A skill score of 1 indicates perfect proxy-model agreement. A skill score of 0 indicates that the model and reference state perform equally well with respect to the null hypothesis of no change from the LGM to present. A negative skill score indicates model error is greater than in the null hypothesis. An undefined skill score (u.d.) occurs when the data-model agreement is closer than within the proxy errors (Hargreaves et al., 2013).

6. Supplement

Text S1: Clumped-isotope derived estimates of water temperature and lake water $\delta^{18}O$

Shoreline tufas analyzed in this study were formed during three different intervals within the Pilot Valley range in the western portion of the Bonneville basin. Around 23 ka, 'Stansbury' tufa was formed during the transgressive phase of the lake; reconstructed water temperatures using four tufa samples range from 8.7 - 14.6°C, with an average value of 11.5 ± 1.3°C. Two tufa samples from the 'Bonneville' shoreline, which was formed around ~18 ka prior to the Bonneville flood and during the lake's highstand, reflect cooler conditions, with average water temperatures 9.5 ± 1.3°C. As lake levels receded following the flood, the 'Provo' shoreline tufas was formed at 16 ka, with an average clumped-isotope derived water temperature of 12.6 ± 0.9°C, reflecting a warming of 3.1°C relative to the lake highstand.

Gastropod and marl samples were collected from six different sites in the northern Bonneville basin and southern Sevier subbasin. Based on the collection elevation, both gastropods and marls were assumed to represent the transgressive phase of Lake Bonneville between the 'Stansbury' and 'Bonneville' shorelines. Water temperatures reconstructed from gastropods during the range from 6.2 - 11.1°C. Gastropods show similar water temperatures in the Bonneville basin (9.2 ± 0.5°C) and Sevier subbasin (8.5 ± 1.2°C). Additionally, estimates of subbasin average $\delta^{18}O_{water}$ derived from clumped isotope analysis remain fairly consistent between basins, differing by 0.6‰.

In contrast, we observe large differences in estimated water temperatures derived from marl samples between the larger, deeper Bonneville basin compared to smaller, shallower Sevier subbasin. Marl samples were collected directly above gastropod shells and are slightly younger than shells from the same location; representing a transition from shoreline to deeper water

conditions. The average water temperature derived from three marl samples in the Sevier subbasin is 24.9 ± 1.1°C, while average water temperatures derived from three marl samples from the Bonneville basin is 17.4 ± 3.8°C, resulting in a temperature difference of 7.5°C between basins. In addition, we also observe a difference of 3.6‰ in $\delta^{18}O_{water}$ values in the Sevier subbasin ($\delta^{18}O_{water}$ = -3.6 ± 0.6‰) relative to the Bonneville basin ($\delta^{18}O_{water}$ = -7.2 ± 0.6‰). Unlike our gastropod samples, results from marl may suggest that the two regions are geochemically and climatically distinct.

Reconstructed water temperatures using marl samples are much higher than the respective temperatures derived from gastropods at the same locations (Fig. 2.A.1). If detrital influence is negligible, this may be indicating a difference in timing of carbonate formation between these two different types of carbonates. Authigenic carbonate precipitation is enhanced by biological activity or elevated water temperature, or some combination of the two. If the marl samples were precipitating due to biologically mediated processes, reconstructed temperatures from clumped isotope analysis would reflect spring temperatures, during peak photosynthesis. However, our water temperatures from marls in this study are biased towards higher temperatures, with four samples closely matching or exceeding modern June-August water temperatures in the Great Salt Lake (Fig. 2.A.1). Higher air temperatures would cause an increase in carbonate saturation state by increasing evaporation rates in the basin, therefore inducing carbonate precipitation.

This disparity may be explained by different responses in each of the basins to summer heating. Depth variation between basins is extreme, with the Sevier Subbasin being roughly 100 meters higher in elevation than the base of the Bonneville floor. We hypothesize that depth differences may have allowed the Sevier Subbasin to be more influenced by summer air

temperatures, resulting in higher water temperatures that are then transferred to higher air temperature estimates. This non-uniform heating due to lake depth is observed in the modern Great Salt Lake, with the smaller and shallower North Arm surface waters being 2-3°C warmer than the South Arm during the summer, despite little variation in air temperature over both arms (Crosman and Horel, 2009).

Due to these differences, we exclude four marl samples that yield unrealistic water temperature estimates that are reflective of carbonate precipitation induced by increased heating from our hydroclimatic modeling exercise (three in the Sevier subbasin and one in the Bonneville basin). Additionally, these samples demonstrate disagreement in $\delta^{18}O_{water}$ between the gastropod shells and marls from the same sites and are likely not representative of average lacustrine conditions. We also acknowledge that there is the possibility that the reconstructed temperatures from these samples could be influenced by detrital carbonate contributions after deposition, depending on their depth and location from the shore at the time of marl deposition. Detrital carbonates have been observed to be in marls extracted from cores in other locations throughout the basin (Pedone and Oviatt, 2016).

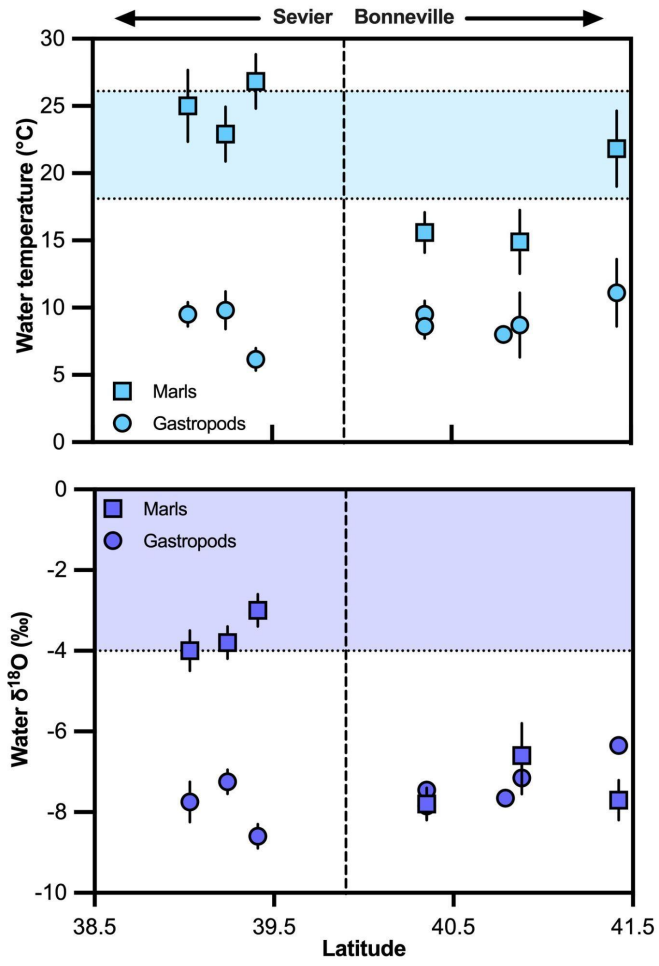

Figure 2.A.1: Spatial trends in marl and gastropod derived water temperature and $\delta^{18}O$. Clumped isotope derived estimates derived from lake Bonneville gastropods (circles) and marls (squares). Vertical dashed line indicates location of separation of the Bonneville basin and Sevier subbasin. Shaded light blue regions in the top panel indicate modern water temperature for the Great Salt Lake values during carbonate precipitation periods. Shaded light purple regions in the bottom panel indicate modern Great Salt Lake $\delta^{18}O$ variation. A correction was applied to lake water $\delta^{18}O$ reconstructions based on sample age to account for ice volume induced enrichment of waters during the LGM (Tripati et al., 2014).

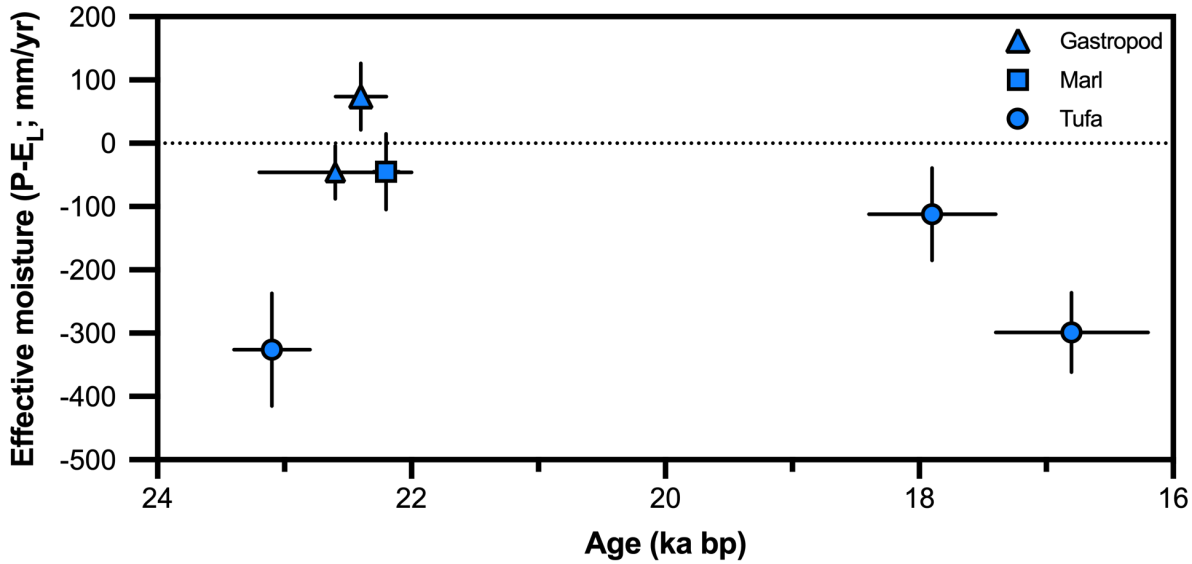

Figure 2.A.2: Temporal evolution of effective moisture (defined the difference between precipitation and lake evaporation) at Lake Bonneville. Increases in effective moisture are observed concurrent with a rapid transgression of the lake between 23 and 22 ka.

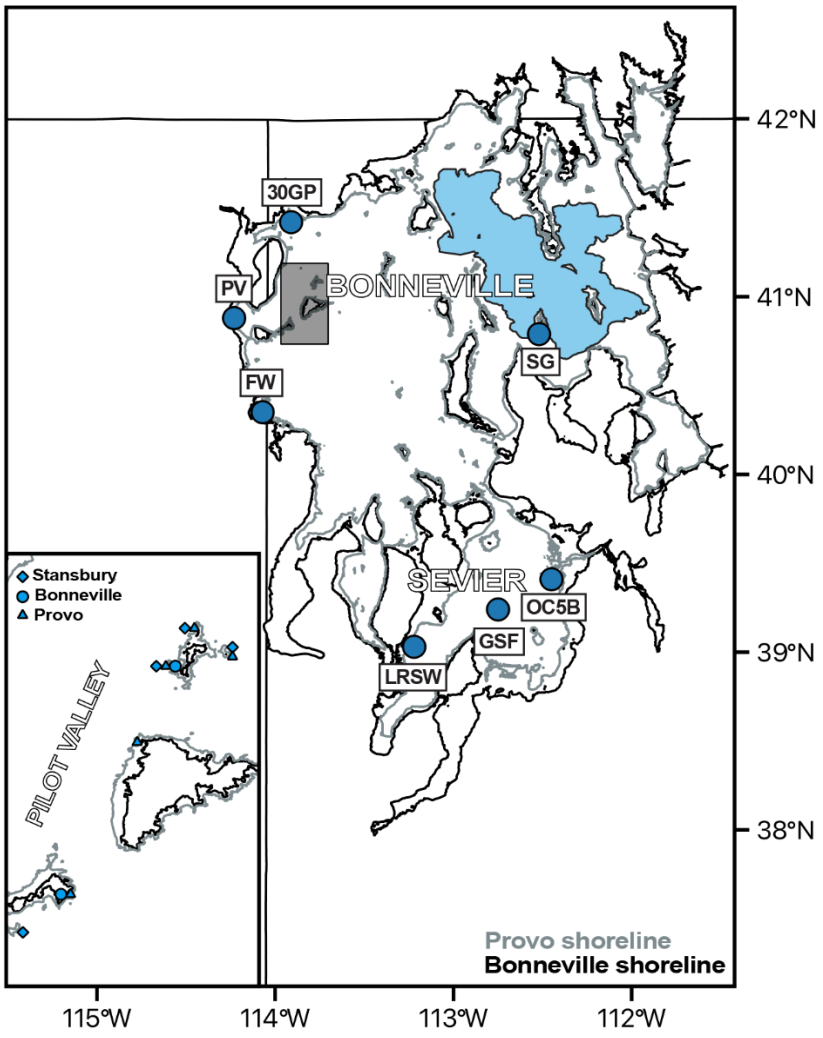

Figure 2.A.3: Map of sampling sites in this study. Lake level contours for Lake Bonneville at its highstand level (black, 1,550 m Bonneville shoreline) and Provo level (gray, 1,450 m Provo shoreline) from Adams and Bills (2016), and for the modern Great Salt Lake (blue, 1,277 m) from Utah Automated Geographic Reference Center (AGRC). Blue circles indicate sampling locations for gastropods and marls. Gray inset within the figure represents the extent of the inset figure. Figure on the bottom left shows the location of tufa in Pilot Valley. Diamonds, circles, and triangles indicate sampling locations for Provo, Bonneville, and Stansbury tufa, respectively.

Supplementary Tables:

Standard	Type	n	$\delta^{13}C$ (‰, VPDB)	$\delta^{18}O$ (‰, VPDB)	Δ_{47} (‰, I-CDES)
TVO3	Carbonate	47	2.8	-8.4	0.697
Carmel Chalk	Carbonate	144	-2.2	-3.9	0.668
Carrera Marble	Carbonate	182	2.1	-1.6	0.368
Veinstrom-01	Carbonate	57	-6.1	-12.6	0.708
ETH-1	Carbonate	12	1.9	-2.1	0.269
ETH-2	Carbonate	7	-10.1	-18.7	0.277
ETH-3	Carbonate	11	1.6	-1.6	0.689
ETH-4	Carbonate	3	-10.1	-18.7	0.532
Bonedry Tank CO_2	25°C gas breakseal	-	-	-	25°C equilibration
Bonedry Tank CO_2	1000°C gas breakseal	-	-	-	Stochastic
Evap DI + Carrera Marble CO_2	25°C gas breakseal	-	-	-	25°C equilibration
Evap DI + Carrera Marble CO_2	1000°C gas breakseal	-	-	-	Stochastic

Table 2.A.1: Average stable and clumped isotope values for standards measured in the Tripati-Eagle lab. $\delta^{13}C$ and $\delta^{18}O$ data are presented with one standard deviation, while Δ_{47} data is presented with one standard error.

Site	Period of Record	Pan Evaporation (mm/yr)
BEAR RIVER BAY	1969-1996	1724.7
BEAR RIVER REFUGE	1948-1984	1297.9
FARMINGTON USU FLD STN	1948-2005	994.4
FISH SPRINGS REFUGE	1960-2005	1927.4
LOGAN 5 SW EXP FARM	1969-2005	1302.8
LOGAN USU EXP STN	1950-1978	1037.6
MILFORD	1906-2005	1988.8
PROVO AIRPORT	1948-1953	1298.7
PROVO BYU	1980-2005	1268.5
PROVO RADIO KAYK	1952-1977	1114.8
SALTAIR SALT PLANT	1956-1991	1873.5
SEVIER DRY LAKE	1987-1993	1451.9
UTAH LAKE LEHI	1928-2003	1356.1
	Average ± 1 S.E.	**1434 ± 94**

Table 2.A.2: Modern pan evaporation rates at all sites within the modern Bonneville Basin. Data is derived from the Desert Research Institute, Western Regional Climate Center.

			Sampling elevation (‰, VSMOW)		Bonneville level - 1550m (‰, VSMOW)	
Site	**Sampling elevation**	**Modern MAAT (°C)**	**$\delta^{18}O$ Weighted Annual Mean**	**95% CI**	**$\delta^{18}O$ Weighted Annual Mean**	**95% CI**
Highway 30 Gravel Pit	1438	8.7	-13.5	0.4	-13.7	0.4
Stansbury Gulch	1362	10.5	-13.2	0.5	-13.6	0.5
Pilot Valley	1465	10.2	-13.4	0.4	-13.5	0.3
Ferber Wash	1453	9.5	-13.2	0.4	-13.3	0.4
Great Stone Face	1449	10.0	-12.8	0.5	-13	0.5
DMAD Reservoir	1434	10.2	-12.9	0.6	-13.1	0.6
Long Ridge Southwest	1402	10.2	-12.6	0.4	-12.9	0.3

Table 2.A.3: Modern MAAT and incoming $\delta^{18}O$ values at sampling sites within this study using each site's modern and highstand elevations. Data is derived from the Online Isotopes in Precipitation Calculator (Bowen, 2022).

7. References

Abatzoglou, J.T., Dobrowski, S.Z., Parks, S.A. & Hegewisch, K.C. (2018) TerraClimate, a high-resolution global dataset of monthly climate and climatic water balance from 1958–2015. *Scientific Data*, *5*(1), 170191. https://doi.org/10.1038/sdata.2017.191.

Adams, K.D. & Bills, B.G. (2016) Isostatic Rebound and Palinspastic Restoration of the Bonneville and Provo Shorelines in the Bonneville Basin, UT, NV, and ID. In: Oviatt, C.G. & Shroder, J.F. (Eds.) *Developments in Earth Surface Processes*, Vol. 20. Elsevier, pp. 145–164. https://doi.org/10.1016/B978-0-444-63590-7.00008-1.

Adams, K.D., Goebel, T., Graf, K., Smith, G.M., Camp, A.J., Briggs, R.W. & Rhode, D. (2008) Late Pleistocene and early Holocene lake-level fluctuations in the Lahontan Basin, Nevada: Implications for the distribution of archaeological sites. *Geoarchaeology*, *23*(5), 608–643.

Alcott, T.I. & Steenburgh, W.J. (2013) Orographic Influences on a Great Salt Lake–Effect Snowstorm. *Monthly Weather Review*, *141*(7), 2432–2450. https://doi.org/10.1175/MWR-D-12-00328.1.

Antevs, E. (1948) *The Great Basin, with Emphasis on Glacial and Postglacial Times: Climatic Changes and Pre-white Man. III.* University of Utah.

Barth, C., Boyle, D.P., Hatchett, B.J., Bassett, S.D., Garner, C.B. & Adams, K.D. (2016) Late Pleistocene climate inferences from a water balance model of Jakes Valley, Nevada (USA). *Journal of Paleolimnology*, *56*(2), 109–122.

Belanger, B.K., Amidon, W.H., Laabs, B.J.C., Munroe, J.S. & Quirk, B.J. (2022) Modelling climate constraints on the formation of pluvial Lake Bonneville in the Great Basin,

United States. *Journal of Quaternary Science*, *37*(3), 478–488. https://doi.org/10.1002/jqs.3394.

Benson, L.V., Smoot, J.P., Lund, S.P., Mensing, S.A., Foit Jr, F.F. & Rye, R.O. (2013) Insights from a synthesis of old and new climate-proxy data from the Pyramid and Winnemucca lake basins for the period 48 to 11.5 cal ka. *Quaternary International*, *310*, 62–82.

Bernasconi, S.M., Daëron, M., Bergmann, K.D., Bonifacie, M., Meckler, A.N., Affek, H.P., Anderson, N., Bajnai, D., Barkan, E., Beverly, E., Blamart, D., Burgener, L., Calmels, D., Chaduteau, C., Clog, M., Davidheiser-Kroll, B., Davies, A., Dux, F., Eiler, J., Elliott, B., Fetrow, A.C., Fiebig, J., Goldberg, S., Hermoso, M., Huntington, K.W., Hyland, E., Ingalls, M., Jaggi, M., John, C.M., Jost, A.B., Katz, S., Kelson, J., Kluge, T., Kocken, I.J., Laskar, A., Leutert, T.J., Liang, D., Lucarelli, J., Mackey, T.J., Mangenot, X., Meinicke, N., Modestou, S.E., Müller, I.A., Murray, S., Neary, A., Packard, N., Passey, B.H., Pelletier, E., Petersen, S., Piasecki, A., Schauer, A., Snell, K.E., Swart, P.K., Tripati, A., Upadhyay, D., Vennemann, T., Winkelstern, I., Yarian, D., Yoshida, N., Zhang, N. & Ziegler, M. (2021) InterCarb: A Community Effort to Improve Interlaboratory Standardization of the Carbonate Clumped Isotope Thermometer Using Carbonate Standards. *Geochemistry, Geophysics, Geosystems*, *22*(5), e2020GC009588. https://doi.org/10.1029/2020GC009588.

Bowen, G.J. (2023) The Online Isotopes in Precipitation Calculator (Version 3.1).

Bowen, G.J. & Revenaugh, J. (2003) Interpolating the isotopic composition of modern meteoric precipitation. *Water Resources Research*, *39*(10). https://doi.org/10.1029/2003WR002086.

Brand, W.A., Assonov, S.S. & Coplen, T.B. (2010) Correction for the 17O interference in

δ(13C) measurements when analyzing CO2 with stable isotope mass spectrometry (IUPAC Technical Report). *Pure and Applied Chemistry*, *82*(8), 1719–1733. https://doi.org/10.1351/PAC-REP-09-01-05.

Brown, L.C. & Duguay, C.R. (2010) The response and role of ice cover in lake-climate interactions. *Progress in Physical Geography: Earth and Environment*, *34*(5), 671–704. https://doi.org/10.1177/0309133310375653.

Cheng, F., Garzione, C., Li, X., Salzmann, U., Schwarz, F., Haywood, A.M., Tindall, J., Nie, J., Li, L. & Wang, L. (2022) Alpine permafrost could account for a quarter of thawed carbon based on Plio-Pleistocene paleoclimate analogue. *Nature Communications*, *13*(1), 1–12. https://doi.org/10.1038/s41467-022-29011-2.

Clark, P.U. & Bartlein, P.J. (1995) Correlation of late Pleistocene glaciation in the western United States with North Atlantic Heinrich events. *Geology*, *23*(6), 483–486. https://doi.org/10.1130/0091-7613(1995)023<0483:COLPGI>2.3.CO;2.

Craig, H. & Gordon, L.I. (1965) Deuterium and oxygen 18 variations in the ocean and the marine atmosphere.

Csank, A.Z., Tripati, A.K., Patterson, W.P., Eagle, R.A., Rybczynski, N., Ballantyne, A.P. & Eiler, J.M. (2011) Estimates of Arctic land surface temperatures during the early Pliocene from two novel proxies. *Earth and Planetary Science Letters*, *304*(3–4), 291–299. https://doi.org/10.1016/j.epsl.2011.02.030.

Dennis, K.J., Affek, H.P., Passey, B.H., Schrag, D.P. & Eiler, J.M. (2011) Defining an absolute reference frame for 'clumped' isotope studies of CO2. *Geochimica et Cosmochimica Acta*, *75*(22), 7117–7131. https://doi.org/10.1016/j.gca.2011.09.025.

Eagle, R.A., Eiler, J.M., Tripati, A.K., Ries, J.B., Freitas, P.S., Hiebenthal, C., Wanamaker,

A.D., Taviani, M., Elliot, M., Marenssi, S., Nakamura, K., Ramirez, P. & Roy, K. (2013) The influence of temperature and seawater carbonate saturation state on 13C–18O bond ordering in bivalve mollusks. *Biogeosciences*, *10*(7), 4591–4606. https://doi.org/10.5194/bg-10-4591-2013.

Eagle, R.A., Risi, C., Mitchell, J.L., Eiler, J.M., Seibt, U., Neelin, J.D., Li, G. & Tripati, A.K. (2013) High regional climate sensitivity over continental China constrained by glacial-recent changes in temperature and the hydrological cycle. *Proceedings of the National Academy of Sciences*, *110*(22), 8813–8818. https://doi.org/10.1073/pnas.1213366110.

Felton, A., Jewell, P.W., Chan, M. & Currey, D. (2006) Controls of Tufa Development in Pleistocene Lake Bonneville, Utah. *The Journal of Geology*, *114*(3), 377–389. https://doi.org/10.1086/501218.

García, A.F. & Stokes, M. (2006) Late Pleistocene highstand and recession of a small, high-altitude pluvial lake, Jakes Valley, central Great Basin, USA. *Quaternary Research*, *65*(1), 179–186. https://doi.org/10.1016/j.yqres.2005.08.025.

Ghosh, P., Adkins, J., Affek, H., Balta, B., Guo, W., Schauble, E.A., Schrag, D. & Eiler, J.M. (2006) 13C–18O bonds in carbonate minerals: a new kind of paleothermometer. *Geochimica et Cosmochimica Acta*, *70*(6), 1439–1456. https://doi.org/10.1016/j.gca.2005.11.014.

Gilbert, G.K. (1890) *Lake Bonneville* (Report No. 1). Washington, D.C. Retrieved from USGS Publications Warehouse.

Harbert, R.S. & Nixon, K.C. (2018) Quantitative Late Quaternary Climate Reconstruction from Plant Macrofossil Communities in Western North America. *Open Quaternary*, *4*(1), 8. https://doi.org/10.5334/oq.46.

Hargreaves, J.C., Annan, J.D., Ohgaito, R., Paul, A. & Abe-Ouchi, A. (2013) Skill and reliability of climate model ensembles at the Last Glacial Maximum and mid-Holocene. *Climate of the Past*, *9*(2), 811–823. https://doi.org/10.5194/cp-9-811-2013.

Hart, I., Jones, K.B., Brunelle, A., DeGraffenried, J., Oviatt, C.G.J., Nash, B., Duke, D. & Young, D.C. (2022) BUILDING A MASTER CHRONOLOGY FOR THE WESTERN LAKE BONNEVILLE BASIN WITH STRATIGRAPHIC AND ELEMENTAL DATA FROM MULTIPLE SITES, USA. *Radiocarbon*, *64*(1), 69–85. https://doi.org/10.1017/RDC.2022.3.

Hostetler, S. & Benson, L.V. (1990) Paleoclimatic implications of the high stand of Lake Lahontan derived from models of evaporation and lake level. *Climate Dynamics*, *4*(3), 207–217.

Hostetler, S.W. & Giorgi, F. (1992) Use of a regional atmospheric model to simulate lake-atmosphere feedbacks associated with Pleistocene Lakes Lahontan and Bonneville. *Climate Dynamics*, *7*(1), 39–44. https://doi.org/10.1007/BF00204820.

Hostetler, S.W., Giorgi, F., Bates, G.T. & Bartlein, P.J. (1994) Lake-Atmosphere Feedbacks Associated with Paleolakes Bonneville and Lahontan. *Science*, *263*(5147), 665–668. https://doi.org/10.1126/science.263.5147.665.

Hren, M.T. & Sheldon, N.D. (2012) Temporal variations in lake water temperature: Paleoenvironmental implications of lake carbonate δ18O and temperature records. *Earth and Planetary Science Letters*, *337*, 77–84. https://doi.org/10.1016/j.epsl.2012.05.019.

Ibarra, D.E., Egger, A.E., Weaver, K.L., Harris, C.R. & Maher, K. (2014) Rise and fall of late Pleistocene pluvial lakes in response to reduced evaporation and precipitation: Evidence from Lake Surprise, California. *GSA Bulletin*, *126*(11–12), 1387–1415.

https://doi.org/10.1130/B31014.1.

Ibarra, D.E., Oster, J.L., Winnick, M.J., Rugenstein, J.K.C., Byrne, M. & Chamberlain, C.P. (2018) Lake area constraints on past hydroclimate in the western United States: Application to Pleistocene Lake Bonneville. *Desert Research Symposium*.

Jewell, P.W. (2007) Morphology and paleoclimatic significance of Pleistocene Lake Bonneville spits. *Quaternary Research*, *68*(3), 421–430. https://doi.org/10.1016/j.yqres.2007.07.004.

John, C.M. & Bowen, D. (2016) Community software for challenging isotope analysis: First applications of 'Easotope' to clumped isotopes: Community software for challenging isotope analysis. *Rapid Communications in Mass Spectrometry*, *30*(21), 2285–2300. https://doi.org/10.1002/rcm.7720.

Jones, M.D., Roberts, C.N. & Leng, M.J. (2007) Quantifying climatic change through the last glacial–interglacial transition based on lake isotope palaeohydrology from central Turkey. *Quaternary Research*, *67*(3), 463–473.

Kaufman, D.S. (2003) Amino acid paleothermometry of Quaternary ostracodes from the Bonneville Basin, Utah. *Quaternary Science Reviews*, *22*(8), 899–914. https://doi.org/10.1016/S0277-3791(03)00006-4.

Kim, S.-T. & O'Neil, J.R. (1997) Equilibrium and nonequilibrium oxygen isotope effects in synthetic carbonates. *Geochimica et Cosmochimica Acta*, *61*(16), 3461–3475. https://doi.org/10.1016/S0016-7037(97)00169-5.

Kim, S.-T., O'Neil, J.R., Hillaire-Marcel, C. & Mucci, A. (2007) Oxygen isotope fractionation between synthetic aragonite and water: Influence of temperature and Mg2+ concentration. *Geochimica et Cosmochimica Acta*, *71*(19), 4704–4715. https://doi.org/10.1016/j.gca.2007.04.019.

Lemons, D.R., Milligan, M.R. & Chan, M.A. (1996) Paleoclimatic implications of late Pleistocene sediment yield rates for the Bonneville Basin, northern Utah. *Palaeogeography, Palaeoclimatology, Palaeoecology*, *123*(1), 147–159. https://doi.org/10.1016/0031-0182(95)00117-4.

Li, H., Liu, X., Arnold, A., Elliott, B., Flores, R., Kelley, A.M. & Tripati, A. (2021) Mass 47 clumped isotope signatures in modern lacustrine authigenic carbonates in Western China and other regions and implications for paleotemperature and paleoelevation reconstructions. *Earth and Planetary Science Letters*, *562*, 116840. https://doi.org/10.1016/j.epsl.2021.116840.

Linacre, E.T. (1993) Data-sparse estimation of lake evaporation, using a simplified Penman equation. *Agricultural and Forest Meteorology*, *64*(3–4), 237–256. https://doi.org/10.1016/0168-1923(93)90031-C.

Linacre, E.T. (1994) Estimating U.S. Class A Pan Evaporation from Few Climate Data. *Water International*, *19*(1), 5–14. https://doi.org/10.1080/02508069408686189.

Lora, J.M. & Ibarra, D.E. (2019) The North American hydrologic cycle through the last deglaciation. *Quaternary Science Reviews*, *226*, 105991. https://doi.org/10.1016/j.quascirev.2019.105991.

Lora, J.M., Mitchell, J.L., Risi, C. & Tripati, A.E. (2017) North Pacific atmospheric rivers and their influence on western North America at the Last Glacial Maximum. *Geophysical Research Letters*, *44*(2), 1051–1059. https://doi.org/10.1002/2016GL071541.

Lora, J.M., Mitchell, J.L. & Tripati, A.E. (2016) Abrupt reorganization of North Pacific and western North American climate during the last deglaciation. *Geophysical Research Letters*, *43*(22), 11,796-11,804. https://doi.org/10.1002/2016GL071244.

Lyle, M., Heusser, L., Ravelo, C., Yamamoto, M., Barron, J., Diffenbaugh, N.S., Herbert, T. & Andreasen, D. (2012) Out of the Tropics: The Pacific, Great Basin Lakes, and Late Pleistocene Water Cycle in the Western United States. *Science*, *337*(6102), 1629–1633. https://doi.org/10.1126/science.1218390.

Madsen, D.B., Rhode, D., Grayson, D.K., Broughton, J.M., Livingston, S.D., Hunt, J., Quade, J., Schmitt, D.N. & Shaver, M.W. (2001) Late Quaternary environmental change in the Bonneville basin, western USA. *Palaeogeography, Palaeoclimatology, Palaeoecology*, *167*(3), 243–271. https://doi.org/10.1016/S0031-0182(00)00240-6.

Magee, M.R. & Wu, C.H. (2017) Effects of changing climate on ice cover in three morphometrically different lakes. *Hydrological Processes*, *31*(2), 308–323. https://doi.org/10.1002/hyp.10996.

McGee, D., Moreno-Chamarro, E., Marshall, J. & Galbraith, E.D. (2018) Western US lake expansions during Heinrich stadials linked to Pacific Hadley circulation. *Science Advances*, *4*(11), eaav0118.

McGee, D., Quade, J., Edwards, R.L., Broecker, W.S., Cheng, H., Reiners, P.W. & Evenson, N. (2012) Lacustrine cave carbonates: Novel archives of paleohydrologic change in the Bonneville Basin (Utah, USA). *Earth and Planetary Science Letters*, *351–352*, 182–194. https://doi.org/10.1016/j.epsl.2012.07.019.

Munroe, J.S. & Laabs, B.J. (2013) Temporal correspondence between pluvial lake highstands in the southwestern US and Heinrich Event 1. *Journal of Quaternary Science*, *28*(1), 49–58.

Munroe, J.S., Laabs, B.J.C., Shakun, J.D., Singer, B.S., Mickelson, D.M., Refsnider, K.A. & Caffee, M.W. (2006) Latest Pleistocene advance of alpine glaciers in the southwestern Uinta Mountains, Utah, USA: Evidence for the influence of local moisture sources.

Geology, *34*(10), 841–844. https://doi.org/10.1130/G22681.1.

Nelson, S.T. & Rey, K.A. (2018) Multi-proxy reassessment of the paleolimnology of Lake Bonneville (western USA) as observed in the restricted Pilot Valley sub-basin. *Journal of Quaternary Science*, *33*(2), 177–193.

Nelson, S.T., Wood, M.J., Mayo, A.L., Tingey, D.G. & Eggett, D. (2005) Shoreline tufa and tufaglomerate from Pleistocene Lake Bonneville, Utah, USA: stable isotopic and mineralogical records of lake conditions, processes, and climate. *Journal of Quaternary Science*, *20*(1), 3–19. https://doi.org/10.1002/jqs.889.

Oviatt, C.G. (2015) Chronology of Lake Bonneville, 30,000 to 10,000 yr BP. *Quaternary Science Reviews*, *110*, 166–171.

Oviatt, C.G., Currey, D.R. & Sack, D. (1992) Radiocarbon chronology of Lake Bonneville, Eastern Great Basin, USA. *Palaeogeography, Palaeoclimatology, Palaeoecology*, *99*(3), 225–241. https://doi.org/10.1016/0031-0182(92)90017-Y.

Oviatt, C.G. & Pedone, V.A. (2024) Chronology of the early transgressive phase of Lake Bonneville. *Quaternary Research*, 1–8. https://doi.org/10.1017/qua.2024.10.

Passey, B.H., Levin, N.E., Cerling, T.E., Brown, F.H. & Eiler, J.M. (2010) High-temperature environments of human evolution in East Africa based on bond ordering in paleosol carbonates. *Proceedings of the National Academy of Sciences*, *107*(25), 11245–11249. https://doi.org/10.1073/pnas.1001824107.

Petryshyn, V.A., Lim, D., Laval, B.L., Brady, A., Slater, G. & Tripati, A.K. (2015) Reconstruction of limnology and microbialite formation conditions from carbonate clumped isotope thermometry. *Geobiology*, *13*(1), 53–67. https://doi.org/10.1111/gbi.12121.

PRISM Climate Group (2024). Oregon State University.

Quirk, B.J., Moore, J.R., Laabs, B.J., Caffee, M.W. & Plummer, M.A. (2018) Termination II, last glacial maximum, and lateglacial chronologies and paleoclimate from Big Cottonwood Canyon, Wasatch Mountains, Utah. *GSA Bulletin*, *130*(11–12), 1889–1902.

Quirk, B.J., Moore, J.R., Laabs, B.J., Plummer, M.A. & Caffee, M.W. (2020) Latest Pleistocene glacial and climate history of the Wasatch Range, Utah. *Quaternary Science Reviews*, *238*, 106313.

Reheis, M.C., Adams, K.D., Oviatt, C.G. & Bacon, S.N. (2014) Pluvial lakes in the Great Basin of the western United States—a view from the outcrop. *Quaternary Science Reviews*, *97*, 33–57. https://doi.org/10.1016/j.quascirev.2014.04.012.

Santi, L., Arnold, A., Mering, J., Arnold, D., Tripati, A., Whicker, C. & Oviatt, C.G. (2019) Lake level fluctuations in the Northern Great Basin for the last 25,000 years. *Exploring Ends of Eras in the Eastern Mojave Desert: 2019 Desert Symposium Field Guide and Proceedings*, 176–186. https://doi.org/10.31223/osf.io/6as7t.

Santi, L., Arnold, A.J., Ibarra, D.E., Whicker, C.A., Mering, J.A., Lomarda, R.B., Lora, J.M. & Tripati, A. (2020) Clumped isotope constraints on changes in latest Pleistocene hydroclimate in the northwestern Great Basin: Lake Surprise, California. *GSA Bulletin*, *132*(11–12), 2669–2683. https://doi.org/10.1130/B35484.1.

Schauble, E.A., Ghosh, P. & Eiler, J.M. (2006) Preferential formation of 13C–18O bonds in carbonate minerals, estimated using first-principles lattice dynamics. *Geochimica et Cosmochimica Acta*, *70*(10), 2510–2529. https://doi.org/10.1016/j.gca.2006.02.011.

Steenburgh, W.J., Halvorson, S.F. & Onton, D.J. (2000) Climatology of Lake-Effect Snowstorms of the Great Salt Lake. *Monthly Weather Review*, *128*(3), 709–727.

https://doi.org/10.1175/1520-0493(2000)128<0709:COLESO>2.0.CO;2.

Swart, P.K., Burns, S.J. & Leder, J.J. (1991) Fractionation of the stable isotopes of oxygen and carbon in carbon dioxide during the reaction of calcite with phosphoric acid as a function of temperature and technique. *Chemical Geology: Isotope Geoscience Section*, *86*(2), 89–96. https://doi.org/10.1016/0168-9622(91)90055-2.

Terrazas, A., Hwangbo, N., Arnold, A.J., Ulrich, R.N. & Tripati, A. (2023) Seasonal lake-to-air temperature transfer functions derived from an analysis of 965 modern lakes: A tool for lacustrine proxy model comparison. *Authorea Preprints*.

Tripati, A.K., Eagle, R.A., Thiagarajan, N., Gagnon, A.C., Bauch, H., Halloran, P.R. & Eiler, J.M. (2010) 13C–18O isotope signatures and 'clumped isotope' thermometry in foraminifera and coccoliths. *Geochimica et Cosmochimica Acta*, *74*(20), 5697–5717. https://doi.org/10.1016/j.gca.2010.07.006.

Tripati, A.K., Sahany, S., Pittman, D., Eagle, R.A., Neelin, J.D., Mitchell, J.L. & Beaufort, L. (2014) Modern and glacial tropical snowlines controlled by sea surface temperature and atmospheric mixing. *Nature Geoscience*, *7*(3), 205–209. https://doi.org/10.1038/ngeo2082.

Versteegh, E.A., Vonhof, H.B., Troelstra, S.R., Kaandorp, R.J. & Kroon, D. (2010) Seasonally resolved growth of freshwater bivalves determined by oxygen and carbon isotope shell chemistry. *Geochemistry, Geophysics, Geosystems*, *11*(8). https://doi.org/10.1029/2009GC002961.

Walter, L.M. (2022) *Reconstructions of Late Pleistocene Mountain Glacier Equilibrium Line Altitudes and Paleoclimate in the Great Basin* (M.S.). North Dakota State University, United States -- North Dakota.

Welker, J.M. (2012) ENSO effects on δ18O, δ2H and d-excess values in precipitation across the US using a high-density, long-term network (USNIP). *Rapid Communications in Mass Spectrometry*, *26*(17), 1893–1898.

Western Regional Climate Center (2023). Available at : https://wrcc.dri.edu/Climate/summaries.php.

Woolway, R.I., Kraemer, B.M., Lenters, J.D., Merchant, C.J., O'Reilly, C.M. & Sharma, S. (2020) Global lake responses to climate change. *Nature Reviews Earth & Environment*, *1*(8), 388–403. https://doi.org/10.1038/s43017-020-0067-5.

Yeager, K.N., Steenburgh, W.J. & Alcott, T.I. (2013) Contributions of Lake-Effect Periods to the Cool-Season Hydroclimate of the Great Salt Lake Basin. *Journal of Applied Meteorology and Climatology*, *52*(2), 341–362. https://doi.org/10.1175/JAMC-D-12-077.1

CHAPTER 3

Clumped Isotope Hydroclimates of Late Pleistocene Pluvial Lakes in the Great Basin

Alexandrea J. Arnold*, Lauren M. Santi*, Daniel E. Ibarra, Rico Lomarda, Juan M. Lora, Aradhna Tripati

*AA and LS contributed equally to this work and are listed based on alphabetical ordering.

Abstract

The Great Basin is a hydrographic and topographic province in southwestern North America, with large-scale endorheic watersheds. The province was once characterized by numerous large-scale lake systems during the Last Glacial Maximum (LGM; ~23,000-19,000 years ago) and subsequent deglaciation (~19,000-11,000 years ago), while today it is known for its desert ecology and arid climate. The contrast between these hydrological states indicates significant changes in the water cycle led to modern aridification, with hypotheses proposed including changes in moisture sources, rainfall intensity, and lake evaporation rates. Here, we use a thermodynamically-based tracer, carbonate clumped isotope thermometry, to constrain four variables in the hydrologic budget (temperature, precipitation rates, lake evaporation rates, and water $\delta^{18}O$) at a subset of four ancient lakes that span the geographic extremes of the Great Basin. Our results quantify a precipitation dipole at the LGM and indicate that different mechanisms sustained the spatially and temporally asynchronous growth and decay of these lakes; two lakes had elevated precipitation compared to modern at maximum lake extent and two had precipitation similar to modern. Our estimates of lake evaporation indicate that evaporation depression contributed to increased effective moisture at all four lake basins. This study sheds

light on controls over hydrological variability in Great Basin watersheds, which is especially valuable in consideration of future environmental responses to climate change.

1. Introduction

The modern Great Basin encompasses a wide range of biomes and ecologies, but is largely characterized as an extensive desert region. It has consistently low levels of precipitation, with many regions receiving under 250 mm of rain a year, especially in the southern Great Basin and in the rain shadow of the Sierra Nevada Mountains (Comstock & Ehleringer, 1992). Sediments and proxy data paint a picture of a region that has experienced dramatic aridification due to changes in the water balance and major shifts in terrestrial ecosystems (Hudson et al., 2017; Matsubara & Howard, 2009; McGee et al., 2018); furthermore, this region is poised to become drier in the future, of major concern given its current water-stressed state (Seager et al., 2014).

Here, we explore the use of climate proxy data for the Last Glacial Maximum (LGM; 23,000-19,000 years ago) and deglacial period (~19,000-11,000 years ago) to understand mechanisms of aridification in the Great Basin. During the LGM and deglacial, large lakes and enhanced precipitation relative to evaporation characterized this region (Lyle et al., 2012; Mifflin & Wheat, 1979; Reheis, 1999). Both lake highstands and the timing of lake disappearance are dated to be asynchronous, including along zonal bands, implying that a complex interplay of factors with significant spatial variability is likely important in the region (Hostetler & Benson, 1990; Munroe & Laabs, 2013). One study suggests there may be a symmetric response of hydroclimate in the Great Basin to global warming and cooling, and that the LGM may thus represent a key time period for the study of future hydroclimate dynamics (Lora, 2018).

Various proxy evidence (including packrat middens, halite inclusions, glaciers, and pollen) indicate cold and wet conditions during the LGM, with reduced evaporation rates compared to modern values (Matsubara & Howard, 2009). However, there is significant uncertainty associated with existing reconstructions. Reconstructed precipitation rates range from 80 – 260% of modern, evaporation rates between 12-90% of modern, and temperature depressions of 3 - 15°C (Ibarra et al., 2014; Matsubara & Howard, 2009). Hence, proxy data is only in rough agreement on the sign of evaporation and temperature changes relative to their modern values, while precipitation changes differ in their sign. Furthermore, the magnitude of these inferred changes varies appreciably between proxy systems. Finally, there are few studies that have examined how specific hydrologic variables vary spatially throughout the Great Basin; the most robust study that exists (constraining both temperature and precipitation rates) is based on pollen (Bartlein et al., 2011).

As further motivation, simulations from the latest cooperative modeling process involving comparisons of paleoclimate simulations with data (the Paleoclimate Modeling Intercomparison Project 3, 'PMIP3') generally exhibit poor agreement in regard to past changes in hydroclimate in the western United States. For example, while some PMIP3 models simulate less rainfall in the Great Basin during the LGM, others simulate more (Lora, 2018; Lora et al., 2017, p. 20; Oster et al., 2015). Discrepancies between model simulations remain, in part because the specific contributions of thermodynamic and dynamic processes to past hydroclimate in the Great Basin during the late-Pleistocene is unclear.

Proposed mechanisms for past lake shrinkage include changes in the strength and position of the polar jet stream (Hostetler & Benson, 1990; Munroe & Laabs, 2013), reduced transport by atmospheric rivers (Lora, 2018; Lora et al., 2016; Rutz et al., 2014), increased

evaporation rates (Lora, 2018; Mering, 2015; Smith & Street-Perrott, 1983), changes in the strength and position of the wintertime Aleutian low and North Pacific high (Unterman et al., 2011), and/or changes in the strength of the summer monsoon (Lyle et al., 2012). Significantly, paleoclimate reconstructions using proxy data can test our process-based understanding and provide observational “benchmarks" for evaluating the accuracy of simulations, both of which can contribute to improved process depiction in models that will play a critical role in policy and environmental planning in the decades to come.

This study examines how hydrologic variables in different lakes in the Great Basin have evolved since the LGM using an interdisciplinary approach that draws on concepts from sedimentary geology, geochemistry, paleoclimate, and hydrology. We estimate temperature, precipitation rates, evaporation rates, and water $\delta^{18}O$ using a thermodynamic tracer – clumped isotope analyses of lake sediments. Field sampling of lakes and geochemical analysis allows us to estimate temperature and water $\delta^{18}O$, while sampling of closed basin lakes allows us to neglect runoff. Therefore, the balance between precipitation and evaporation would dictate lake elevation. Thus, precipitation can be derived using steady-state mass-balance approaches that incorporate basin hypsometry, while evaporation can be modeled as a function of temperature. This approach lets us determine the quantitative contributions of changing precipitation and evaporation rates as mechanisms modulating lake levels in the Great Basin through time. Sample localities cover an extensive spatial range that allow for insights into how climate evolved through both time and space, including a greater understanding of atmospheric processes that have affected the growth and retreat of pluvial lakes. We test a hypothesis that a precipitation dipole existed in the Great Basin during the LGM (Oster et al., 2015), and quantify both precipitation rates and evaporation rates in the transect, and evaluate the origins of spatial

patterns in precipitation and evaporation. We use this information to evaluate the regional predictions of global climate models, and examine how climate change can alter ecosystem water balance in the West.

2. Methods

2.1 Carbonate clumped isotope thermometry

To provide well-constrained assessments of paleoclimate in the Great Basin, our study adds thermodynamically-based temperature, precipitation, and evaporation constraints derived from a set of novel approaches that utilize a stable isotope proxy, clumped isotopes. Clumped isotope analysis is based on the measurement of the overabundance of "clumped" or doubly-substituted bonds in carbonate groups of minerals above their stochastic distributions, which is temperature dependent (Ghosh et al., 2006; Schauble et al., 2006). The utility of clumped isotope analysis lies in the thermodynamic preference for clumped bonds to occur at certain temperatures; clumping decreases with increased temperature, and this trend scales with $1/T^2$ (T in Kelvin). The isotope exchange reactions that form clumped bonds take place at equilibrium within a single phase, with lower temperatures favoring a greater abundance of clumped bonds (Schauble et al., 2006). Hence, the temperature of carbonate formation can be determined from the quantification of specific carbonate isotopologues in a sample, without knowledge of the isotopic composition of the fluid in which a given sample formed.

2.2 Clumped isotope measurements

Mass spectrometry was completed at UCLA on a trio of mass spectrometers, with at least four replicates of each sample unless limited sample material inhibited replication. Error is

reported as standard error of the mean. All clumped and stable isotope data is included in the Supplement (Table 3.A.2).

Modern microbialites, tufas, and other types of lacustrine carbonates indicate clumped isotope measurements of mass 47 ('Δ_{47}') can be robustly used to reconstruct carbonate formation temperature, with water temperatures typically indicating formation during different intervals in the spring through fall (Horton et al., 2016; Hren & Sheldon, 2012; Petryshyn et al., 2016). We calculate water temperature ('T_w') by applying material-specific carbonate clumped isotope temperature calibration equations derived from modern fluvial and lacustrine samples[42]. For this analysis, we use a biogenic and biologically-mediated calibration developed in Arnold et al. (2023) for gastropods and tufa/stromatolites, respectively. Next, MAAT is estimated using a seasonally-biased lake water to MAAT transfer function (Terrazas et al., 2023). A Spring (April - June) seasonality for preferential carbonate formation in the spring for Lake Franklin, Lake Surprise, and Lake Chewaucan and summer (June - August) for Mud Lake, based on prior work (Hudson et al., 2017; Petryshyn et al., 2016; Santi et al., 2020) and each basins' modern climatological setting (Hren & Sheldon, 2012).

Past evaporation rates were estimated using a modified version of the Penman equation, derived specifically for lake evaporation, as applied in existing regional paleoclimate studies (Ibarra et al., 2014; Mering, 2015). This equation uses input of wind speed, temperature, dew point temperature, elevation, and latitude to estimate lake evaporation (Supplementary Equation 1). We assume past values of wind speed, elevation, and latitude are identical to modern values. Dew point temperature is assumed to be a constant offset from air temperature. We convert estimates of lake evaporation rate to basin-scale evaporation rates by assigning a weight to lake evaporation based on the relative area of the lake during each time period, and scaling

evapotranspiration on land by the relative area of the tributary (Supplementary Equation 2). Finally, we estimate past precipitation rates using a clumped isotope-constrained modeling approach used previously on Lake Bonneville (Mering, 2015), combined with an isotope mass balance model developed from previous publications (Ibarra et al., 2014; Jones et al., 2007; Santi et al., 2020). Descriptions and derivations of the above equations are included in the Supplement.

3. Results

Samples are derived from the shorelines of a series of closed basin paleolakes that span much of the spatial area in the Great Basin (Fig. 3.1). We collected carbonate sediments from paleoshorelines of Lake Franklin, Mud Lake, and Lake Surprise, and included novel geochemical analysis on previously published samples from the above lake basins, as well as Lake Chewaucan (Dickerson, 2006, 2009; Egger et al., 2018; Hudson et al., 2017; Ibarra et al., 2014; Santi et al., 2019). These lake basins were selected because they span a significant zonal and meridional range, and remained closed-basin lakes even at their highest extents (Mifflin & Wheat, 1979; Reheis, 1999). Modern climate data (including temperature, precipitation, and pan evaporation), is compiled in Table 3.1.

3.1 Geochemical evidence of closed basin behavior from $\delta^{13}C$ and $\delta^{18}O$

Calculation of precipitation rates from clumped and bulk isotope values using a steady-state model is dependent on the assumption that samples are taken from a closed basin; that is, the only input of water is from precipitation and the only output is from evaporation. Strong positive covariance between $\delta^{13}C$ and $\delta^{18}O$ has been associated with closed basin behavior and evaporative enrichment (Horton et al., 2016; Talbot, 1990). A plot of $\delta^{13}C$ against $\delta^{18}O$ for each lake basin is presented in the Supplement (Fig. 3.A.1), along with the Pearson Correlation

Coefficients (PCC) for each data set. To a first order, all lake basins show positive covariation in $\delta^{13}C$ and $\delta^{18}O$, consistent with closed basin behavior and justifying our steady-state modeling assumptions.

3.2 Clumped isotope constraints on past hydroclimates

For each basin, we plot the temporal evolution of mean annual air temperature ('MAAT') anomalies (Fig. 3.2a), water $\delta^{18}O$ (Fig. 3.2b), lake evaporation anomalies (Fig. 3.2c), and precipitation anomalies (Fig. 3.2d). The derivations and descriptions of the equations defining the above variables are provided in the Supplement. Table 3.A.2 and 3.A.3 contain all isotopic measurements and hydrologic modeling results.

To a first order, average MAATs during the LGM are less than or equal to their modern values at each of the four lake basins. During the mid-deglacial period, MAAT temperature increases at Lake Chewaucan, ultimately climbing to above-modern values, concurrent with the Bølling/Allerød. At Mud Lake, MAAT decreases throughout the deglacial period, remaining below modern MAAT during most of the studied period. At Lake Franklin and Lake Surprise, MAAT remains roughly constant, but shows a significant degree of variability.

Water $\delta^{18}O$ shows both temporal and spatial variability (Fig. 3.2b). Samples from Lake Surprise have the highest temporal resolution, and indicate a maximum variability of ~3‰ in water $\delta^{18}O$. Mud Lake shows much less variability in water $\delta^{18}O$, although large gaps of time separate data points. Data from Lake Chewaucan and Lake Franklin indicate large positive excursions in water $\delta^{18}O$ during relatively short (~2 ka) periods of time. While some basins indicate significant $\delta^{18}O$ excursions (~4-5‰ in 2 ka for some lake basins), this magnitude of variability has been observed in other lake $\delta^{18}O$ proxy reconstructions on similar timescales

(Wolfe et al., 2007). Water $\delta^{18}O$ from Mud Lake, located furthest southwest, is isotopically enriched compared to the other three lake basins.

Reconstructed lake evaporation at all four lakes are suppressed relative to modern values (Fig. 3.2c). Generally, increases in reconstructed lake evaporation rates for all basins is observed towards the late-deglacial. Lake evaporation rates increase towards near-modern values at Lake Chewaucan and Lake Surprise during the Bølling/Allerød, suggesting that a significant degree of warming that likely induced evaporation occurred regionally.

Reconstructed precipitation rates are variable throughout the period of study, but decrease during the deglacial period at all four lakes, but the magnitude of this decrease varies between basins. Further, the minimum precipitation rate constrained at each basin lies below modern values only at Lake Chewaucan and Lake Surprise. At Lake Franklin and Mud Lake, precipitation rates are well above their modern averages throughout a majority of the period of study.

For each basin, we estimate the thermodynamic and dynamic contributions to changes in lake level, for both the LGM and deglacial period (Supplementary Equation 11; Ibarra et al., 2018). This calculation assumes that all changes in lake moisture balance are due to either reduced temperatures or increased precipitation delivered by dynamic mechanisms.

3.2.1 Lake Chewaucan

Clumped isotope data for ~18 ka at Lake Chewaucan yield an average air temperature anomaly of 12.0 ± 0.6°C (Hudson et al., 2017), implying substantially cooler air temperatures compared to modern. Utilizing these data in our model, we reconstruct a 10 ± 6% decrease in precipitation and a 66 ± 2% decrease in evaporation rates relative to modern. The maximum temperature depression is reached around 15 ka (14.4°C cooler than modern), followed by

warming conditions similar to modern temperatures. There is a decrease in MAAT during the deglacial, with the lowest temperatures achieved during the early to mid-deglacial, followed by subsequent warming (Fig. 3.2a). Between 14-15 ka, precipitation rates oscillate between 30% increases and 30% decreases in precipitation relative to modern and return towards modern values by 13 ka (Fig. 3.2c).

3.2.2 Lake Franklin

Between 15.7 to 14.6 ka, 6.2°C of cooling is estimated at Lake Franklin, followed by 3.0°C warming by 14.3 ka. Evaporation rates follow a similar pattern throughout our study interval, with a suppression relative to modern of 20 ± 6% at ~15.7 ka, reaching a minimum of 43 ± 7% lower than modern at ~14.6 ka, and returning to 28 ± 4% modern values at 14.3 ka. Precipitation rates remain elevated relative to modern throughout the mid-deglacial, by 31-92%. A large positive precipitation anomaly and a negative evaporation anomaly indicate that within this watershed, lake highstands were likely driven by a combination of decreasing evaporation rates from temperature depression and increased precipitation rates. We note that evaporation rates and precipitation rates are at a minimum and maximum, respectively, during the time of the lake highstand (~16 ka; Munroe & Laabs, 2013; Santi et al., 2019).

3.2.3 Lake Surprise

At Lake Surprise, we calculate an average LGM temperature anomaly of -8.8 ± 2.9°C, along with evaporation and precipitation rates that are 37 ± 27% and 18 ± 28% lower than modern values. During the deglacial, we calculate climatological anomalies that are largely similar to LGM anomalies, indicating depressed temperature and lake evaporation rates. On average, deglacial temperatures were higher than during the LGM, but suppressed -7.1 ± 2.7°C

relative to modern. The 1.7°C increase in average temperatures from the LGM to the deglacial is reflected in reconstructed evaporation rates, with an 18 ± 21% suppression in rates relative to the deglacial. Precipitation rates during the deglacial return to similar to modern values.

3.2.4 Mud Lake

At Mud Lake, gradual warming is observed from the early-LGM into the mid-deglacial, with MAAT returning close to modern conditions by 16 ka. From ~ 23 ka to ~16 ka, precipitation rates were elevated (~2.5 to 3.8x modern values), reaching modern values by ~12 ka. Evaporation rates were enhanced in the early and mid-deglacial, and decreased between the mid to late-deglacial. The lowest temperature, precipitation, and evaporation rates occur during the late deglacial, concurrent with the Younger Dryas. There are large temporal gaps between samples at Mud Lake, and conditions may have fluctuated but not been sampled.

4. Discussion

4.1 Lake Chewaucan

The MAAT depression of 12.0 ± 0.6℃ at ~18 ka (Hudson et al., 2017) is cooler or similar to those implied by other proxy analyses, including pollen (-10 to -11℃)(Galloway, 1970), hydrologic mass balance modeling (-10℃ & -2.5℃)(Smith & Street-Perrott, 1983; Thompson et al., 1999) and packrat midden plant assemblages (-5℃ & -8℃)(Antevs, 1952; Thompson et al., 1999). Abrupt warming is observed during the deglacial, concurrent with the Bølling-Allerød, based on our new data, and published work (Hudson et al., 2017). Warming has also been reported from other regional proxy data, including the timing of the retreat of glaciers in the Northern Great Basin (Liccardi et al., 2004) and transitions to vegetation types that require less moisture availability (Grigg et al., 1997; Briles et al., 2017). Water $\delta^{18}O$ from Lake

Chewaucan tufa shows a significant degree of variability, from -7.1‰ at 18 ka, increasing to a maximum of 0.7‰ by ~13 ka. This ~8‰ increase in water $\delta^{18}O$ could be consistent both with changes in the dominant lake moisture source (e.g. decreasing contribution from the isotopically depleted North Pacific storm track versus the comparatively enriched atmospheric rivers) or with changes in the seasonality of precipitation, whereby summer precipitation is isotopically enriched relative to winter precipitation in the Great Basin (Welker, 2012). Alternatively, this increase could be explained by changing temperature (ΔT = 16.4°C from 18 to 13 ka), with a change of 0.24‰ to 0.48‰ per °C expected for water warming from a starting temperature of 20°C (Dansgaard, 1964) and/or increases in temperature and evaporation promoting enrichment in lake water $\delta^{18}O$.

Throughout the entire study interval, our calculations demonstrate thermodynamic controls as the dominant driver of effective moisture. At 18 ka, the thermodynamic controls are larger than the dynamic controls (69% and 31%, respectively). The largest dynamic contribution is observed at 14.2 ka at the lake highstand, and the remainder of the study interval is dominated by thermodynamics due to rising temperatures increasing evaporation rates (Fig. 3.3). This suggests that temperature and evaporation changes were important controls on past hydroclimate at Lake Chewaucan (Supplementary Equation 10).

Precipitation rates at Lake Chewaucan were generally consistent during the early deglacial period, with most tufa indicating precipitation rates roughly 10% lower than modern values. Between 14-15 ka, changes in precipitation range from a decrease of 35% to an increase of 30% relative to modern. After 14 ka, precipitation rates returned towards similar to modern precipitation rates. Conversely, lake evaporation rates show constant values throughout the early and mid-deglacial period, with a sharp increase immediately following the lake highstand (~14.5

ka). Prior to this increase, basin-scale evaporation rates were consistently lower than the modern estimated lake evaporation rate. We conclude that Lake Chewaucan's highstand (13-14 ka; Egger et al., 2018; Hudson et al., 2017) was likely sustained in the late deglacial period by lower evaporation rates, with modestly increasing precipitation rates during this time.

4.2 Lake Franklin

At Lake Franklin, temperature depression during the deglacial period ranges from 3.1 to 7.9°C cooler than modern. These estimates are smaller than what has been derived using a combined hydrologic and glacial modeling approach in the Ruby Mountains, adjacent to Lake Franklin, which yielded 7.8 to 9.5°C of cooling during the lake highstand (Dahle, 2021). Other proxies in the Great Basin, including glaciers and pollen (10-11°C; Galloway, 1970) and hydrologic mass balance models (10°C; Smith & Street-Perrott, 1983), estimate a larger degree of cooling than our study. Similar to Lake Chewaucan, we observe an increasing trend in temperatures between 14-15 ka, however, the increase observed at Lake Franklin is smaller in magnitude. Additionally, similarly to Lake Chewaucan, water $\delta^{18}O$ increases by ~4‰ at Lake Franklin between ~14-16 ka, but in this case, it is not coincident with a notable concurrent increase in air temperature. In this case, we infer that changing water $\delta^{18}O$ is likely due to variations in precipitation source rather than temperature.

Precipitation rates at Lake Franklin reached their peak at ~16 ka and decreased slightly throughout the late deglacial to 14 ka, but were consistently elevated compared to modern values. This trend is coincident with a gradual regression of lake levels following the lake highstand at ~16 ka (Munroe & Laabs, 2013; Santi et al., 2019). On average, precipitation rates between 16-14 ka are 1.6 ± 0.3 times the modern value (456 mm/yr). This is similar, albeit slightly less than estimates of precipitation change from nearby Jakes Lake (1.9 times; Barth et

al., 2016; Quirk et al., 2018). Conversely, hydrologic modeling of Lake Franklin combined with glacial modeling in the Ruby Mountains suggests less precipitation than our study during this time, ranging from 1-1.2 times modern (Dahle, 2021). Lake evaporation rates were consistently lower than modern and were reduced 20-43% throughout our study interval. In summary, our results suggest that elevated precipitation rates, rather than reduced evaporation rates, were important in the growth of post-LGM Lake Franklin, as precipitation were at local maxima during the lake highstand. We estimate a lower thermodynamic contribution to water balance at Lake Franklin (25%) during the deglacial, implying the dynamic transport of water vapor played an important role in driving lake growth (Fig. 3.3).

4.3 Lake Surprise

At Lake Surprise, using modern weather station data and LGM temperatures, we calculate an average LGM temperature anomaly of -8.8 ± 2.9°C. This estimate is similar to other proxy estimates of temperature anomalies in the Great Basin including from pollen (-10 to -11°C; Galloway, 1970), hydrologic mass balance modeling (-10°C; Smith & Street-Perrott, 1983), and packrat midden plant assemblages (-8°C; Thompson et al., 1999). Water $\delta^{18}O$ decreases by ~3‰ during the LGM and deglacial, likely reflecting evaporative enrichment of lake waters as temperatures warm.

LGM precipitation rates are lower than the modern average of 566 mm/yr, increasing from 20 ka to the deglacial, then declining during the deglacial to plateau at 59% of modern. Tufa-derived estimates suggest values that were 1.3 times modern during the lake highstand at 15.2 ka.

Evaporation rates show similar trends, decreasing in variability (and slightly in magnitude) during the deglacial period, generally plateauing below the estimated modern lake

evaporation rate (derived from modern pan evaporation rates) of 905 mm/yr. This increasing trend in lake evaporation, coupled with contemporaneous decreasing precipitation, indicate that evaporation depression likely played an important role in driving the growth of Lake Surprise. This finding is consistent with previous work (Lora, 2018; Oster et al., 2015), which suggests that Great Basin precipitation exhibited a pronounced dipole during the LGM, whereby northern Great Basin pluvial lakes (e.g. Lake Surprise and Lake Chewaucan) were driven more by temperature depression and subsequent reductions in evaporation rate, rather than by increased precipitation rates, as in the southern Great Basin. Our calculations show the increasing importance of thermodynamic controls throughout the LGM into the deglaciation, supporting the conclusion that temperature suppression was the most integral factor for the existence of Lake Surprise (Fig. 3.3).

4.4 Mud Lake

Throughout the LGM and mid-deglacial, mean annual air temperatures at Mud Lake were slightly cooler than modern and fairly constant. Our data suggest that the coolest temperatures occurred during the late deglacial (12 ka), with MAAT of -3.3 ± 3.2°C, and a maximum temperature depression of 14.4 ± 3.3°C. This is concurrent with the Younger Dryas, a period of cooling and glacial advance in the Northern Hemisphere (Alley, 2000).

We calculate a large precipitation anomaly during the LGM (165 ± 66%) and mid-deglacial (287 ± 38%), consistent with a substantially wetter late Pleistocene climate compared to modern. The largest precipitation forcing observed is at roughly 16 ka, synchronous with Heinrich Event 1, a time associated with lacustrine advance in the Great Basin (McGee et al., 2018). Packrat middens roughly 100 miles away from Mud Lake indicate that precipitation rates were elevated to ~260% of their current value during the late deglacial period (12-14 ka), similar

to our estimates for the mid-deglacial (Thompson et al., 1999). While this amount of rainfall is significantly greater than modern precipitation rates near Mud Lake (164 mm/yr), it is similar to modern precipitation rates at similar latitudes, just east of the Sierra Nevada Mountains (Smith & Reimann, 2008).

Average evaporation rates were suppressed relative to modern during the early LGM (-73 ± 18%), increasing to near-modern values at 23 and 16 ka (-5 ± 11% and -4 ± 7%), and decreasing during the late deglacial (-47 ± 15% relative to modern).

Water $\delta^{18}O$ at Mud Lake ranges by 3.1‰, with no discernible trend likely due to the low resolution of our samples. The absolute values of water δ18O that we reconstruct is slightly enriched compared to the other lake basins. As Mud Lake is significantly farther south than Lake Chewaucan, Lake Franklin, and Lake Surprise, this likely reflects differences in the dominant moisture source or seasonality of precipitation. Proportionally, southeast Nevada receives a larger amount of its precipitation in the summer compared to the more northern lake basins (Higgins et al., 1996; Xie & Arkin, 1996), and summer precipitation is known to be isotopically enriched relative to winter precipitation in the southwest United States (Yapp, 1985).

Mud Lake is representative of the southern side of the proposed LGM and deglacial precipitation dipole, whereby southern Great Basin paleolakes were thought to be sustained by enhanced precipitation rather than reduced evaporation rates (Lora, 2018; Oster et al., 2015). As expected in the southern Great Basin, we find a significant increase in precipitation rates at Mud Lake between the early LGM and mid deglacial period (peaking at ~3.7x modern values), coupled with a comparatively small degree of evaporation depression during the LGM.

Despite the strong precipitation forcing observed throughout our record, a first order calculation to determine thermodynamic versus dynamic controls on lake levels shows no clear

trends. We calculate roughly equal thermodynamic and dynamic controls on both LGM and deglacial (~49%) water balance, implying that dynamic transport of water vapor and temperature depression were both essential to driving the persistence of Mud Lake throughout the late Pleistocene (Fig. 3.3). Taken together, we conclude that Mud Lake, similar to Lake Franklin (and in contrast to Lake Chewaucan and Lake Surprise), was sustained by enhanced precipitation rather than decreasing levels of lake evaporation driven by temperature depression.

4.5 Evaluation of climate model simulations of hydroclimate change

We quantitatively evaluate model skill with respect to simulations of past hydroclimate parameters (Hargreaves et al., 2013)(Fig. 3.4; Supplementary Equation 12). In this analysis, model skill represents the ability of climate models to reproduce the magnitude of temperature and precipitation anomalies derived from clumped isotopes. Here, we use a transient model (TraCE-21 ka) to assess climate model skill for temperature and precipitation throughout the LGM into the deglaciation (Fig. 3.4). TraCE-21 ka is a transient climate model and is forced using evolving greenhouse gas concentrations, orbital configuration, ice sheet extent and thickness, and meltwater conditions (He, 2011).

Model skill for temperature is positive for all intervals that contain clumped-isotope measurements from two or more basins, ranging from a minimum of 0.09 to a maximum of 0.51. Model skill for temperature is highest at 18 ka and decreases throughout the deglaciation, with the minimum skill score occurring due to proxy-model disagreements on the magnitude of warming during the Bolling/Allerod at Lake Chewaucan. From 18 ka to 14 ka, model skill for precipitation is positive for intervals that contain clumped-isotope measurements from two or more basins, ranging from indicating agreement between model and proxy (scores ranging from

0.18 - 0.71). Similar to skill score results for temperature, we calculate the lowest skill score for precipitation around 12.7 ka (-0.28), due to the disparity in precipitation rates observed in our study at Lake Surprise and the TraCE-21 ka model. Overall, the TraCE-21 ka model generally performs well with respect to our proxy reconstructions for temperature and precipitation in the Northern Great Basin, however, we note that the resolution of TraCE-21 ka (3.75° by 3.75°) is likely a limiting factor given the small spatial scales over which hydroclimate changes occurred in the Great Basin.

5. Conclusions

In this work, we use clumped isotopes to reconstruct and compare the hydrological histories of four post-LGM pluvial lakes in the Great Basin. Δ_{47}-derived hydroclimate parameters allow us to disentangle the causes of a north-south effective precipitation dipole, as we are able to quantify precipitation and evaporation in each watershed. We see evidence for a wide range in causal mechanisms driving lake growth and aridification. Lake Chewaucan, located furthest North, transitions from cool conditions around ~18 ka (~12.0°C cooler than modern) to near-modern temperatures and evaporation rates during the Bølling-Allerød around ~14 ka. Reconstructed MAATs are consistently suppressed for Lake Surprise, located roughly 100 km south of Lake Chewaucan, are 8.8°C cooler than modern and increase by ~2°C during the deglacial, resulting in consistent reductions in evaporation rate through the entire late-Pleistocene. Average deglacial temperatures at Lake Franklin in northern Nevada are 5.1°C cooler than present day, resulting in evaporation rates roughly ⅔ of present day. Mud Lake, located furthest south in Nevada, MAAT transitions from a large extent of cooling (~2°C) to near modern MAAT and evaporation rates during the the deglacial. The analysis of northernmost

Great Basin lakes, Lake Surprise and Lake Chewaucan, yields precipitation rates that are similar or less than modern during the LGM and deglacial. In contrast, the more southerly basins, Lake Franklin and Mud Lake, experienced 2x and 4x modern precipitation forcing, respectively, during the deglacial.

Given the disparity between large changes in precipitation reconstructed from lakes in the continental interior but relatively arid conditions closer to the coasts, it is unlikely that a southerly shift in the jet stream is solely responsible for deglacial hydroclimatic shifts. The north-south precipitation gradient reconstructed in this study demonstrates that moisture advected from the south into the continental interior were influential. Moisture advected from the North American Monsoon may have been influential for deglacial lakes, however, the distance between Lake Franklin and Lake Mud from the typical domain of the North American Monsoon makes this unlikely. Thus, winter-derived, southward-shifted atmospheric rivers that bring subtropical moisture into the continental interior seem most plausible as a causal mechanism for the patterns observed in our data. summer-derived monsoonal precipitation are possible moisture sources. Ultimately, we suggest that our work could be extended to other lake basins, providing a valuable dataset for evaluation of model simulations, to provide a more comprehensive understanding of post-LGM hydroclimate in the Great Basin.

6. Figures

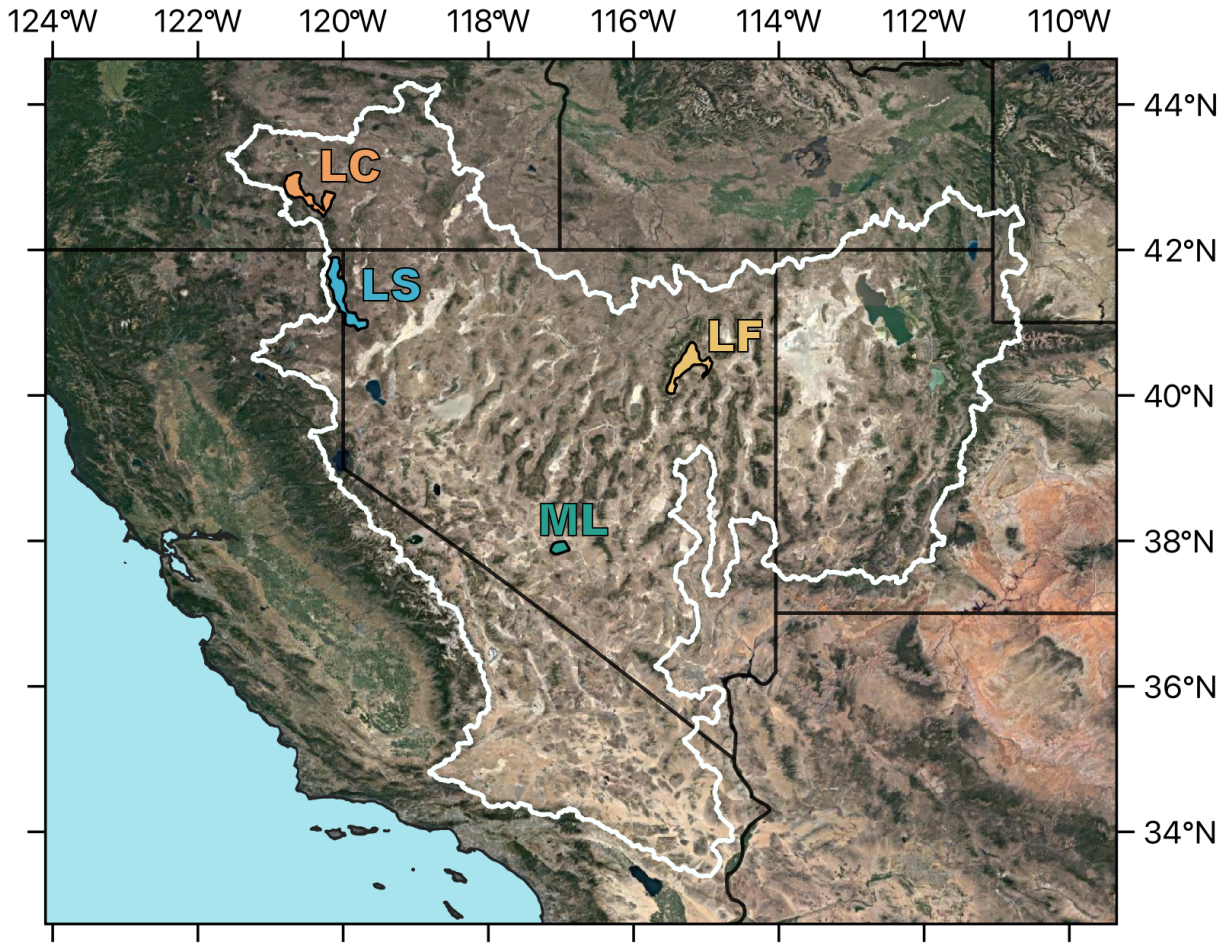

Figure 3.1: Map of the western United States, with the estimated maximum extent of pluvial lakes in blue. The locations of Lake Chewaucan (LC), Lake Franklin (LF), Mud Lake (ML), and Lake Surprise (LS) are indicated. White line indicates the extent of the Great Basin.

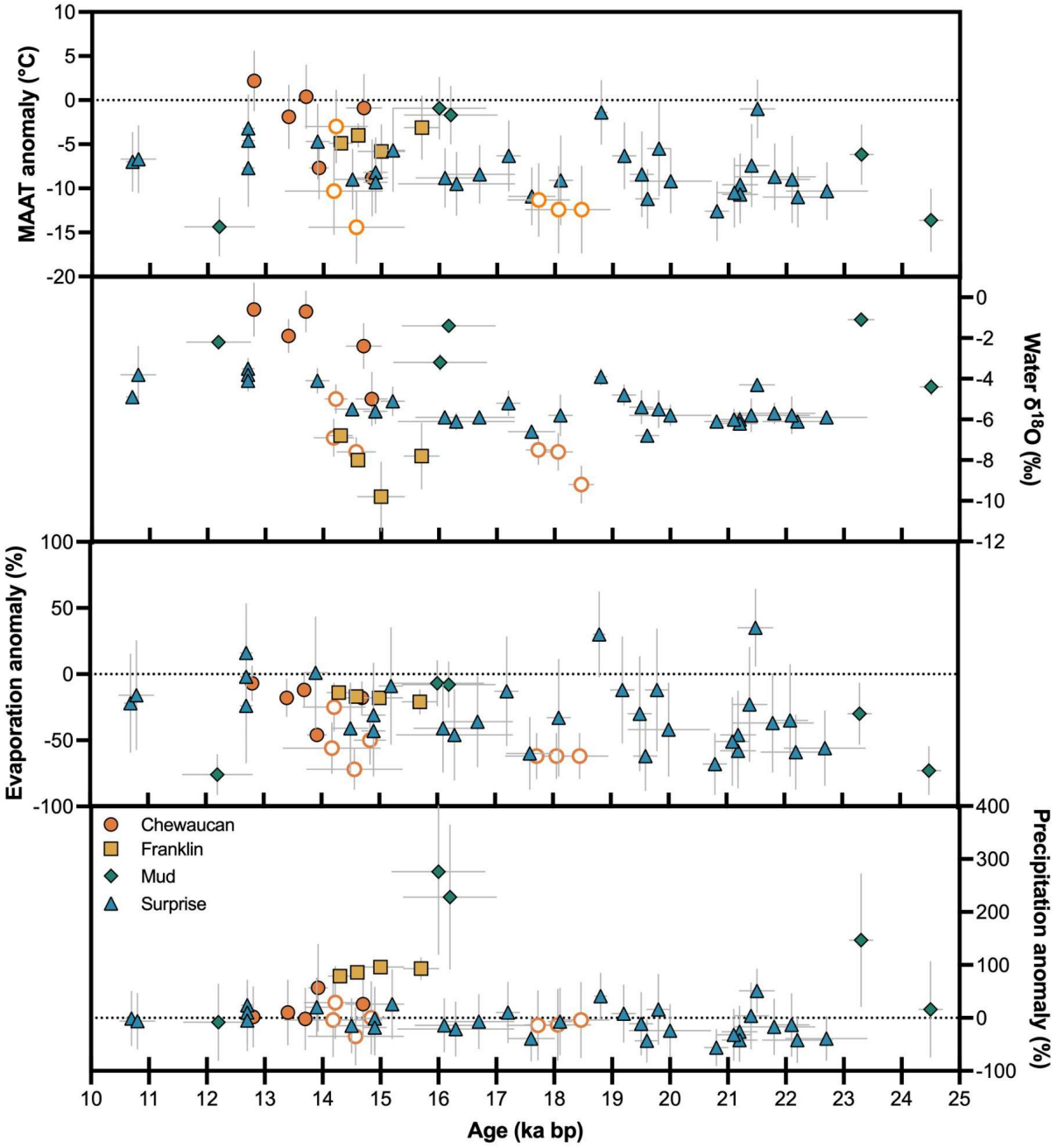

Figure 3.2: Temporal evolution of hydroclimatic variables. (A) Mean annual air temperature (MAAT) anomalies, (B) lake water $\delta^{18}O$, (C) evaporation anomalies, and (D) precipitation anomalies. Modern values for each site can be found in Table 3.1. For MAAT, error is propagated in quadrature from water temperature error and the reported standard deviation of the corresponding transfer function. For lake water $\delta^{18}O$, errors are reported as standard error of the mean of all replicates. The equations used to constrain precipitation rate and weighted evaporation rate from MAAT are derived and included in the Supplement (Supplementary

Equations 7 & 2, respectively). Error estimates for precipitation and evaporation anomalies are the standard error of all replicates using a Monte-Carlo method (see Methods). Filled symbols indicate new clumped isotope measurements from this study, open symbols indicate clumped-isotope analyses and clumped-isotope parameters (water temperature and lake water $\delta^{18}O$) are directly taken from another study (Hudson et al., 2017).

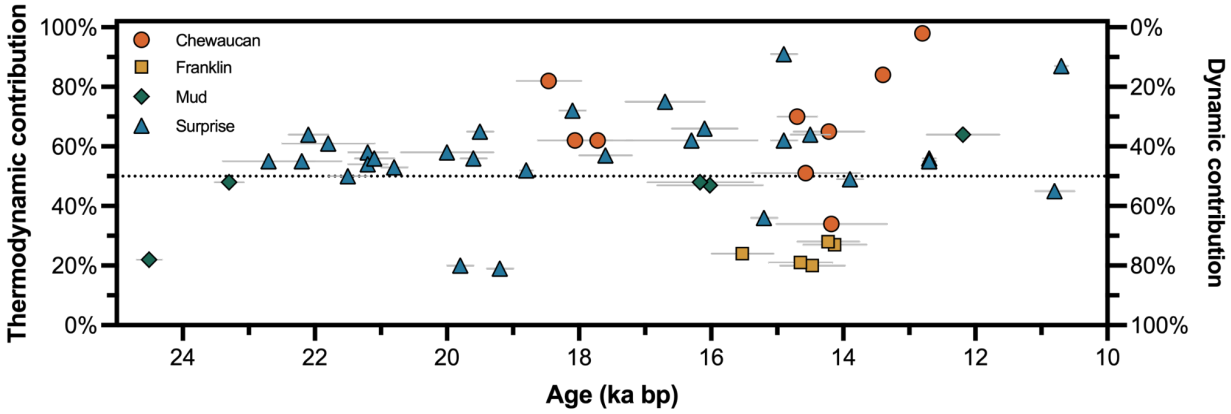

Figure 3.3: Partitioning of dynamic and thermodynamic controls on lake levels through time. Derivation of thermodynamic and dynamic contributions can be found in the Supplementary Material (Supplementary Equation 11).

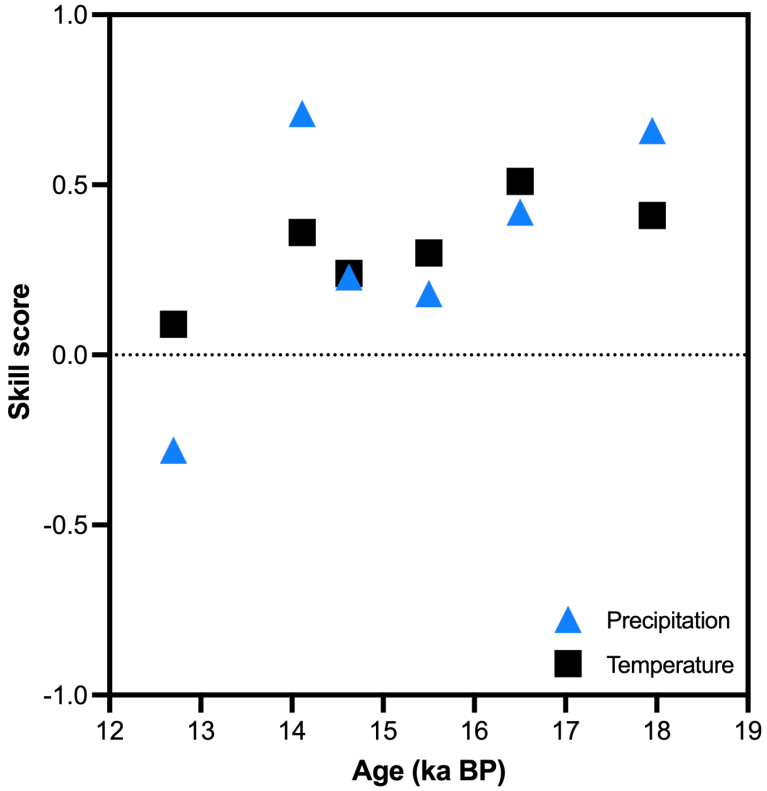

Figure 3.4: Model skill evaluation for simulations of surface temperature and annual precipitation anomalies using TraCE-21 ka. Black and blue symbols reflect the skill score for temperature and precipitation, respectively. Skill scores are calculated during intervals that contain samples with two or more basins (Table 3.A.5). Modern climatological data is included in Table 3.1. To calculate anomalies from TraCE-21ka, we use temporal averages for each interval relative to the preindustrial simulation.

7. Tables

Lake Basin	GPS Location	Location of Modern Climate Data	Mean Annual Air Temperature (°C)	Mean Annual Precipitation Rate (mm/yr)	Mean Annual Pan Evaporation Rate (mm/yr)	Lake Highstand Age (ka BP)
Lake Chewaucan	42.7°N, 120.5°W	Summer Lake, OR	9.6 ± 0.7	377 ± 90	1364 ± 80	13.0 - 14.5
Lake Franklin	40°N, 115°W	Ruby Valley, NV	8.2 ± 0.7	456 ± 90	1307 ± 90	16.8 – 15.1
Mud Lake	37.8°N, 118°W	Tonopah, NV	11.1± 0.8	164 ± 80	1615 ± 80	Unknown
Lake Surprise	41.5°N, 120°W	Cedarville, CA	9.4 ± 0.8	566 ± 165	1066 ± 80	15.2

Table 3.1: Modern climatological averages at each lake basin**.** Modern climatological data is compiled from previous sources (Ibarra et al., 2014; Licciardi, 2001; Munroe & Laabs, 2013; Santi et al., 2019; Western Regional Climate Center, 2023) and this study.

8. Supplement

Text S1: Methods Supplement

Radiocarbon Dating

Samples from Lake Surprise were radiocarbon dated via Accelerator Mass Spectrometry (AMS) at UC Irvine (Santi et al., 2019), Beta Analytic, Inc (Ibarra et al., 2014), and DirectAMS (Egger et al., 2018). Samples from Lake Franklin were dated using AMS methods at UC Irvine (Santi et al., 2019), the National Ocean Sciences Accelerator Mass Spectrometry facility (NOSAMS) (Munroe & Laabs, 2013), or by a combination of AMS and traditional radiocarbon dating (Lillquist, 1995). Samples from Mud Lake in this study were dated via AMS methods at UC Irvine (Santi et al., 2019), while those from previous publications were dated using conventional radiocarbon techniques (Dickerson, 2009). Samples from Lake Chewaucan were dated by the Arizona AMS Laboratory (Hudson et al., 2017). For all samples, we use *IntCal13* to convert conventional ^{14}C ages to calibrated ^{14}C ages, expressed as thousands of years before present, "ka". We plot the median calibrated probability and the 2σ uncertainty. All conventional and calibrated ages are included in previous publications (Santi et al., 2019).

Clumped Isotope Measurements

Mass spectrometry was completed at UCLA on a trio of mass spectrometers. On the first of the three machines, a Thermo 253 Dual Inlet Gas Source isotope ratio mass spectrometer (IRMS), 5 mg of carbonate is introduced using a McCrea-style common acid bath for sample digestion. Acid temperature is held constant between 89.0°C to 90.5°C. After dissolution of carbonate samples in the common acid bath, the resultant mixture of gas (primarily CO_2, but also N_2, O_2, and other trace gases) is purified in an automated vacuum line, which removes

contaminant gases based on their differential freezing points. The liberated gas passes through two separate gas traps to ensure removal of water and other compounds: the first, containing ethanol, is kept at -76°C using dry ice, and the second is kept at -196°C by liquid nitrogen. The sample gas is then passed through a silver wool "getter", which removes sulfur compounds. Remaining trace contaminants (e.g. halocarbons and hydrocarbons) are separated by moving the resultant gas through a Thermo Trace GC Ultra gas chromatograph column, which is filled with a divinylbenzene polymer trap, Porapak Q, at -20°C. After reaction in the GC, the sample is moved to a dual inlet IRMS. The ion source is maintained at 16,000 mV, and the amount of reference gas is automatically adjusted to produce a gas pressure that matches that of the standard. Each sample is measured for a total of nine acquisitions over the course of 2.3 hours, with each acquisition consisting of a peak centering, background adjustment, and ten measurements of alternate cycling between sample and reference gas ionization (Spencer & Kim, 2015). CO_2 gas standards (equilibrated at 25 and 1000°C), ETH 1-4 (Bernasconi et al., 2021), and in-house carbonate standards (Lucarelli et al., 2023) with known isotopic composition were run every 2-3 analyses.

The other two mass spectrometers contain nuCarb sample preparation systems interfaced to a Nu Perpsective IRMS. These machines both utilize the acid drip method, whereby a small amount (200 μL) of phosphoric acid is released into individual vials containing 0.5 mg of carbonate sample, and the resultant CO_2 gas from each vial is sequentially analyzed on the mass spectrometer. After conversion to CO_2 gas, an initial sample beam is recorded for each sample. Depending on the magnitude of this beam, samples are either stored in the sample bellows or the sample coldfinger (a small volume chamber in front of the capillary), before transfer to the mass spectrometer. Each gas sample is measured in the Perspective IRMS for a total of three

acquisitions with 20 sample-reference measurement cycles. Throughout each measurement, the sample and reference beams are monitored and adjusted, such that a beam current of 50 nA (user-specified) is maintained. The total measurement time for the NuCarb coupled to the Perspective IRMS is ~1.5 hours per sample, and the internal precision is 0.01‰. Carbonate standards, including the ETH suite and in-house standards, were measured between every 3-4 samples. Standard values for each machine configuration can be found in Table 3.A.4.

Raw mass spectrometer data for $\delta^{13}C$, $\delta^{18}O$, Δ_{47}, and Δ_{48} were processed in Easotope (John & Bowen, 2016) using the Brand parameter set. Samples measured using the Thermo MAT 253 used two compositions of CO_2 gas standards equilibrated at two temperatures, ETH-1, and ETH-2 were used to correct for non-linearity within the mass spectrometer. Non-linearity in samples measured using the nuCarb system were corrected for using only ETH-1 and ETH-2. For all machines, raw Δ_{47} values were projected into the Intercarb-Carbon Dioxide Equilibration Scale (I-CDES) using the ETH suite of materials and in-house standards, with accepted values from Bernasconi et al. (2021) and Lucarelli et al. (2023), respectively.

Replicates were excluded due to elevated organic content (anomalous Δ_{48} or Δ_{49} values; 3σ threshold) or anomalous values of Δ_{47} (I-CDES), $\delta^{13}C$ (VPDB) or $\delta^{18}O$ (VPDB) (3σ threshold from the remaining replicates), which can reflect incomplete digestion or contamination (Tripati et al., 2015). Each sample was replicated at least three times, unless there was insufficient material available. For samples with three or more replicates, uncertainty is reported as one standard error. For samples with less than three replicates, uncertainty is estimated by propagating both the internal standard error for the sample and the average external reproducibility of the samples in this study.

Hydroclimate modeling

The following description of hydroclimate modeling is based on methodology developed in previous publications (Hren & Sheldon, 2012; Ibarra et al., 2014; Jones et al., 2007; Linacre, 1993), and is also previously reported as supplemental text to published manuscripts (Santi et al., 2020).

Estimating Lake Area and Basin Hypsometry

The pluvial hydrologic index, $(A_l/(A_w - A_l))$, or "*HI*" is a physical basin parameter that describes the ratio of lake surface area (A_l) to tributary area (A_w), and is a primary input in our precipitation rate calculation. Historically, it has been used as a means to determine the partitioning of rainfall into runoff and evaporation and otherwise approximate past hydroclimate, assuming minimal change in drainage area and a basin's hypsometric curvature (Ibarra et al., 2014, 2018; Mifflin & Wheat, 1979; Reheis, 1999). We calculate the *HI* corresponding to each shoreline as a function of sample elevation using a hypsometric curve from the HydroSHEDS/HydroBASINS datasets (Lehner et al., 2008; Lehner & Grill, 2013).

Lake Evaporation Rate

In this work, we use a robust equation for lake-based evaporation (Linacre, 1993) that relies on inputs of latitude (*Lat*), temperature (*T*), dew-point temperature (T_d), wind speed (u), and elevation (z), and has been used for previous paleoclimate reconstructions (Ibarra et al., 2014; Mering, 2015; Santi et al., 2020). For our primary calculations, we assume u and z have remained constant through time, and that T_d is offset a constant amount from temperature, which is reasonable, assuming small changes in relative humidity, *RH* (Ibarra et al., 2014; Mering,

2015; Santi et al., 2020). Estimates of *RH*, T_d, and *u* for each sample site are derived from the North American Regional Reanalysis (Mesinger et al., 2006). We assume that *T* is equal to MAAT, but this assumption may bias our calculated evaporation rates to high values, where the lake was frozen over (thus inhibiting evaporation) for a significant amount of each year.

$$E_L(mm/yr) = [0.015 + 4 * 10^{-4}T + 10^{-6}z] \times [\frac{480(T+0.006z)}{84-Lat} - 40 + 2.3u(T - T_d)] \quad (1)$$

To calculate evaporation anomalies, we translate modern pan evaporation rates to modern lake evaporation rates using a pan coefficient of 0.9 (Linacre, 1994; Matsubara & Howard, 2009).

Weighted Evaporation Rate

To allow for more direct comparison between our clumped isotope derived lake evaporation rates (E_L) and PMIP3 evapotranspiration (‘*ET’)* rates, we create a weighted evaporation that scales E_L and *ET* from our models by the size of lake area and tributary area, respectively. *ET* is estimated as precipitation (‘P’) minus runoff, (‘k_{run}’), both of which are calculated in our model (see below).

$$Weighted\ Evaporation = \frac{(P*(1-K_{run}\times A_t)+E_l\times A_l}{A_t+A_l} \quad (2)$$

Lake Precipitation Rate

Beginning with the time-varying (t) water balance and $\delta^{18}O$ isotope mass balance equations for an inward draining lake and applying the product rule, we derive a function for calculating precipitation rate (modified from equations and derivations in previous publications (Ibarra et al., 2018; Jones et al., 2007; Steinman & Abbott, 2013). The change in lake volume (V_L) is:

$$\frac{dV_L}{dt} = Q_w - Q_e \quad (3)$$

where Q is the input (*w*) and evaporative (*e*) fluxes. Input fluxes are assumed to be both k_{run} and *P* at this point, but are partitioned in subsequent equations using a runoff coefficient. Similarly, the isotope mass balance equation is given by:

$$\frac{d(\delta^{18}O_L \times V_L)}{dt} = (\delta^{18}O_w \times Q_w) - (\delta^{18}O_e \times Q_e) \quad (4)$$

Applying the product rule to equation (4), substituting the mass balance equation into the isotope balance equation and rearranging yields an expression for time-varying changes in lake water:

$$V_L \frac{d(\delta^{18}O_L)}{dt} + \delta^{18}O_L \frac{d(V_L)}{dt} = (\delta^{18}O_w \times Q_w) - (\delta^{18}O_e \times Q_e) \quad (5)$$

$$V_L \frac{d(\delta^{18}O_L)}{dt} = (\delta^{18}O_w - \delta^{18}O_L) \times Q_w - (\delta^{18}O_e - \delta^{18}O_L) \times Q_e \quad (6)$$

Assuming steady state and solving for *P*, and assuming that $Q_e = A_L E_L$ and $Q_w = (P_L \times A_L) + (k_{run} \times P_L \times (A_w - A_L))$, where *A* is area of the lake (A_L) and watershed (A_w), we obtain an expression for the basin average precipitation rate, *P*:

$$P = \frac{E_L}{1 + \frac{k_{run}}{\left(\frac{A_L}{A_w - A_L}\right)}} \times \frac{(\delta^{18}O_e - \delta^{18}O_L)}{(\delta^{18}O_w - \delta^{18}O_L)} \quad (7)$$

This equation includes the commonly used "pluvial hydrologic index", *HI*, modified by the isotope mass balance differences between lake water, input water, and evaporating water vapor. In previous work, a value for k_{run} was assumed (Ibarra et al., 2014); however, modern hydrologic observations suggest a non-linear response of k_{run} to changes in *P* (Greve et al., 2015; Matsubara & Howard, 2009). We use the single parameter formulation for the Budyko curve calibrated for the coterminous United States (Greve et al., 2015).

$$1 - k_{run} = \frac{ET}{P} = 1 + \frac{E_p}{P} - \left(1 + \left(\frac{E_p}{P}\right)^{\omega}\right)^{1/\omega} \quad (8)$$

where E_p is potential evapotranspiration (which we approximate by constraints on E_L from the clumped isotope results, described above), and ω is the adjustable calibrated Budyko landscape

parameter. The use of this Budyko framework in terminal basin hydrologic modeling has been demonstrated in spatially explicit hydrologic modeling (Barth et al., 2016; Matsubara & Howard, 2009), and in similar regional modeling for Plio-Pleistocene watersheds of the Great Basin (Ibarra et al., 2018), justifying the incorporation of ω into this simplified isotope mass balance framework.

Given knowledge of evaporation rates and basin hypsometry, calculation or measurement of $\delta^{18}O$ values and assumptions of ω, equations (7) and (8) can be solved simultaneously for P and k_{run}, given a calculated E_L and lake water $\delta^{18}O$ estimated from clumped isotopes. Because of the non-linear nature of both equations we use a root-finding procedure to solve for the unknowns. This is carried out using the *multiroot* function in the R package 'rootSolve' (Soetaert et al., 2010), which uses a numerical Newton-Raphson method to find the roots of the two equations. Errors are propagated through random draws in the Monte Carlo routine by bootstrapping *RH,* T_d, and u, and assuming normal distributions for all input variable values (mean and standard deviation) except for ω, which has a skewed gamma distribution as calibrated for the continental United States (Greve et al., 2015).

Prior to implementing the simultaneous solution to equations (7) and (8), several model variables need to be determined to populate the equations. We estimate E_L using equation (1). We also implement a transfer function to calculate MAAT from using clumped-isotope derived seasonally biased lake water temperatures water temperatures, T_w (Terrazas et al., 2023), latitude (φ) and elevation (z):

$$\text{AMJ MAAT (°C)} = 0.977 * T_w + 0.0036 * T_w^2 - 0.0597 * \varphi - 0.0006 * z - 4.41 \quad (9)$$

$$\text{JJA MAAT (°C)} = 0.224 * \text{LSWT} + 0.0266 * \text{LSWT}^2 - 0.130 * \varphi - 0.0003 * z - 3.80 \quad (10)$$

Basin hypsometric curves provide constraints on lake area (A_L) and basin area (A_w). Lake water isotopic composition ($\delta^{18}O_L$) is calculated from clumped isotope derived temperature and the temperature dependent equilibrium fractionation factor (Kim et al., 2007). Meteoric water inputs ($\delta^{18}O_w$) into the lake are constrained from the modern average using the Online Isotopes in Precipitation Calculator (Bowen, 2023) and were corrected to reflect the influence of ice caps on the global oxygen isotopic reservoir (Tripati et al., 2014). Finally, to calculate the isotopic composition of evaporation ('$\delta^{18}O_e$'; Craig & Gordon, 1965), the following assumptions are made:

1. We model evaporating vapor $\delta^{18}O$ based on the Craig & Gordon (1965)[30] evaporation model, as simplified by (Gat, 1996). The kinetic fractionation factor is, ε, is a simple function of *RH*: 1000 ln (α_{kin}) ≈ ε = 14.2× (1–*RH*/100)[32].

2. The atmospheric vapor above the basin is in equilibrium with the incoming rainwater, which is calculated using the temperature dependent equilibrium fractionation factor equation (Majoube, 1971). This parameter is needed to estimate $\delta^{18}O_e$ in equation (7).

This approach differs from previous studies, which assume a kinetic fractionation of α_{kin} = 0.994 for $u \leq 6.8$ m/s (Ibarra et al., 2014; Jones et al., 2007). In similar work for closed-basin lake modeling (Ibarra et al., 2014, 2018), the kinetic fractionation factor using the above equation was found to better approximate the range of possible values (given likely variations in *RH*), and has been used elsewhere (Gonfiantini, 1986).

Quantifying Thermodynamic and Dynamical Controls on Lake Level

We estimate the thermodynamic contribution to changing lake levels using the following procedure:

1. We calculate the precipitation anomaly for each sample, using LGM and deglacial precipitation rates (equation 7) along with the modern precipitation rate reported in Table 3.1.
2. We calculate a weighted evaporation anomaly, using LGM and deglacial weighted evaporation rates (equation 2). For modern weighted evaporation rates, we assume a steady state condition, whereby modern weighted evaporation is equal to modern precipitation.
3. We then calculate the thermodynamic contribution as the weighted evaporation anomaly divided by the total anomaly (equation 10). The dynamic contribution is, by definition, (100% minus equation 10).

$$Thermodynamic\ Component\ (\%) = 100 \times \frac{(e_{weighted} - P_{modern})}{(e_{weighted} - P_{modern}) + (P - P_{modern})} \quad (11)$$

Note that this calculation assumes that all changes in *ET* and E_L are due to reduced temperatures and remaining moisture balance to build the lake is driven by increased *P* delivered by dynamic mechanisms. Thus, for samples with higher formation temperatures and thus higher E_L, equation (10) is negative. For these samples we do not report an assessment of thermodynamic vs. dynamic contribution to the mass balance solutions. This framework used here is a first order attempt to link the thermodynamic and dynamic mechanisms for moisture convergence on a region used in studies of the terrestrial moisture budget (Lora, 2018; Seager et

al., 2014), where the thermodynamic mechanism is changes in specific humidity independent of circulation and the dynamic mechanism represents changes in circulation (i.e. moisture delivery) independent of humidity changes.

Quantifying Model Skill

As in previous assessments of climate model performance (Hargreaves et al., 2013; Lora, 2018), we quantify model skill using an equation that weighs the ability of climate models to reproduce the magnitude and distribution of T_w and P estimates from clumped isotopes:

$$SS = 1 - \sqrt{\frac{\sum(m_i - o_i)^2 - \sum(e_i)^2}{\sum(n_i - o_i)^2 - \sum(e_i)^2}} \quad (12)$$

where m_i are the forecast results (from TraCE-21ka), n_i is the reference state (in our case, taken to be zero, or no change between the LGM and present), and o_i are the observations (from clumped isotope analysis). Results should be interpreted as a model's skill in simulating past climatic changes with respect to the null hypothesis, of no change between the LGM and modern. A perfect simulation would have a score of 1, a score of 0 would indicate that the model and reference state (no change) perform equally well, and a negative score would indicate that model error is greater than in the case of the null hypothesis.

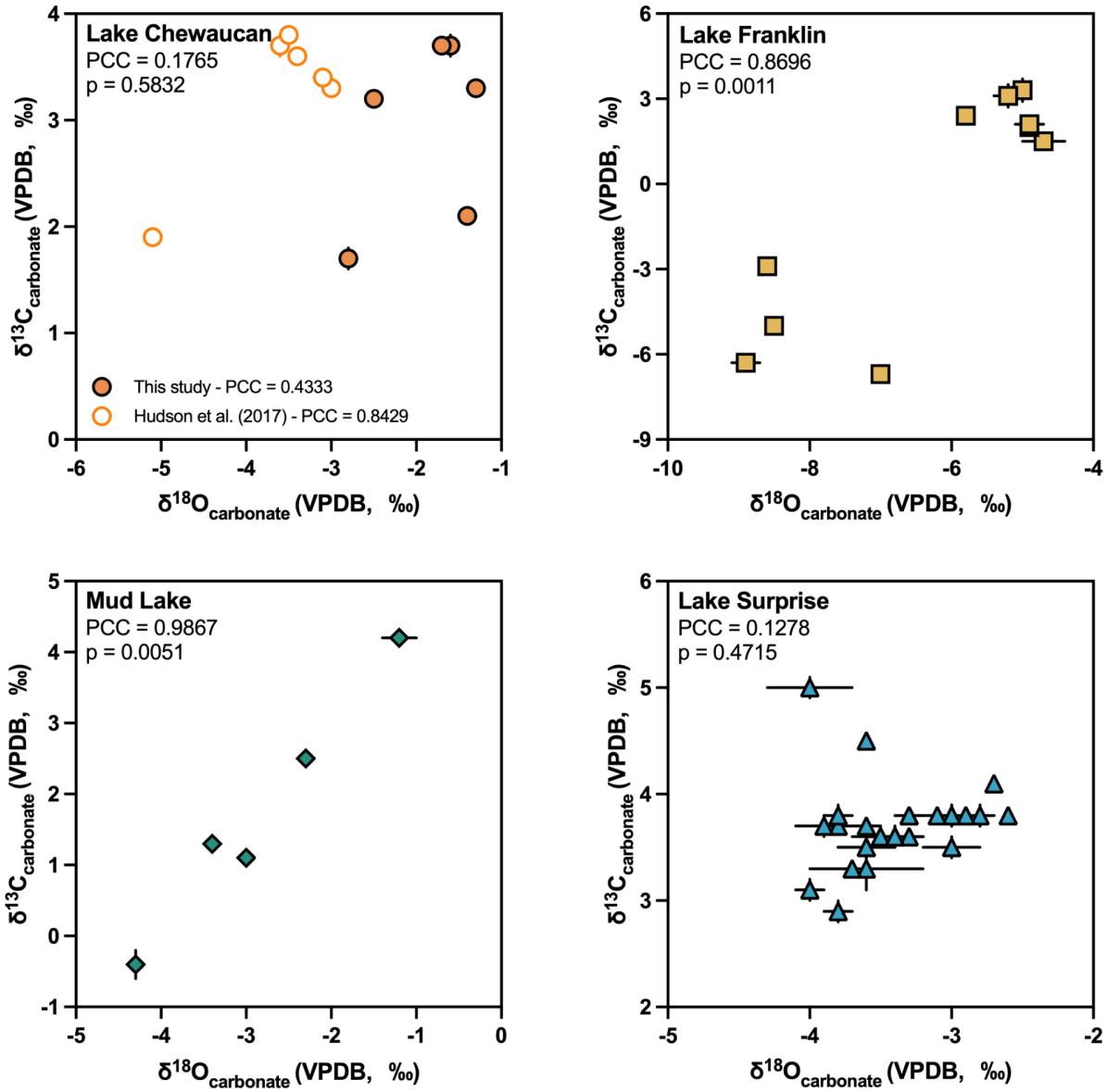

Fig. 3.A.1: $\delta^{13}C$ - $\delta^{18}O$ covariance plots. Positive correlation of carbon and oxygen isotopes provides evidence of closed lake basin behavior. Note that for some samples, error bars are smaller than the marker. Samples from this work (filled circles) and others (open circles) (Dickerson, 2006, 2009; Egger et al., 2018; Hudson et al., 2017; Santi et al., 2020).

Data Supplement

Lake Basin	Sample Name	Sample Type	Elevation (m)	^{14}C Age	^{14}C Age SD	IntCal13 Age (ka)	2σ min	2σ max	Source
Chewaucan	SL15AE02	Tufa	1383	21.92	0.09	26.12	25.92	26.38	Egger et al. (2018)
Chewaucan	SL15AE05	Tufa	1343	11.57	0.04	13.40	13.30	13.48	Egger et al. (2018)
Chewaucan	SL15AE06	Tufa	1328	11.87	0.04	13.68	13.57	13.77	Egger et al. (2018)
Chewaucan	SL15AE08	Tufa	1344	10.98	0.04	12.83	12.73	12.97	Egger et al. (2018)
Chewaucan	SL15JH05	Tufa	1345	12.49	0.05	14.70	14.30	15.03	Egger et al. (2018)
Chewaucan	SLT3-1B	Tufa	1316	12.53	0.04	14.84	14.77	15.11	Egger et al. (2018)
Chewaucan	CHL13-5	Tufa	1346	12.27	0.04	14.22	14.03	14.41	Hudson et al. (2017)
Chewaucan	CHL14-29-1	Tufa	1340	12.26	0.04	14.18	13.84	14.52	Hudson et al. (2017)
Chewaucan	CHL13-2	Tufa	1346	12.44	0.40	14.57	14.24	14.90	Hudson et al. (2017)
Chewaucan	CHL13-22	Tufa	1298	14.54	0.07	17.72	17.51	17.93	Hudson et al. (2017)
Chewaucan	CHL14-30	Tufa	1303	15.19	0.08	18.46	18.25	18.67	Hudson et al. (2017)
Chewaucan	CHL14-32-1	Tufa	1301	14.85	0.09	18.06	17.81	18.31	Hudson et al. (2017)
Franklin	FranklinRW1_60_1A	Gastropod	1826	12.26	0.11	14.23	13.82	14.77	This study
Franklin	FranklinRW1_60_2A	Gastropod	1826	12.37	0.12	14.47	14.04	15.02	This study
Franklin	FranklinRW1_60_2B	Gastropod	1826	12.20	0.13	14.13	13.75	14.72	This study
Franklin	FranklinRW2_90_1A	Gastropod	1838	12.52	0.19	14.71	14.04	15.34	This study
Franklin	FranklinRW2_90_1B	Gastropod	1838	12.40	0.16	14.53	14.00	15.14	This study
Franklin	FranklinRW3_78_1A	Gastropod	1841	12.48	0.12	14.65	14.16	15.12	This study
Franklin	FranklinRW3_78_1B	Gastropod	1841	12.91	0.12	15.44	15.09	15.82	This study
Franklin	FranklinRW3_78_1C	Gastropod	1841	12.67	0.12	15.03	14.38	15.45	This study
Franklin	FranklinHS186_1B	Gastropod	1843	13.23	0.14	15.89	15.41	16.28	This study
Franklin	FranklinHS1_86_1C	Gastropod	1843	12.98	0.16	15.53	15.09	16.03	This study
Mud	CMud17_2	Tufa	1593	10.38	0.19	12.19	11.60	12.70	This study
Mud	ML07-04	Tufa	1590	-	-	16.02	15.86	16.18	Dickerson et al. (2006)
Mud	ML08-03	Tufa	1590	-	-	16.62	16.46	16.78	Dickerson et al. (2006)
Mud	ML08-04	Tufa	1582	-	-	24.75	24.35	25.15	Dickerson et al. (2006)
Mud	RD05-95	Stromatolite	1595	-	-	23.56	23.22	23.90	Dickerson et al. (2006)
Surprise	SVCW17-PT1	Tufa	1439	18.78	0.27	22.70	22.04	23.35	Santi et al. (2019)
Surprise	SVCW17-PT2	Tufa	1439	18.35	0.27	22.18	21.53	22.81	Santi et al. (2019)

Surprise	SVCW17-PT3	Tufa	1473	14.46	0.17	17.61	17.14	18.01	Santi et al. (2019)
Surprise	SVCW 17-PT4	Tufa	1428	18.03	0.28	21.82	21.08	22.44	Santi et al. (2019)
Surprise	SVDI 11-T14-1A	Tufa	1428	16.59	0.29	20.02	19.28	20.71	Ibarra et al. (2014)
Surprise	SVDI 11-T14-1B	Tufa	1475	13.52	0.34	16.30	15.29	17.29	Ibarra et al. (2014)
Surprise	SVDI 11-T14-1C	Tufa	1475	13.39	0.16	16.11	15.64	16.61	Ibarra et al. (2014)
Surprise	SVDI 11-T14-E	Tufa	1477	13.79	0.19	16.68	16.13	17.26	Ibarra et al. (2014)
Surprise	SVDI 11-T2-1	Tufa	1475	8.09	0.11	9.01	8.63	9.31	Ibarra et al. (2014)
Surprise	SVDI 11-T3-2	Tufa	1478	10.79	0.05	12.70	12.64	12.76	Ibarra et al. (2014)
Surprise	SVDI 11-T4-1b	Tufa	1478	10.79	0.05	12.70	12.64	12.76	Ibarra et al. (2014)
Surprise	SVDI 12-T1	Tufa	1478	10.79	0.05	12.70	12.64	12.76	Ibarra et al. (2014)
Surprise	SVDI 12-T10-A	Tufa	1478	10.79	0.05	12.70	12.64	12.76	Ibarra et al. (2014)
Surprise	SVDI 12-T10-B	Tufa	1454	15.93	0.07	19.21	18.99	19.46	Ibarra et al. (2014)
Surprise	SVDI 12-T13	Tufa	1438	17.58	0.07	21.25	20.98	21.51	Ibarra et al. (2014)
Surprise	SVDI 12-T14-1C	Tufa	1431	17.28	0.06	20.84	20.63	21.05	Ibarra et al. (2014)
Surprise	SVDI 12-T14	Tufa	1420	17.56	0.60	21.22	20.97	21.46	Ibarra et al. (2014)
Surprise	SVDI 12-T15-B	Tufa	1517	12.60	0.07	14.96	14.94	15.18	Ibarra et al. (2014)
Surprise	SVDI 12-T3-A	Tufa	1517	12.60	0.05	14.96	14.94	15.18	Ibarra et al. (2014)
Surprise	SVDI 12-T3-B	Tufa	1437	17.49	0.09	21.13	20.84	21.43	Ibarra et al. (2014)
Surprise	SVDI 12-T4-A	Tufa	1531	12.75	0.05	15.19	15.01	15.36	Ibarra et al. (2014)
Surprise	SVDI 12-T4-B	Tufa	1531	10.79	0.05	12.71	12.64	12.76	Ibarra et al. (2014)
Surprise	SVDI 12-T5b	Tufa	1433	16.15	0.07	19.49	19.25	19.70	Ibarra et al. (2014)
Surprise	SVDI 12-T7	Tufa	1444	9.47	0.04	10.71	10.58	10.79	Ibarra et al. (2014)
Surprise	SVDI 12-T9	Tufa	1509	12.42	0.05	14.52	14.18	14.88	Ibarra et al. (2014)
Surprise	SVDI 15-AE01	Tufa	1462	15.55	0.06	18.81	18.66	18.94	Egger et al. (2018)
Surprise	SVDI 15-AE02	Tufa	1470	14.86	0.05	18.07	17.89	18.26	Egger et al. (2018)
Surprise	SVDI 15-AE03	Tufa	1491	12.09	0.05	13.96	13.79	14.10	Egger et al. (2018)
Surprise	SVDI 15-AE05	Tufa	1443	17.70	0.06	21.43	21.17	21.69	Egger et al. (2018)
Surprise	SVDI 15-AE06	Tufa	1437	18.20	0.10	22.07	21.82	22.34	Egger et al. (2018)
Surprise	SVDI 15-BM03	Tufa	1440	14.13	0.06	17.20	16.98	17.44	Egger et al. (2018)
Surprise	SVDI 15-BM04	Tufa	1459	16.20	0.06	19.56	19.34	19.78	Egger et al. (2018)
Surprise	SVDI 15-BM08	Tufa	1441	17.73	0.07	21.46	21.19	21.73	Egger et al. (2018)

Surprise	SVDI 15-BM09	Tufa	1456	16.43	0.06	19.82	19.61	20.03	Egger et al. (2018)

Table 3.A.1: Compiled stable isotope data for carbonate samples. Table includes new data from this study and additional stable isotope data compiled from other publications (Dickerson, 2009; Hudson et al., 2017; Ibarra et al., 2014; Santi et al., 2020)

Lake Basin	Sample Name	n	$\delta^{13}C$ (‰, VPDB)	SD	$\delta^{18}O$ (‰, VPDB)	SD	Δ_{47} (‰, ICDES)	SE	Water $\delta^{18}O$ (‰, VSMOW)	SD
Chewaucan	SL15AE02	10	3.7	0.1	-1.6	0.1	0.635	0.006	-3.0	0.3
Chewaucan	SL15AE05	7	3.2	0.0	-2.5	0.0	0.621	0.007	-3.0	0.6
Chewaucan	SL15AE06	5	3.7	0.0	-1.7	0.0	0.630	0.006	-2.1	0.5
Chewaucan	SL15AE08	10	2.1	0.0	-1.4	0.1	0.614	0.006	-1.0	0.4
Chewaucan	SL15JH05	8	3.3	0.0	-1.3	0.1	0.615	0.006	-1.3	0.4
Chewaucan	SLT3-1B	6	1.7	0.1	-2.8	0.1	0.656	0.009	-4.8	0.8
Chewaucan	CHL13-5*	6	3.3	0.0	-3.0	0.1	0.745	0.011	-3.6	0.7
Chewaucan	CHL14-29-1*	4	3.6	0.0	-3.4	0.0	0.779	0.014	-5.5	0.9
Chewaucan	CHL13-2*	6	3.4	0.0	-3.1	0.1	0.804	0.011	-6.3	0.7
Chewaucan	CHL13-22*	6	3.7	0.1	-3.6	0.0	0.765	0.012	-6.2	0.7
Chewaucan	CHL14-30*	4	1.9	0.0	-5.1	0.0	0.781	0.014	-7.9	0.9
Chewaucan	CHL14-32-1*	4	3.8	0.0	-3.5	0.0	0.777	0.014	-6.3	0.9
Franklin	FranklinRW1_60_1A	11	1.5	0.2	-4.7	0.3	0.632	0.004	-6.6	0.3
Franklin	FranklinRW1_60_2A	9	2.0	0.3	-4.9	0.1	0.631	0.003	-6.8	0.3
Franklin	FranklinRW1_60_2B	7	2.1	0.1	-4.9	0.2	0.632	0.009	-6.9	0.7
Franklin	FranklinRW2_90_1A	10	3.3	0.4	-5.0	0.1	0.644	0.005	-7.9	0.4
Franklin	FranklinRW2_90_1B	8	2.4	0.1	-5.8	0.1	0.638	0.005	-8.2	0.3
Franklin	FranklinRW3_78_1A	7	-6.3	0.1	-8.9	0.2	0.624	0.006	-10.5	0.4
Franklin	FranklinRW3_78_1B	3	-2.9	0.2	-8.6	0.0	0.638	0.004	-11.1	0.3
Franklin	FranklinRW3_78_1C	10	3.1	0.4	-5.2	0.2	0.641	0.004	-7.9	0.3
Franklin	FranklinHS186_1B	5	-5.0	0.1	-8.5	0.1	0.634	0.006	-9.0	0.4
Franklin	FranklinHS1_86_1C	10	-6.7	0.3	-7.0	0.1	0.631	0.006	-6.7	0.4
Mud	CMud17_2	15	4.2	0.1	-1.2	0.2	0.621	0.003	-2.2	0.3
Mud	ML07-04	10	-0.4	0.2	-4.3	0.1	0.617	0.004	-1.1	0.3
Mud	ML08-03	26	2.5	0.0	-2.3	0.1	0.617	0.003	-3.2	0.4
Mud	ML08-04	10	1.1	0.0	-3.0	0.0	0.634	0.005	-1.4	0.3
Mud	RD05-95	4	1.3	0.1	-3.4	0.1	0.603	0.004	-4.4	0.4
Surprise	SVCW17-PT1	6	3.7	0.0	-3.8	0.0	0.652	0.006	-6.1	0.4
Surprise	SVCW17-PT2	8	3.7	0.0	-3.8	0.1	0.649	0.004	-5.9	0.3

Surprise	SVCW17-PT3	8	3.7	0.1	-3.9	0.2	0.648	0.003	-5.9	0.3
Surprise	SVCW 17-PT4	6	3.8	0.1	-3.8	0.1	0.645	0.005	-4.9	0.3
Surprise	SVDI 11-T14-1A	6	4.1	0.0	-2.7	0.0	0.651	0.003	-4.8	0.2
Surprise	SVDI 11-T14-1B	2	3.8	0.0	-2.9	0.0	0.652	0.007	-5.6	0.1
Surprise	SVDI 11-T14-1C	9	3.8	0.1	-2.8	0.1	0.643	0.005	-3.5	0.5
Surprise	SVDI 11-T14-E	1	3.8	0.0	-2.9	0.0	0.640	0.010	-3.8	0.6
Surprise	SVDI 11-T2-1	7	3.8	0.1	-3.0	0.2	0.642	0.006	-4.8	0.5
Surprise	SVDI 11-T3-2	10	3.3	0.2	-3.6	0.4	0.652	0.005	-6.0	0.4
Surprise	SVDI 11-T4-1b	9	3.8	0.1	-3.0	0.1	0.660	0.004	-6.1	0.3
Surprise	SVDI 12-T1	8	3.6	0.1	-3.5	0.1	0.655	0.003	-6.2	0.2
Surprise	SVDI 12-T10-A	11	3.5	0.1	-3.6	0.2	0.649	0.008	-5.6	0.6
Surprise	SVDI 12-T10-B	10	3.6	0.1	-3.4	0.1	0.651	0.005	-5.6	0.4
Surprise	SVDI 12-T13	5	3.8	0.0	-3.3	0.1	0.657	0.008	-6.0	0.5
Surprise	SVDI 12-T14-1C	4	3.7	0.0	-3.6	0.1	0.642	0.009	-5.1	0.7
Surprise	SVDI 12-T14	1	3.8	0.0	-2.6	0.0	0.646	0.010	-4.1	0.5
Surprise	SVDI 12-T15-B	2	3.8	0.0	-3.1	0.0	0.637	0.015	-5.4	0.8
Surprise	SVDI 12-T3-A	9	3.6	0.1	-3.4	0.2	0.650	0.007	-5.7	0.5
Surprise	SVDI 12-T3-B	9	3.6	0.1	-3.4	0.2	0.646	0.005	-5.8	0.5
Surprise	SVDI 12-T4-A	10	3.6	0.0	-3.3	0.1	0.654	0.003	-5.9	0.2
Surprise	SVDI 12-T4-B	7	3.6	0.0	-3.3	0.1	0.657	0.004	-6.1	0.3
Surprise	SVDI 12-T5b	2	3.3	0.0	-3.7	0.0	0.644	0.004	-4.9	0.3
Surprise	SVDI 12-T7	13	5.0	0.1	-4.0	0.3	0.655	0.003	-6.6	0.2
Surprise	SVDI 12-T9	10	3.6	0.0	-3.4	0.1	0.653	0.005	-5.5	0.3
Surprise	SVDI 15-AE01	4	3.8	0.0	-3.3	0.1	0.630	0.006	-3.9	0.4
Surprise	SVDI 15-AE02	3	3.6	0.1	-3.5	0.2	0.632	0.003	-5.8	1.0
Surprise	SVDI 15-AE03	6	3.5	0.1	-3.0	0.2	0.639	0.009	-4.1	0.6
Surprise	SVDI 15-AE05	4	2.9	0.1	-3.8	0.1	0.646	0.011	-5.8	0.8
Surprise	SVDI 15-AE06	4	3.6	0.1	-3.4	0.2	0.640	0.013	-5.8	0.9
Surprise	SVDI 15-BM03	3	4.5	0.0	-3.6	0.0	0.642	0.008	-5.2	0.6
Surprise	SVDI 15-BM04	12	3.1	0.1	-4.0	0.1	0.657	0.004	-6.8	0.3
Surprise	SVDI 15-BM08	4	3.5	0.1	-3.6	0.2	0.626	0.006	-4.3	0.3

Surprise	SVDI 15-BM09	5	3.6	0.1	-3.4	0.2	0.642	0.011	-5.5	0.9

Table 3.A.2: New clumped and stable isotope results for northern Great Basin pluvial lakes. *Existing clumped and stable isotope analyses from Hudson et al. (2017); clumped isotope values are presented in the 25°C CDES reference frame and water temperatures are sourced from the original publication.

Lake Basin	Sample Name	MAAT	MAAT (+/- SE)	E_L	E_L (+/- SD)	P	P (+/- SD)	k_{run}	k_{run} (+/- SD)
Chewaucan	SL15AE02	4.5	3.1	888	292	429	232	0.145	0.101
Chewaucan	SL15AE05	8.7	3.8	1008	263	477	238	0.145	0.100
Chewaucan	SL15AE06	7.7	3.5	1005	256	416	229	0.123	0.101
Chewaucan	SL15AE08	11.8	3.3	1143	174	383	216	0.096	0.090
Chewaucan	SL15JH05	10	3.5	1085	218	368	219	0.099	0.089
Chewaucan	SLT3-1B	0.8	4.2	609	345	376	258	0.195	0.110
Chewaucan	CHL13-5	6.6	4.1	915	304	486	255	0.164	0.106
Chewaucan	CHL14-29-1	-0.7	4.8	541	343	360	261	0.217	0.113
Chewaucan	CHL13-2	-4.8	4.1	344	267	245	205	0.236	0.110
Chewaucan	CHL13-22	-1.7	4.1	468	318	325	245	0.233	0.111
Chewaucan	CHL14-30	-2.8	4.8	469	326	362	269	0.275	0.112
Chewaucan	CHL14-32-1	-2.8	4.8	465	329	327	254	0.237	0.116
Franklin	FranklinRW1_60_1A	3.7	3	861	231	726	221	0.326	0.099
Franklin	FranklinRW1_60_2A	4.1	3	888	226	758	221	0.333	0.1
Franklin	FranklinRW1_60_2B	4	3.9	792	277	665	253	0.325	0.101
Franklin	FranklinRW2_90_1A	0.1	3.2	615	281	544	259	0.398	0.114
Franklin	FranklinRW2_90_1B	1.9	3.1	729	284	648	262	0.417	0.115
Franklin	FranklinRW3_78_1A	6.5	3.3	904	217	840	211	0.458	0.103
Franklin	FranklinRW3_78_1B	1.7	3	576	127	554	114	0.574	0.061
Franklin	FranklinRW3_78_1C	1.1	3	683	278	616	260	0.423	0.115
Franklin	FranklinHS186_1B	4.4	3.3	896	229	853	217	0.474	0.096
Franklin	FranklinHS1_86_1C	9.9	3.5	996	206	902	201	0.389	0.114
Mud	CMud17_2	-3.3	3.2	346	224	151	118	0.117	0.063
Mud	ML07-04	4.9	3.3	1020	335	405	205	0.105	0.062
Mud	ML08-03	10.2	3.4	1358	250	616	255	0.127	0.07
Mud	ML08-04	9.4	3.2	1339	252	538	223	0.108	0.063
Mud	RD05-95	-2.5	3.4	396	254	191	147	0.139	0.074
Surprise	SVCW17-PT1	-0.1	3.3	514	323	446	291	0.308	0.088
Surprise	SVCW17-PT2	0.6	3	568	320	486	284	0.294	0.088
Surprise	SVCW17-PT3	1	3	614	323	525	288	0.297	0.088

Surprise	SVCW 17-PT4	2.1	3.1	733	353	579	300	0.253	0.089
Surprise	SVDI 11-T14-1A	-1.2	3	443	286	337	229	0.246	0.092
Surprise	SVDI 11-T14-1B	-3.4	2.8	279	210	235	183	0.283	0.088
Surprise	SVDI 11-T14-1C	6.2	3.5	1111	356	700	264	0.194	0.093
Surprise	SVDI 11-T14-E	4.8	4.5	944	421	625	312	0.205	0.094
Surprise	SVDI 11-T2-1	3.1	3.5	844	386	609	304	0.231	0.092
Surprise	SVDI 11-T3-2	-0.2	3.2	515	319	421	274	0.27	0.086
Surprise	SVDI 11-T4-1b	-3.2	3	304	224	248	190	0.269	0.083
Surprise	SVDI 12-T1	-1.3	2.9	407	267	328	226	0.261	0.08
Surprise	SVDI 12-T10-A	1.2	3.6	658	377	558	333	0.294	0.097
Surprise	SVDI 12-T10-B	0.1	3.2	543	329	467	292	0.293	0.092
Surprise	SVDI 12-T13	-1.1	3.6	470	318	383	272	0.272	0.088
Surprise	SVDI 12-T14-1C	3.7	4.4	876	422	714	367	0.273	0.099
Surprise	SVDI 12-T14	1.7	4.1	734	411	537	324	0.229	0.093
Surprise	SVDI 12-T15-B	1	4.6	675	413	505	332	0.246	0.094
Surprise	SVDI 12-T3-A	0.7	3.5	604	354	468	292	0.249	0.087
Surprise	SVDI 12-T3-B	0.2	3.3	554	334	432	276	0.254	0.087
Surprise	SVDI 12-T4-A	-0.9	2.9	425	271	344	231	0.263	0.084
Surprise	SVDI 12-T4-B	-1.6	3.1	395	273	327	236	0.277	0.086
Surprise	SVDI 12-T5b	2.4	3	752	357	559	288	0.239	0.088
Surprise	SVDI 12-T7	-1.5	2.9	380	262	343	240	0.352	0.086
Surprise	SVDI 12-T9	0.4	3.1	565	326	482	291	0.288	0.091
Surprise	SVDI 15-AE01	8	3.3	1243	311	797	241	0.201	0.092
Surprise	SVDI 15-AE02	0.3	4.8	644	418	524	359	0.279	0.103
Surprise	SVDI 15-AE03	4.7	4	973	400	682	313	0.222	0.095
Surprise	SVDI 15-AE05	2	4.4	737	413	590	351	0.262	0.092
Surprise	SVDI 15-AE06	0.4	4.7	628	404	492	336	0.259	0.094
Surprise	SVDI 15-BM03	3.1	3.7	831	396	623	323	0.243	0.09
Surprise	SVDI 15-BM04	-1.8	3	363	246	324	224	0.344	0.084
Surprise	SVDI 15-BM08	8.4	3	1299	276	852	230	0.204	0.088
Surprise	SVDI 15-BM09	3.9	5.2	843	443	657	372	0.259	0.099

Table 3.A.3: Hydroclimatic parameter results for individual samples. Mean annual air temperature (MAAT), lake evaporation (E_L), precipitation (P), and runoff coefficient (k_{run}) are displayed with one standard deviation.

Standard	Mass Spectrometer	n	$\delta^{13}C$ (‰, VPDB)	1 s.e.	$\delta^{18}O$ (‰, VPDB)	1 s.e.	Δ_{47} (‰, ICDES)	1 s.e.
Carmel Chalk	BB8-NuCarb	43	-2.2	0.0	-3.9	0.0	0.587	0.003
Carmel Chalk	Chewbacca	244	-2.2	0.0	-4.0	0.0	0.594	0.001
Carmel Chalk	R2D2 - NuCarb	32	-2.2	0.0	-4.0	0.0	0.594	0.004
Carmel Chalk	R2D2-Sar-Bel	49	-2.2	0.0	-3.9	0.0	0.591	0.003
Carrera CalTech	Chewbacca	102	2.3	0.0	-1.7	0.0	0.307	0.002
Carrera Marble	Chewbacca	112	2.1	0.0	-1.5	0.0	0.310	0.002
Carrera Marble	R2D2-Sar-Bel	37	2.0	0.0	-1.5	0.0	0.317	0.004
CMTile	BB8-NuCarb	58	2.0	0.0	-1.5	0.0	0.320	0.002
CMTile	Chewbacca	70	2.0	0.0	-1.5	0.0	0.314	0.002
CMTile	R2D2 - NuCarb	53	2.0	0.0	-1.5	0.0	0.313	0.002
CMTile	R2D2-Sar-Bel	8	2.0	0.0	-1.5	0.0	0.308	0.006
ETH-1	BB8-NuCarb	94	2.0	0.0	-2.2	0.0	0.205	0.002
ETH-1	Chewbacca	132	2.0	0.0	-2.2	0.0	0.207	0.002
ETH-1	R2D2 - NuCarb	47	2.0	0.0	-2.2	0.0	0.206	0.003
ETH-1	R2D2-Sar-Bel	30	2.0	0.0	-2.2	0.0	0.205	0.004
ETH-2	BB8-NuCarb	91	-10.2	0.0	-18.7	0.0	0.206	0.003
ETH-2	Chewbacca	114	-10.2	0.0	-18.7	0.0	0.209	0.002
ETH-2	R2D2 - NuCarb	45	-10.2	0.0	-18.7	0.0	0.206	0.004
ETH-2	R2D2-Sar-Bel	22	-10.1	0.0	-18.7	0.0	0.207	0.005
ETH-3	BB8-NuCarb	37	1.7	0.0	-1.7	0.0	0.608	0.004
ETH-3	Chewbacca	84	1.7	0.0	-1.8	0.0	0.615	0.003
ETH-3	R2D2 - NuCarb	29	1.7	0.0	-1.7	0.0	0.610	0.004
ETH-3	R2D2-Sar-Bel	22	1.7	0.0	-1.8	0.0	0.617	0.005
ETH-4	BB8-NuCarb	48	-10.2	0.0	-18.8	0.0	0.442	0.003
ETH-4	Chewbacca	103	-10.2	0.0	-18.8	0.0	0.447	0.002
ETH-4	R2D2 - NuCarb	21	-10.2	0.0	-18.8	0.0	0.446	0.004
ETH-4	R2D2-Sar-Bel	29	-10.2	0.0	-18.8	0.0	0.451	0.004
IAEA-C1	BB8-NuCarb	21	2.4	0.0	-2.3	0.0	0.295	0.010
IAEA-C1	Chewbacca	22	2.4	0.0	-2.3	0.0	0.302	0.010

IAEA-C1	R2D2 - NuCarb	17	2.4	0.0	-2.3	0.0	0.305	0.012
IAEA-C2	BB8-NuCarb	20	-8.1	0.0	-8.9	0.0	0.644	0.004
IAEA-C2	Chewbacca	13	-8.1	0.0	-8.9	0.0	0.628	0.005
IAEA-C2	R2D2 - NuCarb	14	-8.1	0.0	-8.9	0.0	0.638	0.005
Mallinckrodt	Chewbacca	8	-40.3	0.0	-22.0	0.0	0.470	0.012
MERCK	BB8-NuCarb	26	-42.0	0.0	-15.7	0.1	0.516	0.009
MERCK	Chewbacca	13	-41.9	0.0	-15.8	0.1	0.510	0.013
MERCK	R2D2 - NuCarb	13	-42.0	0.0	-15.7	0.1	0.515	0.013
NBS 19	Chewbacca	7	1.9	0.0	-2.1	0.0	0.326	0.016
Spel 2-8-E	Chewbacca	22	-9.4	0.1	-6.2	0.0	0.610	0.008
TV01	Chewbacca	10	2.4	0.1	-8.8	0.5	0.564	0.051
TV03	Chewbacca	48	2.6	0.0	-8.4	0.0	0.624	0.003
TV03	R2D2-Sar-Bel	31	2.6	0.0	-8.4	0.0	0.625	0.004
TV03-CalTech	Chewbacca	24	3.3	0.0	-8.3	0.0	0.624	0.003
Veinstrom	BB8-NuCarb	69	-6.2	0.0	-12.6	0.0	0.638	0.003
Veinstrom	Chewbacca	147	-6.2	0.0	-12.6	0.0	0.631	0.002
Veinstrom	R2D2 - NuCarb	39	-6.2	0.0	-12.6	0.0	0.636	0.003
Veinstrom	R2D2-Sar-Bel	46	-6.2	0.0	-12.6	0.0	0.633	0.003

Table 3.A.4: Stable and clumped isotope results for standards used for corrections.

Time (ka BP)	Number of basins	Skill score: temperature	Skill score: precipitation
18,400 - 17,501	2 (Chewaucan, Surprise)	0.41	0.46
17,000 - 16,001	2 (Mud, Surprise)	0.23	0.51
16,000 - 15,001	2 (Franklin, Surprise)	0.25	0.39
14,900 - 14,351	3 (Chewaucan, Surprise, Franklin)	0.18	0.48
14,350 - 13,871	3 (Chewaucan, Surprise, Franklin)	0.26	0.53
12,900 - 12,501	2 (Chewaucan, Surprise)	0.06	-0.28

Table 3.A.5: Skill scores calculated for temperature and precipitation anomalies using the TraCE-21ka transient climate model.

Supplementary References

Barth, C., Boyle, D.P., Hatchett, B.J., Bassett, S.D., Garner, C.B. & Adams, K.D. (2016) Late Pleistocene climate inferences from a water balance model of Jakes Valley, Nevada (USA). *Journal of Paleolimnology*, *56*(2), 109–122.

Bernasconi, S.M., Daëron, M., Bergmann, K.D., Bonifacie, M., Meckler, A.N., Affek, H.P., Anderson, N., Bajnai, D., Barkan, E., Beverly, E., Blamart, D., Burgener, L., Calmels, D., Chaduteau, C., Clog, M., Davidheiser-Kroll, B., Davies, A., Dux, F., Eiler, J., Elliott, B., Fetrow, A.C., Fiebig, J., Goldberg, S., Hermoso, M., Huntington, K.W., Hyland, E., Ingalls, M., Jaggi, M., John, C.M., Jost, A.B., Katz, S., Kelson, J., Kluge, T., Kocken, I.J., Laskar, A., Leutert, T.J., Liang, D., Lucarelli, J., Mackey, T.J., Mangenot, X., Meinicke, N., Modestou, S.E., Müller, I.A., Murray, S., Neary, A., Packard, N., Passey, B.H., Pelletier, E., Petersen, S., Piasecki, A., Schauer, A., Snell, K.E., Swart, P.K., Tripati, A., Upadhyay, D., Vennemann, T., Winkelstern, I., Yarian, D., Yoshida, N., Zhang, N. & Ziegler, M. (2021) InterCarb: A Community Effort to Improve Interlaboratory Standardization of the Carbonate Clumped Isotope Thermometer Using Carbonate Standards. *Geochemistry, Geophysics, Geosystems*, *22*(5), e2020GC009588. https://doi.org/10.1029/2020GC009588.

Bowen, G.J. (2023) The Online Isotopes in Precipitation Calculator (Version 3.1).

Craig, H. & Gordon, L.I. (1965) Deuterium and oxygen 18 variations in the ocean and the marine atmosphere.

Dickerson, R.P. (2006) *Old Lakes and Young Playas: The Nellis Air Force Base Geological Study and Quaternary History of Four Playas on the Nevada Test and Training Range*.

US Army Corps of Engineers.

Dickerson, R.P. (2009) Lakes, wetlands, and meadows, paleoclimate and environments of the playas of the Nevada Test and Training Range. *Morgan Printing, Austin, Texas, 154p*.

Egger, A.E., Ibarra, D.E., Weldon, R., Langridge, R.M., Marion, B., Hall, J., Starratt, S.W. & Rosen, M.R. (2018) Influence of pluvial lake cycles on earthquake recurrence in the northwestern Basin and Range, USA. *Geological Society of America Special Paper*, *536*, 1–28. https://doi.org/doi:10.1130/2018.2536(07).

Gat, J.R. (1996) OXYGEN AND HYDROGEN ISOTOPES IN THE HYDROLOGIC CYCLE. *Annual Review of Earth and Planetary Sciences*, *24*(Volume 24, 1996), 225–262. https://doi.org/10.1146/annurev.earth.24.1.225.

Gonfiantini, R. (1986) Environmental isotopes in lake studies. *Handbook of Environmental Isotope Geochemistry*.

Greve, P., Gudmundsson, L., Orlowsky, B. & Seneviratne, S.I. (2015) Introducing a probabilistic Budyko framework. *Geophysical Research Letters*, *42*(7), 2261–2269. https://doi.org/10.1002/2015GL063449.

Hargreaves, J.C., Annan, J.D., Ohgaito, R., Paul, A. & Abe-Ouchi, A. (2013) Skill and reliability of climate model ensembles at the Last Glacial Maximum and mid-Holocene. *Climate of the Past*, *9*(2), 811–823. https://doi.org/10.5194/cp-9-811-2013.

Hren, M.T. & Sheldon, N.D. (2012) Temporal variations in lake water temperature: Paleoenvironmental implications of lake carbonate δ18O and temperature records. *Earth and Planetary Science Letters*, *337*, 77–84. https://doi.org/10.1016/j.epsl.2012.05.019.

Hudson, A.M., Quade, J., Ali, G., Boyle, D., Bassett, S., Huntington, K.W., De los Santos, M.G., Cohen, A.S., Lin, K. & Wang, X. (2017) Stable C, O and clumped isotope systematics

and 14C geochronology of carbonates from the Quaternary Chewaucan closed-basin lake system, Great Basin, USA: Implications for paleoenvironmental reconstructions using carbonates. *Geochimica et Cosmochimica Acta*, *212*, 274–302. https://doi.org/10.1016/j.gca.2017.06.024.

Ibarra, D.E., Egger, A.E., Weaver, K.L., Harris, C.R. & Maher, K. (2014) Rise and fall of late Pleistocene pluvial lakes in response to reduced evaporation and precipitation: Evidence from Lake Surprise, California. *GSA Bulletin*, *126*(11–12), 1387–1415. https://doi.org/10.1130/B31014.1.

Ibarra, D.E., Oster, J.L., Winnick, M.J., Caves Rugenstein, J.K., Byrne, M.P. & Chamberlain, C.P. (2018) Warm and cold wet states in the western United States during the Pliocene–Pleistocene. *Geology*, *46*(4), 355–358.

John, C.M. & Bowen, D. (2016) Community software for challenging isotope analysis: First applications of 'Easotope' to clumped isotopes: Community software for challenging isotope analysis. *Rapid Communications in Mass Spectrometry*, *30*(21), 2285–2300. https://doi.org/10.1002/rcm.7720.

Jones, M.D., Roberts, C.N. & Leng, M.J. (2007) Quantifying climatic change through the last glacial–interglacial transition based on lake isotope palaeohydrology from central Turkey. *Quaternary Research*, *67*(3), 463–473.

Kim, S.-T., O'Neil, J.R., Hillaire-Marcel, C. & Mucci, A. (2007) Oxygen isotope fractionation between synthetic aragonite and water: Influence of temperature and Mg2+ concentration. *Geochimica et Cosmochimica Acta*, *71*(19), 4704–4715. https://doi.org/10.1016/j.gca.2007.04.019.

Lehner, B. & Grill, G. (2013) Global river hydrography and network routing: baseline data and

new approaches to study the world's large river systems. *Hydrological Processes*, *27*(15), 2171–2186. https://doi.org/10.1002/hyp.9740.

Lehner, B., Verdin, K. & Jarvis, A. (2008) New Global Hydrography Derived From Spaceborne Elevation Data. *Eos, Transactions American Geophysical Union*, *89*(10), 93–94. https://doi.org/10.1029/2008EO100001.

Lillquist, K.D. (1995) *Late Quaternary Lake Franklin: Lacustrine chronology, coastal geomorphology, and hydro-isostatic deflection in Ruby Valley and northern Butte Valley, Nevada* (Ph.D.). The University of Utah, United States -- Utah.

Linacre, E.T. (1993) Data-sparse estimation of lake evaporation, using a simplified Penman equation. *Agricultural and Forest Meteorology*, *64*(3–4), 237–256. https://doi.org/10.1016/0168-1923(93)90031-C.

Linacre, E.T. (1994) Estimating U.S. Class A Pan Evaporation from Few Climate Data. *Water International*, *19*(1), 5–14. https://doi.org/10.1080/02508069408686189.

Lora, J.M. (2018) Components and Mechanisms of Hydrologic Cycle Changes over North America at the Last Glacial Maximum. *Journal of Climate*, *31*(17), 7035–7051. https://doi.org/10.1175/JCLI-D-17-0544.1.

Lucarelli, J.K., Carroll, H.M., Ulrich, R.N., Elliott, B.M., Coplen, T.B., Eagle, R.A. & Tripati, A. (2023) Equilibrated Gas and Carbonate Standard-Derived Dual (Δ47 and Δ48) Clumped Isotope Values. *Geochemistry, Geophysics, Geosystems*, *24*(2), e2022GC010458. https://doi.org/10.1029/2022GC010458.

Majoube, M. (1971) Oxygen-18 and deuterium fractionation between water and steam. *J. Clim. Phys.*, *68*(10), 1423.

Matsubara, Y. & Howard, A.D. (2009) A spatially explicit model of runoff, evaporation, and

lake extent: Application to modern and late Pleistocene lakes in the Great Basin region, western United States. *Water Resources Research*, *45*(6). https://doi.org/10.1029/2007WR005953.

Mering, J.A. (2015) *New constraints on water temperature at Lake Bonneville from carbonate clumped isotopes*. University of California, Los Angeles.

Mesinger, F., DiMego, G., Kalnay, E., Mitchell, K., Shafran, P.C., Ebisuzaki, W., Jović, D., Woollen, J., Rogers, E., Berbery, E.H., Ek, M.B., Fan, Y., Grumbine, R., Higgins, W., Li, H., Lin, Y., Manikin, G., Parrish, D. & Shi, W. (2006) North American Regional Reanalysis. *Bulletin of the American Meteorological Society*, *87*(3), 343–360. https://doi.org/10.1175/BAMS-87-3-343.

Mifflin, M.D. & Wheat, M.M. (1979) *Pluvial lakes and estimated pluvial climates of Nevada*, Vol. 94. Mackay School of Mines, University of Nevada.

Munroe, J.S. & Laabs, B.J.C. (2013) Latest Pleistocene history of pluvial Lake Franklin, northeastern Nevada, USA. *GSA Bulletin*, *125*(3–4), 322–342. https://doi.org/10.1130/B30696.1.

Reheis, M. (1999) Highest Pluvial-Lake Shorelines and Pleistocene Climate of the Western Great Basin. *Quaternary Research*, *52*(2), 196–205. https://doi.org/10.1006/qres.1999.2064.

Santi, L., Arnold, A., Mering, J., Arnold, D., Tripati, A., Whicker, C. & Oviatt, C.G. (2019) Lake level fluctuations in the Northern Great Basin for the last 25,000 years. *Exploring Ends of Eras in the Eastern Mojave Desert: 2019 Desert Symposium Field Guide and Proceedings*, 176–186. https://doi.org/10.31223/osf.io/6as7t.

Santi, L., Arnold, A.J., Ibarra, D.E., Whicker, C.A., Mering, J.A., Lomarda, R.B., Lora, J.M. &

Tripati, A. (2020) Clumped isotope constraints on changes in latest Pleistocene hydroclimate in the northwestern Great Basin: Lake Surprise, California. *GSA Bulletin*, *132*(11–12), 2669–2683. https://doi.org/10.1130/B35484.1.

Seager, R., Neelin, D., Simpson, I., Liu, H., Henderson, N., Shaw, T., Kushnir, Y., Ting, M. & Cook, B. (2014) Dynamical and thermodynamical causes of large-scale changes in the hydrological cycle over North America in response to global warming. *Journal of Climate*, *27*(20), 7921–7948. https://doi.org/10.1175/JCLI-D-14-00153.1.

Soetaert, K., Cash, J. & Mazzia, F. (2010) Package bvpSolve, solving boundary value problems in R. *Journal of Statistical Software*, *33*(9), 1–25.

Spencer, C. & Kim, S.-T. (2015) Carbonate clumped isotope paleothermometry: a review of recent advances in CO2 gas evolution, purification, measurement and standardization techniques. *Geosciences Journal*, *19*(2), 357–374. https://doi.org/10.1007/s12303-015-0018-1.

Steinman, B.A. & Abbott, M.B. (2013) Isotopic and hydrologic responses of small, closed lakes to climate variability: Hydroclimate reconstructions from lake sediment oxygen isotope records and mass balance models. *Geochimica et Cosmochimica Acta*, *105*, 342–359. https://doi.org/10.1016/j.gca.2012.11.027.

Terrazas, A., Hwangbo, N., Arnold, A.J., Ulrich, R.N. & Tripati, A. (2023) Seasonal lake-to-air temperature transfer functions derived from an analysis of 965 modern lakes: A tool for lacustrine proxy model comparison. *Authorea Preprints*.

Tripati, A.K., Hill, P.S., Eagle, R.A., Mosenfelder, J.L., Tang, J., Schauble, E.A., Eiler, J.M., Zeebe, R.E., Uchikawa, J., Coplen, T.B., Ries, J.B. & Henry, D. (2015) Beyond temperature: Clumped isotope signatures in dissolved inorganic carbon species and the

influence of solution chemistry on carbonate mineral composition. *Geochimica et Cosmochimica Acta*, *166*, 344–371. https://doi.org/10.1016/j.gca.2015.06.021.

Tripati, A.K., Sahany, S., Pittman, D., Eagle, R.A., Neelin, J.D., Mitchell, J.L. & Beaufort, L. (2014) Modern and glacial tropical snowlines controlled by sea surface temperature and atmospheric mixing. *Nature Geoscience*, *7*(3), 205–209. https://doi.org/10.1038/ngeo2082.

9. References

Antevs, E. (1952) Cenozoic Climates of the Great basin. *Geologische Rundschau*, *40*(1), 94–108. https://doi.org/10.1007/BF01803218.

Barth, C., Boyle, D.P., Hatchett, B.J., Bassett, S.D., Garner, C.B. & Adams, K.D. (2016) Late Pleistocene climate inferences from a water balance model of Jakes Valley, Nevada (USA). *Journal of Paleolimnology*, *56*(2), 109–122.

Bartlein, P.J., Harrison, S.P., Brewer, S., Connor, S., Davis, B.A.S., Gajewski, K., Guiot, J., Harrison-Prentice, T.I., Henderson, A., Peyron, O., Prentice, I.C., Scholze, M., Seppä, H., Shuman, B., Sugita, S., Thompson, R.S., Viau, A.E., Williams, J. & Wu, H. (2011) Pollen-based continental climate reconstructions at 6 and 21 ka: a global synthesis. *Climate Dynamics*, *37*(3), 775–802. https://doi.org/10.1007/s00382-010-0904-1.

Comstock, J.P. & Ehleringer, J.R. (1992) Plant adaptation in the Great Basin and Colorado plateau. *The Great Basin Naturalist*, 195–215.

Dahle, J.R. (2021) Late Quaternary Glacier and Climate Change in the Northeastern Great Basin.

Dansgaard, W. (1964) Stable isotopes in precipitation. *Tellus*, *16*(4), 436–468. https://doi.org/10.3402/tellusa.v16i4.8993.

Dickerson, R.P. (2006) *Old Lakes and Young Playas: The Nellis Air Force Base Geological Study and Quaternary History of Four Playas on the Nevada Test and Training Range*. US Army Corps of Engineers.

Dickerson, R.P. (2009) Lakes, wetlands, and meadows, paleoclimate and environments of the playas of the Nevada Test and Training Range. *Morgan Printing, Austin, Texas, 154p*.

Egger, A.E., Ibarra, D.E., Weldon, R., Langridge, R.M., Marion, B., Hall, J., Starratt, S.W. & Rosen, M.R. (2018) Influence of pluvial lake cycles on earthquake recurrence in the

northwestern Basin and Range, USA. *Geological Society of America Special Paper*, *536*, 1–28. https://doi.org/doi:10.1130/2018.2536(07).

Galloway, R.W. (1970) The Full-Glacial Climate in the Southwestern United States. *Annals of the Association of American Geographers*, *60*(2), 245–256. https://doi.org/10.1111/j.1467-8306.1970.tb00719.x.

Ghosh, P., Adkins, J., Affek, H., Balta, B., Guo, W., Schauble, E.A., Schrag, D. & Eiler, J.M. (2006) 13C–18O bonds in carbonate minerals: a new kind of paleothermometer. *Geochimica et Cosmochimica Acta*, *70*(6), 1439–1456. https://doi.org/10.1016/j.gca.2005.11.014.

Hargreaves, J.C., Annan, J.D., Ohgaito, R., Paul, A. & Abe-Ouchi, A. (2013) Skill and reliability of climate model ensembles at the Last Glacial Maximum and mid-Holocene. *Climate of the Past*, *9*(2), 811–823. https://doi.org/10.5194/cp-9-811-2013.

He, F. (2011) *Simulating transient climate evolution of the last deglaciation with CCSM 3*.

Higgins, R.W., Janowiak, J.E. & Yao, Y.-P. (1996) A Gridded Hourly Precipitation Data Base for the United States [Proprietary Binary]. [object Object], p. 808.236 Mbytes. https://doi.org/10.5065/P6BM-VM62.

Horton, T.W., Defliese, W.F., Tripati, A.K. & Oze, C. (2016) Evaporation induced 18O and 13C enrichment in lake systems: A global perspective on hydrologic balance effects. *Quaternary Science Reviews*, *131*, 365–379. https://doi.org/10.1016/j.quascirev.2015.06.030.

Hostetler, S. & Benson, L.V. (1990) Paleoclimatic implications of the high stand of Lake Lahontan derived from models of evaporation and lake level. *Climate Dynamics*, *4*(3), 207–217.

Hren, M.T. & Sheldon, N.D. (2012) Temporal variations in lake water temperature: Paleoenvironmental implications of lake carbonate δ18O and temperature records. *Earth and Planetary Science Letters*, *337*, 77–84. https://doi.org/10.1016/j.epsl.2012.05.019.

Hudson, A.M., Quade, J., Ali, G., Boyle, D., Bassett, S., Huntington, K.W., De los Santos, M.G., Cohen, A.S., Lin, K. & Wang, X. (2017) Stable C, O and clumped isotope systematics and 14C geochronology of carbonates from the Quaternary Chewaucan closed-basin lake system, Great Basin, USA: Implications for paleoenvironmental reconstructions using carbonates. *Geochimica et Cosmochimica Acta*, *212*, 274–302. https://doi.org/10.1016/j.gca.2017.06.024.

Ibarra, D.E., Egger, A.E., Weaver, K.L., Harris, C.R. & Maher, K. (2014) Rise and fall of late Pleistocene pluvial lakes in response to reduced evaporation and precipitation: Evidence from Lake Surprise, California. *GSA Bulletin*, *126*(11–12), 1387–1415. https://doi.org/10.1130/B31014.1.

Ibarra, D.E., Oster, J.L., Winnick, M.J., Caves Rugenstein, J.K., Byrne, M.P. & Chamberlain, C.P. (2018) Warm and cold wet states in the western United States during the Pliocene–Pleistocene. *Geology*, *46*(4), 355–358.

Jones, M.D., Roberts, C.N. & Leng, M.J. (2007) Quantifying climatic change through the last glacial–interglacial transition based on lake isotope palaeohydrology from central Turkey. *Quaternary Research*, *67*(3), 463–473.

Licciardi, J.M. (2001) Chronology of latest Pleistocene lake-level fluctuations in the pluvial Lake Chewaucan basin, Oregon, USA. *Journal of Quaternary Science: Published for the Quaternary Research Association*, *16*(6), 545–553.

Lora, J.M. (2018) Components and Mechanisms of Hydrologic Cycle Changes over North

America at the Last Glacial Maximum. *Journal of Climate*, *31*(17), 7035–7051. https://doi.org/10.1175/JCLI-D-17-0544.1.

Lora, J.M., Mitchell, J.L., Risi, C. & Tripati, A.E. (2017) North Pacific atmospheric rivers and their influence on western North America at the Last Glacial Maximum. *Geophysical Research Letters*, *44*(2), 1051–1059. https://doi.org/10.1002/2016GL071541.

Lora, J.M., Mitchell, J.L. & Tripati, A.E. (2016) Abrupt reorganization of North Pacific and western North American climate during the last deglaciation. *Geophysical Research Letters*, *43*(22), 11,796-11,804. https://doi.org/10.1002/2016GL071244.

Lyle, M., Heusser, L., Ravelo, C., Yamamoto, M., Barron, J., Diffenbaugh, N.S., Herbert, T. & Andreasen, D. (2012) Out of the Tropics: The Pacific, Great Basin Lakes, and Late Pleistocene Water Cycle in the Western United States. *Science*, *337*(6102), 1629–1633. https://doi.org/10.1126/science.1218390.

Matsubara, Y. & Howard, A.D. (2009) A spatially explicit model of runoff, evaporation, and lake extent: Application to modern and late Pleistocene lakes in the Great Basin region, western United States. *Water Resources Research*, *45*(6). https://doi.org/10.1029/2007WR005953.

McGee, D., Moreno-Chamarro, E., Marshall, J. & Galbraith, E.D. (2018) Western US lake expansions during Heinrich stadials linked to Pacific Hadley circulation. *Science Advances*, *4*(11), eaav0118.

Mering, J.A. (2015) *New constraints on water temperature at Lake Bonneville from carbonate clumped isotopes*. University of California, Los Angeles.

Mifflin, M.D. & Wheat, M.M. (1979) *Pluvial lakes and estimated pluvial climates of Nevada*, Vol. 94. Mackay School of Mines, University of Nevada.

Munroe, J.S. & Laabs, B.J.C. (2013) Latest Pleistocene history of pluvial Lake Franklin, northeastern Nevada, USA. *GSA Bulletin*, *125*(3–4), 322–342. https://doi.org/10.1130/B30696.1.

Oster, J.L., Ibarra, D.E., Winnick, M.J. & Maher, K. (2015) Steering of westerly storms over western North America at the Last Glacial Maximum. *Nature Geoscience*, *8*(3), 201–205.

Petryshyn, V.A., Juarez Rivera, M., Agić, H., Frantz, C.M., Corsetti, F.A. & Tripati, A.E. (2016) Stromatolites in Walker Lake (Nevada, Great Basin, USA) record climate and lake level changes ~35,000years ago. *Palaeogeography, Palaeoclimatology, Palaeoecology*, *451*, 140–151. https://doi.org/10.1016/j.palaeo.2016.02.054.

Quirk, B.J., Moore, J.R., Laabs, B.J., Caffee, M.W. & Plummer, M.A. (2018) Termination II, last glacial maximum, and lateglacial chronologies and paleoclimate from Big Cottonwood Canyon, Wasatch Mountains, Utah. *GSA Bulletin*, *130*(11–12), 1889–1902.

Reheis, M. (1999) Highest Pluvial-Lake Shorelines and Pleistocene Climate of the Western Great Basin. *Quaternary Research*, *52*(2), 196–205. https://doi.org/10.1006/qres.1999.2064.

Rutz, J.J., Steenburgh, W.J. & Ralph, F.M. (2014) Climatological Characteristics of Atmospheric Rivers and Their Inland Penetration over the Western United States. *Monthly Weather Review*, *142*(2), 905–921. https://doi.org/10.1175/MWR-D-13-00168.1.

Santi, L., Arnold, A., Mering, J., Arnold, D., Tripati, A., Whicker, C. & Oviatt, C.G. (2019) Lake level fluctuations in the Northern Great Basin for the last 25,000 years. *Exploring Ends of Eras in the Eastern Mojave Desert: 2019 Desert Symposium Field Guide and Proceedings*, 176–186. https://doi.org/10.31223/osf.io/6as7t.

Santi, L., Arnold, A.J., Ibarra, D.E., Whicker, C.A., Mering, J.A., Lomarda, R.B., Lora, J.M. &

Tripati, A. (2020) Clumped isotope constraints on changes in latest Pleistocene hydroclimate in the northwestern Great Basin: Lake Surprise, California. *GSA Bulletin*, *132*(11–12), 2669–2683. https://doi.org/10.1130/B35484.1.

Schauble, E.A., Ghosh, P. & Eiler, J.M. (2006) Preferential formation of 13C–18O bonds in carbonate minerals, estimated using first-principles lattice dynamics. *Geochimica et Cosmochimica Acta*, *70*(10), 2510–2529. https://doi.org/10.1016/j.gca.2006.02.011.

Seager, R., Neelin, D., Simpson, I., Liu, H., Henderson, N., Shaw, T., Kushnir, Y., Ting, M. & Cook, B. (2014) Dynamical and thermodynamical causes of large-scale changes in the hydrological cycle over North America in response to global warming. *Journal of Climate*, *27*(20), 7921–7948. https://doi.org/10.1175/JCLI-D-14-00153.1.

Smith, D.B. & Reimann, C. (2008) Low-density geochemical mapping and the robustness of geochemical patterns. *Geochemistry: Exploration, Environment, Analysis*, *8*(3–4), 219–227. https://doi.org/10.1144/1467-7873/08-171.

Smith, G.I. & Street-Perrott, F.A. (1983) Pluvial lakes of the western United States. In: *The Late Pleistocene*. Minneapolis, Univ. Minn. Press, pp. 190–212.

Talbot, M.R. (1990) A review of the palaeohydrological interpretation of carbon and oxygen isotopic ratios in primary lacustrine carbonates. *Chemical Geology: Isotope Geoscience Section*, *80*(4), 261–279. https://doi.org/10.1016/0168-9622(90)90009-2.

Terrazas, A., Hwangbo, N., Arnold, A.J., Ulrich, R.N. & Tripati, A. (2023) Seasonal lake-to-air temperature transfer functions derived from an analysis of 965 modern lakes: A tool for lacustrine proxy model comparison. *Authorea Preprints*.

Thompson, R.S., Anderson, K.H. & Bartlein, P.J. (1999) *Quantitative paleoclimatic reconstructions from late Pleistocene plant macrofossils of the Yucca Mountain region*.

US Department of the Interior, US Geological Survey.

Unterman, M.B., Crowley, T.J., Hodges, K.I., Kim, S.-J. & Erickson, D.J. (2011) Paleometeorology: High resolution Northern Hemisphere wintertime mid-latitude dynamics during the Last Glacial Maximum. *Geophysical Research Letters*, *38*(23). https://doi.org/10.1029/2011GL049599.

Welker, J.M. (2012) ENSO effects on δ18O, δ2H and d-excess values in precipitation across the US using a high-density, long-term network (USNIP). *Rapid Communications in Mass Spectrometry*, *26*(17), 1893–1898.

Western Regional Climate Center (2023). Available at : https://wrcc.dri.edu/Climate/summaries.php.

Wolfe, B.B., Falcone, M.D., Clogg-Wright, K.P., Mongeon, C.L., Yi, Y., Brock, B.E., Amour, N.A.St., Mark, W.A. & Edwards, T.W.D. (2007) Progress in isotope paleohydrology using lake sediment cellulose. *Journal of Paleolimnology*, *37*(2), 221–231. https://doi.org/10.1007/s10933-006-9015-8.

Xie, P. & Arkin, P.A. (1996) Analyses of Global Monthly Precipitation Using Gauge Observations, Satellite Estimates, and Numerical Model Predictions. *Journal of Climate*, *9*(4), 840–858. https://doi.org/10.1175/1520-0442(1996)009<0840:AOGMPU>2.0.CO;2.

Yapp, C.J. (1985) D/H variations of meteoric waters in Albuquerque, New Mexico, U.S.A. *Journal of Hydrology*, *76*(1), 63–84. https://doi.org/10.1016/0022-1694(85)90090-3.

CHAPTER 4

Late-Pleistocene hydroclimates in Southwestern North America from clumped isotopes

Alexandrea J. Arnold, Andrew Kowler, Priyadarsi Roy, Alexa Terrazas, Velynda Smith, Lauren Santi, Aradhna Tripati

Abstract

During the Last Glacial Maximum (LGM, ~23,000-19,000 years ago; ka) and deglacial, when greenhouse gas concentrations were reduced and large ice sheets were prevalent, there were numerous pluvial lakes across Western North America. The drivers of these lakes in Mexico and the Southwestern US are poorly constrained and controversial. Here, we apply clumped isotopes to six lakes in Northern Mexico, New Mexico, and Arizona to quantify past lake water temperatures, the oxygen isotopic composition of lake water, evaporation, and precipitation rates, and study summer and winter moisture transport processes. Our results support cooler and wetter conditions prevailing throughout the LGM, with 70-300% increased precipitation in Arizona and New Mexico, relative to modern, largely due to winter-derived precipitation. Lakes in Northern Mexico were sustained by levels of precipitation that were ~50-60% higher than today, likely because of late summer to autumn precipitation from tropical cyclones.

1. Introduction

The Southwestern United States and Northern Mexico are poised to become hotter and more arid in the upcoming decades due to greenhouse gas emissions (Intergovernmental Panel on Climate Change (IPCC), 2023). While all climate models agree that it will warm and be drier, there is disagreement in the magnitude of temperature, evaporation, and precipitation changes,

which in turn poses a challenge to the robust management of water resources in this increasingly populated and drought-prone region. In addition to comparisons with the instrumental record which extends for a few centuries, an approach that can be used to narrow uncertainty in climate models is utilizing paleoclimatic proxies to evaluate and understand responses to changing climate forcings.

The Last Glacial Maximum (LGM; 23,000-19,000 years ago; ka) is a recent interval with well-defined boundary conditions, making it an ideal benchmark for modeling intercomparison projects to evaluate process representation using proxy data within models (Braconnot et al., 2012). During the Last Glacial Maximum and deglaciation, there is evidence for pluvial lakes in Northern Mexico and the Southwestern US (Allen and Anderson, 2000; Hudson et al., 2023; Waters, 1985; Ibarra et al., 2018; Roy et al., 2012, 2013, 2015, 2016). However, in contrast to the Great Basin, proxy data from these basins are much more sparse, limiting our ability to test hypotheses about the drivers of water balance. The presence of lakes could have been due to a reduction in evaporation rates from decreased temperatures, and/or increases in summer or winter precipitation; the magnitude of evaporation depression is unclear due to a lack of robust, quantitative paleotemperature data for lakes in the region. Winter precipitation to western North America was proposed to have been enhanced due to a split, southerly-shifted diverted jet stream and westerly storm track from the presence of large and extensive ice sheets on North America (COHMAP Members, 1988; Lora et al., 2016). The alteration of atmospheric pressure patterns may have diverted the location of atmospheric rivers further south and increased the intensity of winter precipitation delivery in these short-lived events (Lora et al., 2017) during both the LGM and during Heinrich Stadial 1 (HS1) (Oster et al., 2023). However, some past work on lakes from

Mexico has concluded that the influence of winter precipitation did not reach below 29° N (Roy et al., 2013).

Changes in summer precipitation have also been proposed to explain positive shifts in water balance in the region. During the summer months, 40 - 70% of rainfall in Arizona, New Mexico, and Northwestern Mexico occurs as precipitation delivered via the North American Monsoon (NAM) (Douglas et al., 1993). Previous studies have proposed that alteration of semi-permanent pressure systems during the LGM and deglaciation allowed for a strengthened monsoonal circulation, allowing for increased tropical and subtropical moisture transport towards the continental interior (Lyle et al., 2012). Conversely, work using leaf-wax biomarkers has led to the hypothesis that the westerlies, shifted by the ice sheet in the North, caused the mixing of cold and dry air into the NAM region and inhibited the energy necessary for convective precipitation from the NAM (Bhattacharya et al., 2018).

While the NAM is the primary contributor to modern precipitation in the majority of summer precipitation in Northwestern Mexico, precipitation delivered to Northeastern Mexico is derived from the Gulf of Mexico and Caribbean Sea via the Caribbean Lower-Level Jet (CLLJ) (Roy et al., 2019). Changes in insolation as well as sea surface temperatures have been proposed to alter the strength and direction of CLLJ during the LGM (Roy et al., 2016; Wright et al., 2023). Additionally, sites further South can also experience a precipitation maxima in the autumn months from moisture delivery from tropical cyclones in the Atlantic and Pacific (Roy et al., 2019). Increases in tropical cyclone frequency and alterations to cyclone tracks during the LGM has been used to explain regional patterns of wetness and aridity in proxy records throughout Mexico (Roy et al., 2015, 2020).

Here, we use the carbonate clumped isotope geochemistry of lacustrine sediments in endorheic basins from the region to quantify past temperatures, water $\delta^{18}O$, evaporation rates, and precipitation rates, and elucidate the drivers behind changes in terrestrial water balance. Since the balance between evaporation and precipitation is the primary influence on closed-basin lake levels, lacustrine sediments are sensitive to past climatological forcings and act as recorders of hydrologic change (e.g. Allen & Anderson, 2000; Hudson et al., 2023; Kowler, 2015). Carbonate clumped isotope thermometry is a recent tool that has been used on lacustrine carbonates to better understand past fluctuations in terrestrial hydroclimate (Hudson et al., 2017; Mering, 2015; Santi et al., 2020). This method is based on the bond abundance of heavy-isotope, or "clumped", pairs found within a carbonate minerals crystal lattice (Eiler, 2007; Schauble et al., 2006; Tripati et al., 2015). Prior work has shown that there is an inverse correlation between formation temperature of the carbonate and the abundance of ^{13}C-^{18}O bonds, with more (less) "clumping" occurring at lower (higher) temperatures (e.g. Ghosh et al., 2006, Arnold et al., 2023). Clumped isotope-derived estimates of temperature are independent of the composition of the fluid in which the mineral precipitated, therefore, the temperature constraint provided from clumped isotope analysis (denoted by Δ_{47}) paired with the concurrent measurement of the oxygen isotopic composition of the carbonate allows for back-calculation of the composition of the source water. We examine six late-Pleistocene lakes - Lake Cochise in Arizona, Lake Estancia and Playas Lake in New Mexico, and Laguna Babicora, Lake El Potosi, and Lake Santiaguillo in Mexico - that span 24 - 35°N and 104 - 110°W (Fig. 4.1) and compare results to climate model simulations.

2. Methods

2.1 Sample collection

Shorelines at each basin were identified for sampling locations using a combination of literature review and aerial photography from Google Earth. For gastropod samples, holes were dug roughly meter in depth and sediment was sieved, and shells were picked with tweezers. All samples were collected in situ, and GPS locations were recorded at location of sampling. GPS points were used in concert with the USGS Elevation Point Query Service to extract location elevation, which reports 1⁄3 arc-second elevation data with resolution of ~3 meters. Lakes that were sampled were small in area and volume, thus, isostatic rebound is not considered with our elevation estimates, though we note that it has been influential in other lake basins (e.g. Bonneville; Chen and Maloof (2017)). Kowler (2015) outlines site and sample collection for Playas Lake and sample AK-191 from Lake Cochise. Samples from Mexico were collected from pits dug on paleolake margins; more information regarding sample and site selection can be found in the original publications (Roy et al., 2012, 2015, 2016).

2.2 Sample preparation

A dremel drill was used to extract tufas and carbonate cements, with the resultant powder being broken down further with a mortar and pestle. Gastropod shells were scraped and sonicated to remove loose external material. Shells were then left to dry and crushed and powdered using a mortar and pestle. All powdered carbonate was oxidatively cleaned using methods outlined in Santi et al. (2020), in brief, carbonate was reacted with 3% hydrogen peroxide for 1-4 hours to remove organics (Eagle et al., 2013), and the remaining powder was

extracted on a cellulose filter and dried in an oven set at 40°C overnight to prevent bond reordering within the carbonate.

2.3. Dating constraints

Radiocarbon dating was performed at the University of California, Irvine with Accelerator Mass Spectrometry (AMS) for a subset of new samples presented in this study. Table 4.2 contains the uncalibrated ^{14}C ages and the median Intcal13 age for 5 new samples reported in this study. IntCal13 was used for all radiocarbon results (including those from other studies) to correct for reservoir effects (Reimer et al., 2013). The median probability and 2σ uncertainty are plotted (Figure 4.2). Previous studies have outlined the radiometric dating and age models for El Potosi, Santiaguillo, Babicora, Playas, and sample AK-191 in Cochise lake records (Kowler, 2015; Roy et al., 2012, 2015, 2016).

2.4. Stable and clumped isotope analysis

Powdered lacustrine carbonate samples used within this study were run on a trio of mass spectrometers at the University of California, Los Angeles from 2013 - 2021. More details on the suite of mass spectrometers used can be found in (Upadhyay et al., 2021). In brief, samples were run on two different systems: a Thermo MAT 253 used an automated carousel that required 5-6 mg of pure carbonate per analysis into 90°C common phosphoric acid bath and a Nu Perspective system that required 0.5 mg of pure carbonate per analysis with 70°C acid injected into individual vials to produce CO_2. In both cases, the resultant CO_2 first undergoes a water purification step using a series of traps at a gradient of temperatures: the first containing dry ice surrounding ethanol and the second, cooler trap containing liquid nitrogen. Following water

removal, the CO_2 passes through silver wool to remove sulfur compounds, and a gas chromatograph with Porapak Q to remove additional organic compounds. Following transit in the GC, the sample was analyzed in the mass spectrometer and measured against high purity Oztech CO_2 gas. Samples were dispersed between standards in each run. The Thermo MAT 253 used both gas standards (equilibrated at 25°C and 1000°C) and carbonate standards, while the Nu Perspective system used solely carbonate standards.

Raw data was processed using Easotope using a moving-correction window (John & Bowen, 2016). Non-linearity in the mass spectrometer was corrected with the ETH-1 and ETH-2 standards, and included the equilibrated gasses for the correction scheme for the Thermo MAT 253. Data was projected into the I-CDES 90°C reference frame using accepted standard values from Bernasconi et al. (2021) and Lucarelli et al. (2023).

At least four replicates of each sample were analyzed, unless limited sample material inhibited replication. Replicates were excluded from the analysis if there was evidence of contamination, as indicated by elevated raw Δ_{48} or Δ_{49} values. Incomplete digestion or contamination may also produce anomalous values of Δ_{47} (I-CDES), $\delta^{13}C$ (VPDB) or $\delta^{18}O$ (VPDB) (Tripati et al., 2015). We excluded samples if their values were more than 3σ from the remaining replicates.

2.5 Hydrologic modeling

Δ_{47} values were translated to lake water temperatures using material-specific calibrations derived in Arnold et al. (2023). The relationships derived in Kim & O'Neil (1997) and Kim et al. (2007) for calcite and aragonite, respectively, were used with calibrated water temperatures and measured $\delta^{18}O_{carbonate}$ values to calculate lake water $\delta^{18}O$. Water temperatures were then used to

calculate mean annual air temperatures by applying a seasonally-biased transfer function that relates satellite-derived lake water surface temperatures to mean annual air temperatures (Terrazas et al., 2023).

Lake evaporation rates (E_L) were estimated using a modified Penman equation, from (Linacre, 1993). Lake evaporation rates were calculated using mean annual air temperatures derived from clumped isotope analysis, wind speed and dew point temperature for each basin using North American Regional Reanalysis (Mesinger et al., 2006), and sample elevation and latitude. Modern pan evaporation rates were corrected using a pan coefficient of 0.7 to translate into lake evaporation rates (Linacre, 1994; Matsubara & Howard, 2009).

Precipitation rates were calculated using an isotopic mass balance hydrologic modeling framework that has been within other previous publications (Santi et al., 2020) (Equation 1). This approach incorporates basin hypsometry using the pluvial hydrologic index (HI: ratio of lake area to tributary area). Basin HIs were determined using catchment boundaries from HydroSHEDS and a digital elevation model from HydroBASINS (Lehner et al., 2008; Lehner & Grill, 2013). Lake water $\delta^{18}O$ ($\delta^{18}O_L$) was determined from clumped isotope analysis. The $\delta^{18}O$ of evaporation ($\delta^{18}O_E$) was modeled using Craig & Gordon (1965) and Gat (1996). Incoming $\delta^{18}O$ ($\delta^{18}O_w$) was determined using flux-weighted average for each site, using monthly precipitation data from nearby weather stations, and monthly meteoric $\delta^{18}O$ information from the Online Isotopes in Precipitation (Bowen, 2023) (Table 4.1). The runoff coefficient (k_{run}) was determined using a Budyko framework (Greve et al., 2015). More detail on the derivation of Equation 1 can be found in Santi et al. (2020). Precipitation (P) and the runoff coefficient (k_{run}) are solved simultaneously using the rootSolve package in R (Soetaert et al., 2010) and a Monte-Carlo sampling, with the assumption that all input variables are normally distributed.

$$P = \frac{E_L}{1+\frac{k_{run}}{HI}} \times \frac{(\delta^{18}O_e - \delta^{18}O_L)}{(\delta^{18}O_w - \delta^{18}O_L)} \quad (1)$$

2.6 Paleoclimate model skill evaluation

Hydroclimatic parameters constructed from clumped-isotope analyses from this study are compared to climate model output at each of our sites to assess proxy-model agreement. Climate models used in this study contain LGM and pre-industrial (PI) runs from 9 models from the Paleoclimate Modeling Intercomparison Project Phase 3 (PMIP3). Model output is used to calculate mean annual air temperature (variable: *tas*), precipitation (variable: *pr*), and evapotranspiration (variable: *esvpbl*) anomalies to assess model representation of changes from the LGM to the PI. Proxy anomalies are calculated using clumped-isotope derived parameters for the LGM and modern climate data for temperature and precipitation detailed in Table 1. Modern evapotranspiration data is derived from the 1991- 2020 normals from TerraClimate (Abatzoglou et al., 2018). For this analysis, we define the LGM as 21 ± 2 ka, including samples that are within error of the temporal range.

We use skill score as a metric to quantitatively assess proxy-model agreement, as has been done in other paleohydrology studies (Hargreaves et al., 2013; Lora, 2018; Lora & Ibarra, 2019; Santi et al., 2020). In our case, a skill score is testing the null hypothesis of no change from the LGM to the PI and can range from 1 to -∞. Positive values indicate good model performance relative to proxy data, a value of 0 indicates that the model performs no better than the reference state of no change, and negative values indicate accuracy performs worse than the reference state of no change. In equation 2, m_i represents the climate model anomaly, n_i is the reference state (assumed to be zero), and o_i and e_i are the proxy anomalies and their errors, respectively:

$$Skill\ score = 1 - \sqrt{\frac{\sum(m_i - o_i)^2 - \sum(e_i)^2}{\sum(n_i - o_i)^2 - \sum(e_i)^2}} \quad (2)$$

2.7 Partitioning of thermodynamic and dynamic controls on lake levels

We utilize a first-order calculation to partition thermodynamic and dynamic controls on lake levels. For our calculations, changes in evaporation are assumed to be primarily driven by changes in temperature and changes in precipitation are assumed to be delivered via dynamic mechanisms. Additionally, we assume that the modern water balance is in steady state at each site, where modern weighted evaporation rates ($E_{weighted}$) are equal to modern precipitation rates (P_{modern}). Equation 3 and 4 shows the equations used to estimate thermodynamic and dynamic contributions to lake levels:

$$Thermodynamic\ Component\ (\%) = 100 \times \frac{(E_{weighted} - P_{modern})}{(E_{weighted} - P_{modern}) + (P_{proxy} - P_{modern})} \quad (3)$$

$$Dynamic\ Component\ (\%) = 100 - Thermodynamic\ Component \quad (4)$$

Some samples exceed the bounds of possibility for this calculation (e.g. negative percentages or estimates exceeding 100%) - these samples are excluded from the thermodynamic and dynamic contribution to the mass balance solutions.

3. Results and discussion

3.1 Seasonality of carbonate formation

Prior work has shown differences in the timing of lacustrine carbonate formation depending on the carbonate type and regional environmental conditions (e.g. latitude, elevation,

water depth; Hren & Sheldon, 2012; Petryshyn et al., 2015; Horton et al., 2016; Li et al., 2021; Arnold et al., 2023). Table 4.4 contains the transfer functions used for each type in this study. For biogenic carbonates (gastropods) from highstands at lakes Estancia and Playas, an April - June transfer function was used (Terrazas et al., 2023). Water temperatures from biologically-mediated and authigenic carbonates from Babicora and Santiaguillo in Mexico, and Lake Cochise in Arizona, also utilize an April - June transfer function, given the seasonality of precipitation in the basins, which is biased towards the summer and autumn months due to the North American Monsoon and tropical cyclones delivering moisture into the region. Spring is typically an interval of aridity at the basin, where evaporation rates increase and authigenic carbonate precipitation is more likely to be induced due to carbonate supersaturation in lake waters. At El Potosi, there is typically drier period between major precipitation seasons that is the likely interval of increased carbonate supersaturation within the water column and carbonate precipitation (Figure 4.1), and thus, authigenic carbonates from this basin are likely to have formed during the warmest months of the year (June-August) (Arnold et al., 2023). These carbonates are unlikely to be detrital given a negative correlation between Ti and carbonate concentrations (Roy et al., 2016).

3.2 Late-LGM and early deglacial hydroclimate at Lakes Cochise, Estancia, and Playas

Figure 4.2 shows calculated mean annual air temperature anomalies at the three northernmost basins. There was a similar degree of temperature suppression at Lake Cochise and Lake Estancia during the early and late LGM (4.9 ± 3.2°C and 4.3 ± 2.9°C cooler than modern, respectively). Between 19 ka and 18 ka, during highstands at each of the lakes, temperatures were 10.5 ± 2.8°C, 9.4 ± 2.8°C, and 11.3 ± 2.4°C cooler than modern at Lake Cochise, Estancia,

and Playas, respectively. Reconstructed temperature anomalies for all three basins are within error of each other.

At Lake Estancia, during the early LGM (~23 ka), lake evaporation was only slightly reduced (~13 ± 21%), while precipitation was substantially higher (186 ± 73%). In contrast, at Lake Cochise, enhanced precipitation occurred in the late LGM (19.7 ka; ~302 ± 122% higher than today), when there were coeval reductions in evaporation that were smaller (25 ± 21% present rates). In both basins, dynamic controls were more influential on moisture budgets (~70% dynamic/~30% thermodynamic) (Figure 4.A.7). During pluvial maxima at ~19-18 ka, we have substantially lower evaporation rates at each basin (Cochise - 64 ± 15% reduction compared to modern, Playas - 65 ± 11%, Estancia - 48 ± 25%), while precipitation forcing is reduced compared to the LGM. The largest precipitation forcing is at Playas (139 ± 69%), followed by Cochise (94 ± 83%), and Estancia (65 ± 84%). Despite most of the modern precipitation occurring in the summer months associated with the NAM, reconstructions of lake water $\delta^{18}O$ at each basin for the LGM and deglacial samples at all basins are more consistent with a winter-derived source. Lower Δ_{47}-based estimates of lake water $\delta^{18}O$ supports the hypothesis that increases in winter-derived precipitation was integral to sustaining lakes in the region (Table 4.4).

3.3 LGM hydroclimate in Northern Mexico

Figure 4.3 shows reconstructed MAAT for the three basins in Northern Mexico. On first order, temperatures increase during the LGM. MAAT in the Santiaguillo basin abruptly warms ~21.4 ka by 8.5°C, and then returns to cooler conditions. A similar pattern is observed at Babicora, with about half of the magnitude temperature change. After 19.8 ka, the temperature

anomalies at El Potosi, located furthest East, and Babicora are similar, while cooler conditions continue at Santiaguillo. Overall, the largest temperature anomalies are at Lake Santiaguillo (12.1 ± 3.4°C), followed by Lake Babicora (6.6 ± 1.2°C), and Lake El Potosi (4.6 ± 0.8°C). The difference between temperature anomalies at Lake Santiaguillo and Lake El Potosi is 9.1°C, which are at similar latitudes but separated by ~4.5° in longitude and 80 m in elevation (Table 4.5).

Cooler temperatures during the LGM at all three basins led to reduced evaporation rates. On average, LGM lake evaporation rates were 27% to 62% lower than at present. Evaporation rates at Lake Babicora and Lake Santiaguillo show a similar pattern of change over time, while El Potosi shows the smallest degree of suppression (Figure 4.3; Table 4.4). Roy et al. (2015) concluded that precipitation delivery into the Santiaguillo basin was mainly derived from tropical cyclones in the autumn months due to the pattern of regional wetting and drying observed in proxy records. Precipitation maxima at Lake Babicora and Santiaguillo were concurrent with the warming at 21.4 ka (91% and 184% higher than at present, respectively), with the largest changes furthest south at Santiaguillo (Table 4.5). The largest precipitation forcing is at El Potosi, near the end of the LGM.

3.4 Drivers of hydroclimatic change

At present, the climate at all sites examined in this study is dominated by summer and autumn precipitation, with rainfall at five of six sites primarily derived from the North American Monsoon (Figure 4.1). Utilizing the Comrie and Glenn (1998) nomenclature for the North American Monsoon where they identify climatological regions using modern meteorological data, Babicora and Santiaguillo fall into the ‘Monsoon South’ domain, with the largest increases

in summer precipitation driven primarily by the monsoon with a smaller contribution from tropical storms; Cochise and Playas are part of the 'Monsoon West' domain, with less extensive monsoonal precipitation in comparison, and a shorter duration of precipitation; and Lake Estancia is part of the 'Monsoon East' domain, which is still influenced by the monsoon but receives less precipitation than the South and West domains. In contrast, moisture transport in 'Northeastern Mexico' at Lake El Potosi is not dominated by the monsoon, but is typically derived from the Gulf of Mexico and Caribbean Sea, steered by the northward branch of the Caribbean Low Level Jet (CLLJ) in the early summer and by tropical storms sourced from the Atlantic warm pool in the fall (Roy et al., 2019).

Lake water $\delta^{18}O$ from the modern Monsoon South and East domains exhibit values more characteristic of moisture from modern winter rainfall, likely derived from a southwardly displaced storm track delivering increased moisture to this area. Our reconstructions mirror the record from the Fort Stanton speleothem in New Mexico (Asmerom et al., 2010) (Figure 4.A.6), supporting the hypothesis that winter-derived precipitation was dominant throughout the region during this time. We suggest that dynamical changes led to large increases in winter precipitation that in turn were a primary driver of lake highstands in the Southwestern United States, that later shifted to becoming dominated by summer precipitation. Decreased lake sediment transport during the LGM and early deglacial in Baja California (31°N) supports the interpretation that the influence of monsoonal summer precipitation was much lower during this time (Roy et al., 2012). Further, modeling suggests a weakening of monsoonal circulation due to increased LGM ice sheet albedo that caused the advection of cold and dry air into the region (Bhattacharya et al., 2017).

Given the lack of evidence from these sites for an enhanced monsoon, it is likely the increased precipitation at the three southern lakes (in the Monsoon South and Northwestern Mexico domains) is from other sources. Lakes from the Monsoon South domain follow similar hydroclimate trends during the LGM, with average LGM precipitation anomalies at the southern end of the domain (Santiaguillo) that are slightly elevated relative to the central part of the domain (Babicora). Prior work has hypothesized that enhanced moisture delivery in the autumn from southward-curving tropical cyclones from the eastern Pacific could drive increased runoff into Lake Santiaguillo (Ritchie et al., 2011; Roy et al., 2015). The modern climatology of southward curving tropical cyclones shows they tend to make landfall at 20°N (Ritchie et al., 2011), which may explain the slight gradient in LGM precipitation anomalies between Santiaguillo (24°N) and Babicora (29°N). The much higher precipitation anomalies at El Potosi compared to Santiaguillo from ~20-19 ka could indicate additional moisture was brought by tropical cyclones from the Atlantic, and/or from the CLLJ (Comrie & Glenn, 1998; Roy et al., 2019), or alternatively that groundwater discharge may have changed dramatically. As the LGM was a time of relative oceanic cooling, it is uncertain if sea surface temperatures were warm enough to prompt an interval of increased cyclogenesis in the Atlantic Ocean (Lea et al., 2003; Schmidt et al., 2004); a recent modeling study suggests that during the LGM, there was a strengthening of the CLLJ with no associated increases in precipitation (Wright et al., 2023). We note that at present and historically, there is evidence for springs in and near the El Potosi basin (Echelle et al., 1995; Lozano Vilano & Contreras Balderas, 1993; Balderas & Lozano-Vilano, 1996; González et al., 2020; Miller & Walters, 1972).

3.5 Climate model analysis

We utilize the clumped isotope-derived hydroclimate parameters to evaluate9 models from the Paleoclimate Modeling Intercomparison Project Phase 3 and the multi-model ensemble. To assess model-proxy agreement, we use a 'skill score' metric (see Methods) which tests the null hypothesis of no change from the LGM to present, that has previously been used in previous paleoclimatological studies (Hargreaves et al., 2013; Lopez-Maldonado et al., 2023; Lora et al., 2017; Lora & Ibarra, 2019; Santi et al., 2020). A skill score of 1 would represent perfect model-proxy agreement, a skill score of 0 would indicate no improvement in model-proxy agreement beyond the reference state of no change, and a negative skill score would indicate performance worse than the reference state (no change). Data is used from all of the basins except for El Potosi, given the evidence for possible changes in groundwater at that site.

Skill scores for temperature changes range from 0.36 to 0.71. Overall, model runs that estimate a greater magnitude of cooling in subtropical North America demonstrate the highest degree of skill (Figure 4.4; Figure 4.A.3). With respect to our proxy dataset, F-GOALS exhibits the highest skill and estimates the largest temperature change of all models, while CNRM-CM5 does not simulate large changes and performs the worst relative to our proxy estimates.

Model skill for precipitation is much more variable, ranging from -0.12 to 0.53, with three models exhibiting negative skill with respect to our proxy dataset. MPI-ESM-P exhibits the highest degree of skill relative to the other models, with a higher magnitude of precipitation change than most other models (Figure 4.4; Figure 4.A.4). The range of precipitation values in simulations is much smaller for Arizona and New Mexico than in Northern Mexico, where there is as much as a 1500 mm/yr spread at a given point between models (Figure 4.A.4).

Seven out of nine models in the PMIP 3 suite of models exhibit negative skill with respect to evapotranspiration (Figure 4.4). MPI-ESM-P has the highest skill score (0.51) for evapotranspiration, and for precipitation. The lowest scoring model in terms of evapotranspiration anomalies is NCAR-CCSM4 (-0.7) which also has the lowest skill score for precipitation anomalies. In addition to representation of dynamical and/or earth system processes in the region, a factor that may impact skill scores may be model resolution.

4. Conclusion

This study presents some of the first quantitative estimates of hydroclimate parameters for the LGM and deglaciation in Southwestern North America, a relatively understudied region. Clumped isotopes are applied as a tool for studying water balance and probing the relative influence of causal mechanisms in driving lake level and hydrology. Our results for three lakes in Northern Mexico show that at the LGM, cooler temperatures led to reduced evaporation rates relative to modern. There were also increases in temperature and evaporation from the early to the late LGM. In northwestern Mexico, a wetter-than-modern climate persisted throughout the LGM, with larger increases in precipitation further south, consistent with increased moisture delivery from tropical storms. Further north, in the southwestern United States, pluvial maxima at 23 to 19.7 ka are associated with higher precipitation (~1.5 to 3 times modern values). Although today, the region is dominated by monsoonal precipitation, during the LGM and deglacial, water $\delta^{18}O$ values indicate a winter-source; the transition from winter dominated to summer dominated precipitation at present was likely due to the shifting of the westerly storm track as the Laurentide ice sheet receded. These results show how the North American monsoon,

the most important moisture delivery mechanism in the region, is sensitive to large climate forcing.

5. Figures

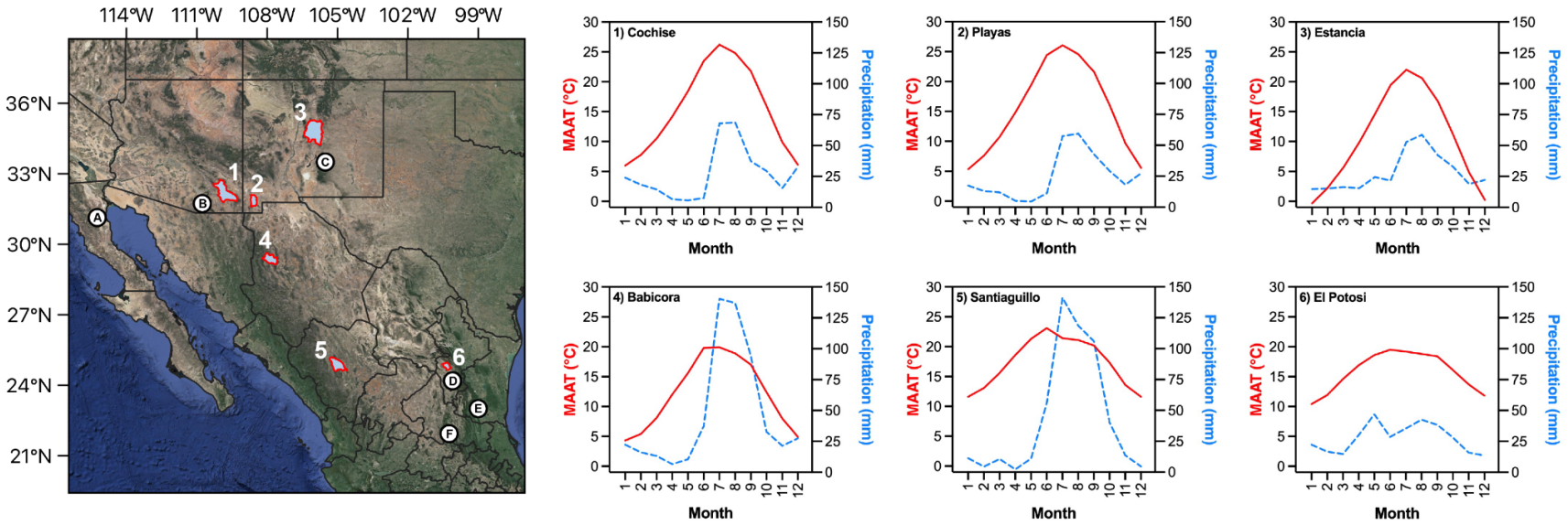

Figure 4.1: Map of sites and modern temperature (red; solid lines) and precipitation (blue; dashed lines) for each site in this study. Six endorheic basins used in this study are outlined in red. Temperature and precipitation information come from the Desert Research Institute and the Servicio Meteorologico Nacional for sites in the United States and Mexico, respectively (more detail can be found in Table 1). Letters represent other locations discussed in this study: A) San Felipe (Roy et al., 2012); B) Cave of the Bells (Wagner et al., 2010), C) Fort Stanton (Asmerom et al., 2010); D) Sandia basin (Roy et al., 2020), E) Cueva Bonita (Wright et al., 2023), F) Grutas de la Catedral (Intveld, 2023)

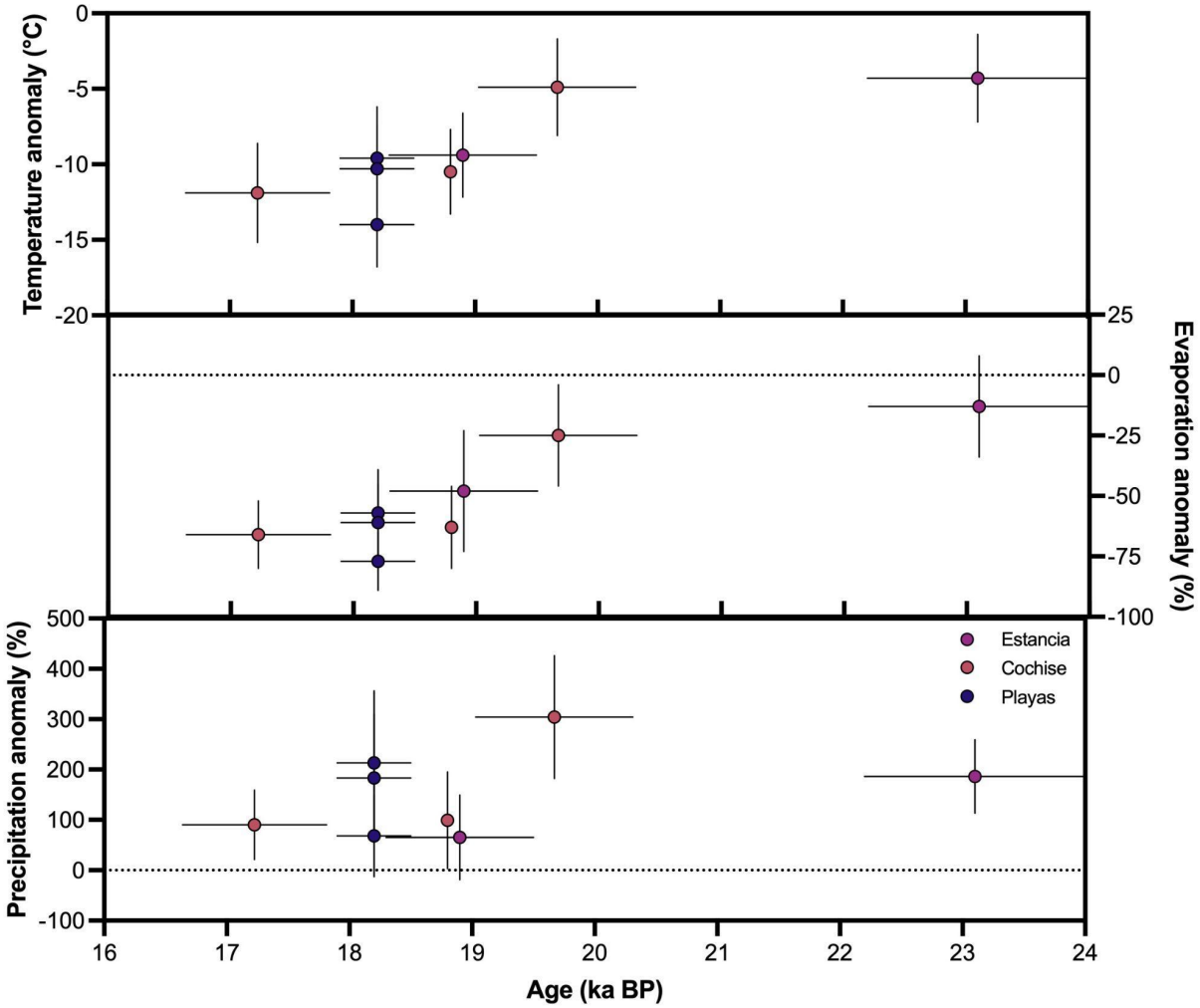

Figure 4.2: Reconstructions of mean annual air temperature, evaporation, and precipitation anomalies during the LGM for three basins in the Southwestern United States (New Mexico: Estancia and Playas, Arizona: Cochise). Modern values used to calculate anomalies can be found in Table 4.1.

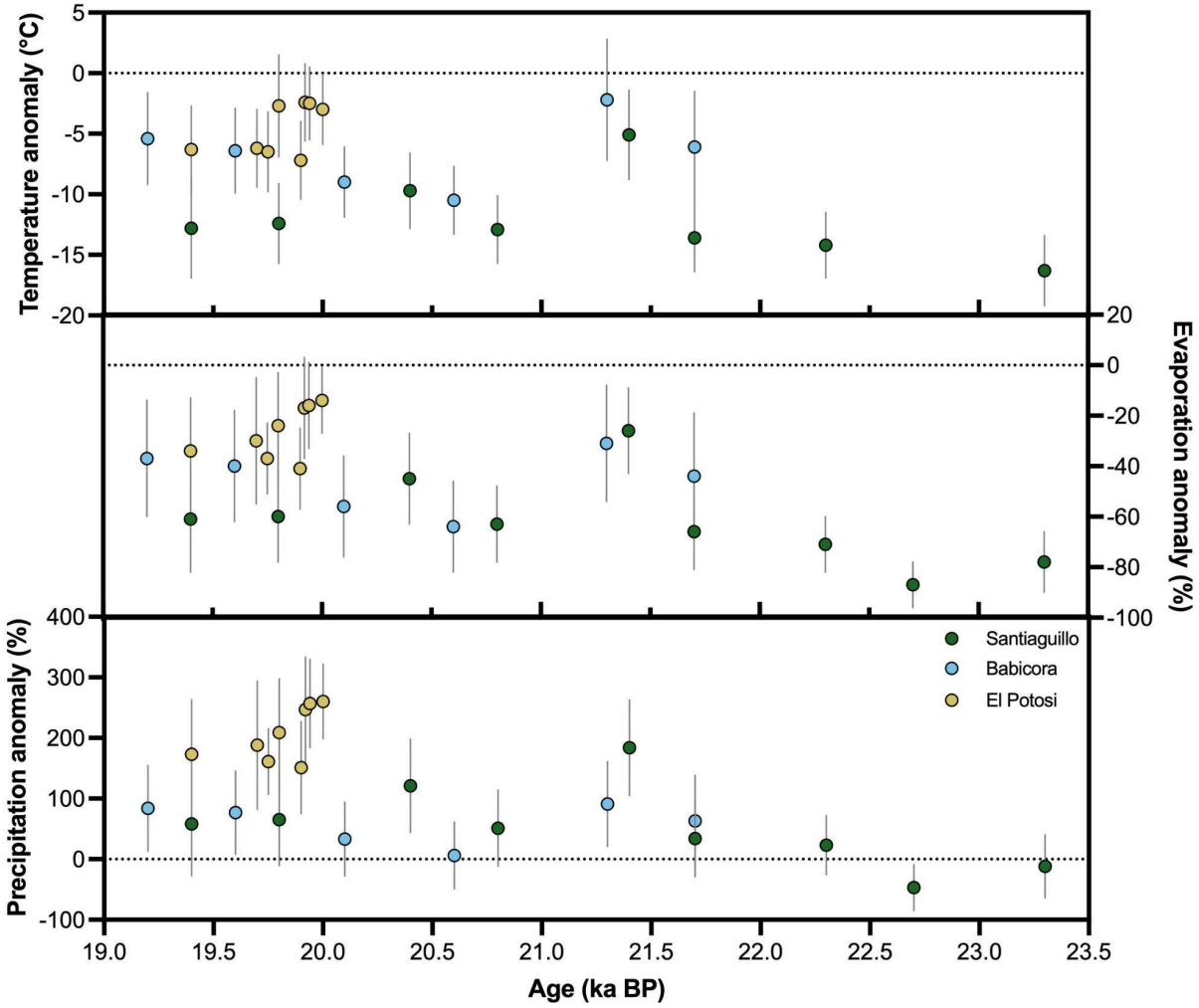

Figure 4.3: Reconstructions of mean annual air temperature, evaporation, and precipitation anomalies during the LGM for three basins in Northern Mexico. Modern values used to calculate anomalies can be found in Table 4.1.

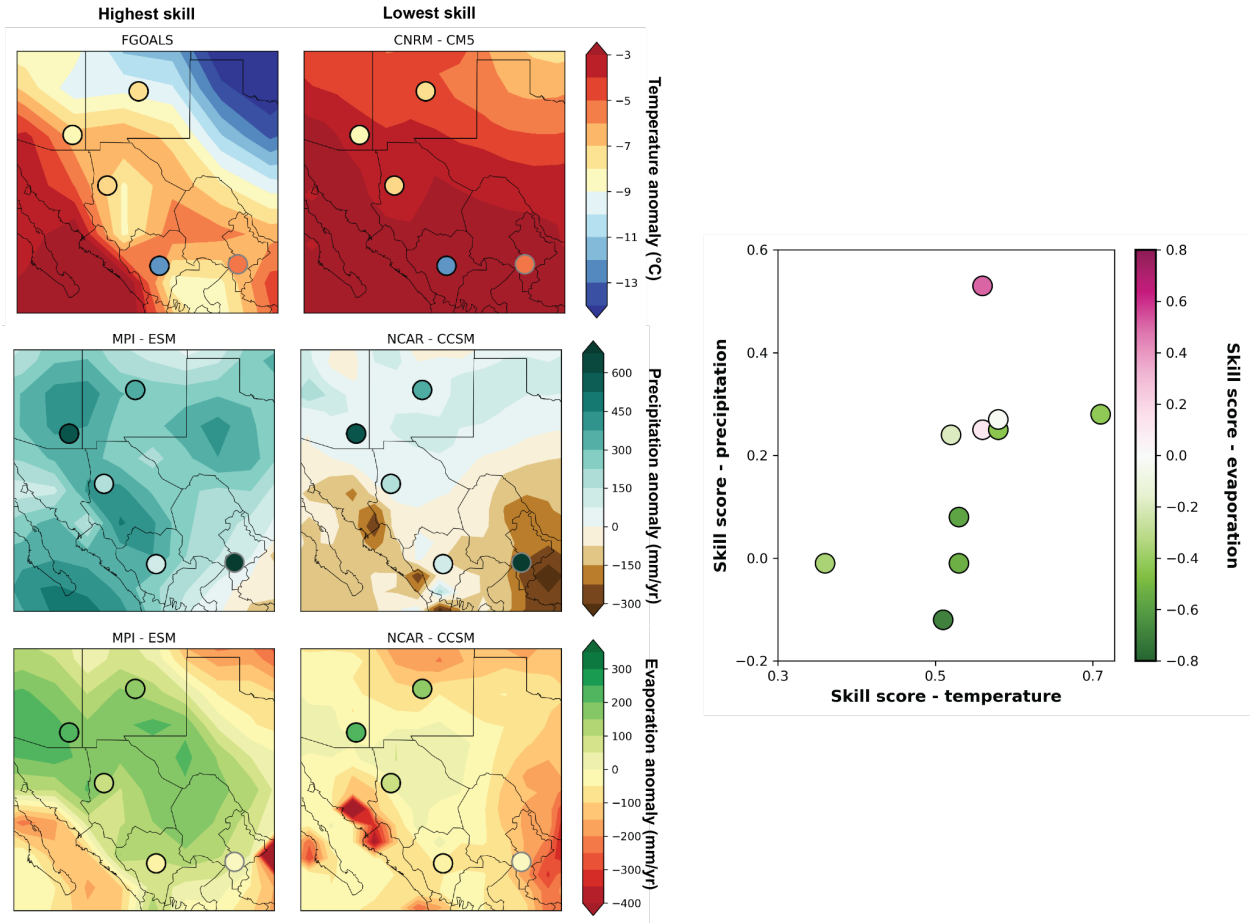

Figure 4.4: Skill score comparison for temperature, evaporation, and precipitation anomalies from the suite of PMIP3 models. For each variable, the model with the highest and lowest skill scores are displayed. Proxy data points with black outlines are included in the skill score analysis. El Potosi (gray outline) is excluded due to potential influence of groundwater. Positive skill is observed in terms of temperature for all models. Models that show increases in precipitation and evaporation have the best model-proxy agreement and higher skill scores.

6. Tables

Basin	Latitude	Longitude	Elevation (m)	Basin area (km^2)	MAAT (°C)	Precipitation (mm/yr)	Pan evaporation (mm/yr)	Lake evaporation* (mm/yr)	Flux-weighted precipitation $\delta^{18}O$ (‰, VSMOW)	Station location
Cochise	32.15	-109.84	1274	4357	15.5	318	2149	1934	-5.5	Willcox, Arizona
Estancia	34.67	-105.96	1856	5828	10.3	328	1413	1272	-7.2	Estancia, New Mexico
Playas	31.86	-108.57	1307	1135	16.1	283	2557	2301	-5.4	Animas, New Mexico
El Potosi	24.83	-100.32	1880	716	15.8	350	1683	1515	-6.1	El Potosi, San Luis Potosi, Mexico
Babicora	29.25	-107.75	2140	1890	12.2	560	2059	1853	-6.7	Bavicora, Chihuahua, Mexico
Santiaguillo	24.73	-104.8	1960	2540	17.4	430	2210	1989	-5.4	Gomez-Farias Station, Durango, Mexico

Table 4.1: Modern climate data for all samples used in this study. Basin areas are calculated using HydroSHEDS. Mean annual air temperature (MAAT), precipitation, and pan evaporation data is from Desert Research Institute, Western Regional Climate Center for sites in the U.S. and the Servicio Meteorológico Nacional for sites in Mexico. Flux-weighted precipitation $\delta^{18}O$ is estimated using the monthly precipitation $\delta^{18}O$ at each location from the Online Isotopes in Precipitation Calculator (Bowen, 2023) and average annual monthly precipitation rates at each site (Servicio Meteorológico Nacional, 2023; Western Regional Climate Center, 2023). *Lake evaporation rates are estimated using a pan coefficient of 0.9 (Linacre, 1994; Matsubara & Howard, 2009).

Basin name	Sample name	^{14}C Age (ka)	^{14}C Age SD	IntCal13 Age (ka BP)	2σ min	2σ max	Elevation
Estancia	Estancia_GPA_1	15.650	0.260	18.932	18.369	19.576	1890
Estancia	Estancia_GPA_Jesse	19.120	0.410	23.057	22.176	24.029	1890
Cochise	Cochise1_61_1	9.780	0.140	11.186	10.717	11.701	1273
Cochise	Cochise_GL1	14.170	0.200	17.226	16.604	17.778	1272
Cochise	Cochise_2_1	16.300	0.260	19.670	19.004	20.287	1274

Table 4.2: New radiocarbon dates for Lake Estancia and Lake Cochise for this study. All samples are calibrated using IntCal13 (Reimer et al., 2013).

Basin	Sample name	Sample type	Age	SD	n	$\delta^{13}C$ (‰, VPDB)	SD	$\delta^{18}O$ (‰, VPDB)	SD	Δ_{47} (‰, ICDES)	SE	Water temperature (°C)	SE	Lake $\delta^{18}O$ (‰, VSMOW)	SE
Babicora	NB 125-127	Authigenic carbonate	19.2	-	2	-3.2	0.0	-1.9	0.1	0.646	0.011	13.8	2.7	-3.0	0.6
Babicora	NB 129-131	Authigenic carbonate	19.6	-	2	-2.6	0.0	-1.7	0.0	0.649	0.009	12.9	2.3	-2.9	0.6
Babicora	NB 135-137	Authigenic carbonate	20.1	-	3	-4.2	0.1	-2.3	0.1	0.659	0.003	10.5	0.8	-4.0	0.2
Babicora	NB 139-141	Authigenic carbonate	20.6	-	2	-1.3	0.1	-0.7	0.0	0.665	0.002	9.1	0.4	-2.7	0.1
Babicora	NB 145-147	Authigenic carbonate	21.3	-	2	0.4	0.0	-0.5	0.0	0.634	0.016	16.8	4.1	-0.9	0.8
Babicora	NB 149-151	Authigenic carbonate	21.7	-	2	-2.4	0.0	-1.2	0.0	0.648	0.015	13.2	3.7	-2.4	0.8
Cochise	Cochise_GL1	Tufa	17.2	0.6	3	-2.7	0.0	-9.5	0.0	0.645	0.006	10.5	1.9	-11.0	0.4
Cochise	AK-191	Beach cement	18.8	0.0	7	-0.9	0.3	-7.2	0.3	0.654	0.002	11.8	0.6	-8.6	0.4
Cochise	Cochise_2_1	Tufa	19.7	0.6	3	0.0	0.0	-8.3	0.1	0.626	0.005	17.0	1.7	-8.7	0.3
El Potosi	EP1 284-286	Authigenic carbonate	19.4	-	3	-2.3	0.0	-9.4	0.1	0.615	0.008	21.9	2.1	-7.6	0.4
El Potosi	EP1 288-290	Authigenic carbonate	19.7	-	4	-1.6	0.0	-9.6	0.1	0.615	0.005	22.0	1.4	-7.9	0.2
El Potosi	EP1 290-292	Authigenic carbonate	19.8	-	4	-1.1	0.0	-9.7	0.1	0.616	0.005	21.8	1.5	-8.0	0.3
El Potosi	EP1 294-296	Authigenic carbonate	19.8	-	2	-2.2	0.0	-9.5	0.1	0.607	0.011	24.4	3.0	-7.3	0.5
El Potosi	EP1 298-300	Authigenic carbonate	19.9	-	4	-1.5	0.0	-9.7	0.1	0.618	0.005	21.3	1.3	-8.1	0.2
El Potosi	EP1 300-302	Authigenic carbonate	19.9	-	3	-1.3	0.0	-9.8	0.1	0.606	0.005	24.6	1.3	-7.5	0.3
El Potosi	EP1 304-306	Authigenic carbonate	19.9	-	4	-0.5	0.6	-10.0	0.3	0.606	0.003	24.5	0.8	-7.8	0.2
El Potosi	EP1 308-310	Authigenic carbonate	20	-	3	-0.9	0.0	-9.9	0.1	0.607	0.001	24.2	0.2	-7.7	0.1
Estancia	Estancia_GPA_1	Gastropod	18.9	0.3	5	-5.4	0.1	-3.9	0.1	0.642	0.003	8.5	0.8	-6.8	0.2
Estancia	Estancia_GPA_1_Jesse	Gastropod	23.1	0.5	2	-4.2	0.0	-7.2	0.0	0.637	0.003	13.3	1.0	-8.3	0.2

Playas	PL Loc1 W Num10 Lym 6-7	Gastropod	18.2	0.3	10	-6.5	0.0	-8.6	0.2	0.627	0.007	13.2	2.1	-8.5	0.3
Playas	PL Loc1 W Num11 Lym 1-2	Gastropod	18.2	0.3	7	-6.5	0.0	-8.5	0.1	0.629	0.004	12.6	1.1	-8.5	0.2
Playas	PL Loc1 W Num11 Lym 3-4	Gastropod	18.2	0.3	6	-6.1	0.0	-8.4	0.3	0.64	0.001	9.1	0.3	-9.2	0.3
Santiaguillo	S2 220-222	Authigenic carbonate	19.4	-	3	-1.4	0.0	-1.7	0.1	0.655	0.012	11.4	3.1	-3.3	0.7
Santiaguillo	S2 224-226	Authigenic carbonate	19.8	-	3	-1.8	0.0	-2.2	0.1	0.654	0.007	11.8	1.8	-3.7	0.5
Santiaguillo	S2 230-232	Authigenic carbonate	20.4	-	3	-1.0	0.0	-1.3	0.2	0.644	0.005	14.3	1.3	-2.2	0.4
Santiaguillo	S2 234-236	Authigenic carbonate	20.8	-	3	-1.1	0.1	-1.4	0.2	0.655	0.002	11.3	0.4	-2.9	0.2
Santiaguillo	S2 240-242	Authigenic carbonate	21.4	-	3	-0.8	0.2	-0.6	0.5	0.628	0.009	18.5	2.4	-0.6	0.8
Santiaguillo	S2 244-246	Authigenic carbonate	21.7	-	3	-0.6	0.0	0.1	0.1	0.658	0.003	10.7	0.7	-1.6	0.1
Santiaguillo	S2 250-252	Authigenic carbonate	22.3	-	3	-3.1	0.0	-3.6	0.0	0.66	0.001	10.1	0.2	-5.4	0.0
Santiaguillo	S2 260-262	Authigenic carbonate	23.3	-	3	-0.6	0.0	-0.1	0.0	0.669	0.004	8.1	1.0	-2.4	0.2

Table 4.3: Stable and clumped isotope results for samples in this study. Radiometric dating and age models for El Potosi can be found in Roy et al. (2016); Babicora in Roy et al. (2012); Santiaguillo in Roy et al. (2015); Playas and Cochise in Kowler (2015).

Basin	Sample name	Assumed seasonality	MAAT (°C)	SE	E_L (mm/yr)	SD	P (mm/yr)	SD	K_{run}	SD	ET (mm/yr)	E_W (mm/yr)	Thermodynamic contribution (%)	Dynamic contribution (%)
Babicora	NB 125-127	AMJ	6.8	3.8	1166	426	1032	396	0.361	0.118	660	800	34	66
Babicora	NB 129-131	AMJ	5.8	3.5	1121	417	989	385	0.371	0.122	621	761	32	68
Babicora	NB 135-137	AMJ	3.2	2.9	818	364	744	340	0.421	0.124	431	539	—	—
Babicora	NB 139-141	AMJ	1.7	2.8	669	339	594	308	0.363	0.117	378	459	—	—
Babicora	NB 145-147	AMJ	10.0	5.0	1274	422	1069	391	0.319	0.119	728	880	39	61
Babicora	NB 149-151	AMJ	6.1	4.6	1046	464	910	422	0.352	0.12	590	716	31	69
Cochise	Cochise_GL1	AMJ	3.6	3.3	661	267	603	221	0.593	0.101	245	271	—	—
Cochise	AK-191	AMJ	5.0	2.8	714	332	633	305	0.420	0.091	367	391	19	81
Cochise	Cochise_2_1	AMJ	10.6	3.2	1445	410	1283	388	0.437	0.093	722	772	32	68
El Potosi	EP1 284-286	JJA	10.2	3.6	994	320	938	311	0.611	0.084	365	655	34	66
El Potosi	EP1 288-290	JJA	10.3	3.2	1053	385	990	363	0.686	0.063	310	686	35	65
El Potosi	EP1 290-292	JJA	10.0	3.3	954	212	899	186	0.706	0.063	264	674	37	63
El Potosi	EP1 294-296	JJA	13.8	4.2	1152	319	1061	306	0.534	0.107	495	736	35	65
El Potosi	EP1 298-300	JJA	9.3	3.2	892	247	862	261	0.72	0.066	241	633	36	64
El Potosi	EP1 300-302	JJA	14.1	3.2	1262	310	1195	299	0.605	0.077	472	807	35	65
El Potosi	EP1 304-306	JJA	14.0	3.0	1272	261	1229	251	0.653	0.044	426	823	35	65
El Potosi	EP1 308-310	JJA	13.5	2.9	1303	197	1237	213	0.725	0.068	340	825	35	65
Estancia	Estancia_GPA_1	AMJ	0.9	2.8	662	324	579	292	0.369	0.112	365	414	22	78

Estancia	Estancia_GPA_1_Jesse	AMJ	6.0	2.9	1108	263	1000	257	0.427	0.105	573	614	29	71
Playas	PL Loc1 W Num10 Lym 6-7	AMJ	6.5	3.4	979	409	823	366	0.332	0.091	550	575	35	65
Playas	PL Loc1 W Num11 Lym 1-2	AMJ	5.8	2.9	901	363	759	326	0.333	0.090	506	530	34	66
Playas	PL Loc1 W Num11 Lym 3-4	AMJ	2.1	2.8	529	269	455	238	0.346	0.086	298	310	13	87
Santiaguillo	S2 220-222	AMJ	4.6	4.1	769	413	678	370	0.409	0.103	401	441	4	96
Santiaguillo	S2 224-226	AMJ	5.0	3.3	798	357	708	325	0.436	0.107	399	444	5	95
Santiaguillo	S2 230-232	AMJ	7.7	3.1	1090	356	950	332	0.383	0.101	586	644	29	71
Santiaguillo	S2 234-236	AMJ	4.5	2.8	733	295	649	272	0.421	0.107	376	416	—	—
Santiaguillo	S2 240-242	AMJ	12.3	3.7	1471	336	1220	339	0.316	0.094	835	910	38	62
Santiaguillo	S2 244-246	AMJ	3.8	2.8	667	300	576	272	0.366	0.099	365	399	—	—
Santiaguillo	S2 250-252	AMJ	3.2	2.7	576	220	529	212	0.534	0.098	246	284	—	—
Santiaguillo	S2 260-262	AMJ	1.1	2.9	428	243	378	221	0.397	0.103	228	250	77	23

Table 4.4: Reconstructed hydroclimatic parameters for six basins in this study using methodology from Santi et al. (2020). Anomalies are calculated using modern values from Table 4.1.

Basin	Temperature anomaly (°C)	SD	Evaporation anomaly (%)	SD	Precipitation anomaly (%)	SD	Thermodynamic contribution (%)	Dynamic contribution (%)
Babicora	-6.6	2.9	-45	12	59	33	34	66
Cochise	-7.7	4.0	-44	27	202	145	26	75
El Potosi	-4.6	2.1	-27	10	206	44	35	65
Estancia	-6.9	3.6	-31	25	126	86	26	75
Santiaguillo	-12.1	3.4	-59	16	66	61	31	69

Table 4.5: Average temperature, lake evaporation, and precipitation anomalies and partitioning of dynamic and thermodynamic controls on lake level fluctuations for LGM aged samples. Modern values to calculate anomalies can be found in Table 4.1 and equations to calculate dynamic and thermodynamic contributions to lake levels are in the Methods section.

7. Supplement

Text S1: Site information

Estancia

Paleolake Estancia was located in central New Mexico. The Estancia basin was ~5700 km^2 in size. and Lake Estancia reached a high stand at 1,890 m, resulting in maximum lake areas of 1125 km^2 and depths of 45 m (Menking et al., 2022). Highstand levels were reached multiple times due to abrupt climate shifts during the LGM and deglaciation (Allen & Anderson, 2000).

Modern mean annual air temperature is 10.6°C, winter (DJF) temperatures are 0.7°C and summer (JJA) temperatures reach 20.7°C. Over half of the modern precipitation received in the Estancia basin is delivered via the North American Monsoon (52%). Winter storms contribute a similar amount to the moisture budget as Lake Cochise and Playas Lake (16%).

Cochise

Lake Cochise was located within the Willcox Basin in southeastern Arizona along the boundary of the Sonoran and Chiuahuan deserts. Mean annual air temperature at Lake Cochise is 15.4°C, with a range in monthly MAAT of 20.2°C due to hot summers and cool winters that characterize the area. 55% of modern precipitation occurs during the North American Monsoon season (June -September), and 25% occurs from frontal storms during the winter months (December - February).

As one of the only closed-basin lake systems in Arizona, Lake Cochise has been a site of interest for the last century (Haynes Jr et al., 1987; Kowler, 2015; Long, 1966; Meinzer et al., 1913; Waters, 1989). Lake Cochise has been proposed to reach up to 1,290 m, but the most prominent ridges in imagery are between 1,271 and 1,274 m. Radiometric dating has suggested

Lake Cochise primarily oscillated around elevation of 1,274 m during the LGM and late Pleistocene, with a maximum surface area of 310 km^2 and a maximum depth of 11 m (Waters, 1989).

Playas

Playas Lake is located in southwestern New Mexico in the Northern Chihuahuan desert, 100 km east of Lake Cochise. Due to the close proximity of the two basins, climatic conditions are similar for the two basins, with a monthly mean annual temperature range of 20.7°C and a mean annual air temperature of 15.6°C for Playas varies significantly. Monsoonal precipitation is the dominant delivery mechanism for Playas Valley, with 57% of precipitation occurring from June - September while 19% is delivered from winter storms.

The modern Playas basin is bounded between two mountain ranges, and has a size of 1120 km^2. Prior work has identified late Pleistocene shoreline features at 1,314 and 1,318 m elevations, resulting in lake areas of 45 and 85 km^2 (Kowler, 2015). Wetter than modern conditions between ~20-13 ka BP have been hypothesized, with a highstand at 1,314 m occurring between ~18.4-17.9 ka BP (Kowler, 2015).

Babicora

Paleolake Babicora is located in the western Chihuahua desert in northern Mexico. Mean annual air temperatures are 12.2 °C, with a monthly mean annual temperature range of 15.6°C. This region is defined by cold and dry winters and warm and wet summers. Mean annual precipitation is 560 mm/year, with the North American Monsoon delivering 73% of modern rainfall to the region. This allows for an ephemeral lake to form during warmer months which

typically desiccates for the remainder of the year (Roy et al., 2013). Laguna Babicora would have occupied 27% of the Babicora basin (1,896 km^2) at its maximum identified extent of 2,160 m during the Pleistocene (Chávez-Lara et al., 2012; Metcalfe et al., 2002).

Santiaguillo

Lake Santiaguillo is located in North central Mexico, on the eastern side of the Sierra Madre Occidental range (Figure 4.1). Mean annual air temperature is 17.4°C, with coldest and warmest temperatures occurring in December (11.6°C) and June (23.1°C), respectively (Servicio Meteorológico Nacional, 2023). Precipitation is seasonally-biased, with 91% of precipitation typically occurring in concert with North American Monsoon and during autumn, the typical interval for tropical cyclones delivering moisture to the region (Roy et al., 2015).

At its maximum extent, Lake Santiaguillo covered roughly 2000 km^2 (Chávez-Lara et al., 2019). However, today, the basin is divided into two sub basins separated by a dam, with the northern subbasin used as a reservoir and the southern subbasin is ephemeral during rainy warm periods, reaching a depth of ~1 m (Quiroz-Jimenez et al., 2017). Further study is required to determine exact lake level elevations during the LGM and deglaciation, but the distribution of lake sediments found in Quiroz-Jiménez et al., (2017) suggest that it reached elevations of at least 1,963 m, encompassing an area of 276 km^2.

El Potosi

Laguna El Potosi was a pluvial lake located in subtropical northeastern Mexico, located in the rain shadow of the Sierra Madre Oriental Mountains. Precipitation at El Potosi is the least variant out of all our sites, with bimodal peaks in precipitation in the early summer and fall

(Servicio Meteorológico Nacional, 2023). Monthly mean annual air temperature ranges from 10.4°C to 19.5°C, with an annual average of 15.8°C (Servicio Meteorológico Nacional, 2023). Lacustrine sediments suggest that Laguna El Potosi basin attained an elevation of at least 1,880 m, with a maximum width and length of 3 km and 7 km, respectively, during the late Pleistocene (Roy et al., 2016).

Text S2: Clumped-isotope-derived hydroclimate reconstructions for individual basins

Estancia

Radiocarbon dating of sediments from Lake Estancia suggested that the lake reached its maximum height of 1890 m multiple times throughout the late Pleistocene (Allen & Anderson, 2000). Radiocarbon dates measured from gastropods collected from the highstand elevation of Lake Estancia for this study, at 18.9 ka to 23.1 ka, support the timing of highstands H3 and H7 proposed in Allen and Anderson (2000) (Table 4.2).

Reconstructed mean annual air temperatures show a temperature depression of 4.3 ± 2.9°C during the early LGM, with cooling continuing to occur in the late-LGM, with a depression of 9.4 ± 2.8°C relative to modern. Unsurprisingly, the reduction in MAAT from the early to late-LGM during each of these highstand events translates into lake evaporation rates 13 ± 21% and 48 ± 25% lower relative to modern, respectively.

Prior numerical modeling has suggested that increases of 50 - 100% precipitation relative to modern times was necessary for the lake to reach its highstand elevation (Menking et al., 2004). Despite the topographic limit of Lake Estancia's extent being 40 m higher in elevation, past work has shown that Lake Estancia never exceeded 1,890 m (Allen and Anderson, 2000). Therefore, researchers have hypothesized that groundwater leakage limited the elevation of the

lake and prevented overflowing conditions at the sill, prohibiting the highstand elevation to rise further than 1890 m at Lake Estancia (Menking et al., 2022). This idea was first proposed in Meinzer (1911), who suggested that significant amounts of groundwater discharge could occur from the Estancia basin due the higher elevation of the basin compared to other basins nearby. If the groundwater divide existed during the late-Pleistocene, the values presented by numerical modeling should represent a minimum, thus, our results are in-line with those proposed by Menking et al. (2004), with our 23.1 ka and 18.9 ka highstand samples estimating 186 ± 73% and 69 ± 84% increases in precipitation relative to modern. We estimate a stronger forcing in the early-LGM relative to the late-LGM, which is supported by analysis of ostracodes species in the Estancia basin, which suggested a significant degree of freshening at ~23 ka (Menking et al., 2022).

Our calculations to parse out contributions from dynamical and thermodynamical drivers of hydroclimate suggest that changes in lake levels were primarily driven by dynamics (71-78%) rather than by thermodynamic forcings (22-29%). Reconstructed lake water $\delta^{18}O$ for Lake Estancia range from -6.8 to -8.3‰, more consistent with a heavier, winter-derived precipitation source rather than a lighter, monsoonal-derived source, given that the water in the basin was likely to have experienced some degree of evaporative enrichment. Prior work has also suggested that increases in winter precipitation was dominant during this time, due to the abundance of ostracod species with high light requirements that would require settling of sediment suspended in the water before the taxa could survive and thrive in this setting (Menking et al., 2018).

Cochise

Two new radiocarbon dates from Lake Cochise sediments presented in this study (Table 4.2). The oldest tufa sample in the series was collected from the 1,274 m highstand shoreline at 19.7 ka, suggesting that a lake transgression occurred earlier than the 19.2 ka transgression that was proposed in earlier sedimentological work (Kowler, 2015). Following this transgression, lake levels oscillated around the highstand elevation until its regression around 18.9 ka (Kowler, 2015). A radiocarbon date of 17.2 ka we measured from tufa collected 2 m lower than the highstand elevation, suggests that lake levels started to decrease from the 17.4 ka highstand, or another oscillation to near-highstand level was reached following a transgression (Kowler, 2015).

Reconstructed water temperatures from tufas and beach cements range from 10.5°C to 17.0°C, resulting in mean annual air temperature estimates ranging from 3.6°C to 10.6°C. At 19.2 ka, we estimate a temperature depression of 4.5 ± 3.2°C, with increases in temperature suppression through time, with a maximum anomaly of 11.9 ± 3.3°C around 17.2 ka. Reconstructed evaporation rates follow a similar pattern, with a 25% and 66% reduction in evaporation rates relative to modern estimated at 19.7 ka and 17.2 ka, respectively.

Our results from hydroclimatic modeling suggest that large increases in precipitation were necessary for the existence of Lake Cochise. Our estimates suggest 4 times modern precipitation during the initial lake transgression around ~19.7 ka and that subsequent transgressions required at least 2 times modern precipitation to maintain lake levels throughout the deglaciation.

Playas

Prior sedimentological work in Playas Valley showed that intervals of meadows occurred in the basin from wetter-than-modern conditions were prevalent at many points during the deglacial, but the highstand of 1,311 m was only reached once between ~18.4 to 17.9 (Kowler, 2015). A series of gastropod samples used in this study were taken from the highstand elevation and radiocarbon dated in Kowler (2015). Since the lifetime of a gastropod is much smaller than the formation of other abiotic or biologically-mediated lacustrine materials, we averaged multiple gastropods from three different sites on the margin of the highstand paleoshoreline to gain an idea of average conditions at Playas Lake at its maximum extent.

Water temperatures reconstructed from gastropods range from 9.1°C to 13.1°C. Reconstructed MAAT's range from 2.8°C to 6.2°C, resulting in a temperature suppression of 9.6°C to 14.0°C. Colder than modern conditions caused an extensive degree of evaporative suppression, reducing lake evaporation rates 57% to 77% of modern values during the lake highstand.

In addition to large reductions in evaporation, reconstructed precipitation rates suggest increases in precipitation of 1.6 to 2.9 times modern values. A first-order calculation to partition thermodynamic and dynamic controls on lake levels show a strong preference to dynamics (65-87% contribution), implying changes in precipitation was more influential in reaching its highstand elevation.

Reconstructed $\delta^{18}O$ using gastropod samples range from -10.4‰ to -11.1‰, suggesting a source that is isotopically heavier than the modern flux-weighted composition of -6.4‰, which is largely driven by summer moisture from the North American monsoon. Overall, our results suggest that a large winter precipitation forced the growth of Playas Lake to make its highest ascent.

Babicora

Over the course of ~2.5 ka during the LGM, clumped-isotope derived water temperatures for samples in this study samples ranged by 7.7°C (9.1°C to 16.8°C). Prior work using Mg/Ca thermometry on ostracodes estimated water temperatures ranging from 5.6–9.9°C, slightly cooler than estimates derived in this study (Palacios-Fest et al., 2002). However, more recent work suggested the distribution of ostracode species implies warmer conditions prevailed in the lake during this time (>13°C; Chávez-Lara et al., 2012).

Mean annual air temperature increases between 22 ka and 21 ka, reaching a maximum MAAT of 10.0 ± 5.0°C, resulting in a temperature anomaly of 2.2°C at ~21.3 ka. This peak in MAAT results in higher modeled lake evaporation rates in this study (31 ± 23% lower than modern) and increases in lake evaporation is supported by increased abundances of *L. bradburyi* around ~22 ka, which can tolerate a more saline environment (>1000 ppm; Chávez-Lara et al., 2012). A return to cooler conditions is estimated at ~20.6 ka and subsequent warming occurs throughout the rest of the LGM. Between 21 ka and 19 ka, estimated MAATs increase from 1.7°C to 6.8°C and estimates of lake evaporation rates roughly double.

Throughout the LGM, our hydrologic modeling estimate increases in precipitation, ranging from 6 - 91% higher than modern values, with an increase from roughly modern precipitation rates starting at ~20.6 ka. These findings contradict prior work, which has suggested below average runoff, and thus, below average rainfall in the Babicora basin during the LGM (Roy et al., 2013). Overall, our results show temperature and evaporation rates throughout the interval are consistently suppressed relative to modern, with slight increases in precipitation during the LGM relative to modern (Figure 4.3).

Santiaguillo

Average LGM water temperatures derived from the Santiaguillo basin is 11.1 ± 1.3°C, ranging from a maximum of 18.5 ± 2.4°C and a minimum of 8.1 ± 1.3°C. The distribution of ostracod species in lacustrine sediment implies that lake water was warmer (>13°C) and less saline at during the LGM (Chávez-Lara et al., 2015). Our results suggest similar, but slightly cooler conditions, particularly in the early-LGM. Lake water $\delta^{18}O$ demonstrated 4.8‰ of variability throughout the LGM and shows evidence for evaporative enrichment relative to the modern meteoric flux-weighted meteoric $\delta^{18}O$ of -4.3‰.

Overall, our clumped-isotope derived results estimate that on average, the Santiaguillo basin is 12.1 ± 1.2°C cooler than modern conditions. Between 23.3 and 21.4 ka BP, MAAT increases from 1.1 ± 2.9°C to 12.4 ± 3.7°C. Following this warming, estimated MAAT's range from 4.5 to 7.7°C, remaining fairly stable for the rest of the LGM.

The large degree of temperature suppression implies an extensive degree of evaporative suppression during the LGM. Average evaporation rates for the LGM are 59 ± 6% lower than modern values. Trends in evaporation rates mirror changes in temperature, with the lowest and highest evaporation rates occurring at the beginning of the LGM (78 ± 12% lower than modern) and at 21.4 ka (26 ± 17% lower than modern), respectively.

At the start of the LGM, reconstructed precipitation rates are like modern and increase to their maximum extent of 184 ± 79% modern at 21.4 ka. Following the peak, precipitation rates decrease for the remainder of the LGM but still lie above modern values (Figure 4.3). Our estimates are in line with the conclusions drawn from Ti concentrations from the same sequence,

suggesting above average runoff between 18 ka to 26 ka, implying wetter conditions in the Santiaguillo basin (Roy et al., 2015).

El Potosi

The calculated $\delta^{18}O$ of lake waters for samples in the El Potosi basin range from -8.3‰ to -9.1‰, which is isotopically lighter than the typical distribution of incoming precipitation (-4.3‰ to -10.0‰; Bowen, 2023), given the modern seasonality of precipitation. Estimates of LGM lake water $\delta^{18}O$ from Lake El Potosi are comparatively depleted relative to the other basins in Northern Mexico from this study and records from nearly speleothems (Table 4.3; Figure 4.A.2; Figure 4.A.6 Intveld, 2023; Wright et al., 2023). Given that modern moisture sourced from the Caribbean and Gulf of Mexico during the early-summer and fall months, respectively, would likely have an isotopic signature that is more enriched than our estimates, a few possibilities exist to explain this disparity if estimated $\delta^{18}O$ values are truly reflecting the $\delta^{18}O$ of incoming precipitation. First, the lower lake water $\delta^{18}O$ values may stem from enhanced moisture delivery through tropical cyclones originating in the Pacific with a southward-deflected track that penetrated the continental interior as proposed in Roy et al. (2015). Rayleigh fractionation would further deplete the isotopic composition of precipitation delivered over the course of the longer distance from the Pacific to Lake El Potosi. Second, enhanced moisture transport from tropical cyclones originating in the Atlantic, could further deplete the isotopic composition of precipitation delivered to the basin due to the intensity of precipitation and increases of precipitation delivery in a short time span, as has been observed in Texas (Sun et al., 2022). Third, the elevated water temperatures we observe reflect summer seasonal biases, thus,

the disparity we observe between records could possibly be explained by enhanced depletion of oxygen isotopes in incoming precipitation due to deep convection and the amount effect.

However, below-average Ti concentrations in El Potosi sediments contradict this possibility of the last two scenarios, as the intensity and amount of precipitation would increase runoff and thus Ti within the basin (Roy et al., 2016). The Sandia basin, located ~75 km south from Lake El Potosi also observed decreases in clay mineral abundance during this time, which suggests decreases in moisture delivery and runoff concurrent with when we estimate maximum precipitation at Lake El Potosi (Roy et al., 2020).

Given the disagreement between proxies and the small amount of variance in reconstructed lake water $\delta^{18}O$ within the ~500 year interval, it is possible that the $\delta^{18}O$ of lake water may be influenced by groundwater inputs. A survey of the geochemical composition of modern-day groundwater at the El Potosi basin in 2019 showed a shallow water table, ranging from 20 to 80 m below the surface, despite extensive groundwater pumping occurring in the region (Roy et al., 2022). Modern groundwater recharge occurs primarily from tropical storms, sourced within higher elevations where cooler temperatures paired with the amount effect deplete $\delta^{18}O$ values (Roy et al., 2022). All considered, modern groundwater $\delta^{18}O$ values are more broadly consistent with the values that we derive in our study and may be a source of past water for Lake El Potosi (Roy et al., 2022).

The disparity between estimated LGM $\delta^{18}O$ values and modern meteoric $\delta^{18}O$ values estimated from OIPC causes our hydrologic model to fail to derive hydroclimatic parameters using modern, flux-weighted values for $\delta^{18}O$ that are corrected to account for the ice-volume effect during the LGM (Tripati et al., 2014). Additionally, the sparsity of precipitation $\delta^{18}O$ measurements in Mexico may be biasing the interpolation model used to estimate precipitation

$\delta^{18}O$ within our study region may be overestimating the seasonal changes in precipitation $\delta^{18}O$. Therefore, to estimate past climatic conditions, we utilize the range of modern groundwater compositions, which has been shown to reflect the seasonal variability of modern precipitation in the basin (Roy et al., 2022).

The sample sequence in this study shows that Lake El Potosi demonstrates an average of 4.6 ± 0.8°C of cooling during the late-LGM. A temperature transition within our sample set occurs around 19.8 ka, with older samples in our study consistently reflecting a smaller extent of cooling (2.7 ± 0.3°C), while younger samples consistently reflect a larger extent of cooling (6.6 ± 0.4°C). Consequently, the cooling observed within the record at El Potosi reduces reconstructed evaporation rates for this sequence, ranging from 14-37% lower than modern values, and tends to decrease throughout the study period.

Reconstructed precipitation rates range from 862 - 1237 mm/yr, a significant increase relative to the modern value of 350 mm/yr (Table 4.1), reflecting a 151 - 260% increase in precipitation in the late LGM relative to modern. Our estimates of increased precipitation rates disagree with conclusions drawn from inorganic geochemistry, with lower-than-average Ti concentrations providing the basis for evidence for below average runoff with drier conditions prevailing during the LGM (Roy et al., 2016).

Text S2: Uncertainties in hydroclimate modeling

The modeling framework used in this study requires multiple assumptions to create quantitative estimates of hydroclimatic change for lacustrine sediments. We outline the potential sources of uncertainty in each of our parameters below:

Mean annual air temperature: If the timing of carbonate formation does not coincide with our assumption of seasonality, estimates of mean annual air temperature may be biased, which will propagate through the reconstructions.

Evaporation: In the equation for lake evaporation in Linacre (1994), inputs of latitude, elevation, dew point temperature, wind speed are required. Dew point temperature and wind speed from the North American Regional Reanalysis and assume that the LGM values are identical to modern at each site.

Precipitation: The framework developed in Santi et al. (2020) and used within this study to reconstruct precipitation, requires assumptions of the Budyko parameter, lake area, and meteoric $\delta^{18}O$. For our study, we assume that the Budyko parameter has the same distribution as modern values, as has been done in previous paleoclimatic studies (Greve et al., 2015; Ibarra et al., 2014; Santi et al., 2020).

The meteoric $\delta^{18}O$ value used for each basin was calculated using monthly precipitation $\delta^{18}O$ from the Online Isotopes in Precipitation Calculator and flux-weighted based on monthly precipitation amount, and corrected for ice-volume enrichment using the correction in Tripati et al. (2014). If the meteoric $\delta^{18}O$ was isotopically lighter (heavier) than the corrected value, estimates of precipitation would decrease (increase). Further, if groundwater, which is typically recharged at a higher elevation, thus, isotopically lighter in comparison to meteoric waters, was recharging the lake, our model would overestimate the amount of precipitation received in the basin.

Samples in Southwestern North America were collected from previously identified shoreline features, thus, the uncertainty in lake area for these reconstructions is minimal. On the other hand, authigenic carbonate from Northern Mexico was collected in pits on the lake margin and may not represent the lake level. LGM lake levels for Lake Babicora and Lake El Potosi were taken from Metcalfe et al. (2002) and Chavez-Lara et al. (2019), respectively. LGM lake level for Lake Santiaguillo was estimated using the extent of lacustrine sediments in Roy et al. (2015). Precipitation and lake area are positively related, thus, increases (decreases) in lake area relative to the values used in this study would cause increases (decreases) in precipitation rates. Future work to better constrain lake level fluctuations in the region would help to refine the modeling estimates presented in this study.

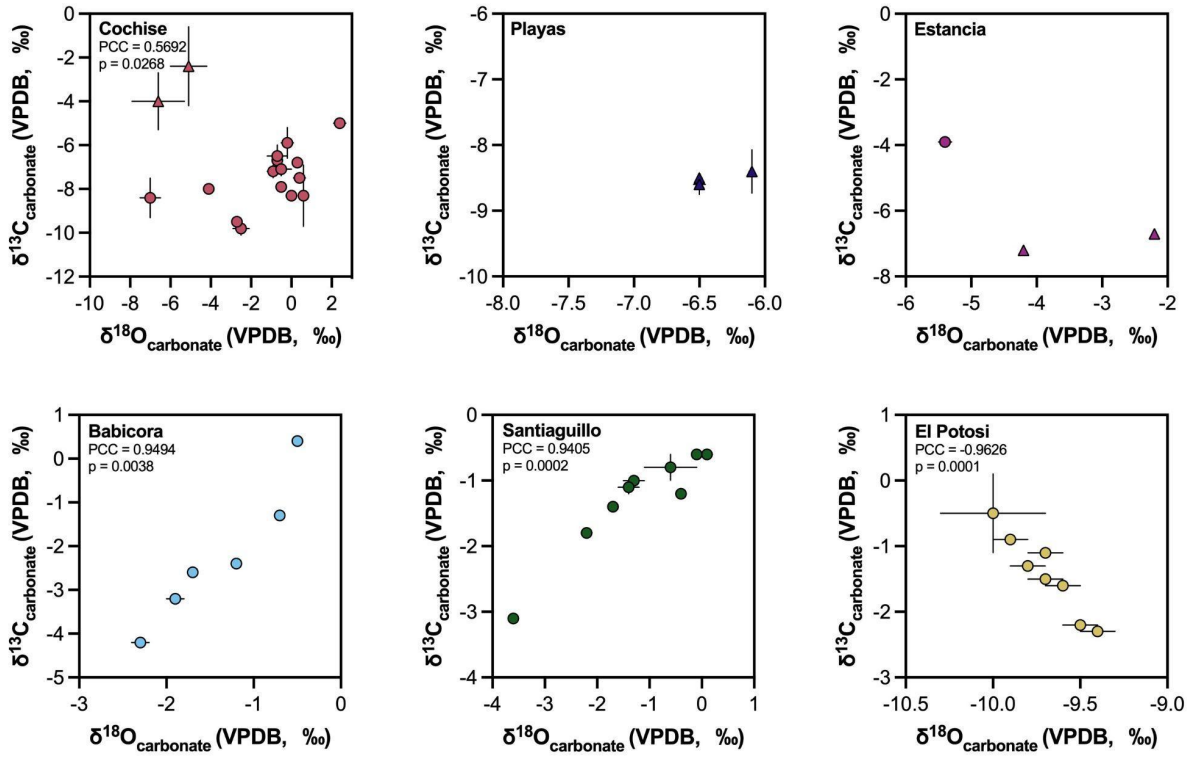

Figure 4.A.1: $\delta^{13}C$-$\delta^{18}O$ covariance in lacustrine sediments at each basin. Pearson's correlation coefficient (PCC) is calculated where there is an adequate sample size. Circles indicate authigenic carbonates or biologically-mediated carbonates, triangles indicate biogenic carbonates.

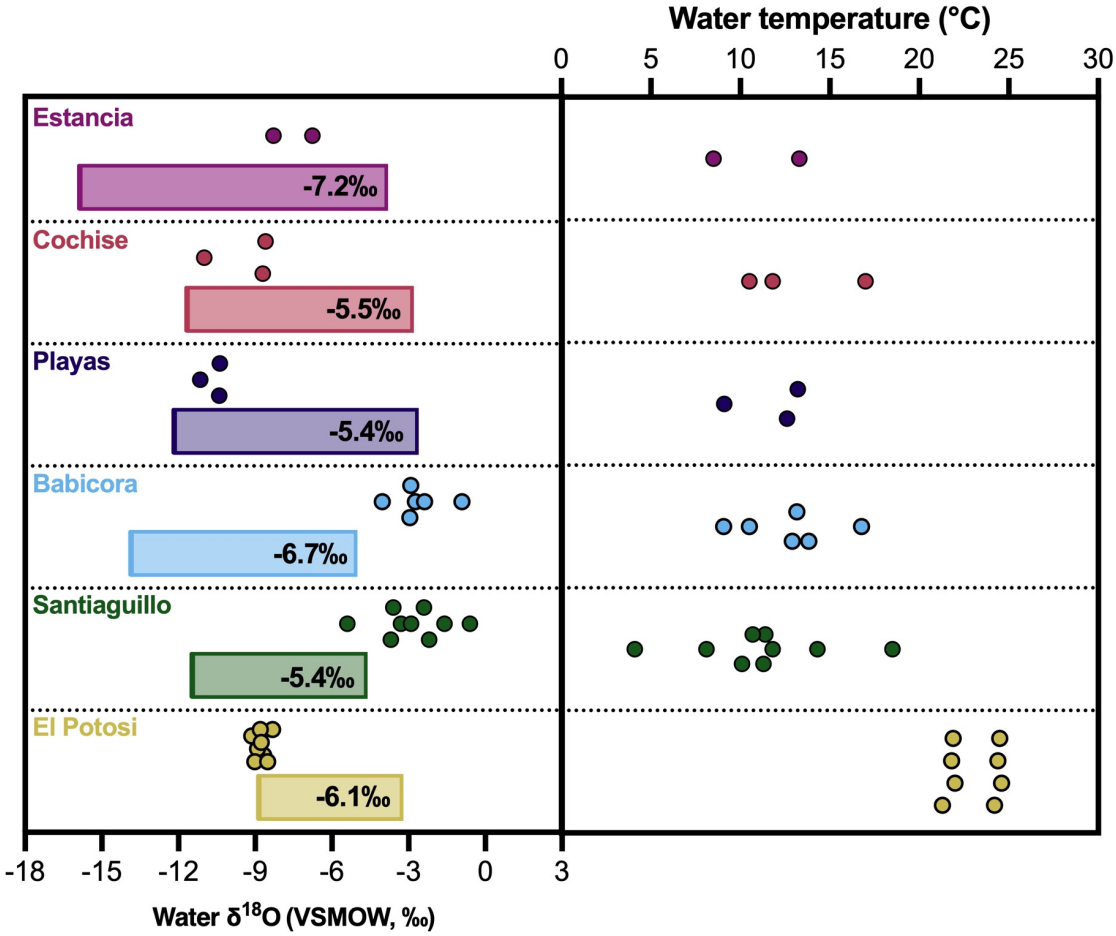

Figure 4.A.2: Reconstructed water $\delta^{18}O$ (left) and water temperatures (right) for paleolakes in this study. Basins are listed from highest latitude to lowest latitude. Values measured in this study are represented by colored circles. Reconstructed water $\delta^{18}O$ for samples is corrected for ice-volume induced enrichment in the global ocean (Tripati et al., 2014). Bars represent the modern range of water isotopes in precipitation for each site from the Online Isotopes in Precipitation Calculator (Bowen, 2023).

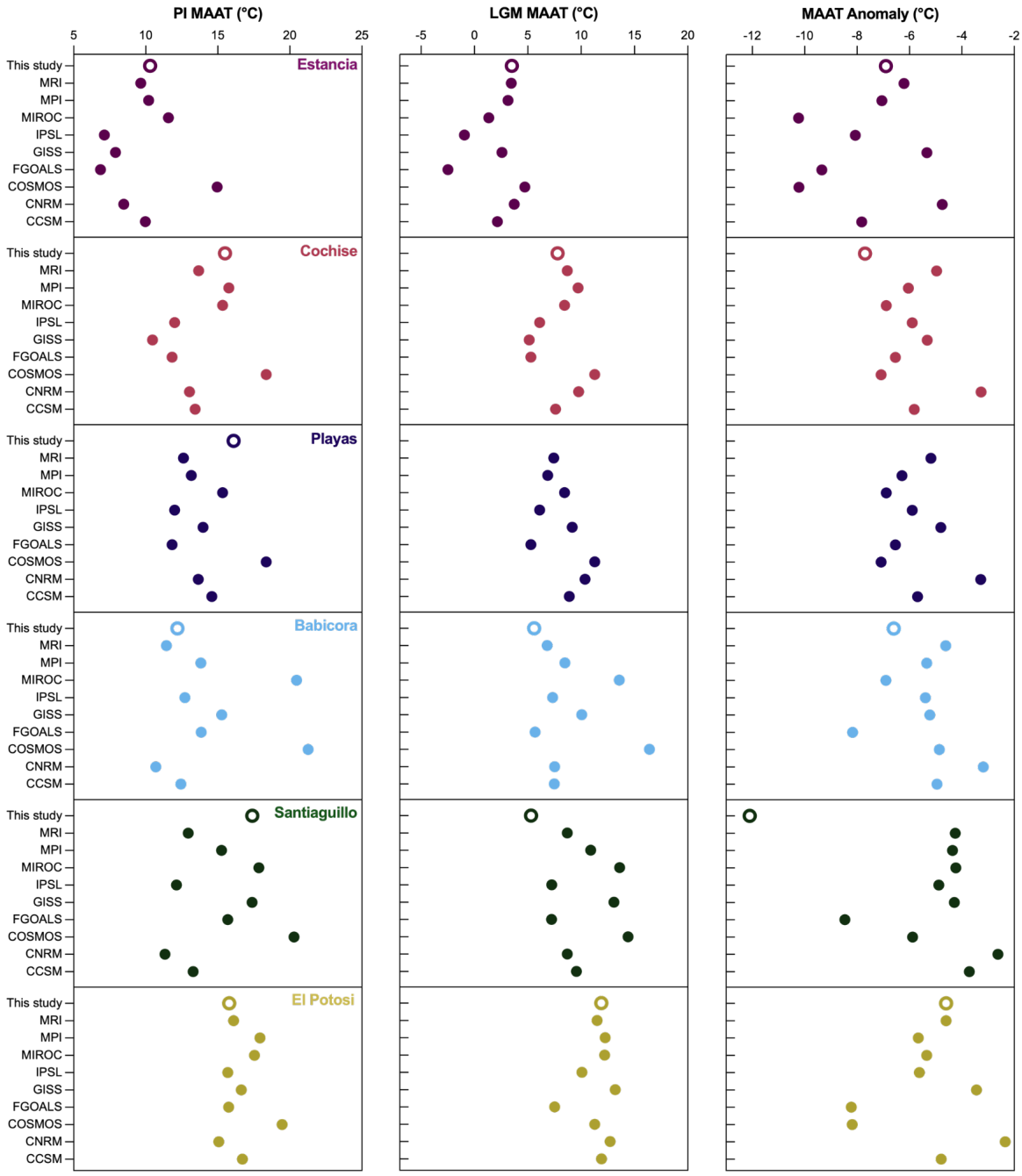

Figure 4.A.3: Comparison of pre-industrial MAAT, Last Glacial Maximum (LGM) MAAT, and temperature anomalies calculated from clumped-isotope analysis or modern climate data (open circles) to nine PMIP3 models (closed circles).

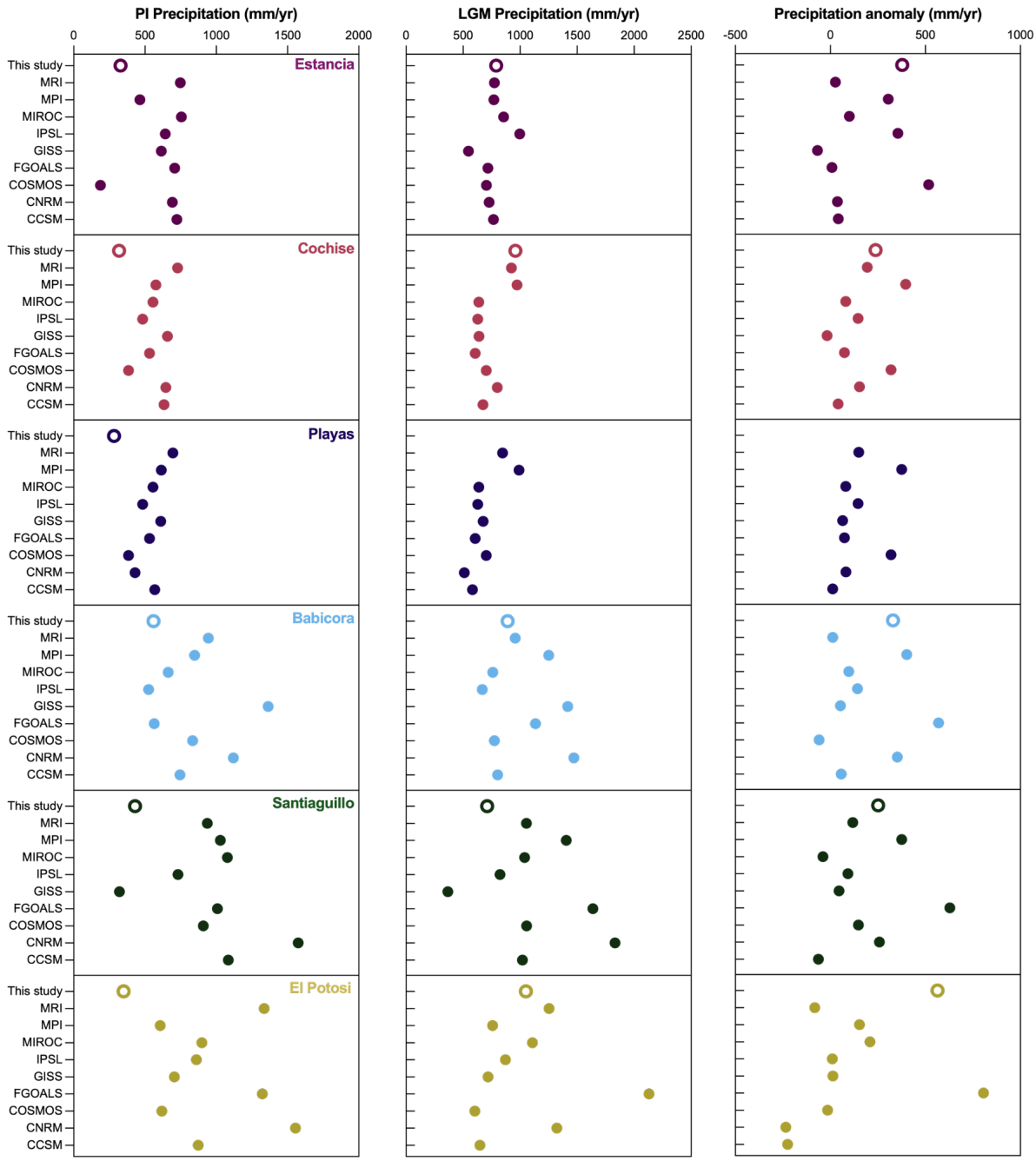

Figure 4.A.4: Comparison of pre-industrial precipitation rates, Last Glacial Maximum (LGM) precipitation rates, and precipitation anomalies calculated from clumped-isotope analysis or modern climate data (open circles) to nine PMIP3 models (closed circles).

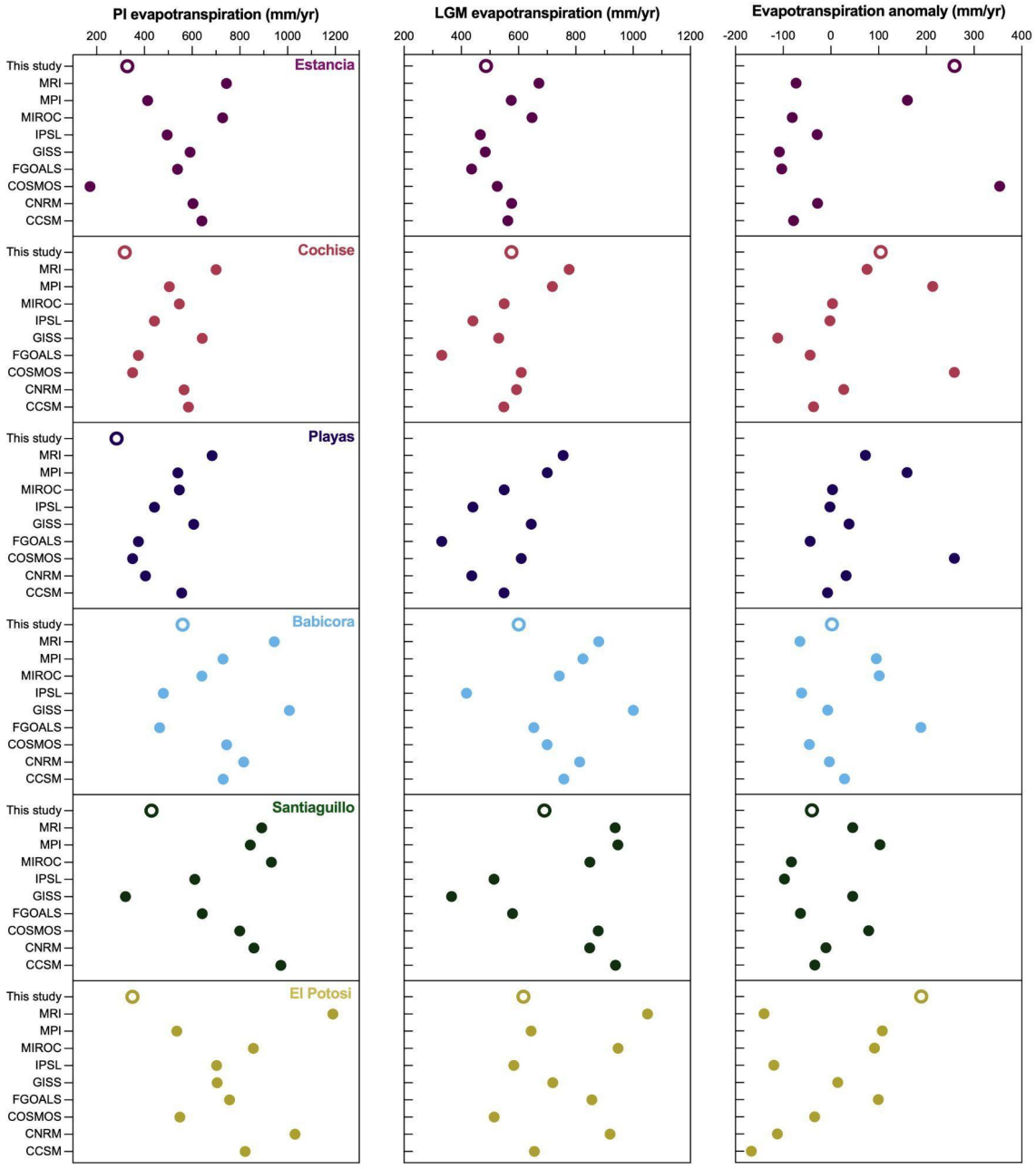

Figure 4.A.5: Comparison of pre-industrial evapotranspiration rates, Last Glacial Maximum (LGM) precipitation rates, and precipitation anomalies calculated from clumped-isotope analysis or modern climate data (open circles) to nine PMIP3 models (closed circles).

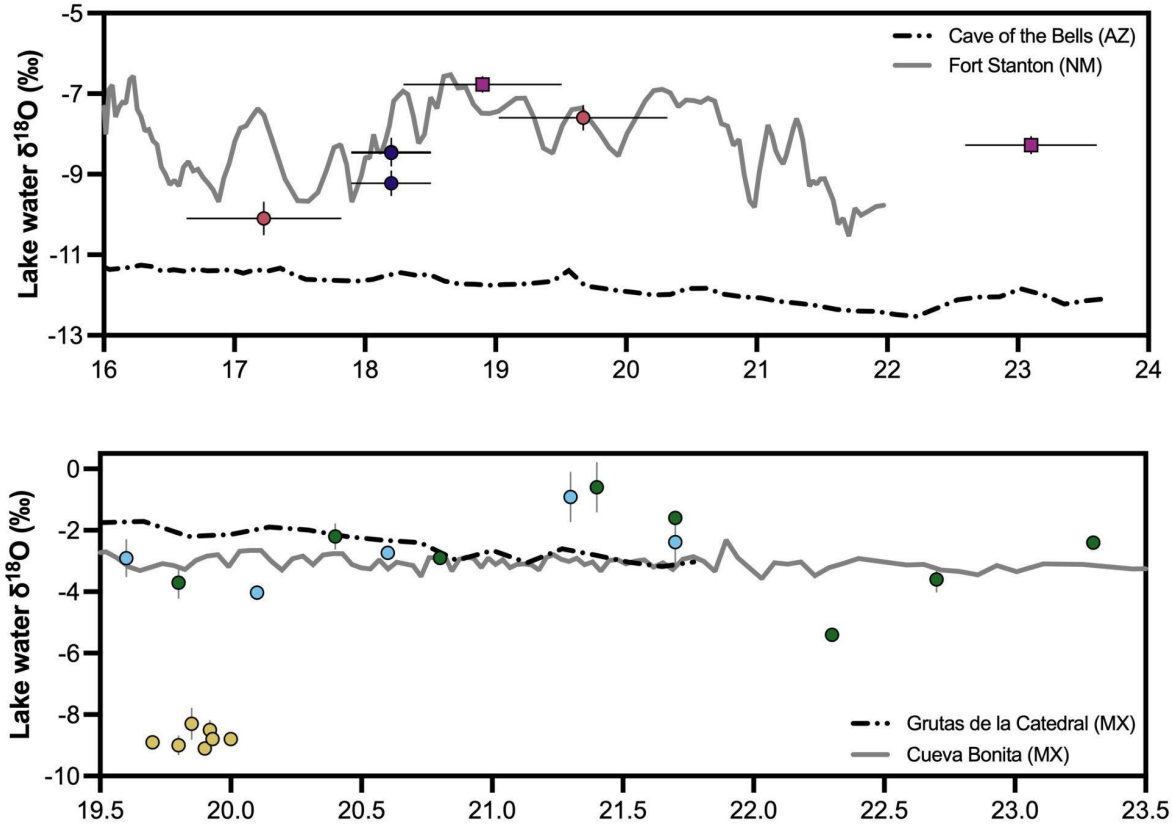

Figure 4.A.6: Temporal evolution of reconstructed lake water $\delta^{18}O$ and nearby speleothem $\delta^{18}O$ records. Speleothem record for Cave of the Bells, Fort Stanton, Cueva Bonita, and Grutas de la Catedral are from Wagner et al. (2010), Asmermom et al. (2010), Wright et al. (2023), and Intveld (2023), respectively.

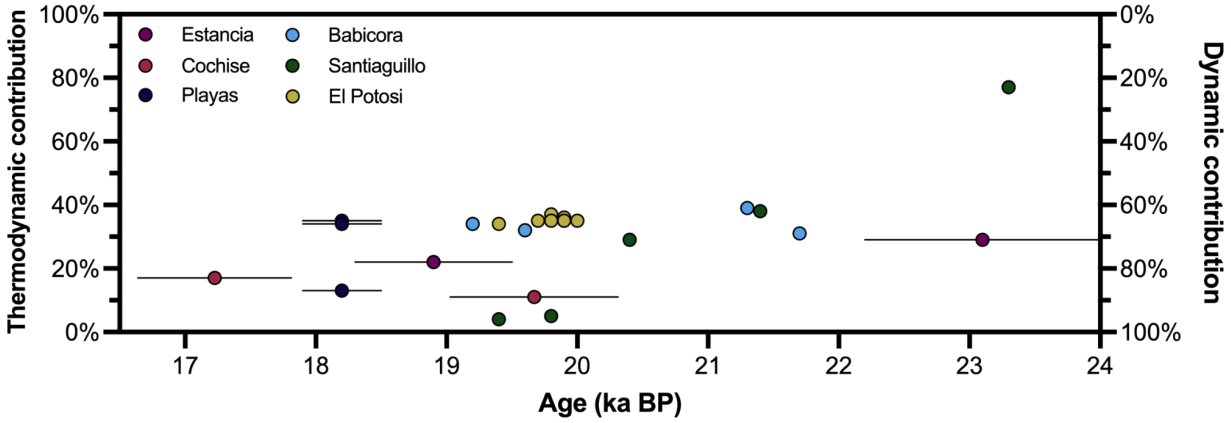

Figure 4.A.7: Partitioning of thermodynamic and dynamic controls on lake levels for basins in Southwestern North America (see Equation 3 and 4). All basins show strong preference for dynamic controls, suggesting that precipitation changes were the dominant influence on lake levels.

8. References

Abatzoglou, J.T., Dobrowski, S.Z., Parks, S.A. & Hegewisch, K.C. (2018) TerraClimate, a high-resolution global dataset of monthly climate and climatic water balance from 1958–2015. *Scientific Data*, *5*(1), 170191. https://doi.org/10.1038/sdata.2017.191.

Allen, B.D. & Anderson, R.Y. (2000) A continuous, high-resolution record of late Pleistocene climate variability from the Estancia basin, New Mexico. *GSA Bulletin*, *112*(9), 1444–1458. https://doi.org/10.1130/0016-7606(2000)112<1444:ACHRRO>2.0.CO;2.

Antinao, J.L. & McDonald, E. (2013) An enhanced role for the Tropical Pacific on the humid Pleistocene–Holocene transition in southwestern North America. *Quaternary Science Reviews*, *78*, 319–341. https://doi.org/10.1016/j.quascirev.2013.03.019.

Asmerom, Y., Polyak, V.J. & Burns, S.J. (2010) Variable winter moisture in the southwestern United States linked to rapid glacial climate shifts. *Nature Geoscience*, *3*(2), 114–117. https://doi.org/10.1038/ngeo754.

Balderas, S. & Lozano-Vilano, L. (1996) Extinction of most Sandia and Potosí valleys (Nuevo León, Mexico) endemic pupfishes, crayfishes and snails. *Ichthyol. Explor. Freshwaters*, *7*.

Bernasconi, S.M., Daëron, M., Bergmann, K.D., Bonifacie, M., Meckler, A.N., Affek, H.P., Anderson, N., Bajnai, D., Barkan, E., Beverly, E., Blamart, D., Burgener, L., Calmels, D., Chaduteau, C., Clog, M., Davidheiser-Kroll, B., Davies, A., Dux, F., Eiler, J., Elliott, B., Fetrow, A.C., Fiebig, J., Goldberg, S., Hermoso, M., Huntington, K.W., Hyland, E., Ingalls, M., Jaggi, M., John, C.M., Jost, A.B., Katz, S., Kelson, J., Kluge, T., Kocken, I.J., Laskar, A., Leutert, T.J., Liang, D., Lucarelli, J., Mackey, T.J., Mangenot, X., Meinicke, N., Modestou, S.E., Müller, I.A., Murray, S., Neary, A., Packard, N., Passey,

B.H., Pelletier, E., Petersen, S., Piasecki, A., Schauer, A., Snell, K.E., Swart, P.K., Tripati, A., Upadhyay, D., Vennemann, T., Winkelstern, I., Yarian, D., Yoshida, N., Zhang, N. & Ziegler, M. (2021) InterCarb: A Community Effort to Improve Interlaboratory Standardization of the Carbonate Clumped Isotope Thermometer Using Carbonate Standards. *Geochemistry, Geophysics, Geosystems*, *22*(5), e2020GC009588. https://doi.org/10.1029/2020GC009588.

Bhattacharya, T., Tierney, J.E., Addison, J.A. & Murray, J.W. (2018) Ice-sheet modulation of deglacial North American monsoon intensification. *Nature Geoscience*, *11*(11), 848–852. https://doi.org/10.1038/s41561-018-0220-7.

Bhattacharya, T., Tierney, J.E. & DiNezio, P. (2017) Glacial reduction of the North American Monsoon via surface cooling and atmospheric ventilation. *Geophysical Research Letters*, *44*(10), 5113–5122. https://doi.org/10.1002/2017GL073632.

Bowen, G.J. (2023) The Online Isotopes in Precipitation Calculator (Version 3.1).

Braconnot, P., Harrison, S.P., Kageyama, M., Bartlein, P.J., Masson-Delmotte, V., Abe-Ouchi, A., Otto-Bliesner, B. & Zhao, Y. (2012) Evaluation of climate models using palaeoclimatic data. *Nature Climate Change*, *2*(6), 417–424. https://doi.org/10.1038/nclimate1456.

Chávez-Lara, C.M. (2019) Ecosystem changes and paleoclimatic implications from the Chihuahua Desert (Mexico) during the late Pleistocene and Holocene.

Chávez-Lara, C.M., Holtvoeth, J., Roy, P.D. & Pancost, R.D. (2019) Lipid biomarkers in lacustrine sediments of subtropical northeastern Mexico and inferred ecosystem changes during the late Pleistocene and Holocene. *Palaeogeography, Palaeoclimatology, Palaeoecology*, *535*, 109343. https://doi.org/10.1016/j.palaeo.2019.109343.

Chávez-Lara, C.M., Roy, P.D., Caballero, M.M., Carreño, A.L. & Lakshumanan, C. (2012) Lacustrine ostracodes from the Chihuahuan Desert of Mexico and inferred Late Quaternary paleoecological conditions. *Revista Mexicana de Ciencias Geológicas*, *29*(2), 422–431.

Chávez-Lara, C.M., Roy, P.D., Pérez, L., Muthu Sankar, G. & Lemus Neri, V.H. (2015) Ostracode and C/N based paleoecological record from Santiaguillo basin of subtropical Mexico over last 27 cal kyr BP. *Revista Mexicana de Ciencias Geológicas*, *32*(1), 1–10.

COHMAP MEMBERS (1988) Climatic Changes of the Last 18,000 Years: Observations and Model Simulations. *Science*, *241*(4869), 1043–1052. https://doi.org/10.1126/science.241.4869.1043.

Comrie, A.C. & Glenn, E.C. (1998) Principal components-based regionalization of precipitation regimes across the southwest United States and northern Mexico, with an application to monsoon precipitation variability. *Climate Research*, *10*(3), 201–215. https://doi.org/10.3354/cr010201.

Craig, H. & Gordon, L.I. (1965) Deuterium and oxygen 18 variations in the ocean and the marine atmosphere.

Douglas, M.W., Maddox, R.A., Howard, K. & Reyes, S. (1993) The mexican monsoon. *Journal of Climate*, *6*(8), 1665–1677.

Eagle, R.A., Risi, C., Mitchell, J.L., Eiler, J.M., Seibt, U., Neelin, J.D., Li, G. & Tripati, A.K. (2013) High regional climate sensitivity over continental China constrained by glacial-recent changes in temperature and the hydrological cycle. *Proceedings of the National Academy of Sciences*, *110*(22), 8813–8818. https://doi.org/10.1073/pnas.1213366110.

Echelle, A.A., Echelle, A.F., Contreras-Balderas, S. & Lozano-Vilano, L. (1995) Genetic

Variation in the Endangered Fish Fauna (Atheriniformes: Cyprinodontidae) Associated with Pluvial Lake Sandia, Nuevo Leon, Mexico. *The Southwestern Naturalist*, *40*(1), 11–17.

Eiler, J.M. (2007) “Clumped-isotope” geochemistry—The study of naturally-occurring, multiply-substituted isotopologues. *Earth and Planetary Science Letters*, *262*(3), 309–327. https://doi.org/10.1016/j.epsl.2007.08.020.

Gat, J.R. (1996) OXYGEN AND HYDROGEN ISOTOPES IN THE HYDROLOGIC CYCLE. *Annual Review of Earth and Planetary Sciences*, *24*(Volume 24, 1996), 225–262. https://doi.org/10.1146/annurev.earth.24.1.225.

Ghosh, P., Adkins, J., Affek, H., Balta, B., Guo, W., Schauble, E.A., Schrag, D. & Eiler, J.M. (2006) 13C–18O bonds in carbonate minerals: A new kind of paleothermometer. *Geochimica et Cosmochimica Acta*, *70*(6), 1439–1456. https://doi.org/10.1016/j.gca.2005.11.014.

González, A.V., Estévez, L.M., Villeda, M.E.Á. & Ceballos, G. (2020) The extinction of the Catarina pupfish Megupsilon aporus and the implications for the conservation of freshwater fish in Mexico. *Oryx*, *54*(2), 154–160. https://doi.org/10.1017/S003060531800056X.

Goodwin, D.H., Schöne, B.R. & Dettman, D.L. (2003) Resolution and Fidelity of Oxygen Isotopes as Paleotemperature Proxies in Bivalve Mollusk Shells: Models and Observations. *PALAIOS*, *18*(2), 110–125. https://doi.org/10.1669/0883-1351(2003)18<110:RAFOOI>2.0.CO;2.

Greve, P., Gudmundsson, L., Orlowsky, B. & Seneviratne, S.I. (2015) Introducing a probabilistic Budyko framework. *Geophysical Research Letters*, *42*(7), 2261–2269.

https://doi.org/10.1002/2015GL063449.

Hargreaves, J.C., Annan, J.D., Ohgaito, R., Paul, A. & Abe-Ouchi, A. (2013) Skill and reliability of climate model ensembles at the Last Glacial Maximum and mid-Holocene. *Climate of the Past*, *9*(2), 811–823. https://doi.org/10.5194/cp-9-811-2013.

Haynes Jr, C.V., Long, A. & Jull, A. (1987) Radiocarbon dates at Willcox Playa, Arizona, bracket the Clovis occupation surface. *Current Research in the Pleistocene*, *4*, 124–126.

Horton, T.W., Defliese, W.F., Tripati, A.K. & Oze, C. (2016) Evaporation induced 18O and 13C enrichment in lake systems: A global perspective on hydrologic balance effects. *Quaternary Science Reviews*, *131*, 365–379. https://doi.org/10.1016/j.quascirev.2015.06.030.

Hren, M.T. & Sheldon, N.D. (2012) Temporal variations in lake water temperature: Paleoenvironmental implications of lake carbonate δ18O and temperature records. *Earth and Planetary Science Letters*, *337*, 77–84. https://doi.org/10.1016/j.epsl.2012.05.019.

Hudson, A.M., Quade, J., Ali, G., Boyle, D., Bassett, S., Huntington, K.W., De los Santos, M.G., Cohen, A.S., Lin, K. & Wang, X. (2017) Stable C, O and clumped isotope systematics and 14C geochronology of carbonates from the Quaternary Chewaucan closed-basin lake system, Great Basin, USA: Implications for paleoenvironmental reconstructions using carbonates. *Geochimica et Cosmochimica Acta*, *212*, 274–302. https://doi.org/10.1016/j.gca.2017.06.024.

Hudson, A.M., Quade, J., Holliday, V.T., Fenerty, B., Bright, J.E., Gray, H.J. & Mahan, S.A. (2023) Paleohydrologic history of pluvial lake San Agustin, New Mexico: Tracking changing effective moisture in southwest North America through the last glacial transition. *Quaternary Science Reviews*, *310*, 108110.

https://doi.org/10.1016/j.quascirev.2023.108110.

Ibarra, D.E., Egger, A.E., Weaver, K.L., Harris, C.R. & Maher, K. (2014) Rise and fall of late Pleistocene pluvial lakes in response to reduced evaporation and precipitation: Evidence from Lake Surprise, California. *GSA Bulletin*, *126*(11–12), 1387–1415. https://doi.org/10.1130/B31014.1.

Intergovernmental Panel on Climate Change (IPCC) (Ed.) (2023) North America. In: *Climate Change 2022 – Impacts, Adaptation and Vulnerability: Working Group II Contribution to the Sixth Assessment Report of the Intergovernmental Panel on Climate Change*. Cambridge, Cambridge University Press, pp. 1929–2042. https://doi.org/10.1017/9781009325844.016.

Intveld, A.B. (2023) *Speleothem-Based Hydroclimate Reconstruction of Northeastern Mexico Across the Last Deglaciation* (Thesis). Massachusetts Institute of Technology.

John, C.M. & Bowen, D. (2016) Community software for challenging isotope analysis: First applications of 'Easotope' to clumped isotopes: Community software for challenging isotope analysis. *Rapid Communications in Mass Spectrometry*, *30*(21), 2285–2300. https://doi.org/10.1002/rcm.7720.

Kaufman, D.S. (2003) Amino acid paleothermometry of Quaternary ostracodes from the Bonneville Basin, Utah. *Quaternary Science Reviews*, *22*(8), 899–914. https://doi.org/10.1016/S0277-3791(03)00006-4.

Kim, S.-T. & O'Neil, J.R. (1997) Equilibrium and nonequilibrium oxygen isotope effects in synthetic carbonates. *Geochimica et Cosmochimica Acta*, *61*(16), 3461–3475. https://doi.org/10.1016/S0016-7037(97)00169-5.

Kim, S.-T., O'Neil, J.R., Hillaire-Marcel, C. & Mucci, A. (2007) Oxygen isotope fractionation

between synthetic aragonite and water: Influence of temperature and Mg2+ concentration. *Geochimica et Cosmochimica Acta*, *71*(19), 4704–4715. https://doi.org/10.1016/j.gca.2007.04.019.

Knutti, R. & Sedláček, J. (2013) Robustness and uncertainties in the new CMIP5 climate model projections. *Nature Climate Change*, *3*(4), 369–373. https://doi.org/10.1038/nclimate1716.

Kowler, A. (2015) *Late Pleistocene Palehydrologic Reconstructions and Radiocarbon Dating in the Southeastern Basin and Range, USA*. The University of Arizona.

Lea, D.W., Pak, D.K., Peterson, L.C. & Hughen, K.A. (2003) Synchroneity of Tropical and High-Latitude Atlantic Temperatures over the Last Glacial Termination. *Science*, *301*(5638), 1361–1364. https://doi.org/10.1126/science.1088470.

Lehner, B. & Grill, G. (2013) Global river hydrography and network routing: baseline data and new approaches to study the world's large river systems. *Hydrological Processes*, *27*(15), 2171–2186. https://doi.org/10.1002/hyp.9740.

Lehner, B., Verdin, K. & Jarvis, A. (2008) New Global Hydrography Derived From Spaceborne Elevation Data. *Eos, Transactions American Geophysical Union*, *89*(10), 93–94. https://doi.org/10.1029/2008EO100001.

Lemons, D.R., Milligan, M.R. & Chan, M.A. (1996) Paleoclimatic implications of late Pleistocene sediment yield rates for the Bonneville Basin, northern Utah. *Palaeogeography, Palaeoclimatology, Palaeoecology*, *123*(1), 147–159. https://doi.org/10.1016/0031-0182(95)00117-4.

Leonard, E.M., Laabs, B.J.C., Robertson, A., Plummer, M.A., Ibarra, D.E. & Caffee, M.W. (2023) Late Pleistocene glaciation in the southernmost Sangre de Cristo Mountains, New

Mexico – Chronology and paleoclimate. *Quaternary Science Advances*, *9*, 100070. https://doi.org/10.1016/j.qsa.2023.100070.

Li, H.-C. & Ku, T.-L. (1997) *δ*13C–*δ*18C covariance as a paleohydrological indicator for closed-basin lakes. *Palaeogeography, Palaeoclimatology, Palaeoecology*, *133*(1), 69–80. https://doi.org/10.1016/S0031-0182(96)00153-8.

Linacre, E.T. (1993) Data-sparse estimation of lake evaporation, using a simplified Penman equation. *Agricultural and Forest Meteorology*, *64*(3–4), 237–256. https://doi.org/10.1016/0168-1923(93)90031-C.

Linacre, E.T. (1994) Estimating U.S. Class A Pan Evaporation from Few Climate Data. *Water International*, *19*(1), 5–14. https://doi.org/10.1080/02508069408686189.

Long, A. (1966) Late Pleistocene and recent chronologies of Playa lakes in Arizona and New Mexico.

Lopez-Maldonado, R., Bateman, J.B., Ellis, A., Bader, N.E., Ramirez, P., Arnold, A., Ajoku, O., Lee, H.-I., Jesmok, G., Upadhyay, D., Mitsunaga, B., Elliott, B., Tabor, C. & Tripati, A. (2023) Paleoclimate Changes in the Pacific Northwest Over the Past 36,000 Years From Clumped Isotope Measurements and Model Analysis. *Paleoceanography and Paleoclimatology*, *38*(2), e2021PA004266. https://doi.org/10.1029/2021PA004266.

Lora, J.M. (2018) Components and Mechanisms of Hydrologic Cycle Changes over North America at the Last Glacial Maximum. *Journal of Climate*, *31*(17), 7035–7051. https://doi.org/10.1175/JCLI-D-17-0544.1.

Lora, J.M. & Ibarra, D.E. (2019) The North American hydrologic cycle through the last deglaciation. *Quaternary Science Reviews*, *226*, 105991. https://doi.org/10.1016/j.quascirev.2019.105991.

Lora, J.M., Mitchell, J.L., Risi, C. & Tripati, A.E. (2017) North Pacific atmospheric rivers and their influence on western North America at the Last Glacial Maximum. *Geophysical Research Letters*, *44*(2), 1051–1059. https://doi.org/10.1002/2016GL071541.

Lora, J.M., Mitchell, J.L. & Tripati, A.E. (2016) Abrupt reorganization of North Pacific and western North American climate during the last deglaciation. *Geophysical Research Letters*, *43*(22), 11,796-11,804. https://doi.org/10.1002/2016GL071244.

Lozano Vilano, M. de L. & Contreras Balderas, S. (1993) Four new species of Cyprinodon from southern Nuevo León, Mexico, with a key to the C. eximius complex (Teleostei: Cyprinodontidae). *Ichthyological Exploration of Freshwaters*, *4*(4), 295–307.

Lucarelli, J.K., Carroll, H.M., Ulrich, R.N., Elliott, B.M., Coplen, T.B., Eagle, R.A. & Tripati, A. (2023) Equilibrated Gas and Carbonate Standard-Derived Dual (Δ47 and Δ48) Clumped Isotope Values. *Geochemistry, Geophysics, Geosystems*, *24*(2), e2022GC010458. https://doi.org/10.1029/2022GC010458.

Lyle, M., Heusser, L., Ravelo, C., Yamamoto, M., Barron, J., Diffenbaugh, N.S., Herbert, T. & Andreasen, D. (2012) Out of the Tropics: The Pacific, Great Basin Lakes, and Late Pleistocene Water Cycle in the Western United States. *Science*, *337*(6102), 1629–1633. https://doi.org/10.1126/science.1218390.

Matsubara, Y. & Howard, A.D. (2009) A spatially explicit model of runoff, evaporation, and lake extent: Application to modern and late Pleistocene lakes in the Great Basin region, western United States. *Water Resources Research*, *45*(6). https://doi.org/10.1029/2007WR005953.

Meinzer, O.E. (1911) *Geology and Water Resources of Estancia Valley, New Mexico: With Notes on Ground-water Conditions in Adjacent Parts of Central New Mexico*. U.S.

Government Printing Office.

Meinzer, O.E., Kelton, F. & Forbes, R.H. (1913) *Geology and water resources of Sulphur spring valley, Arizona*. College of Agriculture, University of Arizona (Tucson, AZ).

Menking, K.M., Anderson, R.Y., Shafike, N.G., Syed, K.H. & Allen, B.D. (2004) Wetter or colder during the Last Glacial Maximum? Revisiting the pluvial lake question in southwestern North America. *Quaternary Research*, *62*(3), 280–288. https://doi.org/10.1016/j.yqres.2004.07.005.

Menking, K.M., Bixby, R.J. & Cutler, S.M. (2022) Diatom evidence for a groundwater divide that limited the extent of Lake Estancia, New Mexico, USA, highstands during the Last Glacial Maximum. *GSA Bulletin*, *135*(1–2), 407–419. https://doi.org/10.1130/B36283.1.

Menking, K.M., Polyak, V.J., Anderson, R.Y. & Asmerom, Y. (2018) Climate history of the southwestern United States based on Estancia Basin hydrologic variability from 69 to 10 ka. *Quaternary Science Reviews*, *200*, 237–252. https://doi.org/10.1016/j.quascirev.2018.09.030.

Mering, J.A. (2015) *New constraints on water temperature at Lake Bonneville from carbonate clumped isotopes*. University of California, Los Angeles.

Mesinger, F., DiMego, G., Kalnay, E., Mitchell, K., Shafran, P.C., Ebisuzaki, W., Jović, D., Woollen, J., Rogers, E., Berbery, E.H., Ek, M.B., Fan, Y., Grumbine, R., Higgins, W., Li, H., Lin, Y., Manikin, G., Parrish, D. & Shi, W. (2006) North American Regional Reanalysis. *Bulletin of the American Meteorological Society*, *87*(3), 343–360. https://doi.org/10.1175/BAMS-87-3-343.

Metcalfe, S., Say, A., Black, S., McCulloch, R. & O'Hara, S. (2002) Wet Conditions during the Last Glaciation in the Chihuahuan Desert, Alta Babicora Basin, Mexico. *Quaternary*

Research, *57*(1), 91–101. https://doi.org/10.1006/qres.2001.2292.

Miller, R.R. & Walters, V. (1972) A new genus of cyprinodontid fish from Nuevo Leon, Mexico. *Contributions in Science*, *233*, 1–13. https://doi.org/10.5962/p.241217.

Oster, J.L., Macarewich, S., Lofverstrom, M., de Wet, C., Montañez, I., Lora, J.M., Skinner, C. & Tabor, C. (2023) North Atlantic meltwater during Heinrich Stadial 1 drives wetter climate with more atmospheric rivers in western North America. *Science Advances*, *9*(46), eadj2225. https://doi.org/10.1126/sciadv.adj2225.

Palacios-Fest, M.R., Carreño, A.L., Ortega-Ramírez, J.R. & Alvarado-Valdéz, G. (2002) A paleoenvironmental reconstruction of Laguna Babícora, Chihuahua, Mexico based on ostracode paleoecology and trace element shell chemistry. *Journal of Paleolimnology*, *27*(2), 185–206. https://doi.org/10.1023/A:1014215818589.

Quiroz-Jimenez, J.D., Roy, P.D., Lozano-Santacruz, R. & Giron-García, P. (2017) Hydrological responses of the Chihuahua Desert of Mexico to possible Heinrich Stadials. *Journal of South American Earth Sciences*, *73*, 1–9. https://doi.org/10.1016/j.jsames.2016.11.001.

Reimer, P.J., Bard, E., Bayliss, A., Beck, J.W., Blackwell, P.G., Ramsey, C.B., Buck, C.E., Cheng, H., Edwards, R.L., Friedrich, M., Grootes, P.M., Guilderson, T.P., Haflidason, H., Hajdas, I., Hatté, C., Heaton, T.J., Hoffmann, D.L., Hogg, A.G., Hughen, K.A., Kaiser, K.F., Kromer, B., Manning, S.W., Niu, M., Reimer, R.W., Richards, D.A., Scott, E.M., Southon, J.R., Staff, R.A., Turney, C.S.M. & Plicht, J. van der (2013) IntCal13 and Marine13 Radiocarbon Age Calibration Curves 0–50,000 Years cal BP. *Radiocarbon*, *55*(4), 1869–1887. https://doi.org/10.2458/azu_js_rc.55.16947.

Ritchie, E.A., Wood, K.M., Gutzler, D.S. & White, S.R. (2011) The Influence of Eastern Pacific Tropical Cyclone Remnants on the Southwestern United States. *Monthly Weather*

Review, *139*(1), 192–210. https://doi.org/10.1175/2010MWR3389.1.

Roy, P.D., Caballero, M., Lozano, S., Morton, O., Lozano, R., Jonathan, M.P., Sánchez, J.L. & Macías, M.C. (2012) Provenance of sediments deposited at paleolake San Felipe, western Sonora Desert: Implications to regimes of summer and winter precipitation during last 50 cal kyr BP. *Journal of Arid Environments*, *81*, 47–58. https://doi.org/10.1016/j.jaridenv.2012.01.008.

Roy, P.D., Chávez-Lara, C.M., Beramendi-Orosco, L.E., Sánchez-Zavala, J.L., Muthu-Sankar, G., Lozano-Santacruz, R., Quiroz-Jimenez, J.D. & López-Balbiaux, N. (2015) Paleohydrology of the Santiaguillo Basin (Mexico) since late last glacial and climate variation in southern part of western subtropical North America. *Quaternary Research*, *84*(3), 335–347. https://doi.org/10.1016/j.yqres.2015.10.002.

Roy, P.D., Quiroz-Jiménez, J.D., Chávez-Lara, C.M. & Sánchez-Zavala, J.L. (2019) Holocene Hydroclimate of the Subtropical Mexico: A State of the Art. In: Torrescano- Valle, N., Islebe, G.A. & Roy, P.D. (Eds.) *The Holocene and Anthropocene Environmental History of Mexico: A Paleoecological Approach on Mesoamerica*. Cham, Springer International Publishing, pp. 39–68. https://doi.org/10.1007/978-3-030-31719-5_3.

Roy, P.D., Quiroz-Jiménez, J.D., Pérez-Cruz, L.L., Lozano-García, S., Metcalfe, S.E., Lozano-Santacruz, R., López-Balbiaux, N., Sánchez-Zavala, J.L. & Romero, F.M. (2013) Late Quaternary paleohydrological conditions in the drylands of northern Mexico: a summer precipitation proxy record of the last 80 cal ka BP. *Quaternary Science Reviews*, *78*, 342–354. https://doi.org/10.1016/j.quascirev.2012.11.020.

Roy, P.D., Rivero-Navarrete, A., Sánchez-Zavala, J.L., Beramendi-Orosco, L.E., Muthu-Sankar, G. & Lozano-Santacruz, R. (2016) Atlantic Ocean modulated hydroclimate of the

subtropical northeastern Mexico since the last glacial maximum and comparison with the southern US. *Earth and Planetary Science Letters*, *434*, 141–150. https://doi.org/10.1016/j.epsl.2015.11.048.

Roy, P.D., Selvam, S., Gopinath, S., Logesh, N., Sánchez-Zavala, J.L. & Lakshumanan, C. (2022) Geochemical evolution and seasonality of groundwater recharge at water-scarce southeast margin of the Chihuahuan Desert in Mexico. *Environmental Research*, *203*, 111847. https://doi.org/10.1016/j.envres.2021.111847.

Roy, P.D., Vera-Vera, G., Sánchez-Zavala, J.L., Shanahan, T.M., Quiroz-Jiménez, J.D., Curtis, J.H., Girón-García, P., Lemus-Neri, V.H. & Muthusankar, G. (2020) Depositional histories of vegetation and rainfall intensity in Sierra Madre Oriental Mountains (northeast Mexico) since the late Last Glacial. *Global and Planetary Change*, *187*, 103136. https://doi.org/10.1016/j.gloplacha.2020.103136.

Santi, L., Arnold, A.J., Ibarra, D.E., Whicker, C.A., Mering, J.A., Lomarda, R.B., Lora, J.M. & Tripati, A. (2020) Clumped isotope constraints on changes in latest Pleistocene hydroclimate in the northwestern Great Basin: Lake Surprise, California. *GSA Bulletin*, *132*(11–12), 2669–2683. https://doi.org/10.1130/B35484.1.

Schauble, E.A., Ghosh, P. & Eiler, J.M. (2006) Preferential formation of 13C–18O bonds in carbonate minerals, estimated using first-principles lattice dynamics. *Geochimica et Cosmochimica Acta*, *70*(10), 2510–2529. https://doi.org/10.1016/j.gca.2006.02.011.

Schmidt, M.W., Spero, H.J. & Lea, D.W. (2004) Links between salinity variation in the Caribbean and North Atlantic thermohaline circulation. *Nature*, *428*(6979), 160–163. https://doi.org/10.1038/nature02346.

Servicio Meteorológico Nacional (2023). Available at : https://smn.conagua.gob.mx/es/.

Soetaert, K., Cash, J. & Mazzia, F. (2010) Package bvpSolve, solving boundary value problems in R. *Journal of Statistical Software*, *33*(9), 1–25.

Sun, C., Tian, L., Shanahan, T.M., Partin, J.W., Gao, Y., Piatrunia, N. & Banner, J. (2022) Isotopic variability in tropical cyclone precipitation is controlled by Rayleigh distillation and cloud microphysics. *Communications Earth & Environment*, *3*(1), 1–10. https://doi.org/10.1038/s43247-022-00381-1.

Terrazas, A., Hwangbo, N., Arnold, A.J., Ulrich, R.N. & Tripati, A. (2023) Seasonal lake-to-air temperature transfer functions derived from an analysis of 965 modern lakes: A tool for lacustrine proxy model comparison. *Authorea Preprints*.

Tripati, A.K., Hill, P.S., Eagle, R.A., Mosenfelder, J.L., Tang, J., Schauble, E.A., Eiler, J.M., Zeebe, R.E., Uchikawa, J., Coplen, T.B., Ries, J.B. & Henry, D. (2015) Beyond temperature: Clumped isotope signatures in dissolved inorganic carbon species and the influence of solution chemistry on carbonate mineral composition. *Geochimica et Cosmochimica Acta*, *166*, 344–371. https://doi.org/10.1016/j.gca.2015.06.021.

Tripati, A.K., Sahany, S., Pittman, D., Eagle, R.A., Neelin, J.D., Mitchell, J.L. & Beaufort, L. (2014) Modern and glacial tropical snowlines controlled by sea surface temperature and atmospheric mixing. *Nature Geoscience*, *7*(3), 205–209. https://doi.org/10.1038/ngeo2082.

Upadhyay, D., Lucarelli, J., Arnold, A., Flores, R., Bricker, H., Ulrich, R.N., Jesmok, G., Santi, L., Defliese, W., Eagle, R.A., Carroll, H.M., Bateman, J.B., Petryshyn, V., Loyd, S.J., Tang, J., Priyadarshi, A., Elliott, B. & Tripati, A. (2021) Carbonate clumped isotope analysis (Δ47) of 21 carbonate standards determined via gas-source isotope-ratio mass spectrometry on four instrumental configurations using carbonate-based standardization

and multiyear data sets. *Rapid Communications in Mass Spectrometry*, *35*(17), e9143. https://doi.org/10.1002/rcm.9143.

Van der Schalie, H. & Berry, E.G. (1973) *Effects of temperature on growth and reproduction of aquatic snails*, Vol. 73. US Government Printing Office.

Versteegh, E.A., Vonhof, H.B., Troelstra, S.R., Kaandorp, R.J. & Kroon, D. (2010) Seasonally resolved growth of freshwater bivalves determined by oxygen and carbon isotope shell chemistry. *Geochemistry, Geophysics, Geosystems*, *11*(8). https://doi.org/10.1029/2009GC002961.

Wagner, J.D., Cole, J.E., Beck, J.W., Patchett, P.J., Henderson, G.M. & Barnett, H.R. (2010) Moisture variability in the southwestern United States linked to abrupt glacial climate change. *Nature Geoscience*, *3*(2), 110–113.

Waters, M.R. (1989) Late Quaternary Lacustrine History and Paleoclimatic Significance of Pluvial Lake Cochise, Southeastern Arizona. *Quaternary Research*, *32*(1), 1–11. https://doi.org/10.1016/0033-5894(89)90027-6.

Western Regional Climate Center (2023). Available at : https://wrcc.dri.edu/Climate/summaries.php.

Wright, K.T., Johnson, K.R., Marks, G.S., McGee, D., Bhattacharya, T., Goldsmith, G.R., Tabor, C.R., Lacaille-Muzquiz, J.-L., Lum, G. & Beramendi-Orosco, L. (2023) Dynamic and thermodynamic influences on precipitation in Northeast Mexico on orbital to millennial timescales. *Nature Communications*, *14*(1), 2279. https://doi.org/10.1038/s41467-023-37700-9.

Yan, H., Lee, X., Zhou, H., Cheng, H., Peng, Y. & Zhou, Z. (2009) Stable isotope composition of the modern freshwater bivalve Corbicula fluminea. *Geochemical Journal*, *43*(5), 379–

387. https://doi.org/10.2343/geochemj.1.0035

SUMMARY

This thesis advances the understanding of past and future hydroclimates using clumped isotope data from modern and Pleistocene freshwater carbonates. Chapter 1 focuses on the modern systematics of clumped isotopes in four different archives of modern freshwater carbonates: biogenic (gastropods and bivalves), fine-grained authigenic, biologically-mediated (tufas and stromatolites), and travertine carbonates. We use independently derived estimates of water temperature in concert with measurements of Δ_{47} to constrain the Δ_{47}-temperature dependence, and find evidence for material-specific differences. The calibrations presented in this chapter pave the way for more robust reconstructions of formation temperature and source water $\delta^{18}O$, and are applied in Chapters 2-4.

Chapter 2 explored the drivers of positive water balance that allowed Lake Bonneville to reach an area of 52,000 km^2, similar to the size of modern-day Lake Superior. In Bonneville's initial ascent at ~23-22 ka, when there was an abrupt rise in lake level of over 100 m, there was a 1.5 - 2.0 times modern precipitation forcing. Lake levels rose more gently until the highstand was reached at 18 ka, when there was the largest degree of temperature depression, when the suppression of evaporative-fueled lake growth.

Chapter 3 aimed to test for and quantify the magnitude and extent of a hypothesized precipitation dipole in Nevada and California and Oregon, using four lakes from the Northern Great Basin. Results for the northwestern lakes demonstrate that rising lake levels were primarily governed by reductions in temperatures and evaporation rates that led to a positive water balance. In contrast, the two basins in Nevada showed elevated lake levels due mainly to increased precipitation, with values ranging from 2 - 4 times modern rates.

Chapter 4 examines lakes in Arizona, New Mexico, and Northern Mexico, a region that today is dominated by summer monsoonal precipitation. The lake highstands in the southwestern US were associated with increased precipitation (1.5 - 3 times modern values) that is isotopically consistent with a winter-derived moisture source. In Northern Mexico, there were colder and wetter climates, with higher positive precipitation anomalies further south, likely derived from increases in Eastern Pacific cyclones delivering moisture in the late summer and autumn months.

Given the disagreement of precipitation change in model projections in the face of anthropogenic climate change, the paleoclimatic record can help in reducing the uncertainty in water availability in these drought-prone regions. All together, the data presented in this dissertation provide observational benchmarks that contribute to the understanding of drivers of changes in the water cycle under different climate forcings. Evaluation of climate models using paleoclimatic proxies, such as those presented in Chapters 2-4, can improve process-representation in climate models and provide important insights relevant to navigating challenges in future water resources.